Passively Q-Switched and Mode-Locked Pulse Generation in a Ho:YAG Laser

Jonte Reilly

Thesis submitted for the degree of

Master of Philosophy

in

Physics

at The University of Adelaide

Faculty of Sciences, Engineering and Technology

School of Physics, Chemistry and Earth Sciences

June 2024



THE UNIVERSITY of ADELAIDE

Contents

Abstract **xvii**

Signed Statement **xix**

Acknowledgements **xx**

Dedication **xxi**

1 Introduction 1

1.1 Ultrashort and Short Pulsed Lasers 1

1.2 Applications of USPL Sources at 2.1 µm 2

1.2.1 Ultrashort Spectroscopy 2

1.2.2 Biomedical 3

1.2.3 Materials Processing 4

1.2.4 LiDAR and Atmospheric Sensing 5

1.2.5 Pump Sources for Mid-Infrared Generation 6

1.2.6 Soft x-rays via High Harmonic Generation 7

1.2.7 Frequency Combs 8

1.2.8 Defence and Aerospace 8

1.3 SESAM Mode-Locked Bulk Lasers 9

1.4 SESAM Q-Switched Bulk Lasers 13

1.5 Research Objectives 14

1.6 Thesis Outline 16

2 Theoretical Framework 18

2.1 Introduction 18

2.2 Optical Pulses 19

2.2.1 Introduction to Pulses 19

2.2.2 Time-Bandwidth Product 21

2.2.3 Gain Bandwidth and Gain Narrowing 22

2.2.4 Dispersion 24

2.3 Nonlinear Pulse Propagation 31

2.3.1 The Optical Kerr Effect 32

2.3.2 The Nonlinear Schrödinger Equation 36

2.4 Passive Pulse Generation 39

2.4.1 Mode Superposition Theory 39

2.4.2 Q-Switching Theory 41

2.4.3 Saturable Absorbers 43

2.4.4 Semiconductor Saturable Absorber Mirrors 44

2.4.5 Passive Mode-Locking Models 50

2.5 Passive Mode-Locking Regimes 53

2.5.1 Q-switched Mode-Locking 54

2.5.2 Continuous-Wave Mode-Locking 55

2.5.3 Multi-Pulse Mode-Locking 55

2.6 Pulse Characterisation Techniques 56

2.6.1 Intensity Noise and Timing Jitter 56

2.6.2 Characterisation Apparatus 58

2.6.3 Diagnostics Overview 62

2.7 Chapter Summary 63

3 Development and Characterisation of the Thulium-Fibre Pump Source 64

3.1 Introduction 64

3.2 Ho:YAG Gain Media for Pulsed Operation 65

3.3 Ho:YAG Absorption Spectroscopy 66

3.4 Thulium-Fibre Laser Development 69

3.4.1 Diode Power Characterisation 69

3.4.2 Cavity Configuration 70

3.4.3 Wavelength Tuning 72

3.5 Characterisation 75

3.6 Chapter Summary 79

4 Continuous-Wave Operation and SESAM Q-Switching of a Ho:YAG Laser 80

4.1 Introduction 80

4.2 Resonator Architecture 81

4.2.1 Laser Cavity Design and Modelling 81

4.2.2 Diagnostic Setup 84

4.3 Continuous-Wave Lasing Characterisation 86

4.4 Passive SESAM Q-Switching Results 89

4.4.1 SESAM Specifications 89

4.4.2 SESAM Q-Switching with 1.2% Modulation Depth 91

4.4.3 SESAM Q-Switching with 12% Modulation Depth 98

4.4.4 SESAM Q-Switching with 18% Modulation Depth 102

4.5 Discussion and Comparison 107

4.6 Chapter Summary 111

5 Q-Switching and Continuous-Wave Mode-Locking of a Ho:YAG Laser 113

5.1 Introduction 113

5.2 Resonator Configuration 114

5.2.1 Laser Cavity Design and Modelling 114

5.2.2 Diagnostic Setup 119

5.2.3 Extended Cavity Continuous-Wave Lasing Characterisation 120

5.3 SESAM Mode-Locking Results and Discussion 122

5.3.1 Preamble 122

5.3.2 Q-Switched Mode-Locking 124

5.3.3 Continuous-Wave Mode-Locking 127

5.4 Chapter Summary 133

6 Conclusion 135

6.1 Introduction 135

6.2 Summary of Results 137

6.2.1 Continuous-Wave Laser Resonator Results 137

6.2.2 Q-Switched Results 138

6.2.3 Mode-Locked Results 139

6.3 Future Work 140

6.3.1 Improvements to the Pump Source 140

6.3.2 Q-Switched Pulse Train Stability and Power Scaling 141

6.3.3 SESAM Optimisation for Q-Switching 142

6.3.4 Q-Switching Capabilities Across Output Couplers 142

6.3.5 Additional Spectrum Generation for Mode-Locking 142

6.3.6 Pulse Energy and Peak Power Measurements 143

6.3.7 Dispersion Management 144

6.3.8 Alignment Precision Controls and SESAM Cooling 144

6.4 Final Remarks 144

A Two-Photon Absorption **146**

B Frequency-Resolved Optical Gating **148**

C Ho:YAG Energy Scheme **150**

D Introduction to Optical Fibres **152**

E Beam Quality Assessment **154**

F Beam Profiling Camera Error Assessment **161**

References **164**

List of Tables

Table 1.1: Summary characteristics for relevant 2 µm SESAM mode-locked bulk lasers. 10
Table 1.2: Summary characteristics for a range of SESAM Q-switched bulk lasers. 14
Table 2.1: Nonlinear refractive indices for materials commonly used in optical elements [70]. 32
Table 2.2: Summary on the characteristic parameters of a SESAM. 50
Table 2.3: Summary on the diagnostic instruments required for a pulse train characterisation. 62
Table 4.1: Characteristic parameters of the three SESAMs under investigation. 90
Table 6.1: Continuous-wave laser resonator performance summary. 138
Table 6.2: Q-switched Ho:YAG laser resonator performance summary. 139
Table 6.3: Mode-locked Ho:YAG laser resonator performance summary. 140
Table F.1: Beam diameter at 7 locations using the beam profiler. 162
Table F.2: Statistics on the beam diameters at 7 locations using the beam profiler. 162

List of Figures

Figure 2.1: Typical time evolution of the electric field of few-cycle laser pulses. 19
Figure 2.2: (a) A positively chirped pulse and (b) a negatively chirped pulse. Pulse duration of 100 as, centre wavelength of 8 nm, $GDD = 0.5\times10^{-3}$ as^2 (a) and $GDD = -0.5\times10^{-3}$ as^2 (b) [105]. 28
Figure 2.3: The effect of $GDD = 5$ fs^2 (red) and $GDD = -5$ fs^2 (blue) on an unchirped 6.7 fs pulse (black) of 100 nm spectral bandwidth centred at 800 nm [120]. 29
Figure 2.4: Normal and anomalous dispersion regimes for *GVD* and the corresponding wavelength ranges [121]. 29
Figure 2.5: Schematic representation of a chirped mirror with negative *GDD* where $\lambda_1 < \lambda_2 < \lambda_3$ [122]. 30
Figure 2.6: Instantaneous frequency (red) of an initially bandwidth-limited pulse (blue) which has experienced SPM. 35
Figure 2.7: The total electric field of 10 (blue), 50 (red), and 100 (purple) longitudinal modes with a fixed phase relation. 41
Figure 2.8: Temporal evolution of the output power (blue) compared to the total losses (purple) and gain (red) in a passively Q-switched laser. 42
Figure 2.9: Generic architecture and sequencing of a SESAM. 45
Figure 2.10: Typical structures of (a) resonant and (b) anti-resonant GaAs/AlAs Bragg mirror SESAMS, with the incident field intensity represented by the green and red trace respectively. 46
Figure 2.11: Example of a nonlinear reflectance profile for a SESAM with a modulation depth of $\Delta R = 1.5\%$ and non-saturable loss of $\Delta R_{ns} = 0.5\%$ as a function of saturation. 48
Figure 2.12: Fundamental passive mode-locking models: (a) fast saturable absorber mode-locking, (b) slow saturable absorber mode-locking with dynamic gain and, (c) slow saturable absorber mode-locking without dynamic gain but supported by soliton shaping. 51

Figure 2.13: A pulse train intensity with pulse period *T*. Intensity noise *ΔI(t)* and timing jitter *ΔT(t)* are illustrated as small deviations from ideal stability. 57
Figure 2.14: Optical intensity autocorrelation using SHG in a non-collinear configuration. 61
Figure 3.1: Experimental setup for absorption spectroscopy of the Ho:YAG crystal as the target medium. 67
Figure 3.2: Absorption spectra of a 40 mm 0.7 wt.% doped Ho:YAG slab at 295 K. 68
Figure 3.3: Absorption spectra of a 40 mm 0.7 wt.% doped Ho:YAG slab at 295 K (orange) with the normalised atmospheric absorption superimposed (blue). 68
Figure 3.4: Output power of the 75 W, 793 nm diode (BrightLase, ES-6207-0001) as a function of driving current. 70
Figure 3.5: Schematic of the thulium-fibre laser, with splice locations marked with "X." The labelled components include two fibre Bragg gratings and a cladding light stripper. . 71
Figure 3.6: Optical spectrum of the thulium-fibre laser output (blue) superimposed on the normalised absorption spectrum of the Ho:YAG crystal (red). 72
Figure 3.7: Atmospheric attenuation of the thulium-fibre laser output power at 1906.45 nm relative to propagation distance through air. The plot illustrates the variation in output power for diode output powers of 34 W and 42 W. 73
Figure 3.8: Thermally tuned emission spectrum of the thulium-fibre laser (blue) superimposed on the room-temperature emission spectrum (blue – dashed) and the Ho:YAG absorption spectrum (red). 74
Figure 3.9: Temperature of the HR FBG to the active splice as a function of diode output power, indicating a maximum output power of 19.8 W as the glass transition temperature is approached. 76
Figure 3.10: Power output of the thulium-fibre laser as a function of diode pumping power with a regression line indicating a slope efficiency of 43.98% and a lasing threshold of 7.15 W. 76
Figure 3.11: Optical spectrum of the thulium-fibre laser output indicating a peak wavelength of 1906.75 nm. 77
Figure 3.12: Peak wavelength of the thulium-fibre laser as a function of diode output power. 77

Figure 3.13: Beam profile of the thulium-fibre laser after transmission through an aplanatic lens with an effective focal length of f = 25.5 mm. 78
Figure 4.1: Schematic of the resonator used for the CW operation and SESAM Q-switching of Ho:YAG laser. DM1 and DM2: Dichroic mirrors. 82
Figure 4.2: Beam radius within the primary Q-switched resonator design as a function of distance across the cavity. 84
Figure 4.3: Complete Q-switched resonator setup with the diagnostic arrangement used to characterise all Q-switched results. L1: f = 25.5 mm aplanatic lens. L2: f = 75 mm plano-convex lens. L3: f = 150 mm plano-convex lens. L4: f = 300 mm air-spaced doublet. SM: Steering mirror. DM: Dichroic mirror. OC: Output coupler. BD: Beam dump. FM: Flip mount installed with a 45° HR mirror for 2097 nm. ND: Neutral density filter. WinCamD: Beam profiling camera. PD: Photodetector. FSFC: Free-space to fibre coupler. 85
Figure 4.4: A histogram of the CW Ho:YAG output power fluctuations over 120 seconds at a pump power of 5.6 W. The sample size of 21,600 yields a mean value of 1.507 W with a standard deviation of 5.251×10^{-3} W. 87
Figure 4.5: CW Ho:YAG output power as a function of pump power. The regression line indicates a slope efficiency of 52.65%. 87
Figure 4.6: CW Ho:YAG optical spectrum featuring two peaks at 2090.35 nm and 2096.55 nm. 88
Figure 4.7: Beam profile of the CW Ho:YAG laser, corresponding to a beam quality of M_x^2 = 1.06 and M_y^2 = 1.05. 89
Figure 4.8: Ho:YAG average output power with the ΔR = 1.2% SESAM, plotted as a function of pump power alongside the equivalent CW output power. The regression line specifies a slope efficiency of 50.10%. 91
Figure 4.9: An example of the oscillatory intensity behaviour from the ΔR = 1.2% SESAM Q-switched Ho:YAG pulse train at a pump power of 13.5 W. 92
Figure 4.10: An example of Gaussian pulse curve-fitting with a ΔR = 1.2% SESAM Q-switched Ho:YAG pulse trace at a pump power of 18.5 W. The FWHM yields a pulse duration of 1.11 µs for this trace. 93

Figure 4.11: (a) Pulse durations and repetition rates and (b) pulse energies and peak powers of the ΔR = 1.2% SESAM Q-switched Ho:YAG plotted as a function of pump power. 94
Figure 4.12: Optical spectrum of the ΔR = 1.2% SESAM Q-switched Ho:YAG laser. The spectrum displays dual emission at 2089.85 nm and 2096.95 nm. 95
Figure 4.13: Beam profile of the ΔR = 1.2% SESAM Q-switched Ho:YAG laser. This corresponds to a beam quality of M_x^2 = 1.06 and M_y^2 = 1.05. 95
Figure 4.14: Schematic of the secondary resonator used for the SESAM Q-switching of the Ho:YAG laser under a tighter SESAM spot size. DM1 and DM2: Dichroic mirrors. 96
Figure 4.15: Beam radius within the secondary Q-switched resonator design as a function of distance across the cavity. 96
Figure 4.16: Example of a pulse train obtained from the ΔR = 1.2% SESAM Q-switched Ho:YAG laser. 97
Figure 4.17: Ho:YAG average output power using the ΔR = 12% SESAM, plotted as a function of pump power alongside the equivalent CW output power. The regression line specifies a slope efficiency of 26.12%. 98
Figure 4.18: (a) Pulse durations and repetition rates and (b) pulse energies and peak powers of the ΔR = 12% SESAM Q-switched Ho:YAG, plotted as a function of pump power. 99
Figure 4.19: Optical spectrum of the ΔR = 12% SESAM Q-switched Ho:YAG laser. The spectrum features a single peak emission centred at 2090.15 nm. 100
Figure 4.20: Beam profile of the ΔR = 12% SESAM Q-switched Ho:YAG laser. This illustrates a beam quality of M_x^2 = 1.07 and M_y^2 = 1.08. 100
Figure 4.21: Example of a pulse train obtained from the ΔR = 12% SESAM Q-switched Ho:YAG laser. 101
Figure 4.22: Ho:YAG average output power using the ΔR = 18% SESAM, plotted as a function of pump power alongside the equivalent CW lasing output power. The regression line corresponds to a slope efficiency of 22.80%. 102
Figure 4.23: (a) Pulse durations and repetition rates and (b) pulse energies and peak powers of the ΔR = 18% SESAM Q-switched Ho:YAG laser, plotted as a function of pump power. 103

Figure 4.24: 35 kHz Q-switched Ho:YAG laser pulse train using the ΔR = 18% SESAM and corresponding to a *RIN* of 2.76%. 104
Figure 4.25: Optical spectrum of (a) CW lasing, and ΔR = 18% SESAM Q-switched Ho:YAG lasing at (b) threshold, and (c) a maximum pump power of 19.7 W. 105
Figure 4.26: Beam profile of the ΔR = 18% SESAM Q-switched Ho:YAG laser. This illustrates a beam quality of M_x^2 = 1.06 and M_y^2 = 1.07. 106
Figure 4.27: Comparative plots of (a) slope efficiency, (b) pulse durations, (c) pulse repetition rates, (d) pulse energies, and (e) pulse peak powers for the three characterised SESAMs. 107
Figure 4.28: Relative change in pulse duration from threshold in the three SESAM models plotted against pump power (a) and average output power (b). 109
Figure 4.29: Relative change in pulse repetition rate from threshold in the three SESAM models plotted against pump power (a) and average output power (b). 109
Figure 4.30: Pulse energy per output power (a) and pulse peak power per output power (b) as a function of pump power of each of the three characterised SESAM models. 110
Figure 5.1: Resonator schematic for the SESAM mode-locking of the Ho:YAG laser. DM1 and DM2: Dichroic mirrors. The optional array of chirped mirrors for dispersion tuning is outlined in blue. A sapphire window is positioned between the r = 500 mm mirror and the SESAM. 115
Figure 5.2: Tangential (orange) and sagittal (blue) beam radius within the mode-locked Ho:YAG resonator as a function of the distance across the cavity from the output coupler. 118
Figure 5.3: Tangential (orange) and sagittal (blue) beam radii at the SESAM and tangential (green) and sagittal (red) beam radii in the centre of the Ho:YAG slab as a function of distance between the r = 500 mm mirror and the SESAM. 119
Figure 5.4: Laser resonator setup with the diagnostic arrangement used to characterise mode-locked Ho:YAG dynamics. L1: f = 25.5 mm aplanatic lens. SM1 and SM2: Steering mirror. DM1 and DM2: Dichroic mirror. OC: Output coupler. BD: Beam dump. FM: Flip mount installed with a CaF_2 wedge. M1 and M3: r = 500 mm mirror. M2: r = 1000 mm mirror. W1: 5 mm sapphire window at 60°. HWP: Half-wave plate. CM1-6: -1000 fs^2 chirped mirrors. 119

Figure 5.5: CW Ho:YAG output power for the mode-locking resonator design as a function of pump power, with a regression line indicating a slope efficiency of 15.55%. 121
Figure 5.6: CW Ho:YAG optical spectrum for the mode-locking resonator design. Two emission lines are present, centred at 2090.30 nm and 2096.45 nm. 122
Figure 5.7: Q-switched envelope of the larger scale modulation QML regime (a) and the shorter scaler modulation QML regime (c), accompanied by their respective pulse trains illustrated in (b) and (d). 124
Figure 5.8: Ho:YAG optical spectrum in the QML regime, demonstrating spectral broadening in the form of split emission lines. 126
Figure 5.9: An example of the oscilloscope trace obtained for a highly irregular and asymmetric hybrid pulse regime in the Ho:YAG resonator. 127
Figure 5.10: Ho:YAG average output power for CW (red), QML (yellow), and CML (green) regimes as a function of pump power. The regression line indicates a slope efficiency of 6.71%. 128
Figure 5.11: A typical oscilloscope trace of (a) the Ho:YAG CML train pulse, and (b) an enlarged pulse train featuring 5 pulses. 129
Figure 5.12: RF spectrum of the mode-locked Ho:YAG laser, covering a range of 20 MHz centered around the fundamental frequency of 29.96 MHz. The spectrum was measured using a RBW of 100 kHz. The inset shows a spectrum spanning 180 MHz, encompassing the generated harmonics of the fundamental frequency. 130
Figure 5.13: Ho:YAG optical spectrum in the CML regime, demonstrating dual wavelength mode-locking as well as spectral broadening. 131
Figure C.1: Energy scheme for Ho:YAG, including the relevant transitions for pumping and the Stark splitting distribution. Stark splitting is shown only for 5 I8 for simplicity. 150
Figure D.1: Typical geometry of a step-index, singly clad optical fibre with a core refractive index of n1 and a cladding refractive index of n_2. 152
Figure E.1: Programmable optical breadboard trolley CAD design (LEFT) alongside final product (RIGHT). 157
Figure E.2: Screenshot of the Python GUI used for the beam profiler automation. 158
Figure E.3: Plot of the knife-edge power displacement data for a thulium-fibre laser beam diameter of 405.61 μm. 159

Abstract

Ultrashort and short pulsed lasers (USPL) operating at near-infrared (NIR) wavelengths are of interest for applications in research, ultrafast chemistry, biomedical science, micromachining, remote sensing, imaging, and defence. In this region of the electromagnetic spectrum, laser systems based on holmium-doped gain media emitting at ~ 2 μm have made significant progress over recent years. However, so far only very few have been demonstrated in power-scalable geometries.

The aim of this research is to investigate short and ultrashort pulse generation in a low doped Ho:YAG slab laser via passive Q-switching and mode-locking mechanisms, respectively. This thesis ultilises GaSb-based semiconductor saturable absorber mirrors (SESAMs) and various different cavity designs to selectively transition between pulse regimes in an attempt to achieve short and ultrashort pulse laser operation.

For efficient pumping of a Ho:YAG crystal within an intense zero-phonon absorption peak, a thulium-fibre laser is designed and developed. The emission of the pump source is thermally tuned to align the wavelength with the absorption characteristics of the Ho:YAG gain media. A typical wavelength of 1906.9 nm is achieved with a slope efficiency of 44% and up to 19.7 W of output power. Using this pump source, a dual-wavelength, continuous-wave (CW) Ho:YAG laser at 2090.3 nm and 2096.6 nm with a slope efficiency of 53% up to 9.1 W of output power is demonstrated.

In an attempt to fully understand the SESAM behaviour, three SESAMs with different modulation depths are used within the laser configuration, yielding three distinct Q-switched pulse regimes. Using an 18% modulation depth SESAM, 70 ns pulses at a repetition rate of 59 kHz and wavelength of 2090.1 nm for average powers of 3.6 W are achieved. Furthermore, we report the onset of spectral broadening with output peak powers and pulse

energies of up to 940 W and 87.3 μJ respectively. We consider this to be the threshold for spectral broadening relative to the beam size.

The Q-switching results provide the necessary information for the SESAM fluence, modulation depth, and intracavity power required to achieve mode-locked operation. Hence, a cavity design suitable for mode-locked operation is considered. The experimental measurements indicate 30 MHz pulses at 2090.3 nm and 2096.2 nm with durations of 58.8 ps at an average power of 1.05 W. These results are in agreement for mode-locked pulse operation.

To the best of our knowledge, this work reports the first SESAM Q-switched Ho:YAG laser and the first SESAM mode-locking of a Ho:YAG slab laser. The 58.8 ps pulse duration, which in the ultrashort regime is considered long, is attributed to the low doping concentration used in this work. The lessons learned here present an opportunity for power-scalability in mode-locked operation, circumventing limitations associated with thermal effects and quenching of the upper-state lifetime observed in higher-doped counterparts.

Signed Statement

I certify that this work contains no material which has been accepted for the award of any other degree or diploma in my name, in any university or other tertiary institution and, to the best of my knowledge and belief, contains no material previously published or written by another person, except where due reference has been made in the text. In addition, I certify that no part of this work will, in the future, be used in a submission in my name, for any other degree or diploma in any university or other tertiary institution without the prior approval of the University of Adelaide and where applicable, any partner institution responsible for the joint award of this degree.

I give permission for the digital version of my thesis to be made available on the web, via the University's digital research repository, the Library Search and also through web search engines, unless permission has been granted by the University to restrict access for a period of time.

I acknowledge the support I have received for my research through the provision of an Australian Government Research Training Program Scholarship.

Signed: Date: …… 14/02/2024

Acknowledgements

I acknowledge the support I have received for my research through the provision of a Centre for Advanced Defence Research Scholarship and an Industry Doctoral Training Centre Scholarship, funded by the Government of South of Australia.

This research was supported by Defence Science and Technology Group (DSTG) and the University of Adelaide. The equipment and material support provided by through the DualTech USPL research group has been crucial to the progress of this degree. I also wish to thank them for the opportunity to gain technical and scientific expertise through the STEM Cadetship Program.

I would like to thank my supervisors – Miftar Ganija and Keiron Boyd. I could not have asked for a more supportive, patient, and resourceful supervision team. Their insight and guidance towards my theoretical and experimental research has been second to none. This project would not have been possible without either one of them.

I would also like to thank Alexandros Kolovinos for his support in inducting me into the lab and providing valuable feedback for my work. His extensive knowledge of optical fibres, lab equipment, and general advice has helped shape my project.

Furthermore, I would like to extend my gratitude to my M.Phil colleagues – Andrew and Henry. The enjoyment and excitement we shared throughout our candidatures as well as our endless physics conversations helped motivate much of my research. I am truly thankful for the opportunity to have experienced this journey together.

I am also thankful to all the other students in our research group. Our weekly meetings and discussions were instrumental in developing my scientific knowledge and presentation skills.

Finally, I give thanks to my family, friends, and girlfriend. I am endlessly grateful for the patience, support, and understanding they have shown me through my candidature.

Dedication

I dedicate this thesis to my family for the unwavering support they have given me throughout my life.

Chapter 1

Introduction

1.1 Ultrashort and Short Pulsed Lasers

The invention of the first lasers in the 1960s marked a breakthrough in science and technology, offering coherent and intense sources of light with properties previously unimaginable. This began an entirely new field of research, with countless frontiers to explore in the quest to generate lasers capable of producing exceptionally high powers across various wavelengths.

Since then, researchers have pioneered numerous techniques to advance this technology, culminating in the 2018 Nobel Prize in Physics awarded for the generation of high-intensity, ultrashort pulsed laser (USPL) sources, and subsequently in 2023 for the generation of ultrashort pulses at the attosecond scale [1]. These achievements underscore the ongoing innovation in the development of ultrashort lasers, garnering further attention for this technology in both fundamental science and commercial contexts.

The most popular approach to generating ultrashort pulses from a laser is mode-locking, which produces pulse durations on the order of picoseconds (10^{-12} s) to femtoseconds (10^{-15} s). Fundamentally, it is based on inducing a fixed phase relation between adjacent longitudinal modes in the laser cavity [2]. The superposition of these phase-locked modes results in an ultrashort pulse [2].

Mode-locking consists of two categories: active and passive mode-locking. The active approach utilises electronically controlled devices such as acousto-optic modulators to mode-lock via a sideband generation process [3]. However, this is limited by the electronic constraints of the modulation driving signal, producing pulse durations typically in the range of hundreds of picoseconds.

Alternatively, passive mode-locking leverages the intrinsic nonlinear properties of saturable absorbers such as semiconductor saturable absorber mirrors (SESAMs) to form and shape ultrashort pulses. Since the high-intensity pulse peak saturates the absorber more than its low-intensity wings, the pulse width is shortened in the time-domain, thus generating pulses as short as a few femtoseconds [4].

Over the years, the majority of SESAM research has been focussed around 1 μm lasers. However, more recently, USPL sources in the wavelength region around 2.1 μm have garnered significant attention due to their potential in various scientific and technological applications. This near-infrared (NIR) area of the electromagnetic spectrum offers many advantages, facilitating extensive usage in research [5], ultrafast chemistry [6], biomedical science [6], manufacturing [7], remote sensing [8], and defence [9]. For the NIR spectral region, the rare-earth-doped gain media, Ho:YAG, has emerged as a highly promising candidate for pulsed operation, as will be discussed.

1.2 Applications of USPL Sources at 2.1 μm

1.2.1 Ultrashort Spectroscopy

Ultrashort spectroscopy utilises USPL sources to facilitate the study of atoms, molecules, nanostructures, and solids on extremely short timescales through photoinduced dynamical processes [10]. As the NIR wavelength region contains characteristic fingerprint spectra for many molecules, the use of 2.1 μm USPL sources enables spectroscopic insights into materials which are unobtainable through other wavelengths.

Transient absorption spectroscopy (TAS), a form of pump-probe technique, employs such technology. A material sample is first excited with a femtosecond 'pump' pulse, which acts to modify spectral characteristics. Subsequently, a supercontinuum 'probe' source is used to monitor these changes [11]. The spectral evolution of the sample provides a unique view into the reaction mechanisms which may be used to enhance the yield of reaction products [10].

Ultrashort vibrational spectroscopy is another prevalent use of USPL sources for ultrashort spectroscopic applications [12]. This is used to directly measure nuclear motion on the timescale of induced vibrations, revealing the mechanistic details of a reaction [10]. An example of this is demonstrated by Hegmann *et al.* through the probing of charge-carrier mobility in amorphous organic semiconductors [13, 14]. Using a femtosecond Ti-sapphire laser as an excitation source, a secondary femtosecond source is used as a probe [13]. A similar approach is conducted by Pensack *et al.* to examine charge-carrier dynamics in organic photovoltaic materials [12]. Investigations akin to these deepen the understanding of the refractive index, absorption characteristics, and complex conductivity, thereby enabling the optimisation of the fabrication processes to achieve desired material properties [13-15].

1.2.2 Biomedical

USPL systems offer widespread applications across the biomedical industry [16]. They are directly utilised in time-resolved fluorescence spectroscopy and imaging, which allow for tissue diagnosis of malignant diseases and in cardiovascular research [17]. Additionally, the propagation of photons in scattering media has significant relevance in optical mammography, dosimetry for photodynamic therapy, and the assessment of species concentrations [17].

USPL sources are highly appealing for medical applications due to the capability for cold ablation [18]. Cold ablation refers to the direct vapourisation of material without significant heat conduction [19]. This occurs when the heat diffusion time of the material exceeds the interaction time of the laser pulse, limiting the material response. Plasma formation and

hydrodynamic expansion rapidly dissipates almost all of the input laser energy, leaving minimal heat conduction [19].

Cold ablation increases the precision for surgical procedures beyond sub-micron, theoretically allowing for nano-surgery of individual biological cells [20, 21]. This is especially pertinent for ophthalmic procedures such as laser eye surgery, corneal surgery, and cataract removal [18]. In addition to direct application, cold ablation is also employed in the production of stents which are used to enhance blood flow by insertion into arteries or veins, and in the manufacturing of other implantable medical devices that demand precise dimensions [18].

The scope of biomedical applications for USPL sources is continually broadening. While many of these utilise USPL sources at a wavelength of 1 μm, extensive research suggests that 2.1 μm sources offer significant advantages due to lower ablation thresholds and strong absorption bands for both water and bone [22]. This ensures consistent cutting and vaporisation speeds, irrespective of tissue vascularity [22]. Furthermore, blood coagulation induced from 2.1 μm lasers also results in a cleaner and more efficient process [23]. Unfortunately, the limited availability of pulsed laser sources at 2.1 μm has constrained the medical field primarily to 1 μm sources [23].

1.2.3 Materials Processing

Since the invention of chirped pulse amplification (CPA) for pulsed lasers in 1985, USPL sources have reached power levels that have innovated the landscape of laser-matter interaction [24]. The ability to deliver high-intensity pulses in a highly localised and controlled manner has led to groundbreaking advancements in various manufacturing processes including nano-machining, bio-manufacturing, high-resolution machining, and thin film scribing [24]. These advancements have led to the establishment of high-power, ultrashort pulse laser use in industry.

Saunders *et al.* reports on the ongoing evolution of USPL sources for manufacturing [25]. Additive manufacturing is presented as an avenue for investigating next-generation

manufacturing techniques, with attractive prospects including selective laser sintering, pulsed laser deposition, multiphoton lithography, and welding [25].

Although USPL systems are now common throughout this industry, these typically operate outside the spectral region of 2.1 μm [24]. Nevertheless, various glasses and polymers exhibit strong NIR absorption features, making operation at 2.1 μm desirable for some materials processing [26]. Despite high expectations, the scarcity of commercial suppliers for 2.1 μm lasers as well as the maturity of lasers at 1 μm have limited the number of material processing experiments conducted at this wavelength [26]. Although this is the case, Voisiat *et al.* successfully demonstrated the ability to cut, mark, and weld various polymers using a picosecond laser operating at 2.1 μm [24]. Thus, confirming the viability of the wavelength for this application-space [27].

1.2.4 LiDAR and Atmospheric Sensing

A prevalent challenge encountered in many laser systems is the diffraction of the laser beam over large distances, imposing limitations on precision and power [28]. However, USPL sources offer a unique solution to this. With sufficient peak powers, atmospheric constituents ionise, resulting in the formation of plasma channels which are commonly known as filaments [29-33]. These balance nonlinear self-focusing and defocusing mechanisms to maintain effectiveness across extended distances, which is particularly advantageous for the long range applications required for remote sensing [31, 32, 34, 35].

For effective transmission through the atmosphere, a laser must operate at a wavelength which is not readily absorbed or scattered by atmospheric constituents. Wavelengths which satisfy this condition are known as atmospheric windows [36, 37]. This is exemplified at 2.1 μm. Moreover, this wavelength is outside the ocular focus, meaning that it is absorbed by the vitreous body of the eye rather than focussed onto the retina. It is therefore deemed eye-safe, making this spectral region ideal for free-space communication and remote sensing [38, 39].

An example of this technology is light detection and ranging (LiDAR), which is a remote sensing method that uses pulsed laser light to measure variable distances. This operates on a similar principle to radar systems, determining an object's distance by measuring the time taken for reflected light to return to the sensor [23]. At NIR wavelengths, LiDAR offers much higher resolution and accuracy compared to the longer wavelengths used in radar, regardless of object size or weather conditions [40].

Another important use of USPL sources in this domain is time-resolved absorption spectroscopy to conduct range-resolved multi-trace analysis of atmospheric gases and aerosols simultaneously [41, 42]. This allows for an in-depth examination of the chemical and physical processes that influence atmospheric behaviour, therefore playing a crucial role in weather and climate predictions [42]. Additional applications include wind velocity measurements for predictive purposes and storm tracking [23].

1.2.5 Pump Sources for Mid-Infrared Generation

NIR laser systems also serve as excellent pump sources for frequency conversion processes, notably for the generation of mid-infrared (MIR) wavelengths via optical parametric oscillators (OPOs) [23]. OPOs enable extensive continuous tuning of wavelengths, high peak power outputs, and efficient energy conversion [23]. They operate based on nonlinear optical frequency down-conversion, where one pump photon is converted into two lower-energy photons with longer wavelengths. The combined energy of these two newly generated photons matches that of the pump photon, but they often do not have the same energy. For convention, the photon with the higher energy is called the ‘signal’ and the one with the lower energy is called the ‘idler’ [43]. For high-power applications in the mid-infrared region, OPOs utilising ZGP (zinc germanium phosphide) are preferred and can be optimally pumped with systems operating around 2 μm [44-47].

Although OPOs can be pumped by 1 μm laser sources, 2 μm offers double the possible upper conversion efficiency and enables the use of nonlinear crystals with a higher nonlinearity [48]. This reduces the amount of power required from the pump source for the OPO to reach

its operational threshold. Most OPOs meet this requirement with nanosecond pulses produced from a Q-switched laser, however, for the generation of ultrashort pulses, an OPO can instead be synchronously pumped with a mode-locked laser [49, 50]. Due to the low duty cycle of typical mode-locked lasers, the average optical power required can be well below 1 W [50].

1.2.6 Soft x-rays via High Harmonic Generation

In the late 1980's, McPherson discovered integer multiples of a driving laser frequency generated by a phenomenon known as high harmonic generation (HHG) [51]. This process is understood as a three-step model considering electrons bound to atoms in a gas. An electron is liberated by a strong external field (i.e. a laser pulse), whereby the driving laser field distorts the Coulomb barrier and the electron tunnels out. Under the influence of the laser field, free electrons are coherently driven until recombination. This results in the emission of an integer multiple of the driving field as excess kinetic energy is released. For higher-order harmonics, the relative intensity of the n^{th} harmonic is generally less than that of the $(n-1)^{th}$ harmonic [52].

For shorter wavelengths, the average energy of an electron perturbed by the light field, also known as the ponderomotive energy, remains low, resulting in low intensity harmonics. Since the ponderomotive energy has a λ^2 dependency however, the use of NIR or MIR wavelengths produces a much stronger yield of harmonics [53]. These may stretch far across the electromagnetic spectrum, paving the way for the only demonstrated route to generating stable, tabletop soft x-ray pulses [54]. Thus, highlighting the need for USPL NIR sources for direct HHG or HHG through MIR generation. Uses of soft x-rays include medical dosimetry [55], spectroscopy in the water window [56], imaging [57], and metrology [58].

1.2.7 Frequency Combs

A frequency comb consists of discrete, equidistant frequency components. These act as precision optical synthesisers and enable the precise transfer of phase and frequency information from a high-stability reference to thousands of narrow spectral coherent lines in the optical domain [59, 60]. This offers an unrivalled degree of frequency measurement precision that has proven crucial in the advance of modern technology [60]. Originally invented in the 1990s to count the cycles from optical atomic clocks, the 2005 Nobel Prize in Physics was awarded for developments in frequency combs [61]. In more recent years, extensive usage has been seen in precision spectroscopy, metrology, telecommunications, and quantum technology [60, 62-64].

The most popular approach to the generation of frequency combs is through mode-locked lasers [61]. Such lasers produce a series of optical pulses separated in time by the round-trip time of the laser cavity. The spectrum of the pulse train approximates a series of Dirac delta functions with spacing equal to the pulse repetition frequency [61].

In the NIR-MIR wavelength range, ultrafast frequency combs offer a distinct advantage due to the presence of vibronic molecular resonances, commonly referred to as the 'molecular fingerprint region' [65]. To comprehensively analyse the structure of molecules with these resonances, it's essential to have precise, accurate, and dependable frequency references (i.e., frequency combs) available at those wavelengths [65, 66]. Hence NIR and MIR frequency combs are particularly attractive [67].

1.2.8 Defence and Aerospace

High energy pulsed lasers at 2.1 μm with high repetition rates offer extended range for directed energy (DE) applications. As previously discussed, this wavelength region contains atmospheric windows which allow for high transmission. Consequently, USPL systems show significant potential for direct use in ablating distant targets. However, they face

several challenges. For instance, laser filamentation induces plasma formation on a small portion of the target's surface [28]. If this newly formed plasma is not allowed to dissipate, it can act as a barrier against subsequent laser pulses, thus limiting the effectiveness of ablation [34]. While this phenomenon has been a subject of research for decades, ongoing studies aim to determine if a sequence of rapidly fired pulses may overcome this issue [29, 31, 33-35, 41].

In addition to DE applications, these sources are used in Directional Infra-Red Counter-Measures (DIRCM) systems, a class of anti-missile systems designed to eliminate or redirect heat-seeking missiles [68]. These systems are based on sensor blinding through supercontinuum generation and electronic interference. Similar Ho:YAG sources to the one proposed in this research have been established as attractive options for pumping ZGP OPO-based DIRCM systems [69].

Furthermore, the work conducted by Day *et al.* highlights the use of 2.1 μm sources for detecting ‘markers’ of gassing, decomposition, or residue for various complex explosive compounds and chemo-biological agents [23, 70]. This has the potential for expediting security screening procedures, such as those implemented at airports, while also bolstering the overall safety of the public and armed forces where security may be of concern [23].

1.3 SESAM Mode-Locked Bulk Lasers

The intracavity element required for passive mode-locking is a saturable absorber, the most important of which, is considered to be the SESAM [71]. This semiconductor device offers a compact, self-starting mechanism which has been successfully demonstrated in high-power laser systems [72]. The parameters of a SESAM can be adjusted during the manufacturing process to cover a wide range. An appropriately designed SESAM can therefore be used to mode-lock a variety of lasers, in particular bulk systems such as Ho:YAG lasers.

In addition to SESAM mode-locking, there are also various other types of passive mode-locking techniques, the most prominent of which is Kerr lens mode-locking (KLM). This

technique relies on artificial saturable absorption created through nonlinear phase shifts which produces the fastest absorber response times and therefore generates the shortest pulse durations [73]. However, as covered in Chapter 2, the onset of the Kerr effect requires the resonator to operate close to its stability limit. Consequently, the resonator design is very limited, and long-term stability is difficult to achieve [74]. Furthermore, KLM is often not self-starting and hence requires an external trigger to simulate power fluctuations [75].

Here, we present a review into recent advancements in SESAM mode-locked bulk lasers at 2 μm, with emphasis on Ho:YAG based systems. As further detailed in Chapter 3, Ho:YAG offers a largely untapped potential for power-scalable pulsed operation. The typical emission wavelengths of Ho:YAG around 2.1 μm present an attractive option for many of the aforementioned applications such as the efficient pumping of ZGP OPOs. A summary of relevant publications is shown in Table 1.1 with a brief discussion on each given below.

Table 1.1: Summary characteristics for relevant 2 μm SESAM mode-locked bulk lasers.

Lead author	Year	SESAM	Gain media	Doping (at. %)	Central wavelength (nm)	Spectral FWHM (nm)	Pulse duration (ps)	Average power (W)	Repetition rate (MHz)	Cavity length (m)	Output coupling (%)
Tomilov **[72]**	2022	GaSb	Ho:YAG (thin disk)	2	2090	4.5	1.13	50	24	6.2	3
Tomilov **[72]**	2022	GaSb	Ho:YAG (thin disk) (double pass)	2	2090	7	0.692	30.6	63.2	2.37	2
Tomilov **[76]**	2021	GaSb	Ho:YAG (thin disk)	2	2091	3	1.66	40.5	52.2	X	3
Zhao **[77]**	2021	GaSb	Tm:$LuYO_3$ (ceramic)	3	2040.5	75	0.069	0.133	78	1.92	1.5
Wang **[78]**	2020	InGaAsSb	Tm,Ho:CNGG	Tm: 2.6 Ho: 0.55	2061	62	0.073	0.036	89.3	1.68	0.5
Wang **[79]**	2016	GaSb	Ho:YAG (ceramic)	1	2121	1.4	15.6	0.230	82.1	1.83	1.5
Yang **[80]**	2013	GaSb	Tm,Ho:YAG	Tm: 5 Ho: 0.4	2091	0.4	21..3	0.063	107	X	2
Yang **[80]**	2013	GaInAs	Tm,Ho:YAG	Tm: 5 Ho: 0.4	2091, 2097	0.4	56.9	0.285	107	X	2

The recent work by Tomilov *et al.* demonstrates the leading research in high power SESAM mode-locked lasers based on Ho:YAG [72, 76]. Departing from the traditional slab or rod bulk media geometry, Tomilov *et al.* specialise in thin-disk laser (TDL) resonators. These

offers numerous desirable thermomechanical properties which are necessary to support the thermal stresses associated with the Ho^{3+} ion doping concentration of 2 at. % at high powers [72]. This concentration, which is considered to be high, is chosen to increase the spectral content of the laser, increasing the number of supported longitudinal modes and therefore the intensity of the mode-locked pulses. Due to the thin nature of the Ho:YAG disk however, deformable mirrors are required to ensure the thulium-fibre laser pump has multiple passes to maximise the absorption efficiency. For the research conducted by Tomilov *et al.*, the pumping configuration facilitates 72 pump passes through the Ho:YAG, achieving an absorption efficiency of 98%. This creates significant complexity in the overall design of the system [72, 76].

Additionally, in contrast to slabs or rods, thin-disk geometries provide minimal dispersive and nonlinear contributions to the cavity. However, to support stable, self-sustaining, soliton pulse shaping dynamics for mode-locking, a balance of both is required [81]. To address this, Tomilov *et al.* incorporates multiple chirped mirrors into the cavity to provide the necessary dispersion. Additionally, a thin sapphire window is employed and translated across a focal point within the cavity until the desired level of spectral broadening is achieved [72, 76].

These works highlight the advancement of thulium-fibre laser-pumped Ho:YAG TDLs, achieving power outputs of 30 W, 40 W, and 50 W, with corresponding pulse durations of 692 fs, 1.66 ps, and 1.13 ps, respectively [72, 76]. Notably, these mark the highest average power mode-locked lasers recorded in the 2 μm wavelength region [72]. Although power-scalability is postulated, a higher gain (thicker gain media, higher doping concentration) is necessary, in addition to higher power, higher modulation depth SESAMs, and a more careful treatment of intracavity losses.

Zhao *et al.* and Wang *et al.* also present promising work at 2 μm, using $Tm:LuYO_3$ and Tm,Ho:CNGG as alternative host materials to YAG, respectively [77, 82]. Both studies use nearly identical resonator designs, combining a linear cavity with a ring cavity to effectively mitigate mode competition [82]. While both gain media exhibit broad emission spectra, the co-doped CNGG experiences challenges in power-scaling due to up-conversion mechanisms that excite higher Tm^{3+} ion levels rather than Ho^{3+} ions. Additionally, $Tm:LuYO_3$ demonstrates significantly lower pump absorption compared to Tm:YAG, limiting overall

efficiency [23]. Moreover, using Tm^{3+} ions as the primary dopant instead of Ho^{3+} ions results in a lower emission wavelength. Given that water vapor strongly absorbs below 2 μm, it is often desirable for laser systems to operate at wavelengths slightly above this range for various applications [83].

In the work presented by Wang *et al.*, a Ho:YAG ceramic laser operating at ~ 2.1 μm is investigated, with a focus on passive mode-locking using a GaSb-based SESAM as a saturable absorber [79]. Their research showcases stable and self-starting mode-locked operation spanning the tuning range from 2059 nm to 2121 nm using a Lyot filter [79]. While similar in nature to the research proposed in this investigation, the work by Wang *et al.* uses a ceramic instead of a crystalline host for the gain media. This is justified through the beneficial thermal properties of ceramics and the potential for less restrictive bandwidth limitations compared to crystalline hosts [79]. The work by Wang *et al.* also underscores the relatively limited exploration of passive mode-locking in Ho:YAG, despite its strong potential [79].

Yang *et al.* presents two mode-locked Tm,Ho:YAG sources, each using a different SESAM technology – a GaSb-based SESAM and a GaInAs-based SESAM [80]. While the gain media is subject to the same power-scaling constraints that affect co-doped media as previously discussed, the primary objective of the investigation is to directly compare the performance of the GaSb-based SESAM and the GaInAs-based SESAM within the same resonator design. The findings reveal that the GaSb-based SESAM yields shorter pulse durations than the GaInAs-based SESAM but at the expense of limited output power due to its lower damage threshold [80]. An onset of undesirable pulse regimes is also observed but suppressed at higher intracavity powers. Yang *et al.* concludes by stating that both types of SESAMs demonstrate potential for stable mode-locking and represent promising options for generating ultrashort pulses at a wavelength of 2.1 μm [80].

The reviewed mode-locked systems use doping concentrations in the range of 1-3 at. % (excluding the co-doped gain media). This favours mode-locked operation but considerable power-scaling limitations are noted due to increased thermal stresses and an onset of undesirable energy transfer processes, such as quenching, which can drastically decrease system efficiency. These concepts are further explored in Chapter 2.

Moreover, a high output coupling reflectivity is consistently used across all mode-locking studies. This increases the spectral content through intracavity spectral broadening, but also meets the saturation fluence requirements of the SESAM when the spot size is on the scale of tens of micron without damaging the absorber.

1.4 SESAM Q-Switched Bulk Lasers

When only a small number of longitudinal modes are supported by the cavity and the fluence on the SESAM is low, the SESAM can favour Q-switching instead of mode-locking. While covered in more detail in Chapter 2, Q-switching is based on the principle of storing energy and releasing it as a microsecond or nanosecond pulse. Achieving this with a SESAM has an extensive range of applications but is scarcely demonstrated in literature in bulk laser resonators, with the few reported experiments often representing unsuccessful endeavours aimed at mode-locking rather than dedicated resonator designs for Q-switching. Nevertheless, a selection of SESAM Q-switched sources spanning a range of wavelengths have been collected, with their key characteristics summarised and presented in Table 1.2.

The work conducted by Mateos *et al.* represents one of the only documented SESAM Q-switched bulk lasers at 2 μm [84]. In this study, a thin disk Ho:$KY(WO_4)_2$ is ultilised in a relatively simple and compact resonator design spanning a total length of only 175 mm [84]. The pulse durations achieved are 201 ns at a repetition rate of 135 kHz and average power of 551 mW [84]. This corresponds to a pulse peak power of 10 W.

The work by Parali *et al.* and Pollock *et al.* both demonstrate similar resonator setups, but with a difference in output coupling fraction: Parali *et al.* uses 1% transmission, whereas Pollock *et al.* opts for 8% transmission. [85, 86]. The 8% transmission allows for a greater fraction of the intracavity power to be extracted each round-trip, resulting in a much greater average output power yield [85, 86]. Both publications suggest that the Q-switched behavior, rather than mode-locked behavior, is attributed to a shorter cavity length and a weaker focus on the SESAM [85, 86].

Finally, Evans *et al.* reports on the impact of the output coupling ratio on SESAM Q-switching performance [87]. By maintaining all other parameters, this study demonstrates stable Q-switching using five different output couplers, ranging from 6% transmission to 56% transmission [87]. As depicted in Table 1.2, an increase in transmission leads to an increase in both pulse duration and repetition rate. This research underscores the adaptability of SESAMs for achieving consistent Q-switching across various intracavity power levels, in contrast to the highly sensitive parameter requirements to achieve mode-locking [87].

Table 1.2: Summary characteristics for a range of SESAM Q-switched bulk lasers.

Lead Author	Year	SESAM	Gain Media	Doping (%)	Central Wavelength (nm)	Spectral FWHM (nm)	Pulse Duration (ns)	Average Power (mW)	Repetition rate (kHz)	Cavity Length (m)	Output Coupling (%)
Mateos [84]	2018	GaSb	Ho:KY(WO_4)$_2$ (thin disk)	3	2056	X	201	551	135	0.175	3
Parali [85]	2018	X	Alexandrite	X	740	0.5	550	41	27	0.142	1
Evans [87]	2014	GaSb	Fe:ZnSe	X	4045	X	56.1	111	683	X	6
							62.6	184	712	X	10
							63.5	395	766	X	29
							64	515	851	X	40
							64.5	627	867	X	56
Pollock [86]	2005	X	Cr:ZnSe	X	2500	X	50	532	1000	0.100	8

X: Not Specified.

1.5 Research Objectives

The aim of this thesis is to investigate the effects of various GaSb-based SESAMs with different modulation depths in a low-doped Ho:YAG slab laser to achieve Q-switching and ultimately, mode-locking. Although significant progress has been made in Ho:YAG based laser systems in recent years, few have demonstrated an ability to scale to high powers in pulsed or CW regimes outside of complex TDL architectures [88, 89]. We believe that despite the limited spectral content offered from a low-doping concentration, if the initial mode-locking can be achieved, reduced quenching and thermal stresses offer a pathway towards a mode-locked, power-scalable laser geometry.

The research presented seeks to address the following objectives:

- The design, development, characterisation, and thermally induced wavelength tuning of a thulium-fibre laser to serve as a pump source.

- The design, development, and characterisation of a CW Ho:YAG laser cavity operating at 2.1 μm.

- The first design, demonstration, and characterisation of Q-switching in a Ho:YAG slab laser using a SESAM.

- The first direct comparison of different modulation depth SESAMs on pulsed performance.

- The first design, demonstration, and characterisation of mode-locking in a Ho:YAG slab laser using a SESAM.

As discussed in Section 1.2, USPL sources at 2.1 μm have an extensive application-space across a vast range of industries. However, development of such sources is lacking, leaving a significant gap in literature regarding the realisation of different pulse regimes by use of a SESAM.

This work details one of the only reported accounts of SESAM Q-switching around 2.1 μm, and the first instance of SESAM Q-switching in a Ho:YAG slab laser. Furthermore, this work reports on the first SESAM mode-locking of a Ho:YAG laser outside of thin disk geometries and ceramics.

1.6 Thesis Outline

Chapter 1 introduced the core concepts necessary for understanding the project, along with a variety of applications of USPL sources operating at 2.1 μm. These applications included ultrafast spectroscopy, biomedical science, materials processing, LiDAR and atmospheric sensing, pumping nonlinear frequency conversion processes, soft x-rays generation via high harmonic generation, frequency comb generation, and defence applications. Additionally, a literature review and an outline of the thesis objectives were presented.

Chapter 2 explores the theoretical framework concerning the propagation and evolution of the electric field associated with an optical pulse. By expanding on the fundamental concepts introduced in Chapter 1, this chapter delves into the mechanisms of pulse shaping formed by the interplay of dispersive and nonlinear effects. Additionally, it offers an overview of mode-locking and Q-switching theory, along with an examination of saturable absorbers and SESAMs. Finally, Chapter 2 concludes with a discussion on the characterisation methods for various pulse regimes.

Chapter 3 outlines the process for developing a diode-pumped CW thulium-fibre laser designed for pumping the Ho:YAG gain medium. This section encompasses the absorption spectroscopy of the Ho:YAG which is used for the temperature tuning of the thulium-fibre

laser to ensure optimal absorption. A characterisation of the thermal load, slope efficiency, emission spectrum, and beam quality of the thulium-fibre laser is conducted.

Chapter 4 explores the design, development, and characterisation of a CW Ho:YAG resonator, followed by the integration of a SESAM for passive Q-switching. By characterising pulse durations, repetition rates, pulse energies, pulse peak powers, and pulse train stabilities, a discussion is held regarding the performances achieved using three SESAMs, each featuring a different modulation depth.

Chapter 5 investigates different mode-locking regimes using a low-doped Ho:YAG slab as a gain medium. Based on the SESAM fluences necessary for stable operation, intracavity intensities required for nonlinear spectral broadening, and the general pulse dynamics observed through Q-switching in Chapter 4, a resonator configuration is designed to favour mode-locking. Essential characteristics needed to assess each mode-locking regime's performance are measured. Techniques to introduce dispersion and additional nonlinearities are applied, and the resulting pulse dynamics are characterised.

Chapter 6 concludes the thesis, presenting a summary of results, an outline of future work, and final remarks.

Chapter 2

Theoretical Framework

2.1 Introduction

This chapter presents the theoretical framework underpinning the driving mechanisms responsible for passive pulse operation in laser resonators. The primary focus here is placed on the use of SESAMs and different cavity configurations to attain various pulse regimes within a Ho:YAG laser.

In Section 2.2, the fundamental concepts used to describe the electric field associated with an optical pulse are introduced. This includes a discussion into the temporal and spectral constraints, in addition to an examination of dispersive effects. Subsequently, Section 2.3 explores the nonlinear effects relevant to the propagation of optical pulses, namely those resulting from the Kerr effect. This subsection provides an overview of the equations employed to model pulse evolution, including the physical significance of the most mathematically stable solutions.

Section 2.4 builds upon the principles outlined in the previous two subsections by addressing the pulse generation mechanisms of a SESAM as well as mode-locking and Q-switching theory. Section 2.5 covers the distinctive features of various mode-locking regimes and the conditions under which each regime is favoured. An assessment into the characterisation methodology and equipment is then presented in Section 2.6. Section 2.7 concludes the chapter with a summary of the discussed topics.

2.2 Optical Pulses

2.2.1 Introduction to Pulses

The time evolution of an optical pulse's electric field is described as a fast sinusoidal oscillation (the carrier), multiplied by a more slowly varying envelope function as illustrated in Figure 2.1 [1].

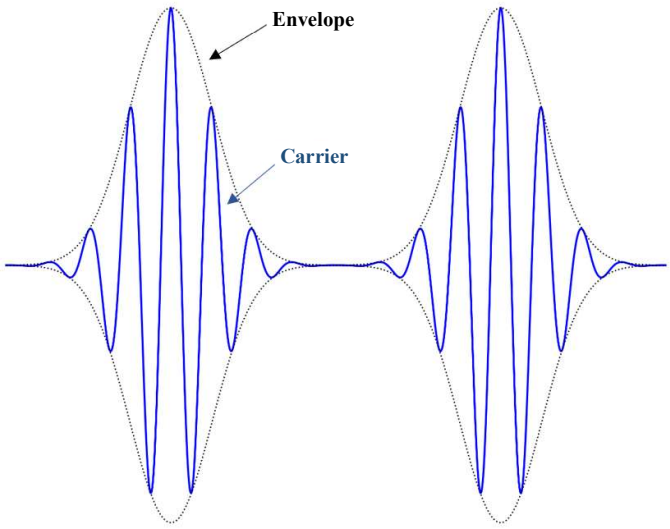


Figure 2.1: Typical time evolution of the electric field of few-cycle laser pulses.

In general, a wave travelling in the $+\hat{x}$ direction with wavenumber k, at time t, and frequency ω can be mathematically represented by the one-dimensional wave equation given in Equation (2.1) [2].

$$q(x,t) = e^{i(kx-\omega t)} \tag{2.1}$$

The wavenumber is related to wavelength λ by Equation (2.2) [2].

$$k = \frac{2\pi}{\lambda} \tag{2.2}$$

In a vacuum, light waves exhibit a constant velocity for all wavelengths. However, when light travels through a medium with a wavelength-dependent refractive index $n(\lambda)$, this uniformity no longer holds true. As strictly monochromatic waves do not naturally occur, an optical pulse contains a spread of wavelengths [3]. The notion of group index N is used to describe the behaviour of such a range of wavelengths centred about λ_0, as given by Equation (2.3) [2, 4].

$$N_{group} = n(\lambda_0) - \lambda_0 \frac{d\mathrm{n}}{d\lambda_0} \tag{2.3}$$

Using this concept, the velocity of the wave packet envelope, known as the group velocity, can be established. This corresponds to the rate of frequency change with respect to the wavenumber and thus directly influences the rate at which energy propagates within the wave packet. This relates to the group index by Equation (2.4) [2].

$$v_{group} = \frac{d\omega}{dk} = \frac{c}{N_{group}} \tag{2.4}$$

Analogous to the group velocity is the phase velocity. This refers to the velocity at which the carrier of the wave advances through the medium and is defined by Equation (2.5) [3].

$$v_{phase} = \frac{dx}{dt} = \frac{\omega}{k} = \frac{c}{n} \tag{2.5}$$

In a non-dispersive and linear medium, the group velocity and phase velocity are equal. Hence, the wave packet maintains its shape as it propagates. When dispersion and nonlinearities are introduced however, a discrepancy arises between the velocity

components, creating an offset between the optical phase and the peak of the wave envelope [1]. This is referred to as the carrier-envelope offset and gains significance for pulse durations approaching the attosecond scale [5]. While the implications of this are heavily explored across literature, additional investigation in this area exceeds the scope of this research [6-8].

2.2.2 Time-Bandwidth Product

The time-bandwidth product (TBP) is a fundamental concept for signals with limited temporal or spectral bandwidth [9]. Mathematically, it is defined as the product of the signal's temporal duration at full width at half maximum (FWHM), $\Delta\tau$, and its spectral width at FWHM, $\Delta\nu$, as given by Equation (2.6) [10]. The TBP can also be expressed in terms of central wavelength λ_0 and pulse wavelength bandwidth at FWHM, $\Delta\lambda$, by evaluating the derivative of frequency with respect to wavelength.

$$\text{TBP} = \Delta\nu\Delta\tau = \frac{\Delta\lambda c}{\lambda_0^2}\Delta\tau \tag{2.6}$$

Heisenberg's uncertainty principle states that a signal cannot be arbitrarily compact in both the time and frequency domain [11]. This means that if a signal has a short temporal duration, its spectral representation (the Fourier transform) will spread out over a broad frequency range, and vice versa. This represents an "uncertainty" lower bound for an optical pulse's TBP. For a Gaussian pulse, this value is equal to $\frac{2ln2}{\pi} = 0.441$ whereas a hyperbolic-secant-squared (sech^2) pulse shape, which is typically assumed when durations are on the femtosecond scale, yields a TBP of 0.315 [10].

At the lower bound of the TBP, a pulse becomes incompressible both temporally and spectrally. This property, known as bandwidth-limited, means that additional bandwidth is required in one domain to reduce the bandwidth in the other [12]. To highlight this, for a

Ho:YAG laser operating at 2097 nm, Equation (2.6) can be used to show that a 1 ps bandwidth-limited Gaussian pulse would require a spectral bandwidth of at least 6.45 nm.

Although the time and frequency domain are intrinsically linked, an increase in one does not necessarily decrease the other; rather, it facilitates the reduction of the other through appropriate conditions. This phenomenon is evident during propagation of a bandwidth-limited pulse with high peak power through a highly nonlinear material. Spectral broadening can occur without a significant change in temporal duration, increasing the TBP and resulting in non-bandwidth-limited pulses [13]. To restore the value of the TBP to its lower limit for the respective pulse shape, the additional spectral content generated allows for dispersion compensation techniques to reduce the pulse duration [13]. Further exploration of this concept is provided in Section 2.3.2.1.

2.2.3 Gain Bandwidth and Gain Narrowing

Gain bandwidth defines the wavelength range a laser gain medium can effectively amplify and is proportional to the number density of active ions [14]. In the case of Ho:YAG, a higher concentration of Ho^{3+} ions result in a broader gain and emission bandwidth due to an increased population inversion which creates a greater range of transition energy levels. Since the spectral and temporal content of an optical pulse are intrinsically linked, the concept of gain bandwidth becomes a necessary consideration.

Typically, high doping concentrations are desirable for achieving the shortest mode-locked pulses as seen in the literature review conducted in Chapter 1. However, a number of challenges associated with high doping concentrations can arise.

At high powers, high doping concentrations lead to the quenching of the upper-state lifetimes, raising the lasing threshold and reducing the gain. This phenomenon occurs from energy transfer between ions, particularly when they cluster together. For instance, if two active ions are initially in the upper laser level and one ion reaches the ground state, it can transfer its energy to the second ion. The latter ion then quickly relaxes to the upper laser

level, effectively resulting in the loss of one of the two excitations. To prevent this, a sufficient distance between neighboring ions to avoid energy transfer processes should be maintained. If achieving this separation is not feasible due to fabrication limitations or a high number density, the doping concentration should be reduced to avoid quenching.

Furthermore, as highlighted by Paschotta *et al.*, stronger doping densities also increase the dissipated power per unit volume. This results in a greater increase in the temperature of the gain, which may decrease the efficiency and stability of the laser through unwanted thermal effects such as thermal lensing [15].

Chang *et al.* reports Equation (2.7) as an expression for calculating the gain bandwidth $\Delta\lambda$ of a medium in terms of wavelength [16]. By utilising a measurement of the gain cross-section, the FWHM of the curve, $\Delta\lambda_a$, may be found, as well as the wavelength at which the cross-section peaks λ_a, and the dB gain at the peak wavelength, $G_{dB}(\lambda_a)$ [16].

$$\lambda = \Delta\lambda_a \sqrt{\frac{3}{G_{dB}(\lambda_a) - 3}} \tag{2.7}$$

As the gain bandwidth is centred around a specific wavelength, there exists a central region of the optical spectrum where amplification is more effective compared to the spectral wings [16]. Consequently, when a pulse passes through the gain medium, the central wavelengths experience greater amplification, leading to a reduction in the spectral bandwidth of the amplified light relative to the broader input spectrum. This effect is known as gain narrowing [17].

For circulating bandwidth-limited pulses, this increases the temporal width, placing another constraint on the achievable pulse duration. For a gaussian pulse with a pulse duration of τ, gain bandwidth of $\Delta\lambda$, and central gain wavelength of λ_a, Chang *et al.* quantifies this constraint with Equation (2.8) [16].

$$\tau = \frac{2ln2}{\pi c}\left(\frac{\lambda_a^2}{\Delta\lambda}\right) \tag{2.8}$$

Ti:sapphire crystals are hence the most used gain media in ultrashort pulse generation due to having the broadest gain bandwidth of any medium [16]. In ideal conditions, the theoretical limit imposed by gain narrowing restricts pulses to no shorter than 2.6 fs, however most conventional Ti:sapphire lasers vary, operating with gain narrowing limits closer to 10 fs [16].

Various compensatory techniques have been reported which provide a means to surpass the limitation on pulse duration set by gain narrowing. Using dielectric spectral filters, Seres *et al.* produces 10 fs pulses from a Ti:sapphire gain with a bandwidth that should restrict it to no less than 20 fs [18]. These pulses are launched into a hollow-core fibre which provide enough spectral broadening to allow compression to sub 10 fs, corresponding to peak powers of ~ 0.3 TW [18].

The work reported by Morgner *et al.* presents the generation of 5 fs pulses directly from a Ti:sapphire laser [19]. Using double-chirped mirror pairs for dispersion compensation and a second focus in a BK7 glass plate for additional spectral broadening, the spectra extends from 600 nm to 1350 nm, well exceeding the limit imposed by gain narrowing [19].

2.2.4 Dispersion

Dispersion refers to the passive, frequency-dependent phase variations of an optical pulse as it propagates through a dispersive medium [14]. For a bandwidth-limited pulse, this manifests as temporal broadening, thus making dispersive effects a key consideration for pulsed laser systems.

Although dispersion is classed into three primary categories—intermodal, polarisation mode, and chromatic—the first two find limited relevancy in the scope of this research as they exclusively manifest within waveguides [20]. Therefore, the focus is placed on chromatic dispersion and its significance in pulsed systems.

Chromatic dispersion is largely due to material dispersion, a product of the wavelength-dependent nature of phase velocity and group velocity [21, 22]. As light traverses a material, a disparity emerges between the velocities of longer and shorter wavelength components due to the refractive index dependence. This results in a phase difference in the wavefront, inducing a temporal distortion in the pulse's temporal profile [21].

The impact on pulse duration is quantified by the material dispersion coefficient, denoted as $D_{material}$ and described in Equation (2.9) [21]. For a centre wavelength of λ_0, it is expressed in units of the pulse duration increase per unit length and unit bandwidth.

$$D_{material} = -\frac{\lambda_0}{c}\frac{d^2n}{d\lambda^2} \tag{2.9}$$

Although material dispersion is the principal contributor to chromatic dispersion, in systems involving waveguide propagation, waveguide dispersion becomes a secondary factor. This refers to the temporal distortion of a pulse imposed by the geometric configuration of the waveguide [23]. In the case of optical fibres, it arises from the dependence of the field distribution on the ratio of the core radius to the wavelength [23, 24]. Consequently, the distribution of optical power between the core and cladding varies with wavelength. Since the phase velocities in the core and cladding differ, the group velocity of the mode is modified, resulting in a broadening of the pulse duration [24].

The impact of waveguide dispersion on pulse duration is quantified by the waveguide dispersion coefficient $D_{waveguide}$ and described in Equation (2.10) [24]. This incorporates the fibre V parameter, mode propagation constant β_m and is in units of pulse duration increase per unit length and unit bandwidth.

$$D_{waveguide} = -\left(\frac{1}{2\pi c}\right)\mathrm{V}^2\left(\frac{d^2\beta_m}{dV^2}\right) \tag{2.10}$$

$D_{waveguide}$ does not account for the material dispersion originating from the waveguide's material itself. Therefore, this factor is separately considered.

The quantification of the net chromatic dispersion is not strictly a summation of material and waveguide dispersion. Instead, it is based on the propagation constant β, representing the phase shift per unit length as given by Equation (2.11) [16, 25]

$$\beta(\omega) = \frac{\omega}{c} n_I(\omega) \tag{2.11}$$

Where $n_I(\omega)$ is the imaginary refractive index as a function of frequency ω. Expanding this into a Taylor series with central frequency ω_0 yields Equation (2.12) [16].

$$\beta(\omega) = \sum_{m=0}^{\infty} \frac{1}{m!} \frac{d^m \beta}{d\omega^m}\bigg|_{\omega_0} (\omega - \omega_0)^m \tag{2.12}$$

The zero-order term in this expansion describes a common phase shift and the first-order term signifies an overall time delay which does not affect the pulse shape [16, 26, 27]. The second-order term introduces variation in the pulse width, referred to as group velocity dispersion (*GVD*), and is quantified in units of time squared per unit length, as defined by Equation (2.13). An expression in terms of wavelength may also be derived when used in conjunction with Equation (2.3) and Equation (2.4).

$$GVD = \frac{d^2\beta}{d\omega^2}\bigg|_{\omega_0} = \frac{d}{d\omega}\left(\frac{1}{v_{group}}\right) = \left(\frac{\lambda^3}{2\pi c^2}\right)\left(\frac{d^2 n}{d\lambda^2}\right) \tag{2.13}$$

Although higher-order dispersions may be considered, these only have a significant effect on ultrabroad optical spectra and thus are outside the scope of this research [16, 26, 27].

For materials with wavelength-dependent refractive indices, a common approach for estimating $\frac{d^2n}{d\lambda^2}$ is to use the Sellmeier formula given in Equation (2.14), where *A, B1, B2, B3, C1, C2,* and *C3* are Sellmeier coefficients [28, 29]. Thus, a value for *GVD* can be obtained.

$$n(\lambda) = \sqrt{A + \frac{B_1\lambda^2}{\lambda^2 - C_1} + \frac{B_2\lambda^2}{\lambda^2 - C_2} + \frac{B_3\lambda^2}{\lambda^2 - C_3}} \tag{2.14}$$

The net effect of *GVD* over a length L can be conveniently expressed by the group delay dispersion (*GDD*), which is given in units of unit time squared. The *GDD* is related to *GVD* by Equation (2.15) [16].

$$GDD = GVD \times L \tag{2.15}$$

For a bandwidth-limited Gaussian input pulse with pulse duration τ_{in}, the output pulse duration τ_{out} after transmission through a medium is calculated using Equation (2.16) [16].

$$\tau_{out} = \tau_{in}\sqrt{1 + \left(4ln2\left(\frac{GDD}{\tau_{in}^2}\right)\right)^2} \tag{2.16}$$

The dependence on the input pulse duration in this equation indicates that shorter pulses are more susceptible to temporal distortions for a given *GDD* than longer pulse durations.

2.2.4.1 Normal and Anomalous Dispersion

The magnitude of *GVD* determines the pulse-broadening rate, while the sign of *GVD* affects the phase of the optical pulse envelope. This indicates whether the dispersion acts in the normal or anomalous regime [30].

Normal dispersion is characterised by a positive *GVD*, resulting in an instantaneous frequency that increases with time. This is referred to as positive chirp or up-chirp [24, 30]. In contrast, anomalous dispersion corresponds to a negative *GVD*, leading to an instantaneous frequency that decreases with time, known as negative chirp or down-chirp [24, 30]. The difference between positive and negative chirp is illustrated in Figure 2.2.

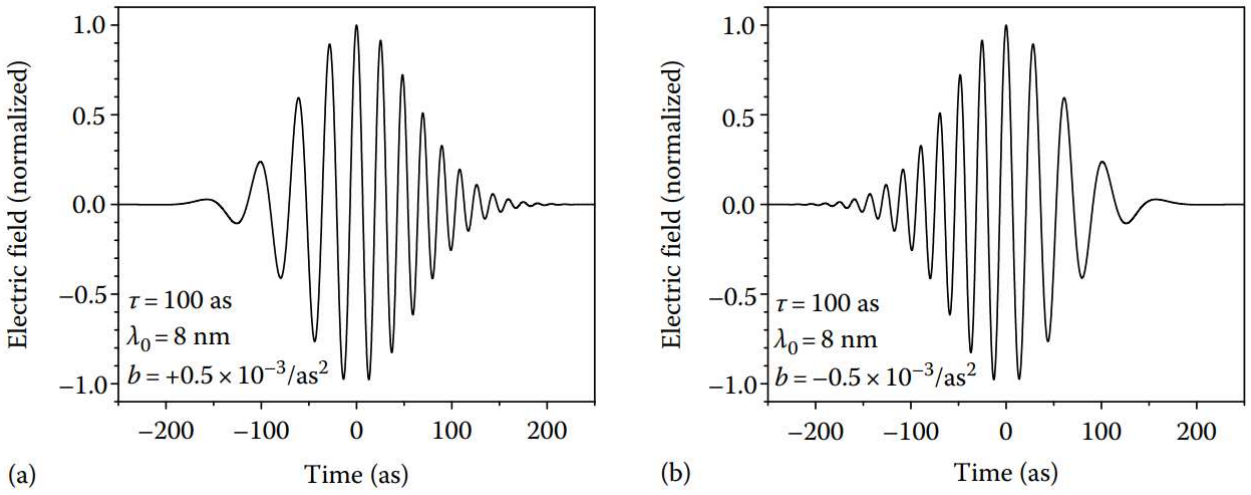


Figure 2.2: (a) A positively chirped pulse and (b) a negatively chirped pulse. Pulse duration of 100 as, centre wavelength of 8 nm, $GDD = 0.5\times10^{-3}$ as^2 (a) and $GDD = -0.5\times10^{-3}$ as^2 (b) [105].

The shortest pulse durations are associated with unchirped pulses. This is illustrated in Figure 2.3.

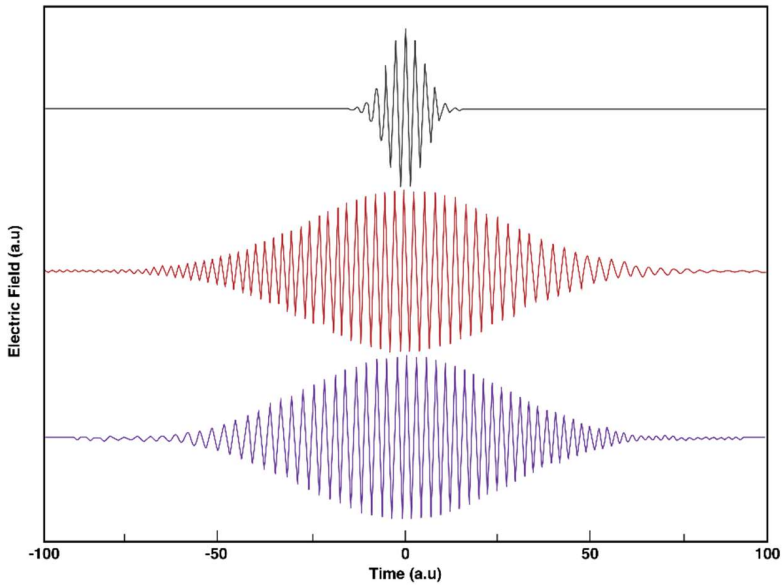


Figure 2.3: The effect of GDD = 5 fs^2 (red) and GDD = -5 fs^2 (blue) on an unchirped 6.7 fs pulse (black) of 100 nm spectral bandwidth centred at 800 nm [120].

The wavelength of light determines the dispersion regime encountered while traversing a medium. For conventional single mode fibre, wavelengths below 1.3 μm result in normal dispersion, leading to a positive chirp [31]. Conversely, wavelengths exceeding 1.3 μm induce anomalous dispersion, leading to negative chirp. Between these regimes exists a zero-dispersion wavelength in which no chirp is produced [31]. This is summarised in Figure 2.4.

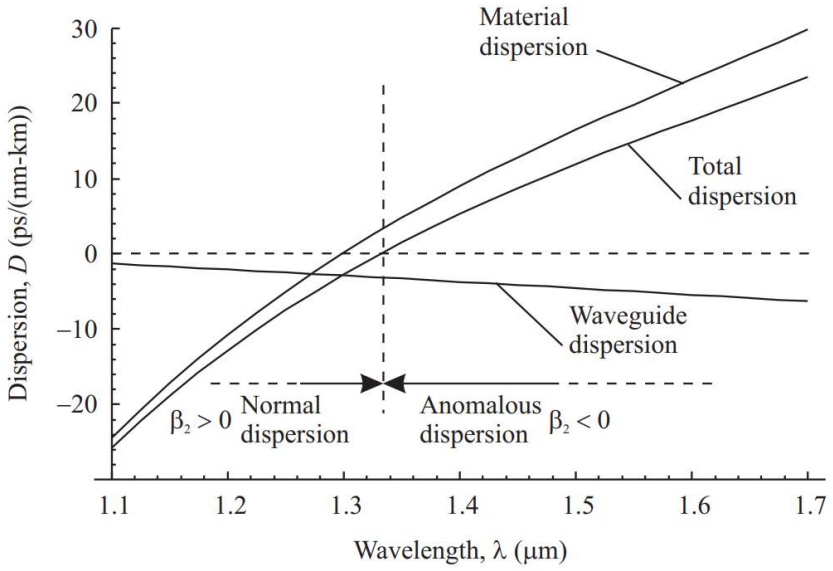


Figure 2.4: Normal and anomalous dispersion regimes for *GVD* and the corresponding wavelength ranges for conventional single mode fibre [121].

While operating around the zero-dispersion wavelength may be advantageous in some applications, nonlinearities dominate under these conditions [26]. A more effective approach is to utilise dispersion compensation optics to create a balance between negative and positive *GVD*.

2.2.4.2 Dispersion Compensation

When a pulse exhibits excessive positive or negative chirp, it may require the use of dispersion compensation optics or nonlinear techniques (see Section 2.3.1.2) to introduce the opposing chirping effect, thereby acting to restore the pulse's temporal shape.

A common method for dispersion compensation involves the use of chirped mirrors. These mirrors are constructed with reflective coatings that vary in thickness gradually [32]. The sequence of coatings is designed such that longer wavelengths penetrate further before reflection, while shorter wavelengths are reflected from the surface layer (or vice versa). This creates a path difference between longer and shorter wavelength components, enabling the slower of the two to 'catch up' to the other, essentially introducing controlled dispersion. When a pulse is reflected off these mirrors, the introduced dispersion can counteract the original chirp, leading to temporal compression. Depending on the arrangement of the coatings, a chirped mirror may introduce positive or negative chirp for a specific operational wavelength [32]. A schematic representation of a negative *GDD* chirped mirror is given in Figure 2.5.

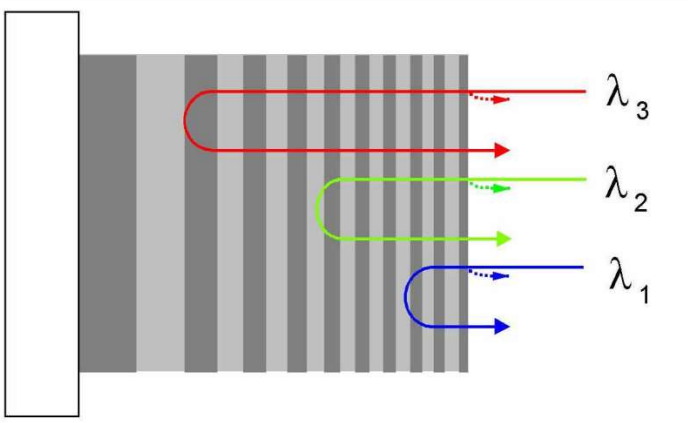


Figure 2.5: Schematic representation of a chirped mirror with negative *GDD* where $\lambda_1 < \lambda_2 < \lambda_3$ [122].

Alternatively, prism pairs with opposing dispersion characteristics may be used [33]. As the pulse traverses the first prism, it undergoes spatial separation into distinct wavelength components, inducing a path difference between longer and shorter wavelengths. Subsequently, a second prism is used to spectrally recombine the pulse, enabling the longer or shorter wavelengths to synchronise before reintegration [33]. These prisms can therefore be positioned to achieve a specific dispersion profile that counters the pulse's initial chirp.

Diffraction gratings are also an effective measure to introduce *GDD* through angular dispersion in a single or double pass configuration. However, gratings typically induce large losses and thus, are primarily used outside of the laser cavity [34].

2.3 Nonlinear Pulse Propagation

The interaction between the polarisation density $P(t)$ of a medium at time t and the incident electric field $E(t)$ of light is described by Equation (2.17) [35].

$$\boldsymbol{P}(t) = \varepsilon_0(\chi^{(1)}\mathbf{E}(\mathrm{t}) + \chi^{(2)}\mathbf{E}^2(\mathrm{t}) + \chi^{(3)}\mathbf{E}^3(\mathrm{t}) + \cdots) \tag{2.17}$$

Where ε_0 is the electric constant, and $\chi^{(n)}$ is the n^{th}-order electric susceptibility of the medium.

For a uniform, non-dispersive, and isotropic dielectric medium, only the first-order electric susceptibility holds significance, resulting in a linear response to the electric field [35]. Conversely, for nonlinear media, higher-order terms may result in various nonlinear effects such as frequency mixing processes and the optical Kerr effect [10].

While nonlinearities underscore the complexity of many optical phenomena, the scope of this research will be constrained only to those intertwined with pulse propagation and the generation of ultrashort pulses.

2.3.1 The Optical Kerr Effect

Due to the presence of higher-order susceptibilities, the refractive index of a nonlinear material may vary in response to the electric field of an electromagnetic wave. This is referred to as the optical Kerr effect and is described by Equation (2.18) [36].

$$n(\lambda, I) = n_0(\lambda) + n_2 I \tag{2.18}$$

Where $n_0(\lambda)$ is the linear refractive index, n_2 is the nonlinear refractive index, and I is the intensity.

The n_2 value of a medium is commonly associated with the third-order susceptibility $\chi^{(3)}$ [37]. This can significantly modify beam propagation through effects known as self-focusing and self-phase modulation under high intensities [10].

Although the n_2 value of materials can be found through a variety of databases, there is often a lack of coverage within select wavelength ranges. Consequently, models frequently rely on approximations of n_2 values derived from nearby measurements or data concerning analogous substances. Table 2.1 provides the directly measured nonlinear refractive index for a variety of common materials.

Table 2.1: Nonlinear refractive indices for materials commonly used in optical elements [70].

Material	**Linear Refractive Index $n_0(\lambda)$**	**Nonlinear Refractive Index n_2 (cm^2/W)**
Sapphire (Al_2O_3)	1.76 @ 850 nm	3.1×10^{-16}
Fused Quartz	1.45 @ 1.06 µm	2.74×10^{-16}
BK7 Glass	1.774 @ 1.06 µm	3.62×10^{-16}
YAG	1.815 @ 1.064 µm	6.24×10^{-16}
ZnSe	2.483 @ 1.06 µm	63×10^{-16}
Air (1 bar / 300 K)	$1 + 0.274 \times 10^{-3}$ @ 1.06 µm	4×10^{-19}

This shows that while numerous solid-state substances exhibit a nonlinear refractive index on the order of 10^{-16} cm²/W, air possesses three orders of magnitude less. Hence, in the absence of extreme optical fields, it is generally permissible to disregard the nonlinear influence of air.

2.3.1.1 Self-Focusing

Self-focusing occurs in materials with a positive nonlinear refractive index [37]. During the propagation of an optical pulse, the intensity dependence of the refractive index induces a phase delay through the optical Kerr effect. This is most pronounced along the central axis of the beam and gradually attenuates towards the periphery, forming a virtual lens known as a Kerr lens [37]. For a Gaussian beam, the focal length of the lens is determined by the optical power P, beam radius ω and material thickness d, as described by Equation (2.19) [38]. The focusing effect by a Kerr lens is referred to as self-focusing and forms the basis for ascertaining values of n_2 [39]. Conversely, for a material with a negative nonlinear refractive index, self-defocusing will occur [37].

$$f = \frac{\pi\omega^4}{8n_2Pd} \tag{2.19}$$

As focusing condenses the beam radius, Equation (2.19) indicates a subsequent increase in the strength of the Kerr lens. If not adequately accounted for, a run-away effect may occur, culminating in the total collapse of the beam radius and optical damage to the medium [16, 39]. This is known as catastrophic self-focusing and transpires when the optical power exceeds the critical power P_{crit}, as defined by Equation (2.20) [16].

$$P_{crit} = \frac{0.148\lambda^2}{n_0 n_2} \tag{2.20}$$

Under some conditions however, self-focusing can be balanced with diffraction, allowing for stable propagation of a beam far beyond the critical power [16]. In such circumstances, a magnitude of complicated dynamics such as filamentation may occur as well as plasma generation, which itself has a defocusing effect [39].

2.3.1.2 Self-Phase Modulation

When an optical pulse propagates through a nonlinear medium of length L, the influence of the optical Kerr effect results in a phase modulation that follows the intensity profile $I(t)$ of the pulse. This phenomenon is known as self-phase modulation (SPM) and is the temporal analogue of self-focusing [40]. The nonlinear phase shift $\phi_2(t)$ is given by Equation (2.21), where δ is the SPM coefficient [34].

$$\phi_2(t) = \left(-\frac{2\pi}{\lambda} n_2 L\right) I(t) = \delta I(t) \tag{2.21}$$

The total effect of SPM is often quantified by the on-axis phase shift per unit optical power. For a Gaussian beam with constant beam radius ω, this is given by the proportionality constant γ_{SPM} defined by Equation (2.22) and expressed in units of rad/W [41].

$$\gamma_{SPM} = \frac{2\pi}{\lambda} n_2 L \left(\frac{\pi}{2}\omega^2\right)^{-1} = \frac{4 n_2 L}{\lambda \omega^2} \tag{2.22}$$

In situations where intensity cannot be considered constant throughout the propagation distance z, the B-integral is instead used to quantify the total on-axis nonlinear phase shift, given by Equation 2.23 [34].

$$B = \int_0^L \phi_2(t,z)\,dz = \frac{2\pi}{\lambda}\int_0^L n_2 I(t,z)dz \tag{2.23}$$

As the derivative of the phase gives rise to the instantaneous frequency of an optical pulse, the introduction of SPM results in the generation of new frequency components. Depending on the initial chirp of the pulse, the net interference of these new components with those already present in the pulse may be constructive or destructive, leading to spectral broadening or spectral narrowing respectively [34, 42].

In the case of a bandwidth-limited (unchirped) pulse where only SPM is present, spectral broadening will occur and the accumulated spectral phase will be positive, resulting in a positive chirp as seen in Figure 2.6 [41]. However, the temporal envelope remains unaffected by this, implying that through the compression of the introduced chirp, it becomes possible to attain pulse durations shorter than the initial duration due to the increase in spectral bandwidth [36].

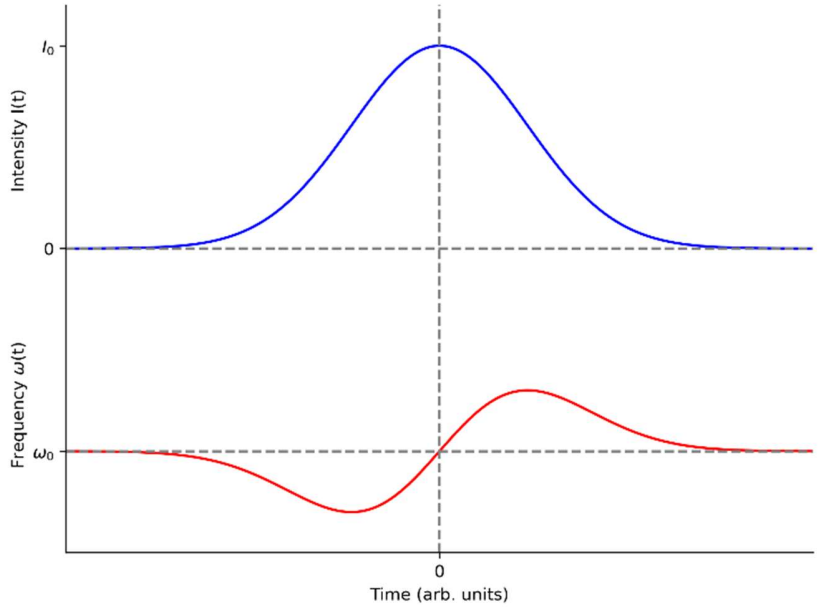


Figure 2.6: Instantaneous frequency (red) of an initially bandwidth-limited pulse (blue) which has experienced SPM.

The output spectral FWHM obtained for an unchirped pulse after undergoing SPM is given by Equation (2.24), where $\Delta\lambda_{in}$ is the input spectral FWHM [16].

$$\Delta\lambda_{out} = 0.86B\Delta\lambda_{in} \tag{2.24}$$

In practice however, dispersive elements (including the nonlinear media itself) introduces chirp to an optical pulse through *GDD*. In the normal regime, the effect of SPM is largely the same as for an unchirped pulse, monotonically broadening the spectrum as the pulse propagates [43]. For negatively chirped pulses however, the opposite effect is true, spectrally compressing the pulse [43, 44]. Planas *et al.* derives an expression for this behaviour in the form of Equation (2.25) [45]. This shows that for a negative chirp parameter C_0, nonlinear parameter Γ, pulse width T_0 and amplitude $|E_0|^2$, compression of spectral bandwidth will occur. Furthermore, this highlights that the initial rate of spectral narrowing is proportional to the input power.

$$\left.\frac{\partial\Delta\omega}{\partial z}\right|_{z=0} = \frac{2\Delta\omega_0\,\Gamma|E_0|^2 C_0 T_0^2}{1 + C_0^2 T_0^4} \tag{2.25}$$

However, as SPM continues to introduce an up-chirping effect, it works to counteract the initial negative chirp, with the maximum spectral compression occurring when the SPM and initial chirp are in equilibrium. This forms the basis for soliton formation (see Section 2.3.2.1) [43, 46]. Beyond this, any additional SPM will flip the dispersion regime and spectral broadening will occur [45].

2.3.2 The Nonlinear Schrödinger Equation

If both the effects of dispersion and SPM act simultaneously on an optical pulse, the field envelope obeys the Nonlinear Schrödinger Equation (NLSE), given by Equation (2.26) [36, 37, 47].

$$\frac{\partial A(z,t)}{\partial z} = \frac{\beta_2}{2}\frac{\partial^2 A}{\partial T^2} - \gamma|A|^2 A \tag{2.26}$$

Where z is the propagation distance, t is time, $A(z,t)$ is the pulse envelope, β_2 is the *GVD*, and γ is the SPM proportionality constant.

2.3.2.1 Solitons

In the anomalous regime, the NLSE is known to have exact solutions, commonly referred to as solitons. These correspond to a balance between the competing effects of SPM and negative dispersion, resulting in ultrashort, self-stabilising pulses that can propagate distortion-free for relatively long distances [47, 48]. Assuming negligible higher-order dispersion, one solution gives the fundamental soliton pulse which has the temporal profile of an unchirped sech^2 pulse, as given in Equation (2.27) [10].

$$P(t) = P_p \operatorname{sech}^2\left(\frac{t}{\tau}\right) \tag{2.27}$$

Where P_p is the peak power, τ is the pulse width and t is the FWHM pulse duration which is equivalent to 1.763 times the parameter τ [10].

Under these conditions, the pulse energy E_p follows Equation (2.28) and is initiated through the peak power P_1 given by Equation (2.29) [48, 49].

$$E_p = \frac{2|\beta_2|}{|\gamma|\tau} \tag{2.28}$$

$$P_1 = \frac{|\beta_2|}{\gamma T_0^2} \tag{2.29}$$

To determine the necessary requirements to balance the effects of dispersion and SPM, the length scales at which the dispersive effects (L_D) and nonlinear effects (L_{NL}) achieve significance are compared. Their ratio is conventionally represented as N^2 and is given by Equation (2.30) [49, 50].

$$N^2 = \frac{L_D}{L_{NL}} = \frac{\gamma P_0 T_0^2}{|\beta_0|} \tag{2.30}$$

Where T_0 is the width of the incident pulse, P_0 is the peak power of the incident pulse, $L_D = T_0^2|\beta_0|^{-1}$ and $L_{NL} = (\gamma P_0)^{-1}$.

The value of N^2 provides the following diagnostics on the system:

- If $N \ll 1$, dispersion plays a dominant role in the system's behaviour. In this regime, the dispersive effects are significantly more influential than the nonlinear effects.

- If $N \gg 1$, nonlinear effects become predominant. Here, the nonlinear interactions between the light pulses or waves are considerably stronger than the dispersive effects.

- If $N = 1$, this corresponds to the fundamental soliton.

For integer multiples of N the soliton period z_0 is given by Equation (2.31) [10, 49].

$$z_0 = \frac{\pi}{2} L_D \tag{2.31}$$

For integer values of N greater than or equal to 2, the resulting pulse is referred to as a higher-order soliton. In contrast to the fundamental soliton, higher-order solitons do not exhibit a

constant shape during propagation. Instead, their shape undergoes periodic variations [10, 48]. For this research, higher-order solitons are considered undesirable.

These constraints highlight the delicate balance between dispersive and nonlinear effects required for stable, soliton pulse shaping.

2.4 Passive Pulse Generation

The principles of pulse generation in a laser resonator encompass two primary methods: mode-locking and Q-switching. Mode-locking refers to the synchronisation of multiple longitudinal modes to generate ultrashort pulses lasting picoseconds or even femtoseconds. In contrast, Q-switching involves temporarily reducing the cavity's quality-factor (Q-factor) to store energy before releasing it as a high-energy pulse, typically lasting nanoseconds. While both forms of pulse generation in this research utilise the same optical component, the underlying physics behind each mechanism is fundamentally distinct and thus, are explored independently.

2.4.1 Mode Superposition Theory

Laser light is not monochromatic, but instead operates over some natural bandwidth as discussed in Section 2.2.1. When wavelengths are reinforced by constructive interference after many reflections within a laser cavity of length L, standing wave patterns are produced in the longitudinal axis [51]. These are known as longitudinal modes and are separated by the free spectral range (FSR) as given in Equation (2.32) [34].

$$\Delta\omega_{FSR} = \frac{\pi c}{L} \tag{2.32}$$

In a CW regime, the phase between these modes varies randomly in time, thus producing a continuous output beam. If a coherence is introduced however, the modes may constructively interfere to generate a pulse, thus forming the basis for modelocking [47]. For a single circulating pulse, the pulse repetition rate is given by the inverse round-trip time, as the pulse is out-coupled once per round trip [47].

The electric field is written as a summation of the modes, as given by Equation (2.33) [34].

$$E(t) = \sum_{n=0}^{N-1} E_n \sin\big(\omega_n t + \phi_n(t)\big) \tag{2.33}$$

Where ω_n and $\phi_n(t)$ is the frequency and phase of the n^{th} mode respectively, with N indicating the total number of oscillating modes.

Assuming the simple case in which $\phi_n(t) = 0$ and $E_n = E_0$, the intensity is the squared modulus of this field and is thus given by Equation (2.34), with I_0 being the average intensity of one wave [34, 51].

$$I(t) = I_0 \left(\frac{\sin\left(\frac{N\Delta\omega t}{2}\right)}{\sin\left(\frac{\Delta\omega t}{2}\right)} \right)^2 \tag{2.34}$$

Equation 2.34 indicates that a higher number of oscillating longitudinal modes corresponds to a higher intensity and shorter pulse duration, signifying the importance of a large spectral bandwidth in the generation of ultrashort pulses via modelocking [24]. This is highlighted by the computation and plotting of Equation (2.33) for a various number of modes, as illustrated in Figure 2.7.

Phase coherence is induced by applying periodic losses to the resonator, providing a higher gain/loss ratio for photons concentrated in a pulse [36, 52]. While this can be done by synchronising an acousto-optic or electro-optic modulator with the cavity round trip, an example of active mode-locking, the response time of the modulator limits the attainable pulse width. To generate significantly shorter pulses, the intrinsic properties of specific

materials can be leveraged, a method known as passive mode-locking. This serves as the foundation for this research [36, 52].

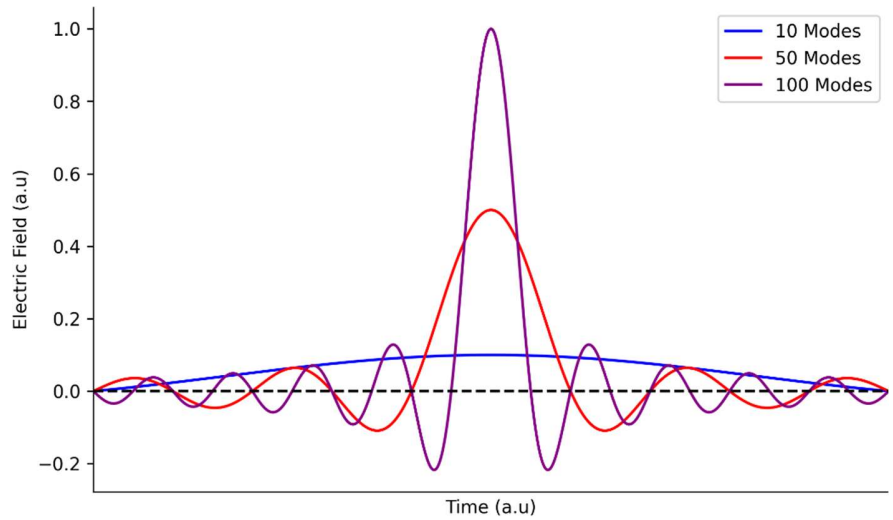


Figure 2.7: The total electric field of 10 (blue), 50 (red), and 100 (purple) longitudinal modes with a fixed phase relation.

2.4.2 Q-Switching Theory

Although there are two primary methods to achieving Q-switching, active and passive, they both revolve around the same two-phase principle [53]. In the first phase, lasing is prevented by high cavity losses while the gain medium is pumped, creating a population inversion. When the stored energy in the gain reaches a maximum, the medium is said to be gain saturated. In the second phase, the high cavity losses are rapidly reduced which results in a sudden release of the stored energy through stimulated emission, producing a large pulse [47]. The relative loss and gain are depicted in Figure 2.8.

In active Q-switching, an external signal modulates cavity losses, while passive Q-switching instead relies on the intrinsic properties of a nonlinear medium. As will be discussed in Section 2.4.3, this is achieved through saturable absorption, which provides the cavity with a variable Q-factor dependent on the energy stored in the gain [47]. While active Q-switching

techniques are the most common due to the versatility of the external driving signal, passive Q-switching offers a simple and cost-effective method suitable for high repetition rates [53].

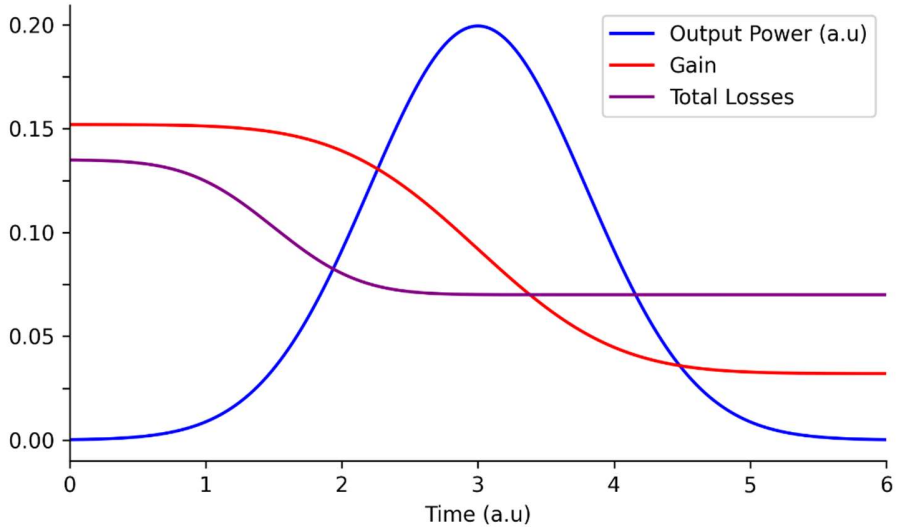


Figure 2.8: Temporal evolution of the output power (blue) compared to the total losses (purple) and gain (red) in a passively Q-switched laser.

Given that the saturation of the gain is driven by the pump, the repetition rate of the pulses is proportional to the pumping rate. Moreover, the strength of the absorber dictates the energy accumulation required for the Q-factor to switch between low and high states. A stronger absorber therefore yields greater pulse energies with reduced repetition rates and shorter pulse durations. Additionally, the duration of pulses is impacted by the resonator's round-trip time [54, 55]. With a shorter cavity length, there's a decreased timeframe for energy accumulation as the distance for energy propagation within the cavity is reduced.

In contrast to mode-locking, a large number of longitudinal modes is not required for Q-switching. In fact, Q-switching will ideally only operate in one mode [36, 53]. Since the number of longitudinal modes supported is proportional to the cavity length, as shown in Equation (2.32), a shorter cavity will not only minimise pulse durations but will also act to suppress mode-locking tendencies. This allows for extremly compact resonator designs, an approach commonly used in SESAM Q-switched microchip systems [56-62].

Keller *et al.* presents Equation (2.35) as a condition for initiating Q-switching [63].

$$\left|\frac{dR}{dI}\right| I > r\left(\frac{T_R}{\tau_2}\right) \tag{2.35}$$

Where R is the absorber reflectiveity, I is the CW intensity, r detmines how many times the laser is pumped above threshold, T_R is the cavity round trip time, and τ_2 is the upper state lifetime of the laser gain medium.

From Equation (2.35), it can be concluded that Q-switching is supported under the following conditions: low saturation intensities, gain not pumped significantly above threshold, a short resonator length, and a gain medium with a long upper-state lifetime for an increased population inversion [63].

2.4.3 Saturable Absorbers

The most common approach to passive pulse generation relies on elements which exhibit saturable absorption. This property refers to an intensity dependent loss due to nonlinear absorption [36]. Depending on the implementation of the saturable absorber, this feature may be used to reflect or transmit high intensities, like those found in optical pulses, while absorbing and consequently suppressing any other signal components. Since optical pulses consist of a high peak intensity with a low intensity peripheral, the saturable absorber acts to both self-start pulse generation from high intensity noise fluctuations as well as to sharpen the pulse shape through subsequent passes through the absorber [36].

While most materials demonstrate some degree of saturable absorption, it's typically only observed at very high optical intensities [36]. For laser pulse generation, saturable absorbers that demonstrate this effect at intensities found within laser cavities are required. When an ultrashort pulse circulates within the laser cavity, it modulates the intracavity loss, which subsequently modulates the circulating pulse. As a result, the loss modulation naturally

synchronises with the pulse train [64]. Moreover, if the response time of the nonlinearity is fast enough, the modulation increases for shorter pulse durations, hence allowing for the pulse-shortening mechanism to remain effective for extremely short pulse durations [65]. Depending on how rapidly the absorber recovers with respect to the pulse duration, they are classified as either fast or slow [10].

Semiconductor materials exhibit significant saturable absorption through the exchange of electrons between the valence and conduction band [47, 52]. When a semiconductor is exposed to light with an appropriate photon energy, it excites electrons from the valence band to the conduction band. When the optical field intensity is low, only a small number are excited, and the semiconductor's absorption remains unsaturated. However, when the optical field intensity is significantly increased, absorption decreases as electrons accumulate in the conduction band, leading to a corresponding depletion in the valence band. This phenomenon results in high transmission through the saturable absorber for high intensity field intensities [66]. Furthermore, the versatile engineering of semiconductors allows for the tailoring of band gap energies, enabling a wide range of absorption wavelengths and hence making semiconductor materials a popular choice for saturable absorbers [47].

There are also various techniques to emulate saturable absorbers without relying on any absorption mechanism [65]. Components utilising these methods are referred to as artificial saturable absorbers and may be used to induce other types of pulse generation such as Kerr lens modelocking [65, 67].

2.4.4 Semiconductor Saturable Absorber Mirrors

2.4.4.1 Resonant and Anti-Resonant Architectures

When a reflective element is integrated with a semiconductor saturable absorber, the result is a device whose reflectivity increases as the incident optical intensity increases [52, 66].

This is known as a semiconductor saturable absorber mirror (SESAM) (or simply SAM = saturable absorber mirror).

A Bragg mirror, also known as a dielectric mirror, is the most common reflective optic chosen amongst SESAM designs [68]. The mechanism is based on the Fresnel reflections formed between the interfaces of an alternating banded sequence of two materials. If the thickness of each band is equal to one-quarter of the operational wavelength and the materials are selected such that the reflection coefficients for the interfaces have alternating signs, the Fresnel reflections constructively interfere, resulting in a strong reflection [69].

The integration of the Bragg mirror with a saturable absorber often comes with the addition of various optical coatings as well as a substrate material on which the reflector is grown [70]. Figure 2.9 illustrates the sequence of the components in the typical structure of a SESAM.

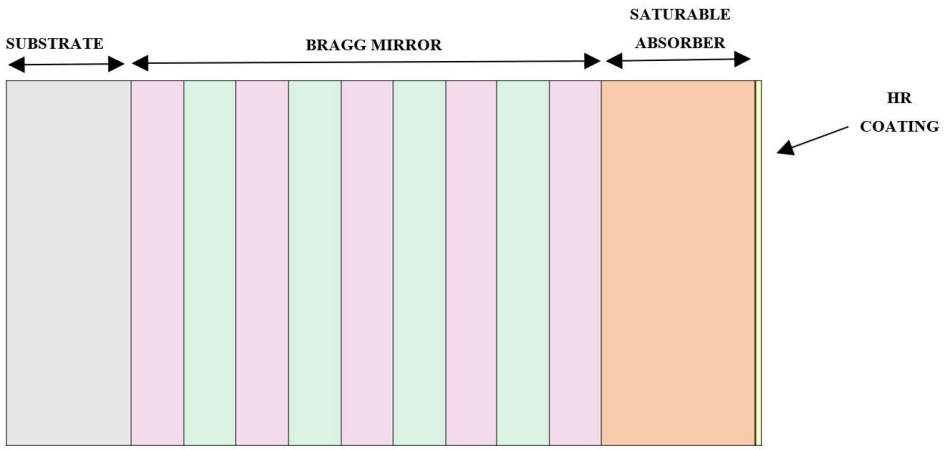


Figure 2.9: Generic architecture and sequencing of a SESAM.

Although not a standard practice in commercial SESAMs, Diebold *et al.* have shown that removing the substrate from a SESAM leads to superior surface quality and improved heat dissipation in high-power applications compared to SESAMs with intact substrates [70].

While the configuration and variety of optical coatings may vary significantly between designs, the architecture of a SESAM can be classified into two primary categories: resonant and anti-resonant [71, 72]. When used in place of a cavity mirror, the optical field standing wave may experience an anti-node at the surface of the SESAM structure [72]. In this case,

when a high-reflectance (HR) coating is applied to the surface to modulate incoming power, and the absorber layer is encased in a cavity between the Bragg mirror and HR coating, a resonance effect is induced [71]. This is known as a resonant SESAM and is characterised by a higher modulation depth and lower saturation fluence (see Section 2.4.4.2), significant *GDD*, as well as an overall narrower operational wavelength range [72, 73]. The typical architecture of a resonant design is seen in Figure 2.10 (a).

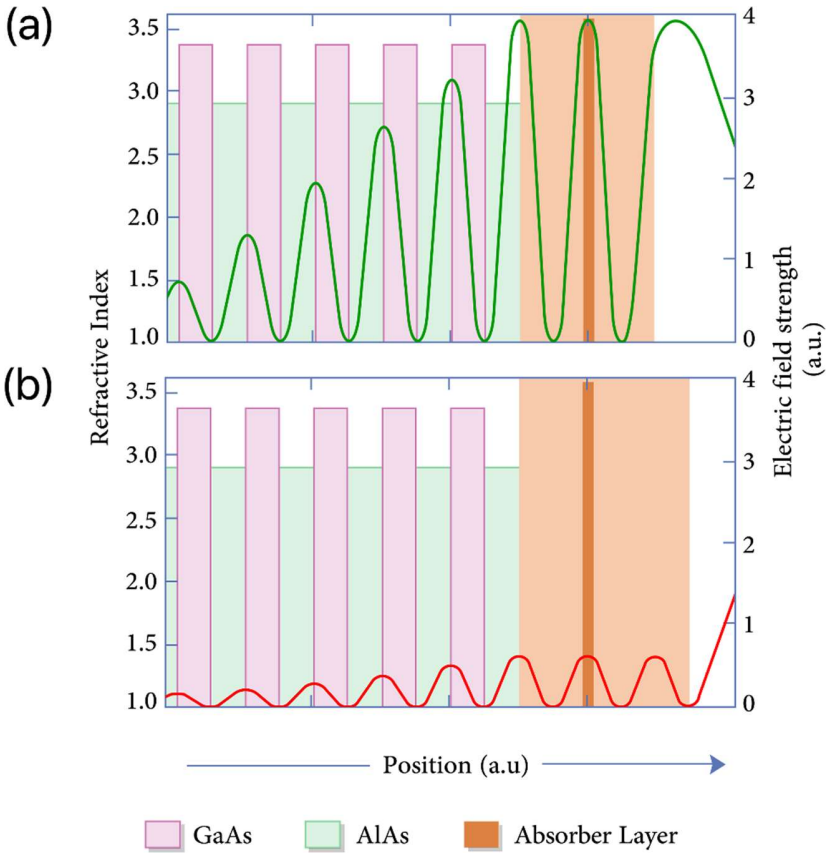


Figure 2.10: Typical structures of (a) resonant and (b) anti-resonant GaAs/AlAs Bragg mirror SESAMS, with the incident field intensity represented by the green and red trace respectively.

In contrast to the resonant design, the anti-resonant design exhibits a node in the optical field intensity at the front surface of the SESAM [74]. Substituting the HR coating with an anti-reflectance (AR) coating also acts to limit any resonance within the device itself. Such features allow for much higher damage thresholds, lower modulation depths and a smaller *GDD* [72]. An example of this architecture is illustrated in Figure 2.10 (b).

2.4.4.2 Characteristic Parameters

The performance of a SESAM to passively generate pulses is dependent on various macroscopic properties. The most important of these include modulation depth, absorption, saturation fluence, recovery time, and nonsaturable loss [66, 72, 75]. These are summarised in Table 2.2.

Modulation Depth:

The modulation depth of a SESAM, denoted as ΔR, is defined as the maximum nonlinear change in reflectance between an unsaturated and saturated saturable absorber, expressed as a percentage [75]. This is often considered the most influential parameter in the pulse generation mechanism as it determines the degree of pulse shaping per pass. From the point of view of pulse width and stability, Abouelez *et al.* highlights the inverse proportionality between pulse width and modulation depth [66]. While this implies the need for higher modulation depths to form shorter pulses, excessive pulse shaping may also contribute to Q-switching instabilities, forcing the system into undesirable pulse regimes if many longitudinal modes are present, such as Q-switched mode-locking (see Section 2.5.1) [75-77]. Hence, an upper limit for modulation depth is dictated by the pulse shaping requirements of the system. The greatest discrepancy in the degree of required pulse shaping arises between fibre and free-space lasers due to the added waveguide dynamics and dispersive effects. For mode-locked fibre lasers, typical modulation depths exceed 10%, whereas mode-locked free-space lasers are often operated around $\Delta R \sim 1\%$ [68, 77].

Unsaturated and Saturated Absorption and Reflection:

Unsaturated absorption, A_0, and unsaturated reflectance, R_0, refers to the absorption and reflectance of the saturable absorber when completely unsaturated. This corresponds to the maximum absorbance of the device and hence, minimum reflectance [72]. Conversely, saturated absorption, A_c, and saturated reflectance, R_c, refers to the absorption and reflectance of the saturable absorber when completely saturated, corresponding to minimum absorbance and maximum reflectance [72]. Whether absorption or reflectance is used to express the

performance of the device varies across literature but either nomenclature is generally acceptable.

Non-Saturable Loss:

The non-saturable loss is defined as the difference in absorption, ΔA_{ns}, or reflectance, ΔR_{ns}, of a SESAM at saturation relative to ideal saturation performance. This difference is primarily attributed to growth defects, residual transmission, and scattering losses [75]. Since ideal saturation performance suggests 0% absorbance and 100% reflection, ΔA_{ns} is equivalent to A_c, and ΔR_{ns} must be equated using Equation (2.36).

$$\Delta R_{ns} = 1 - R_c \tag{2.36}$$

Modulation depth, unsaturated reflectance, and non-saturable loss can therefore be related using Equation (2.37), which is further emphasised by the nonlinear reflectance profile of a typical SESAM as depicted in Figure 2.11.

$$R_0 + \Delta R + \Delta R_{ns} = 1 \tag{2.37}$$

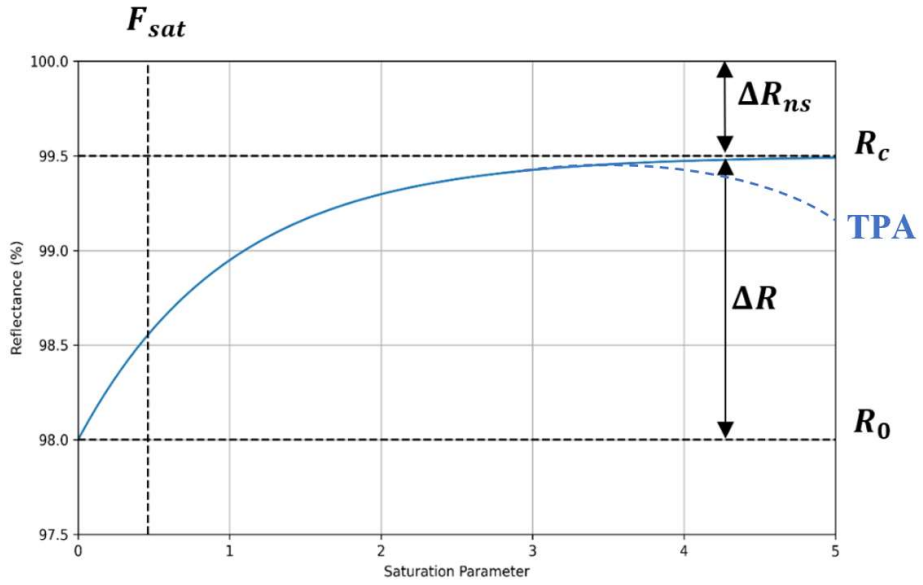


Figure 2.11: Example of a nonlinear reflectance profile for a SESAM with a modulation depth of ΔR = 1.5% and non-saturable loss of ΔR_{ns} = 0.5% as a function of saturation.

Saturation Fluence:

The saturation fluence, F_{sat}, is defined as the fluence of an incident pulse required to induce significant saturable absorption [66, 73]. Mathematically, it is defined as the fluence at which the absorption coefficient drops to 1/e of its original value, as illustrated in Figure 2.10 [75]. Therefore, a low saturation fluence corresponds to a lower power required to initiate mode-locking [72, 73]. Where appropriate, this parameter may also be expressed in terms of saturation energy, E_{sat}, or saturation intensity, I_{sat}. It is noted however, that while a certain fluence is required to saturate the absorber and thus increase the reflectivity, excess values of saturation fluence may result in the opposite effect. For higher fluences, the probability of additional nonlinear absorption processes such as two-photon absorption (TPA) increases. This creates a reflectivity 'roll-off', as indicated in Figure 2.11. For further information on TPA, refer to Appendix A.

Recovery Time:

The recovery time τ_s, also known as the relaxation time, is the time taken for the loss induced by the saturable absorber to revert to 1/e of its original value following saturation from an incident pulse [75]. In the case that this time is significantly above the pulse duration, the saturable absorber element is referred to as a 'fast saturable absorber'. Conversely, if the opposite holds true, it is referred as a 'slow saturable absorber' [75, 78, 79]. While faster dynamics are often preferred to achieve efficient pulse formulation with high repetition rates, both classifications of absorbers can be used for mode-locking, each with their own distinct mechanism [66, 75, 78, 79]. These methods are commonly referred to as 'fast SESAM mode-locking' and 'slow SESAM mode-locking', as expanded on in Section 2.4.5 [78].

Table 2.2: Summary on the characteristic parameters of a SESAM.

Quantity	Symbol	Description	SI Units
Modulation Depth	ΔR	The change in reflectance between the unsaturated and saturated device states.	%
Unsaturated Absorption/Reflectance	$\frac{A_0}{R_0}$	The absorption/reflectance of the device in its unsaturated state, i.e., low-intensity optical field.	%
Saturated Absorption/Reflectance	$\frac{A_c}{R_c}$	The absorption/reflectance of the device in its saturated state, i.e., high-intensity optical field.	%
Non-Saturable Loss	$\frac{\Delta \mathrm{A_{ns}}}{\Delta R_{ns}}$	The absorption/reflectance discrepancy from ideal performance, attributed to various losses.	%
Saturation Fluence	F_{sat}	Incident pulse fluence required to decrease device absorption to 1/e of its unsaturated value.	J/m^2
Recovery Time	τ_s	The time taken for the absorber to revert to 1/e of its unsaturated absorption following saturation from an incident pulse.	s

2.4.5 Passive Mode-Locking Models

Historically it was believed that only fast saturable absorbers, with the shortest net gain windows, could effectively support mode-locked pulses [78]. However, recent years have shown a shift in this understanding, with three primary mode-locking mechanisms accepted for the formation of ultrashort pulses using saturable absorbers. The dynamics of these are explained by three fundamental mode-locking models: fast saturable absorber mode-locking, slow saturable absorber mode-locking, and soliton mode-locking [36, 80].

2.4.5.1 Fast Saturable Absorber Mode-Locking

As briefly introduced in Section 2.4.4.2, fast saturable absorber mode-locking refers to the mode-locking process in which the incident pulse has a duration shorter than the recovery

time of the saturable absorber. This allows for the absorption profile of the saturable absorber to recover fast enough to maintain consistent pulse shaping between the leading and trailing edge of each pulse, while discriminating against all else [81]. Assuming the relaxation time of the laser medium is long enough to produce a relatively time-independent laser gain, the result is a symmetric pulse intensity profile as shown in Figure 2.12 (a) [80].

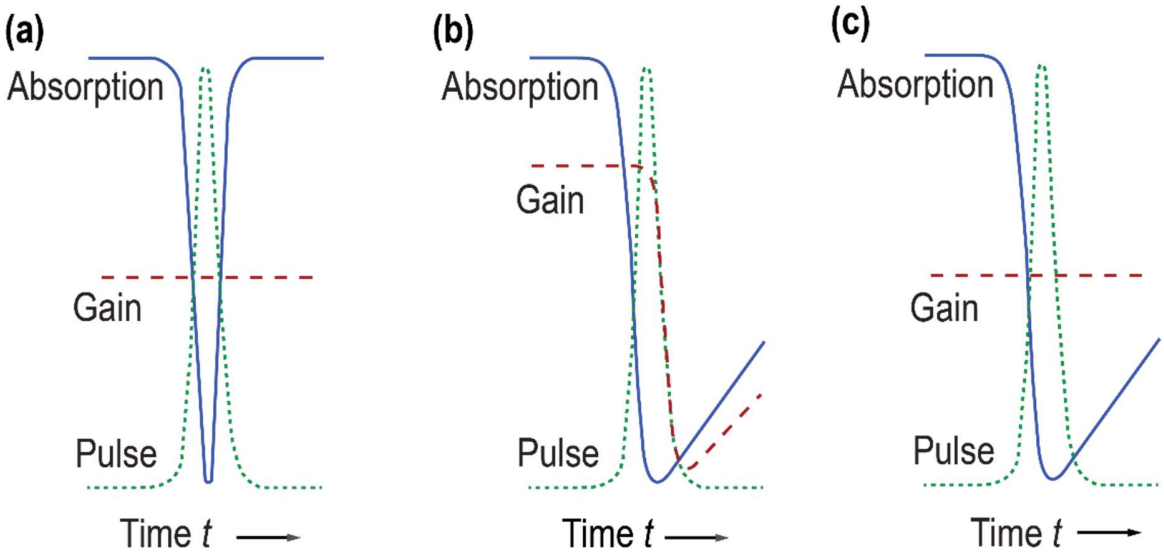


Figure 2.12: Fundamental passive mode-locking models: (a) fast saturable absorber mode-locking, (b) slow saturable absorber mode-locking with dynamic gain and, (c) slow saturable absorber mode-locking without dynamic gain but supported by soliton shaping.

The dynamics presented by fast saturable absorber mode-locking are commonly described across literature by a generalisation of the NLSE known as the Haus Master equation, as given in Equation (2.38) [36, 47, 82-91].

$$\frac{\partial u}{\partial z} = \left[-i\phi - \frac{l}{2} + \frac{g(|u|)}{2}\left(1 + \frac{1}{2\omega_g^2}\frac{\partial^2}{\partial t^2}\right) - \frac{i\beta''}{2}\frac{\partial^2}{\partial t^2} + i\gamma|u|^2\right]u + f_{sa}(|u|)u, \quad (2.38)$$

Where $u(t,z)$ is the complex field envelope, t is time, z is the propagation distance, ϕ is the phase rotation per unit length, l is the linear loss coefficient, $g(|u|)$ is the saturated gain, β''

is the *GVD*, γ is the Kerr coefficient, ω_g is the gain bandwidth, and $f_{sa}(|u|)$ is the fast saturable absorption factor.

Under certain conditions, stable pulse propagation parameters for various resonator designs may be found through analytic solutions of the Haus Master equation [91]. This breaks down however for slow saturable absorbers due to the added complexity of the time-dependent loss and hence only applies for fast saturable absorber mode-locking without considerable modifications [91].

2.4.5.2 Slow Saturable Absorber Mode-Locking

Slow saturable absorber mode-locking describes the mode-locking mechanism in which the incident pulse's duration exceeds the recovery time of the saturable absorber. As a result, the absorption only reverts to its original strength well after the pulse has passed, as shown in Figure 2.12 (b) [92]. This poses a stability issue as any noise directly behind a pulse would be subject to constant gain, producing an asymmetry and destabilising the pulse [78]. For semiconductor, dye and colour-centre lasers however, the gain media also exhibits significant saturation, a property known as dynamic gain [80, 93]. While this avoids the amplification of noise following the pulse while the gain is recovering, the same logic cannot be applied to bulk lasers, which do not exhibit dynamic gain [90].

An explaination for the existance of such systems is instead based on the inbalance between the saturable absorber-induced attenuation of the leading and trailing pulse wings [90]. This causes the temporal centre of each pulse to be shifted into any noise behind it, wiping it up before any amplification of noise can accumlate [90].

2.4.5.3 Soliton Mode-Locking

An alternative method using slow saturable absorbers is to harness soliton mode-locking dynamics [94]. As discussed in Section 2.3.2.1, an optical soliton is formed when the

competting effects of negative dispersion and SPM are balanced. Under these conditions, the saturable absorber is only required for starting and stabilising the solitons against the growth of background noise, with the primary pulse shaping dominated by the interplay between dispersive and nonlinear effects [95]. The degree of pulse shaping is therefore dependent on the extent of the equilibrium established. This results in the generation of the shortest and most stable pulses within the mode-locking models presented without the need for artificial saturable absorbers [80, 96].

In optical fibres, the effects of *GDD* and SPM act simultaneously on the pulse during propagation, resulting in a genuine "true" soliton [95]. In contrast, bulk lasers exhibit varying levels of dispersion and nonlinearity throughout different optical elements in a resonator. Hence for bulk systems, the balance between dispersion and nonlinearity only pertains to the overall phase shift occurring per round trip, giving rise to what are referred to as quasi-soliton pulses [95]. This represents the most common methodology to achieve mode-locking in bulk lasers [96].

The onset of soliton pulses may be established through the existence of Kelly sidebands in the optical spectrum. The details of such are elaborated on further in Section 2.6.2.3.

2.5 Passive Mode-Locking Regimes

A laser resonator with an intracavity SESAM has the capacity to function in a wide range of pulsed regimes, largely influenced by the specific SESAM parameters, resonator configuration, and pump characteristics. While not all strictly mode-locked, these regimes offer unique pulse profiles ranging from microsecond to femtosecond, each serving as the basis for extensive areas of study. For the purpose of this research, the regimes of relevance include Q-switched mode-locking (QML), continuous mode-locking (CML), and multi-pulse mode-locking (MPML) [63, 97-99].

2.5.1 Q-switched Mode-Locking

The use of a saturable absorber to achieve mode-locked pulses suffers from a Hopf bifurcation known as the Q-switching instability, resulting in a slow full scale modulation of an otherwise mode-locked pulse train due to unstable energy oscillations [100]. This is typically observed as a burst of mode-locked pulses with a repetition rate on the order of MHz, confined to a Q-switched envelope with a repetition rate in the kHz region [97]. While such modulations have some practical applications in nonlinear-frequency conversion, microstructure fabrication, and surgery, these are often limited [97]. Thus, this regime is largely undesirable and rarely seen as more than an intermediate step to achieving stable mode-locking.

Expanding on the conditions set to suppress Q-switching, Keller *et al.* presents Equation (2.39) as a method to avoid QML, where the absorber saturation is induced by pulse energy E_P [63].

$$\left|\frac{dR}{dE_p}\right| E_p < r\left(\frac{T_R}{\tau_2}\right) \tag{2.39}$$

Under appropriate simplifications, this condition is given in terms of the saturation energy of the gain medium, $E_{sat,g}$, the saturation energy of the saturable absorber, $E_{sat,a}$, and the modulation depth, ΔR, as presented in Equation (2.40) [97].

$$E_P^2 > E_{sat,g} E_{sat,a} \Delta R \tag{2.40}$$

Hence, mode-locking is typically enforced by a high SESAM fluence in addition to a minimal modulation depth for the pulse shaping requirements of the resonator. It is noted however, that an excessive value of E_P may also result in the onset of multiple pulsing [101].

2.5.2 Continuous-Wave Mode-Locking

Continuous-wave mode-locking (CML) refers to the stable regime where soliton pulse formation leads to the generation of picosecond to femtosecond pulses [53]. In this mode, a solitary pulse is emitted with uniform energy during each round trip within the laser cavity. Ideally all the laser power is confined exclusively within the pulse, with no lasing products occuring in the intervals between successive pulses [53].

While CML is considered the most quintessential form of mode-locking, the constraints outlined in Equation (2.35), Equation (2.39), Equation (2.40), and the pulse shaping prerequisites of the resonator present substantial challenges in attaining this regime. It is a common trend in literature to observe the onset of Q-switching or QML as intermediate steps toward realising CML [102-107].

2.5.3 Multi-Pulse Mode-Locking

In addition to Q-switching instabilities, CML may also suffer from phenomena known as multi-pulse instabilities, giving rise to the multi-pulse mode-locking (MPML) regime. This occurs when a single circulating pulse splits into multiple pulses, resulting in several pulses of varying intensity and duration being outcoupled from the cavity per round trip [108]. Despite various studies, the dynamics of this behaviour are not well understood, with the transition process between single and multi-pulse operation characterised by a chaotic nature [109]. Consequently, even though higher repetition rates can be attained, the inconsistency in pulse energy constrains the practical use of this regime only to applications capable of tolerating highly variable pulse energies and peak powers [110].

Although there are many competing theories concerning the fundamental mechanisms driving multi-pulsed behaviour, the basis for these investigations are centred on extreme nonlinear distortions [109, 111]. When the pulse energy is increased, the spectral profile of the pulse undergoes broadening due to SPM. While this is an important aspect of ultrafast

pulse generation, excessive broadening may exceed the bandwidth limit of the gain. In which case, the pulse becomes energetically unfavourable and splits into multiple pulses with smaller bandwidths [112]. Hence, MPML regimes are typically associated with high pulse energies and broadly spanning optical pulse frequencies.

Waldburger *et al.* offers an alternative insight using a SESAM mode-locked femtosecond source [110]. Their approach involves a gradual increase in pump power, which reveals a sequence of MPML transitions in hysteresis: starting from CML, evolving into a MPML state characterised by a satellite pulse accompanying the primary pulse. Subsequently, it progresses to a double-pulse regime, and finally transforms into a regime featuring a combination of a double pulse and a satellite pulse [110]. Waldburger *et al.* attributes the onset of MPML to a short gain lifetime, kinetic hole burning, as well as the gain position within the cavity rather than increased nonlinearities. Furthermore, they note that the MPML regimes offers significantly lower average output powers when compared to CML operation [110].

2.6 Pulse Characterisation Techniques

2.6.1 Intensity Noise and Timing Jitter

Mechanical vibrations, thermomechanical disturbances, spontaneous emission, and intrinsic features of the system, such as quantum fluctuations within the gain medium, all contribute to noise within a pulse train. [36]. Although it can be minimised, some degree of noise will always be present. Hence, classifying and quantifying its extent is an important aspect of any pulse characterisation [113].

There are two primary classifications of noise: intensity noise and timing jitter. Intensity noise refers to the measurement of intensity fluctuations $\Delta I(t)$ of the individual pulses within the pulse train (Figure 2.13). It therefore serves as a quantification of pulse energy, where pulse energy is defined as the integral of the instantaneous pulse power over the duration of

a single pulse [114]. When normalised to the average value, the term relative intensity noise (*RIN*) is used instead. Using σ_{energy} as the standard deviation of pulse energies and μ_{energy} as the mean pulse energy, it is mathematically defined by Equation (2.41) [113].

$$RIN = \frac{\sigma_{energy}}{\mu_{energy}} \tag{2.41}$$

Analogous to intensity noise, timing jitter $\Delta T(t)$ quantifies the fluctuations in temporal pulse position relative to the repetition rate of the system (Figure 2.13) [115]. When specified relative to another oscillatory source, the term residual jitter may also be used [36].

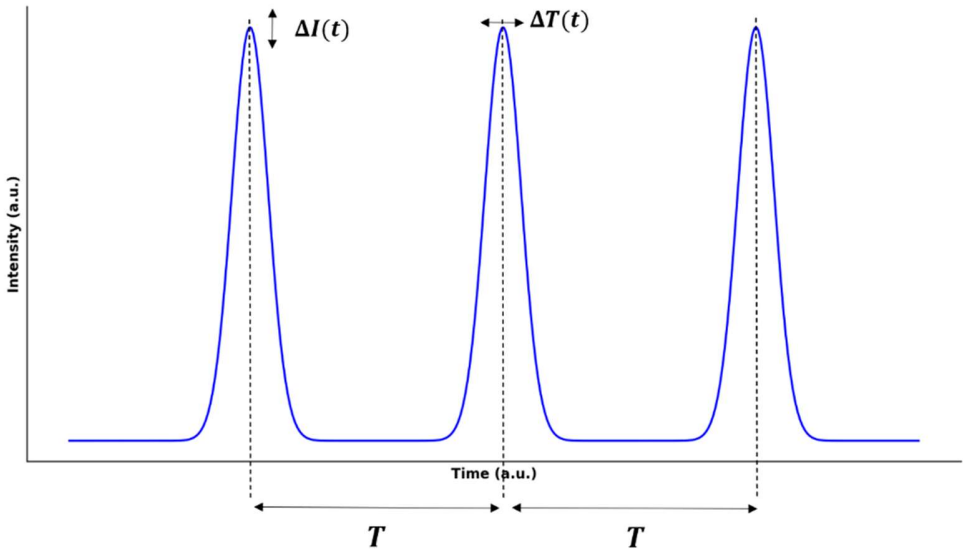


Figure 2.13: A pulse train intensity with pulse period *T*. Intensity noise *ΔI(t)* and timing jitter *ΔT(t)* are illustrated as small deviations from ideal stability.

2.6.2 Characterisation Apparatus

2.6.2.1 Oscilloscope

A photodetector converts photon energy into a voltage proportional to the incident optical power [116]. When connected to an oscilloscope, this provides a means of visualising the pulse train, thus acting as a preliminary tool for identifying whether the laser is producing a pulsed output. For Q-switched pulses, provided an adequate sampling rate, both pulse durations t_p and repetition rates f_R may be obtained via the oscilloscope trace. Pulse energies E_P and pulse peak powers P_{peak} can then be calculated from the average power P_{ave} using Equation (2.42) and Equation (2.43) [117, 118].

$$E_P = \frac{P_{ave}}{f_R} \tag{2.42}$$

$$P_{peak} = 2\sqrt{\frac{\ln(2)}{\pi}}\left(\frac{E_P}{t_p}\right) \tag{2.43}$$

Moreover, the temporal trace produced often indicates the regime and allows assessment into the degree of *RIN*. Nevertheless, the speed and dynamic range of photodetectors fall short by orders of magnitude to adequately sample ultrafast pulses, prompting the need for more sensitive techniques for mode-locked sources [51].

2.6.2.2 Radio Frequency Spectrum Analyser

When paired with a photodetector, a radio frequency (RF) spectrum analyser will generate a Fourier transform of the time-domain signal, providing an assessment into the frequency

content of the pulse train [119]. In the case of an ideal CML pulse train, this yields a frequency comb with frequencies corresponding to harmonics of the cavity round-trip repetition frequency [54]. If regular instabilities are present however, this results in an amplitude modulation over the comb. Thus, the RF spectrum offers important insight into the repetition rate as well as the noise and overall stability of the pulse train where an oscilloscope is unable to [47].

The amplitude modulation of an RF spectrum in a pulse train is usually characterised by a decrease in spectral power as higher harmonics are considered over a set bandwidth. This roll-off is due to the nature of the Fourier transform but becomes more pronounced in the presence of instabilities [120, 121]. To highlight this, a picosecond pulse that yields an RF spectrum with a FWHM of 1 THz would result in a 1.086 μdB roll-off across a 1 GHz range in ideal conditions [121]. However, even minor instabilities often result in a roll-off on the scale of dBs [120].

Furthermore, the stability may also be assessed by examining the signal-to-noise ratio (SNR) centred around the fundamental repetition-rate frequency within the RF spectrum. This value is defined as the difference in the spectral peak power at the fundamental frequency and the spectral power of the noise floor [122-124].

Finally, the RF spectrum of a pulse train provides a measure of timing jitter. As reported on by Zhang *et al.*, timing jitter manifests as harmonic sidebands in the frequency domain [125]. In the presence of only minor amplitude fluctuations, the von der Linde method is frequently used. This refers to the computation of the area under these sidebands as a characterising value for the temporal fluctuations [126].

2.6.2.3 Optical Spectrum Analyser

An optical spectrum analyser (OSA) is an apparatus used to determine the central wavelength and associated spectral FWHM. This is done through a dispersive element which spatially separates incident light at angles proportional to their wavelength [127, 128]. An internal photodetector is then used to measure the intensity of each wavelength, mapping out a

spectral profile over some range. While the optical spectrum produced by an OSA serves as a fundamental tool in characterising CW lasers, it may also provide additional information into pulsed dynamics.

If periodic disturbances are present in a laser resonator, a dispersive wave is supported which may couple to a copropagating soliton [129]. While this interaction has minimal impact on bulk lasers, fibre lasers are particularly susceptible due to their high nonlinearities and dispersion [130]. In such cases, resonant coupling or quasi-phase matching can occur, producing sharp, narrow peaks symmetrically distributed around the central spectral peak of the soliton [131, 132]. These are known as Kelly sidebands and are intensified as the pulse duration decreases [129]. Hence, an OSA trace revealing Kelly sidebands may indicate that the pulse duration is approaching its bandwidth limit.

In many instances, the optical spectrum is measured on a logarithmic scale. In such scenarios, the spectral bandwidth is defined as the width at which the peak of the spectrum decreases by 3 dB from its initial value. This 3 dB reduction corresponds to a 50% decrease in signal power [133].

2.6.2.4 Intensity Autocorrelation

The electronic time resolution of commercial photodetectors is well below the necessary requirements to adequately sample ultrafast pulses as previously mentioned, prompting the need for an alternative method. The most common approach to perform an intensity autocorrelation is to use second harmonic generation (SHG) as shown in Figure 2.14 [36].

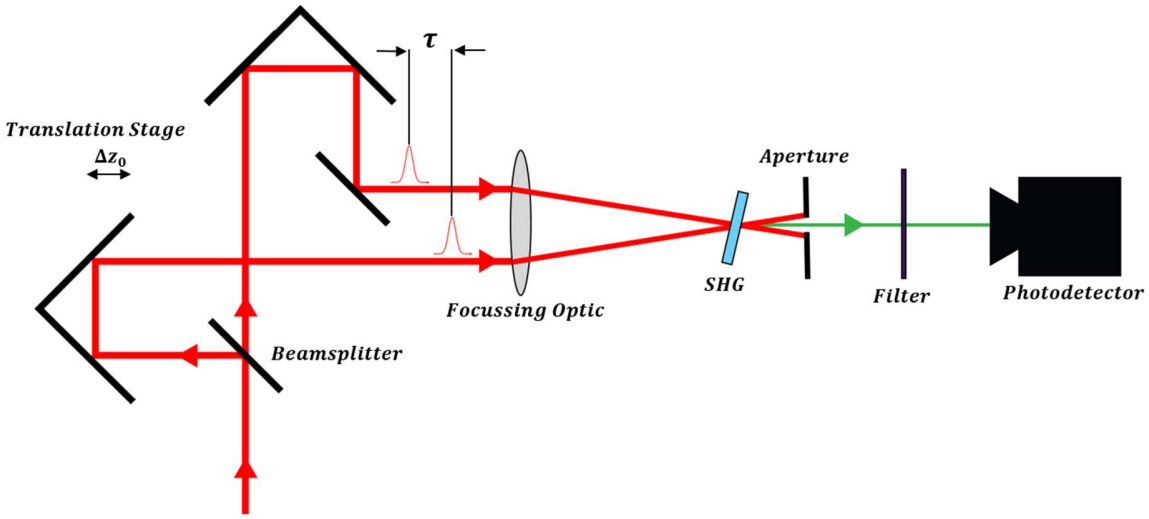


Figure 2.14: Optical intensity autocorrelation using SHG in a non-collinear configuration.

In this setup, an incident pulse train is split into two equal intensity beams with a beam splitter. By adjusting the path length in one of the arms using a translation stage, a temporal delay is introduced to one of the beams relative to the other. Both beams are then focussed into a nonlinear crystal in a non-collinear fashion, generating a frequency-doubled signal through SHG. This is then detected with a photodetector, yielding an intensity which is dependent on the temporal delay τ through the autocorrelation function given in Equation (2.44) [36, 47, 53].

$$I(\tau) = \int P(t)P(t+\tau)dt \tag{2.44}$$

Where $P(t)$ is the optical power at time t.

For a known temporal pulse shape, the true pulse duration is some proportionally constant multiplied by the autocorrelation function. This constant is known as the deconvolution factor [53]. Hence, by scanning the path length through various delays and measuring the corresponding SHG signal intensity, the temporal profile of the pulse is revealed [134].

However, this method does not provide an unambiguous measurement. Following from the fundamental theorem of algebra, an intensity autocorrelation is an example of a one-dimensional phase-retrieval problem [135]. Consequently, the autocorrelation loses all information about the phase and chirp of the pulse. To rectify this, a spectrogram of the underlying electric field may be taken using a frequency resolved optical gating (FROG), as detailed in Appendix B [135].

2.6.3 Diagnostics Overview

As discussed, beyond the standard equipment required to characterise a laser source, a pulsed laser necessitates additional techniques to assess the pulse regime, pulse-to-pulse noise and instability, pulse shaping dynamics, repetition rate, and temporal duration. The equipment used to facilitate these measurements are summarised in Table 2.3.

Table 2.3: Summary on the diagnostic instruments required for a pulse train characterisation.

Apparatus	Measurements
Oscilloscope	➢ Presence of a pulse train. ➢ Q-switched or mode-locked tendencies . ➢ Intensity noise. ➢ Q-switched pulse duration and repetition rate. ➢ Q-switched pulse shape.
Radio-Frequency Spectrum Analyser	➢ Fundamental frequency. ➢ Amplitude modulation roll-off. ➢ Signal-to-noise ratio. ➢ Timing jitter.
Optical Spectrum Analyser	➢ Central wavelength. ➢ Spectral FWHM. ➢ Presence of Kelly sidebands.
Intensity Autocorrelator	➢ Temporal FWHM. ➢ Mode-locked pulse shape.

2.7 Chapter Summary

This chapter introduced and discussed several fundamental topics essential to passive pulse generation and operation in a bulk laser. These included the basics of optical pulses, the effects of dispersive and nonlinear phenomena on propagating pulses, mode-locking and Q-switching theory, saturable absorption and SESAMs, types of passive pulse regimes, and techniques for characterising USPL sources.

Chapter 3

Development and Characterisation of the Thulium-Fibre Pump Source

3.1 Introduction

Ho:YAG is an isotropic gain media with a broad zero-phonon absorption peak at ~ 1907 nm which allows for direct pumping into the upper manifold by thulium-fibre lasers. These are the predominate choice for the pumping of Ho^{3+} ions in YAG due to their sufficient bandwidth and efficient operation in the 1.9 μm region [1]. In this chapter, we discuss the justification for the selection of Ho:YAG for pulsed operation, followed by the development and characterisation of a diode-pumped thulium-fibre laser. This laser will serve as the pump source for the Ho:YAG Q-switching, and mode-locking undertaken in Chapter 4 and Chapter 5 respectively.

Section 3.2 presents an overview of active Tm^{3+} and Ho^{3+} ion doped bulk media. This covers the relevant properties of suitable host materials, highlighting the potential for a pulsed Ho:YAG laser pumped by a thulium-fibre laser. To assess the optimal pump operation wavelength, Section 3.3 details the absorption spectroscopy of the Ho:YAG gain medium to identify the peak absorption wavelength. Furthermore, water absorption lines in this region are identified to ensure overlap with the emission spectrum of the thulium-fibre laser is avoided.

Section 3.4 reports on the development of the thulium-fibre laser, detailing the cavity configuration as well as temperature tuning of the emission wavelength to best align with the peak absorption of the Ho:YAG found in Section 3.3. The characterisation of the system is reported in Section 3.5. The parameters under investigation include the thermal load, slope efficiency, optical spectrum, and beam quality.

Finally, Section 3.6 concludes the chapter with a summary of the covered content, serving as a reference point for understanding the dynamics of the pump source used for the subsequent chapters.

3.2 Ho:YAG Gain Media for Pulsed Operation

To meet the increasing demand for laser sources at 2 μm, the trivalent rare earth ions thulium (Tm^{3+}) and holmium (Ho^{3+}) have emerged as the most promising transitions [1]. Using these ions, laser emission has been achieved across many different host crystals. By far the most investigated of these are oxides and fluorides, among which $Y_3Al_5O_{12}$ (YAG) and $LiYF_4$ (YLF) are the most popular [2]. The similarity of ionic radii with yttrium ensures both Tm^{3+} and Ho^{3+} ions can be doped into the host material without significant lattice distortions [3, 4].

Although both are prevalent amongst laser systems at 2 μm, oxide crystals have superior thermomechanical properties, meaning that YAG can endure higher thermal stresses than YLF [2]. Additionally, garnets are generally more chemically and mechanically stable. Combined with the fact that YAG is isotropic whereas YLF is anisotropic, YAG is considered to be significantly easier to manufacture to ensure high optical qualities suitable for high-power laser systems [2].

Regarding doping ions, Tm^{3+} ions possess a distinct advantage over Ho^{3+} ions, in that they can be directly pumped by commercial 790 nm laser diodes [5]. Additionally, despite a quantum defect of over 60%, Tm:YAG lasers have the potential to achieve a slope efficiency as high as 78% through cross-relaxation processes [6-8].

Alternatively, Ho:YAG exhibits a gain cross-section larger than Tm:YAG as well as a longer upper state lifetime, making it more attractive for pulsed laser operation [1]. To enable efficient lasing at 2.1 μm, Ho:YAG can be in-band pumped at 1907 nm using a thulium-fibre source or at 1150 nm using a commercial diode laser albeit with reduced absorption [1, 9]. Traditionally, flash lamp pumps were used for low efficiency operation or Tm^{3+} ions were added as a co-dopant [1]. These were responsible for transferring energy to the Ho^{3+} ions, but eventually imposed limitations on the overall pump efficiency due to the onset of upconversion mechanisms [1, 10, 11]. The relevant transitions for Ho:YAG are depicted in Appendix C, and the distribution of Stark levels is presented, highlighting its nature as a quasi-three level laser [1, 12].

Although Tm:YAG and Ho:YAG both possess thermomechanical properties akin to Yb:YAG, one of the most extensively used gain media in the 1 μm range for high-power lasers, the higher gain cross-section and longer upper state lifetime of Ho:YAG allows for broader amplification and greater energy accumulation respectively. Despite its potential, pulse generation in Ho:YAG – especially in the ultrashort regime, has received limited attention, further reinforcing the motivation for this research [1, 10, 11].

As the primary focus of this thesis is on passive generation of short and ultrashort pulses in Ho:YAG, less emphasis is placed on the waveguide dynamics governing CW fibre sources such as the thulium-fibre laser. A brief introduction to optical fibres is provided in Appendix D which covers the relevant fundamental parameters and terminology.

3.3 Ho:YAG Absorption Spectroscopy

Measurements of the absorption spectrum of the gain media are performed using a supercontinuum source (SuperK COMPACT, NKT Photonics) and an OSA (Yokogawa AQ6375), which has a resolution of 0.05 nm. A Ho:YAG slab with a nominal Ho^{3+} doping concentration of 0.7 wt.% and dimensions of 2 x 3 x 40 mm is chosen and the characterisation is performed at a room temperature of ~ 295 K.

The supercontinuum source generates unpolarised light spanning wavelengths from 450 nm to 2400 nm. This system ultilises a nanosecond pulsed beam to leverage various nonlinear effects for supercontinuum generation [13]. Subsequently, the output passes through an achromatic lens to produce a collimated beam [13].

The collimated output from the supercontinuum source is focused into the front surface of the Ho:YAG crystal using an achromatic objective lens. This ensures adequate light-material interaction to maximise optical absorption while avoiding aberrations. The beam diameter is fully contained within the crystal and maintains a relatively uniform size throughout the full length. Any unabsorbed light transmitted through the crystal is collected by a parabolic mirror and coupled into the OSA using a single-mode patch cable. The distance between the supercontinuum output and the parabolic mirror is measured to be approximately 1 m. This configuration is depicted in Figure 3.1.

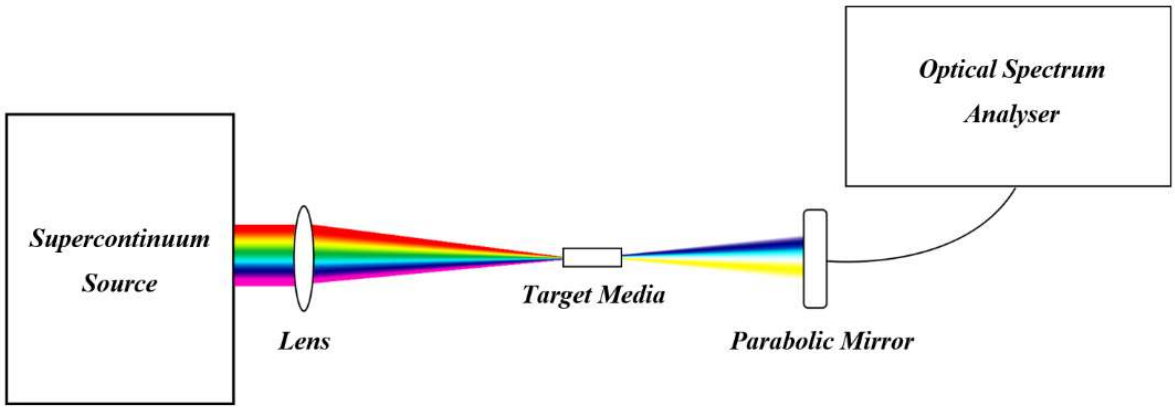


Figure 3.1: Experimental setup for absorption spectroscopy of the Ho:YAG crystal as the target medium.

The Ho:YAG and atmospheric absorption spectra across the wavelength range from 1900 nm to 1940 nm is shown in Figure 3.2.

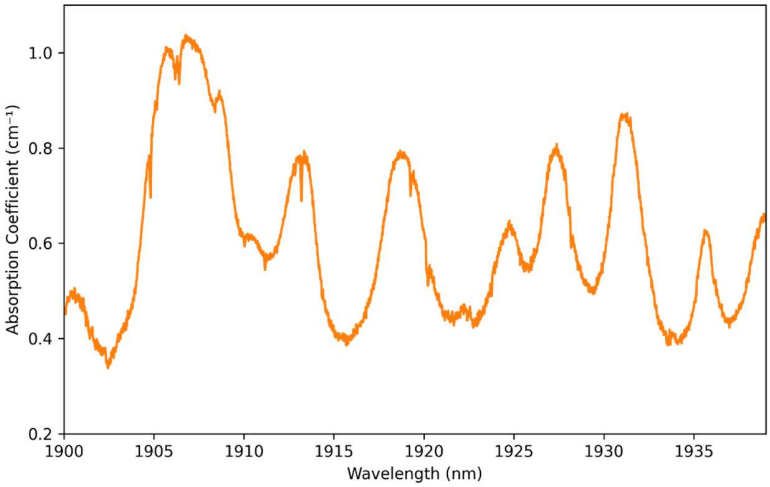


Figure 3.2: Absorption spectra of a 40 mm 0.7 wt.% doped Ho:YAG slab at 295 K.

Despite only being a fraction of the total absorption cross-section, Figure 3.2 clearly illustrates the complex and turbulent nature of the transitions from the ground state $^5I_8$ to the upper 2.1 µm laser level $^5I_7$ (refer to Appendix A for the energy scheme of Ho:YAG) [14, 15].

To allow for the background data subtraction of the absorption measurement, the atmospheric absorption data is recorded using the identical experimental setup, but with the Ho:YAG sample removed. Detailed measurements of the absorption spectra in the 1900 - 1913 nm region are taken, given its correlation with the broad absorption feature around 1907 nm commonly used for pumping Ho:YAG at room temperature [1, 14, 15]. The absorption spectra over this range with the atmospheric absorption superimposed is presented in Figure 3.3.

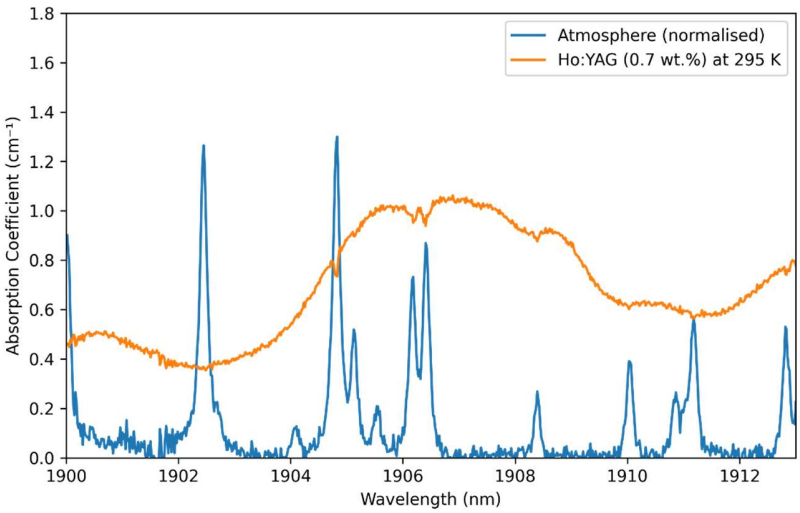


Figure 3.3: Absorption spectra of a 40 mm 0.7 wt.% doped Ho:YAG slab at 295 K (orange) with the normalised atmospheric absorption superimposed (blue).

The spectra closely align with the measurements conducted by Ganija *et al.* on the characterisation of a 49 mm 0.7 wt.% doped Ho:YAG slab [15]. This serves as a guiding parameter for the design and development of the thulium-fibre laser. It is seen from the plot that the peak absorption for the Ho:YAG slab occurs at 1906.90 nm, with strong atmospheric absorption features around 1906.40 nm. These are attributed to water absorption lines and are reflected in the Ho:YAG spectrum as areas of reduced absorption [15].

3.4 Thulium-Fibre Laser Development

3.4.1 Diode Power Characterisation

A power characterisation is conducted for the 75 W, 793 nm BrightLase diode (ES-6207-0001), which is used as a pump source. This is undertaken to later determine the slope efficiency of the completed thulium-fibre laser.

The diode is maintained at 20°C using a copper block which is cooled by a TECA air-cooled thermoelectric liquid chiller (TLC-700). At this temperature, the diode is specified to operate at a central wavelength of 793 nm with a spectral FWHM of 0.25 nm. Although a full wavelength performance characterisation of the diode is not conducted, preliminary assessment indicates close agreement with the manufacturer specifications. The current driver used for this system is a ILX Lightwave LDX-36000, which has the capacity to drive a continuous current of 125 A. However, for the purpose of these measurements, the driver is restricted to a maximum of 46 A to avoid unnecessary degradation of the diode. All power measurements are taken using a Thorlabs S442C Thermal Power Meter which exhibited a 17 Hz sampling rate with a resolution of 100 µW. The performance of the diode as a function of driving current is presented in Figure 3.4.

As seen in Figure 3.4, the diode power experiences a near linear output with respect to the driving current, with a gradual roll-off evident towards higher driving currents. The lasing

threshold for the diode is reached at ~ 10 A of driving current, with each additional ampere providing an increase of ~ 2 W in output power.

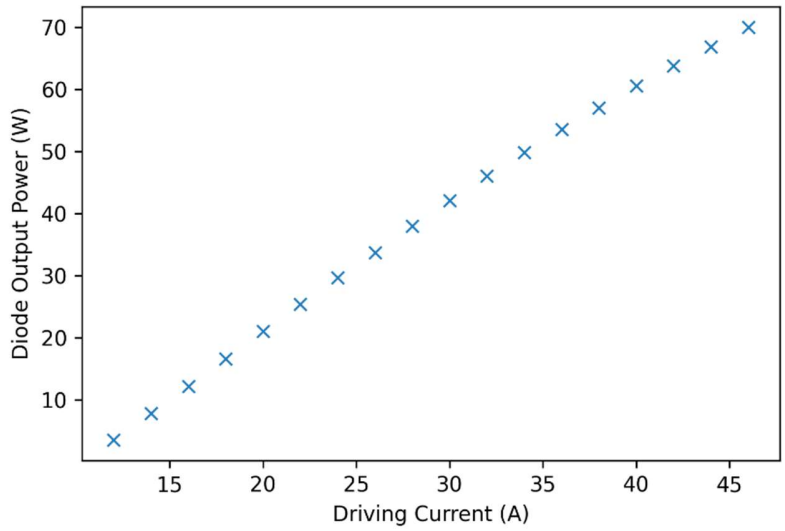


Figure 3.4: Output power of the 75 W, 793 nm diode (BrightLase, ES-6207-0001) as a function of driving current.

3.4.2 Cavity Configuration

The thulium-fibre laser schematic is shown in Figure 3.5. The active fibre is a Coherent low index acrylate coated, Tm^{3+}-doped, double clad fibre of 2 m length with a 25 µm core diameter and an NA of 0.090. The cladding around the core has a diameter of 250 µm with an NA of 0.46 and an absorption of 3.00 dB/m at 793 nm. The length of this fibre is chosen based on the ideal Tm^{3+}-doped fibre lengths for a pump power of 75 W modelled by Zhen-Yue *et al.* to minimise reabsorption losses [16]. The passive fibre is a Coherent germanium core specialty multimode optical fibre with the same geometry as the active fibre but featuring a core NA of 0.11.

All fibre cleaving procedures are performed with a Thorlabs Vytran Cleaver and the splicing operations are undertaken using a Fitel S178 LDF Fusion Splicer, ensuring that estimated splice losses remain below 0.01 dB.

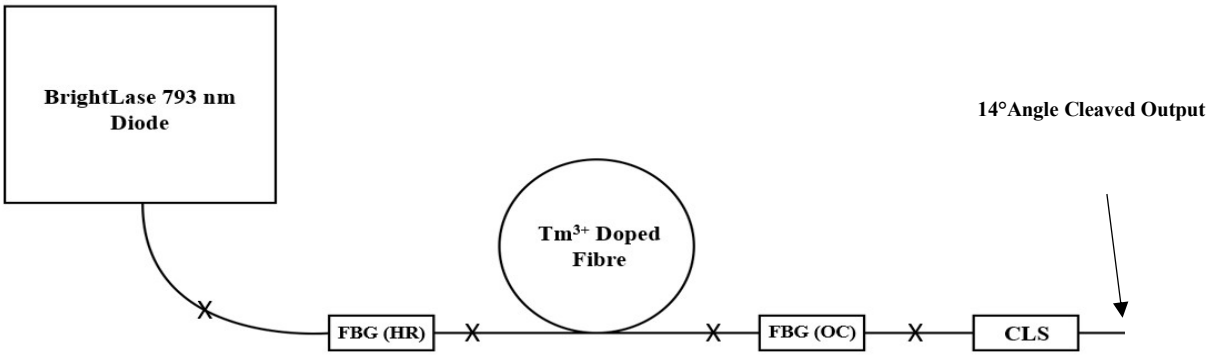


Figure 3.5: Schematic of the thulium-fibre laser, with splice locations marked with "X." The labelled components include two fibre Bragg gratings and a cladding light stripper.

The fibre Bragg gratings (FBGs) used are TeraXion 25/250 FBGs which are designed to operate at a centre wavelength of 1906.43 $\pm$ 0.1 nm in air. The high reflector (HR) and output coupler (OC) FBGs operate with a reflectivity of 99.3% and 7.4%, respectively.

Amplified spontaneous emission, residual pump light at the end of the gain fibre, core light leakage resulting from splice or bend losses, and coupled-in external reflections may contribute to unwanted light propagating through the fibre cladding as outlined by Wang *et al.* [17]. This is detrimental to the beam quality, increases the risk of damage to the components, and in the worst-case scenario, damages the laser diode itself. Boyd *et al.* reports a simple CO_2 laser processing technique for the fabrication of a compact all-glass optical fibre cladding light stripper (CLS) [18]. This technique utilises a 55 W, pulse-width-modulated CO_2 laser, operating at 10.6 μm to ablate channels of various depths, ranging from 5 to 75 μm on one side of an optical fibre [18].

Using the same setup, a cladding light stripper is fabricated for the 25/250 μm fibre. This is placed at the output of the system to terminate cladding light induced from splice or bend losses as well as to prevent backwards propagating light that has coupled into the end of the fibre from external reflections [17-19]. To prevent internal back-reflections, the output end of the fibre is cleaved at 14°.

Fibre bends are also introduced to induce losses for higher-order modes and suppress multiple emission lines within the bandwidth of the FBGs. The location and extent of these is determined experimentally through preliminary measurements of the optical spectrum.

3.4.3 Wavelength Tuning

The efficiency of the Ho:YAG laser largely depends on the wavelength of the pump source. Ganija *et al.* has shown that even minor changes to the pump wavelength from the peak absorption can have a significant impact on efficiency [15].

The optical spectrum of the thulium-fibre laser is measured by coupling a diffuse reflection of the output into a parabolic mirror which is fed into the OSA using a single mode patch cable. The obtained trace is overlaid on the Ho:YAG absorption spectrum as presented in Figure 3.6.

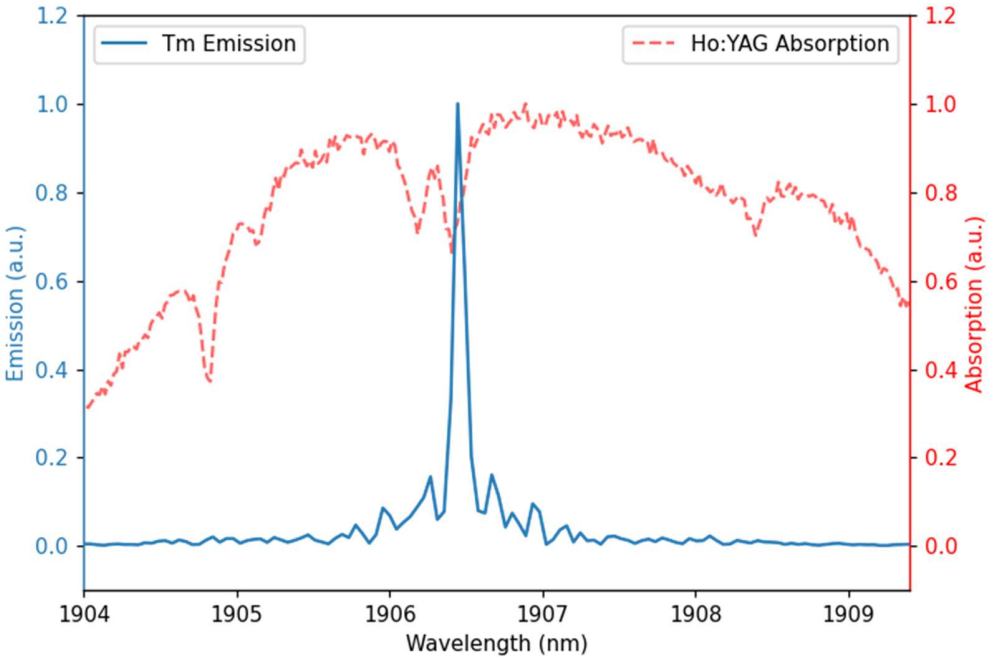


Figure 3.6: Optical spectrum of the thulium-fibre laser output (blue) superimposed on the normalised absorption spectrum of the Ho:YAG crystal (red).

The peak wavelength is measured to be 1906.45 nm, with a FWHM of 0.085 nm. This closely aligns with the specified values for the TeraXion FBGs. However, it also overlaps with a significant atmospheric absorption region.

To demonstrate the atmospheric attenuation at this wavelength, a measurement of output power against propagation distance is conducted. This evaluation is undertaken at two

different diode output powers, 34 W and 42 W, and normalised accordingly. Figure 3.7 presents this along with the corresponding regression lines.

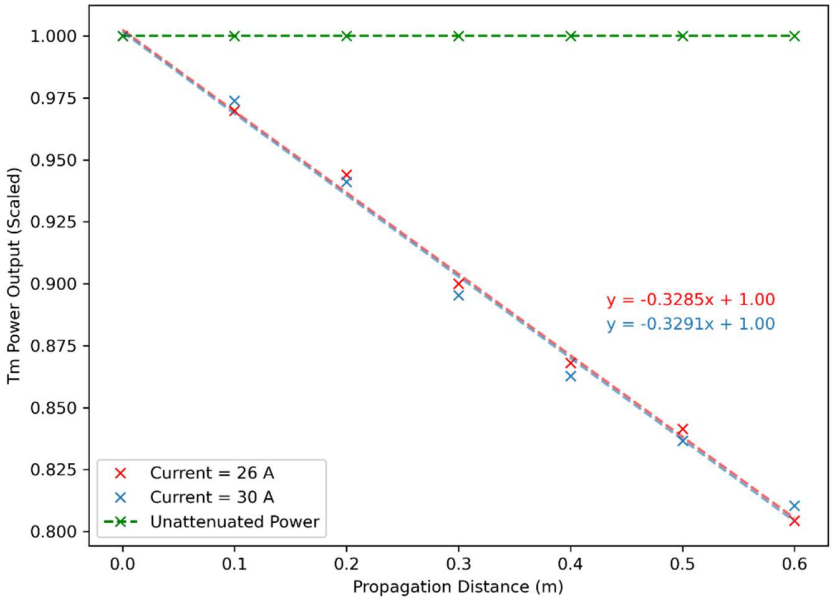


Figure 3.7: Atmospheric attenuation of the thulium-fibre laser output power at 1906.45 nm relative to propagation distance through air. The plot illustrates the variation in output power for diode output powers of 34 W and 42 W.

As seen from Figure 3.7, the measurements taken at diode output powers of 34 W and 42 W display excellent agreement with each other, indicating a 33% attenuation of the 1906.45 nm output power per metre of propagation in air. This constrains the efficiency of the Ho:YAG laser to be dependent on the distance between the pump source and the gain medium.

To mitigate this, the FBGs are mounted on a 40 x 40 x 3.3 mm thermoelectric (Peltier) module (ZP9104), driven by a Thorlabs temperature controller (TED200C). The cooling capacity of the module is rated to 68 W, equating to a temperature differential of 68°C. An FBG functions as a form of Bragg reflector, designed with precise optical spacing of varying material layers to target a particular wavelength. Consequently, heating or cooling induces expansion or contraction of these layers, altering the central wavelength of the FBG and shifting the laser's output wavelength. However, it is important to note that the physical length change of the FBG is minimal due to the low thermal expansion coefficient of silica glass ($0.5 \times 10^{-6}\ K^{-1}$). Instead, the temperature dependence of the Bragg wavelength is

predominantly due to the thermo-optic effect, with a much higher coefficient ($8.4 \times 10^{-6}\ K^{-1}$). Liu *et al.* uses this approach to demonstrate thermal wavelength tuning of FBGs [20]. Scanning through a temperature range of 50°C, a broad tunability of 18 nm is reported.

Unfortunately, the TeraXion gratings used for this research are packaged to be thermally inert, meaning they do not readily change in temperature due to heat input. This is done to maintain a consistent wavelength regardless of thermal load. While this is a desirable feature for many applications, it makes the FBGs largely unresponsive to thermal tuning. Consequently, using the thermoelectric module to heat the external packaging of the FBGs to 50°C only corresponds to a shift of 0.30 nm in the optical spectrum, resulting in central wavelength of 1906.75 nm. Comparison of this shift with the thermo-optic coefficient and the work undertaken by Liu *et al.* suggests that the temperature reached on the FBG is considerably lower than on the external packaging.

However, even though a wavelength of 1906.90 nm is required to target the peak absorption of the Ho:YAG, the shift induced by the thermal tuning is enough to avoid the atmospheric absorption region, as shown in Figure 3.8.

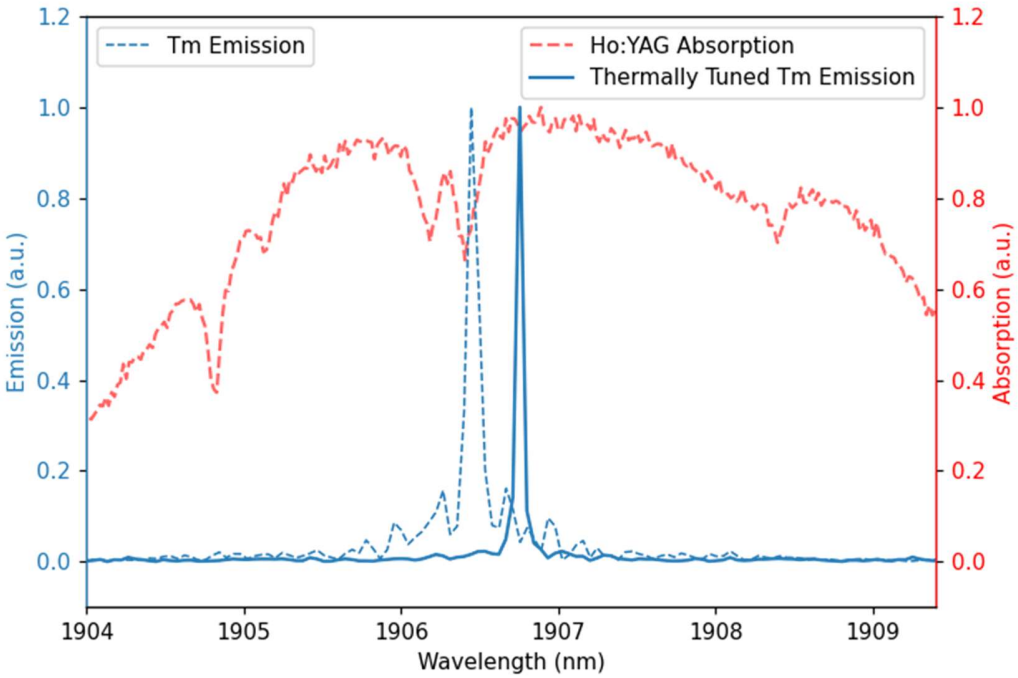


Figure 3.8: Thermally tuned emission spectrum of the thulium-fibre laser (blue) superimposed on the room-temperature emission spectrum (blue – dashed) and the Ho:YAG absorption spectrum (red).

While additional heating might yield an output wavelength of 1906.90 nm, it is evident from Figure 3.8 that this only results in a minimal increase in absorption. Therefore, the decision is made to operate within the lower wavelength region of 1906.75 nm to minimise thermal stresses and prioritise the longevity of the system. Finally, it is noted that in the absence of atmospheric absorption, the thermally tuned spectrum measures a FWHM of just 0.05 nm.

Although the influence of this thermal tuning on the reflectivity of the FBGs is unknown, it is expected to be negligible, provided that the heating is approximately uniform. This notion is reinforced by Liu *et al.*, whose study suggests that considerable reflectivity changes only occur for very large thermal shifts and non-uniformities of the refractive index changes along the FBG [20]. Furthermore, measuring the output power at diode output powers of 34 W and 42 W yields values consistent with the unattenuated powers shown in Figure 3.7. This indicates no observable change in the efficiency due to temperature tuning.

To conclude the development of the thulium-fibre laser, optical power measurements are taken at intervals of 100 mm along a beam path of 3 m. As expected, attenuation of the thermally tuned wavelength is negligible, thus confirming the wavelength shift has avoided significant atmospheric absorption.

3.5 Characterisation

The maximum power of a fibre laser is largely constrained by thermal effects. Therefore, a temperature assessment of the system is undertaken as a function of diode output power. This is conducted using a FLIR A615 thermal camera which has a thermal sensitivity of 0.05°C at 30°C.

According to Schubel *et al.*, the glass transition temperature of acrylate coatings is 65.8°C [21], beyond which the coating loses its specified optical properties due to increasing molecular mobility [22]. Since the greatest energy transfer and therefore heat production occurs where the active fibre is exposed to the highest intensity of 793 nm light, the splice between the high reflectance FBG and the active fibre is identified as the first potential fail

point. Figure 3.9 presents the temperature of this splice as a function of diode output power. It is noted that extreme caution is undertaken to ensure the thermal damage threshold of the optical coating is not exceeded.

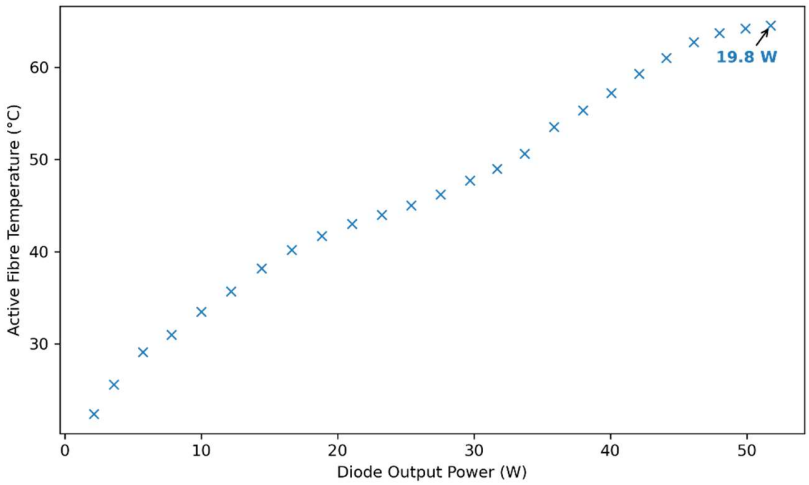


Figure 3.9: Temperature of the HR FBG to the active splice as a function of diode output power, indicating a maximum output power of 19.8 W as the glass transition temperature is approached.

As seen in Figure 3.9, the splice approaches the glass transition temperature at a diode output power of 53.6 W, corresponding to 19.8 W of thulium-fibre laser output power, thereby establishing an upper limit for laser operation.

To determine the slope efficiency of the system, the output power is measured as a function of driving current. The values acquired are then plotted against the corresponding values obtained for the diode output power in Section 3.4.1. The slope efficiency is given by the regression line as shown in Figure 3.10.

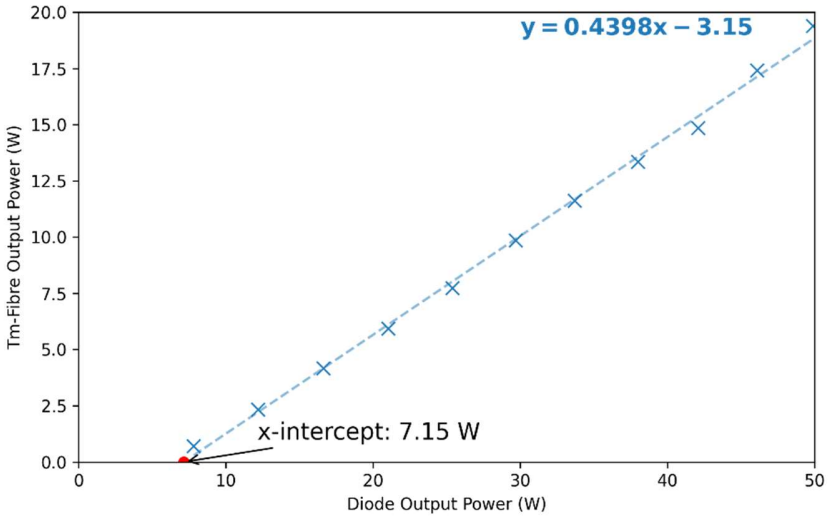


Figure 3.10: Power output of the thulium-fibre laser as a function of diode pumping power with a regression line indicating a slope efficiency of 43.98% and a lasing threshold of 7.15 W.

Hence, Figure 3.10 reveals a slope efficiency of 43.98% and a lasing threshold of 7.15 W. Using this value to cross-reference with Figure 3.4, it is determined that the lasing threshold corresponds to approximately 13.5 A of driving current.

The optical spectrum is presented in Figure 3.11. The peak wavelength is measured to be 1906.75 nm with a FWHM of 0.05 nm. However, this value for FWHM is limited by the resolution of the OSA and is likely to be even narrower. To assess spectral stability, the peak wavelength is recorded as a function of the diode output power, and the findings are displayed in Figure 3.12.

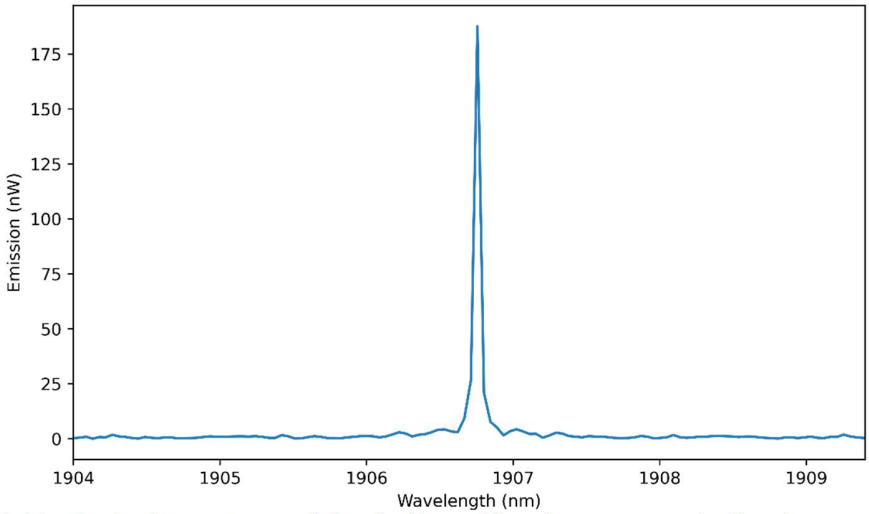


Figure 3.11: Optical spectrum of the thulium-fibre laser output indicating a peak wavelength of 1906.75 nm.

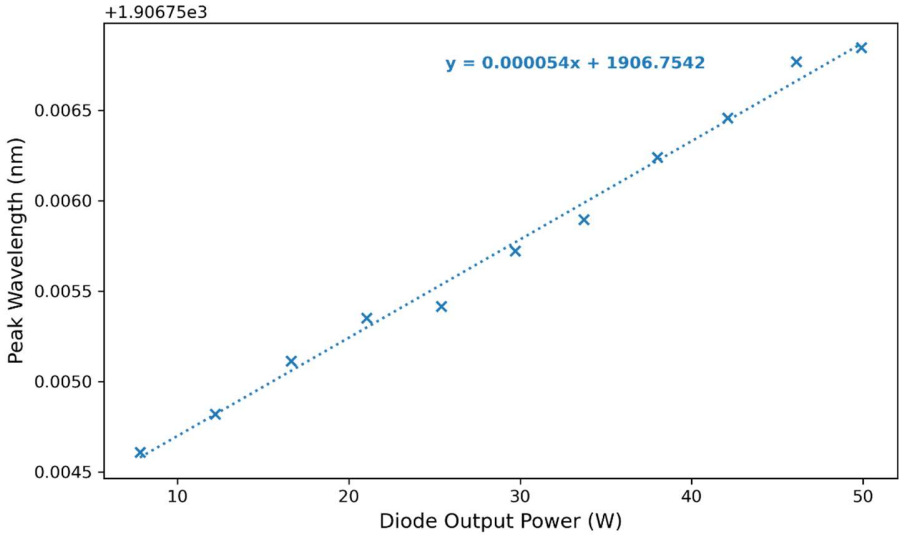


Figure 3.12: Peak wavelength of the thulium-fibre laser as a function of diode output power.

As the pump power increases, more heat is generated within the laser medium and its surroundings. This can cause changes in the refractive index of the laser medium and the optical coatings, leading to a shift in the laser wavelength. The thermal expansion of the laser cavity components can also alter the cavity length, resulting in a wavelength shift. Additionally, higher pump powers can lead to saturation effects in the gain medium. As the gain medium approaches saturation, the peak gain wavelength may shift due to changes in the population inversion and the distribution of energy levels within the medium. However, the regression line in Figure 3.12 indicates a slope of 5.4×10^{-5} nm per watt of diode output power. Furthermore, the total shift in wavelength across the operational bounds of the system is negligible. This demonstrates excellent spectral stability up to at least 19.8 W of output power.

In the subsequent chapters, a beam profiling camera is used to evaluate beam quality. However, the emission wavelength of the thulium-fibre laser is outside the capability of the camera, necessitating the use of an alternative method. Hence, a technique based on the knife-edge method in compliance with ISO 11164-1, an international standard for measuring beam quality, is developed and presented in Appendix E. To avoid optical aberrations, the converging optic selected is a fused silica aplanatic lens with an effective focal length of *EFL* = 25.5 mm, which is placed 20 mm from the fibre output. 15 beam radii are measured 25 mm apart and curve fitted accordingly to produce Figure 3.13. An example of an individual knife-edge measurement and the extracted beam profile is also presented in Appendix E.

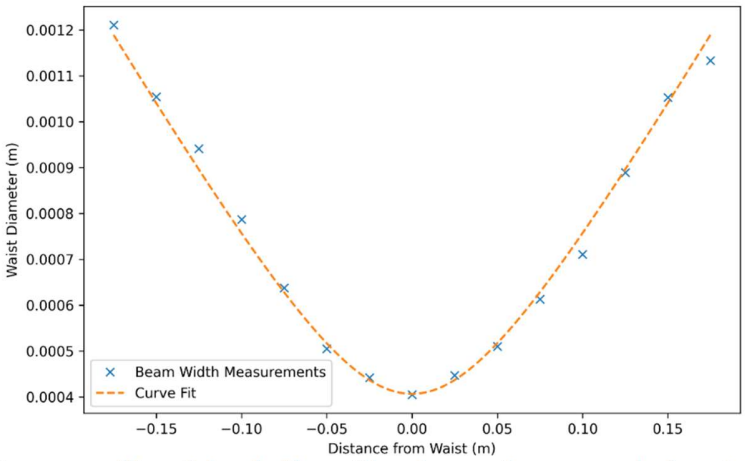


Figure 3.13: Beam profile of the thulium-fibre laser after transmission through an aplanatic lens with an effective focal length of f = 25.5 mm.

The waist diameter is found to be 406.86 μm, occurring 505 mm from the output face of the aplanatic lens. The beam quality and Rayleigh range is computed to be 1.07 and 63.72 mm respectively. Assuming the beam quality remains consistent across the y-axis of the beam's cross-section, it can be inferred that the thulium-fibre laser offers a nearly diffraction-limited beam quality.

3.6 Chapter Summary

In this chapter we have presented the development of a Tm^{3+} doped fibre laser system which will serve as a pump source for the Ho:YAG laser systems presented in the following chapters.

The thulium-fibre laser demonstrated a slope efficiency of 43.98% and achieved a maximum output power of 19.8 W. The laser's optical spectrum was thermally tuned to a central wavelength of 1906.75 nm, which, while not a perfect match with the observed peak absorption wavelength of the Ho:YAG crystal at 1906.90 nm, was found to exhibit minimal differences through spectroscopic analysis. Furthermore, the wavelength shift between the minimum and maximum output power of the system was measured to be negligible, indicating strong spectral stability.

By developing an approach for automated beam profile measurements based on the knife-edge method, the beam quality was found to be 1.07 across the horizontal axis, indicating a nearly diffraction-limited beam quality with a resolution limited spectral FWHM of 0.05 nm. Thus, this system is well suited to serve as the pump source for the Ho:YAG gain media.

Chapter 4

Continuous-Wave Operation and SESAM Q-Switching of a Ho:YAG Laser

4.1 Introduction

One of the longest persisting challenges with a mode-locked laser is its stability. As highlighted in Chapter 2, this is determined by a range of factors such as the type of absorber, cavity configuration, and laser alignment. In this chapter, we present a theoretical and experimental characterisation of a laser cavity design in order to understand the conditions required for stable pulse generation. This is categorised into two sections: CW and Q-switching.

Section 4.2 presents a brief overview of the resonator design for both CW and Q-switched operation. This includes a stability assessment of the cavity, as well as the specifications for the diagnostic equipment required for the characterisation of the different regimes.

Section 4.3 demonstrates dual-wavelength CW operation. Additionally, the efficiency and stability of the laser is examined using time-averaged optical power measurements. The beam quality is measured using a commercial beam profiling camera.

In Section 4.4, three SESAMs with different modulation depths are incorporated into the resonator to facilitate Q-switched operation. The performance of each is evaluated based on slope efficiency, pulse duration, repetition rate, pulse energy, pulse peak power, pulse train stability, optical spectrum, and beam quality. The chosen SESAMs have modulation depths of 1.2%, 12%, and 18%.

Section 4.5 presents a discussion and comparison on the obtained pulse dynamics from each SESAM, as well as how the efficiency, spectrum, and beam quality compared to CW operation.

Section 4.6 summarises the findings of the chapter. Through examination of each SESAM in terms of the absorber modulation depth, fluence, and intensities necessary for stable operation, this chapter aims to build the foundational understanding required to achieve mode-locked operation in Chapter 5.

4.2 Resonator Architecture

4.2.1 Laser Cavity Design and Modelling

The chosen gain medium for the cavity is the 2 x 3 x 40 mm Ho:YAG slab which has a Ho^{3+} doping concentration of 0.7 wt.%, as reported in Chapter 3. This is AR coated for 1907 nm and 2097 nm and mounted in a conduction cooled gain media housing which is water-cooled at 20°C using an SMC Compact Thermo Chiller (HRS012-A-20). The Ho:YAG is then pumped by the thulium-fibre laser developed in Chapter 3. This operates at a centre wavelength of 1906.75 nm which closely overlaps with the peak absorption of the gain media at 1906.90 nm.

The pump beam is guided through a fused silica aplanatic lens with an effective focal length of $EFL = 25.5$ mm. The pump-to-lens distance is unchanged from the beam quality measurements undertaken in the previous chapter. Hence, the waist radius is ~ 203 µm, occurring ~ 505 mm from the output face of the lens. The Rayleigh range measured is

~ 64 mm, providing a relatively uniform beam size throughout the entire length of the gain medium when positioned at the waist of the pump beam.

The cavity is designed and visualised using the optics simulation software package, reZonator, which uses the ABCD ray matrix algorithm for simulating optical elements [1]. The configuration is presented in Figure 4.1.

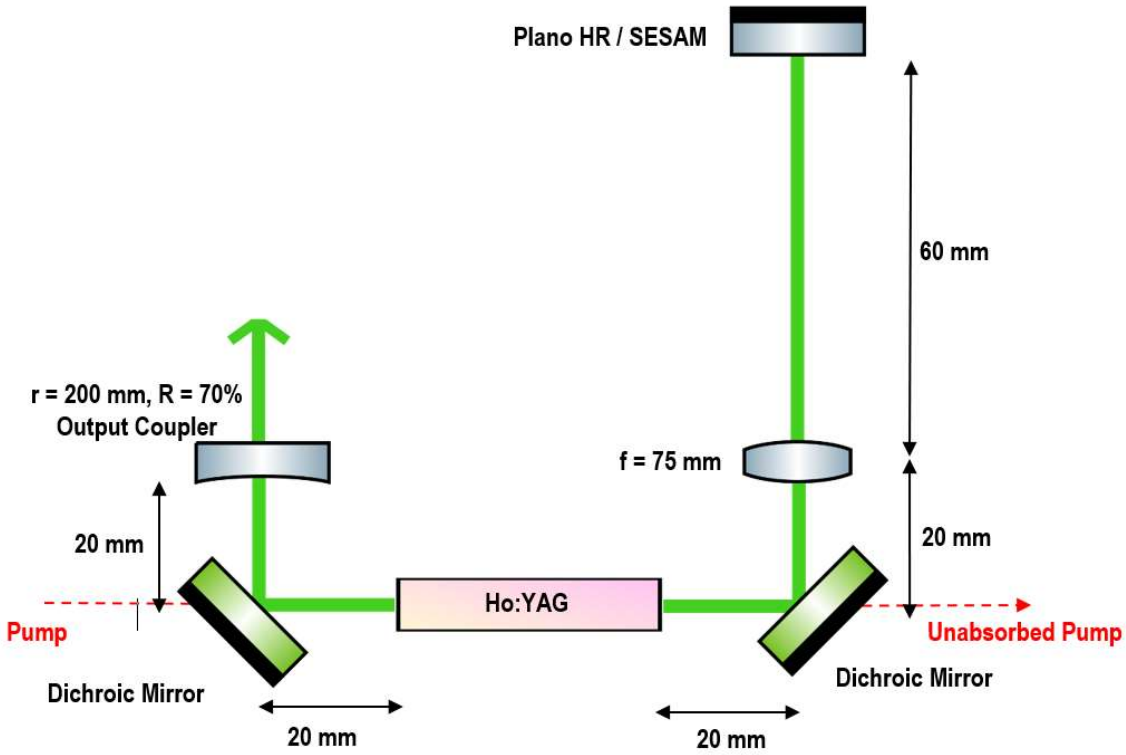


Figure 4.1: Schematic of the resonator used for the CW operation and SESAM Q-switching of Ho:YAG laser. DM1 and DM2: Dichroic mirrors.

This design has a total cavity length of 180 mm. Since the resonator beam is normal to the surface of each element, except for the dichroic mirrors which are designed for a 45° operation angle, the round-trip ABCD matrix remains identical in both the sagittal (S) and tangential (T) planes. This is calculated by the reZonator software and presented in Equation (4.1).

$$M_S = M_T = \begin{bmatrix} -0.862 & -0.0308 \\ 8.36 & -0.862 \end{bmatrix} \tag{4.1}$$

This yields the stability parameter given in Equation (4.2).

$$P_{\mathrm{T}} = P_{\mathrm{S}} = \frac{A + D}{2} = -0.862 \tag{4.2}$$

Thus, the resonator design satisfies the stability criteria of $-1 < P < 1$.

Following from the left in Figure 4.1, the pump beam enters and exits the resonator cavity through two dichroic mirrors, DM1 and DM2 respectively, placed at 45° in the optical path. At this angle, the pump light experiences a reflectivity of $R < 1.0\%$ while 2097 nm light experiences a reflectivity of $R > 99.9\%$. The use of DM1 and DM2 form two distinct cavity arms, one containing an output coupler (on the left of Figure 4.1) and the other containing a CaF_2 plano-convex lens with a focal length of $f = 75$ mm and a plano HR cavity end mirror (on the right of Figure 4.1). This mirror is interchangeable with a SESAM to transition from CW to Q-switched operation.

The output coupler selected for this design has a reflectivity of $R = 70\%$ and a radius of curvature of $r = 200$ mm. The output coupling fraction chosen is consistent with high efficiency Q-switched operation highlighted in Table 1.2 [2].

The resonator configuration consists of two focal points, one at the centre of the Ho:YAG crystal and the other on the end mirror. This is visualised in reZonator, which provides an estimation of the intracavity beam size. The data is extracted from the software and plotted to produce Figure 4.2.

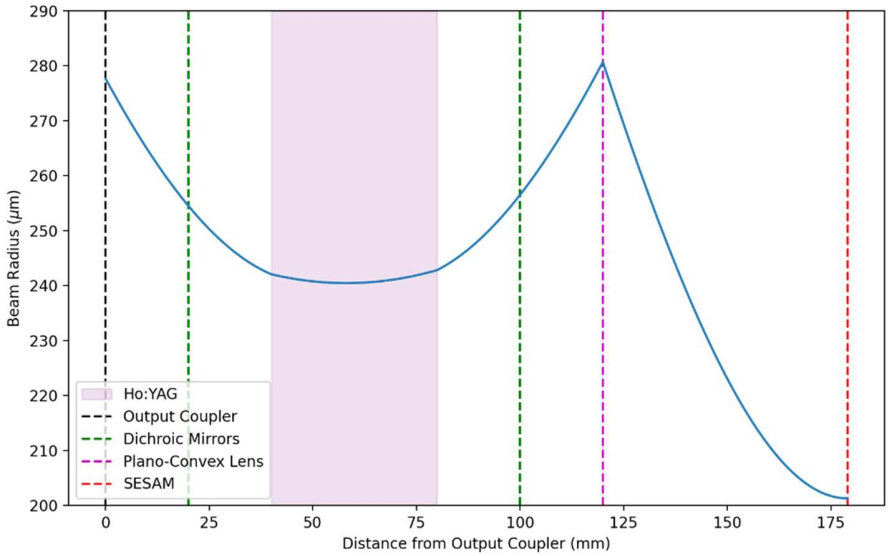


Figure 4.2: Beam radius within the primary Q-switched resonator design as a function of distance across the cavity.

The beam radius at the centre of the crystal is shown to be ~ 240 µm, corresponding to an ~ 84% mode-match between the pump and resonator. This high degree of spatial overlap between the two intensity profiles ensures the excitation of only the fundamental Gaussian mode, as well as a strong conversion efficiency.

The focus of ~ 200 µm on the SESAM is considered large compared to other Q-switching designs seen in the literature reviewed in Chapter 1 [3-7]. However, this is chosen out of caution for the lower damage threshold of the higher modulation depth SESAMs as well as to support a greater range of average output powers.

4.2.2 Diagnostic Setup

To aptly characterise the pulse dynamics across the three SESAMs, a robust and consistent diagnostic arrangement is established. The pump, resonator cavity, and diagnostics layout are illustrated in Figure 4.3.

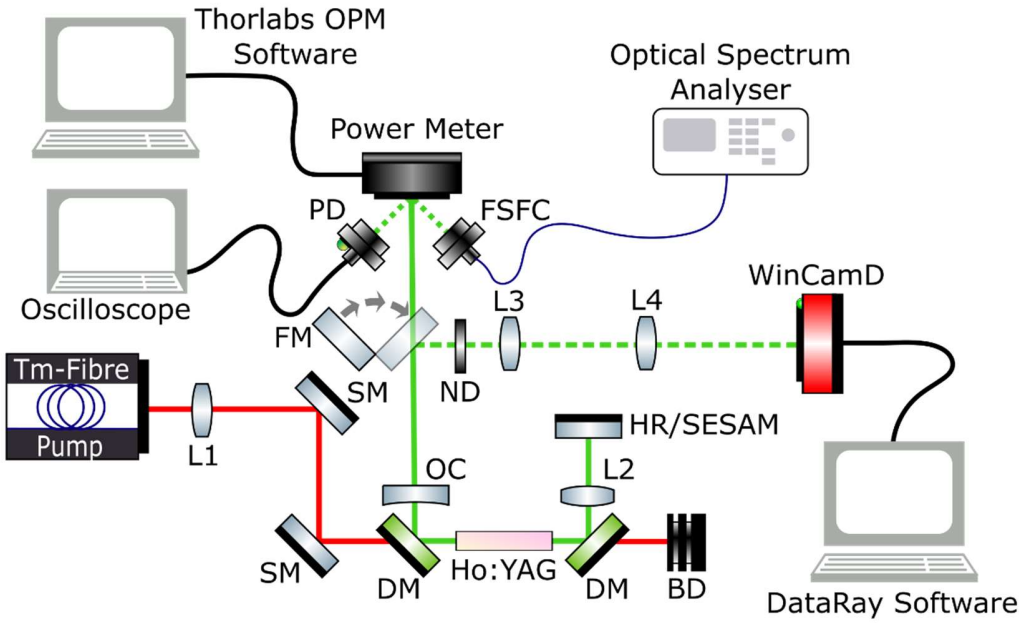


Figure 4.3: Complete Q-switched resonator setup with the diagnostic arrangement used to characterise all Q-switched results. L1: f = 25.5 mm aplanatic lens. L2: f = 75 mm plano-convex lens. L3: f = 150 mm plano-convex lens. L4: f = 300 mm air-spaced doublet. SM: Steering mirror. DM: Dichroic mirror. OC: Output coupler. BD: Beam dump. FM: Flip mount installed with a 45° HR mirror for 2097 nm. ND: Neutral density filter. WinCamD: Beam profiling camera. PD: Photodetector. FSFC: Free-space to fibre coupler.

For the characterisations presented in this chapter, all optical power measurements are undertaken with a Thorlabs S425C-L Thermal Power Meter which is interfaced with the Thorlabs Optical Power Monitor (OPM) software through a Thorlabs PM101 Thermal Power Sensor Interface. Power measurements are sampled at 180 Hz with a resolution of 100 µW, allowing for time-averaging of collected data through the OPM software.

The photodetector used is an ALPHALAS GmbH UPD-5N-IR2-P Ultrafast Photodetector based on InGaAs which exhibits a rise time of less than 200 ps. This is positioned to capture diffuse reflections off the power meter. It is connected to an oscilloscope using a BNC cable which is impedance matched with a Kings 1340-1-m06 BNC 50 Ohm Termination Connector to avoid back-reflections of the signal distorting measurements. The oscilloscope used is an InfiniiVision DSO6102A Digital Storage Oscilloscope. This has a bandwidth of 1 GHz and a sampling rate of 4 GSa/s.

The free-space to fibre coupler uses a D-ZK3 glass aspheric lens with a focal length of $f = 11$ mm to couple diffuse reflections from the power meter into a single mode fibre patch cable. This is then transmitted into a YOKOGAWA AQ6375 OSA which operates at a resolution of 0.05 nm.

A flip mount installed with a 45° 2097 nm HR mirror redirects the Ho:YAG output for an assessment of beam quality. The chosen beam profiling camera for conducting these measurements is a DataRay WinCamD-IR-BB 2-16 µm Beam Profiler. When connected to the DataRay software package, this device measures the second-moment beam diameters with a theoretical resolution of 5 µm. Due to the low damage threshold of the sensor however, a neutral density filter with an optical density of 3.0 must first be used to attenuate the output of the Ho:YAG resonator by a factor of 1000. The beam is then collimated using a CaF_2 plano-convex lens with a focal length of $f = 150$ mm before being focussed down by a CaF_2 air-spaced achromatic doublet with an effective focal length of $EFL = 300$ mm. It is noted however, that preliminary testing using this beam profiler reveals a standard deviation in the measured beam radii up to 3.3% of the mean value. These measurements are presented in Appendix F.

4.3 Continuous-Wave Lasing Characterisation

Prior to pulsed operation, a characterisation is conducted for the CW lasing state. This is done to ensure the cavity design and alignment supports stable lasing. Furthermore, it is used to determine the maximum attainable efficiency and the favoured emission wavelengths.

At each increment of driving current, the laser is allowed a 5-minute period to reach equilibrium with the thermal load before any measurements are recorded. 21,600 samples of optical power are then taken over the course of 120 seconds before the driving current is increased and the process is repeated. The distribution of these samples displays a high degree of symmetry across all driving currents, indicating that the power has had adequate time to thermally stabilise. An example of the Ho:YAG output power distribution over 120 seconds is presented in Figure 4.4.

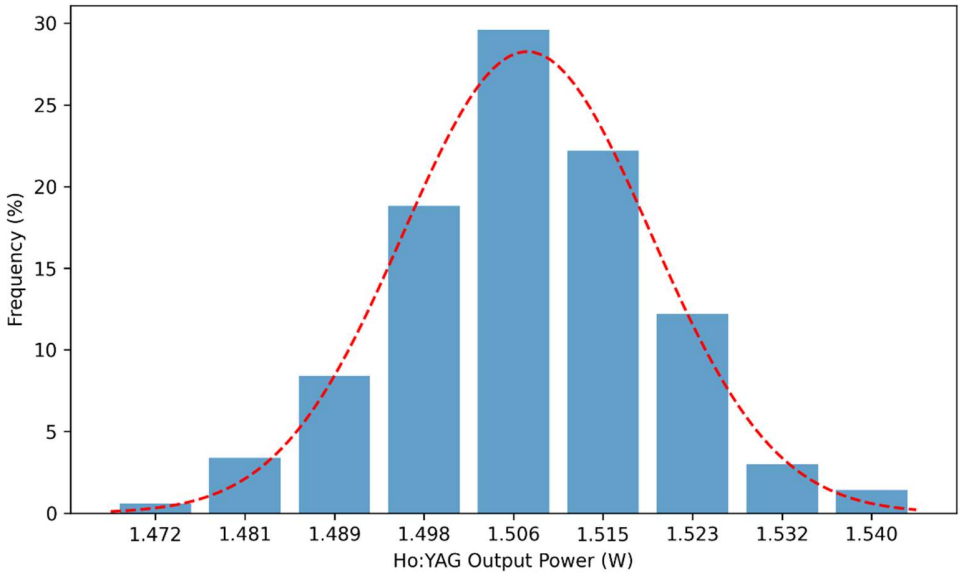


Figure 4.4: A histogram of the CW Ho:YAG output power fluctuations over 120 seconds at a pump power of 5.6 W. The sample size of 21,600 yields a mean value of 1.507 W with a standard deviation of 5.251×10^{-3} W.

Using the mean and standard deviation of each distribution, as well as the output power data for the thulium-fibre laser pump collected in Chapter 3, the slope efficiency for the CW lasing state of the Ho:YAG is computed to be 52.65%. This is shown in Figure 4.5.

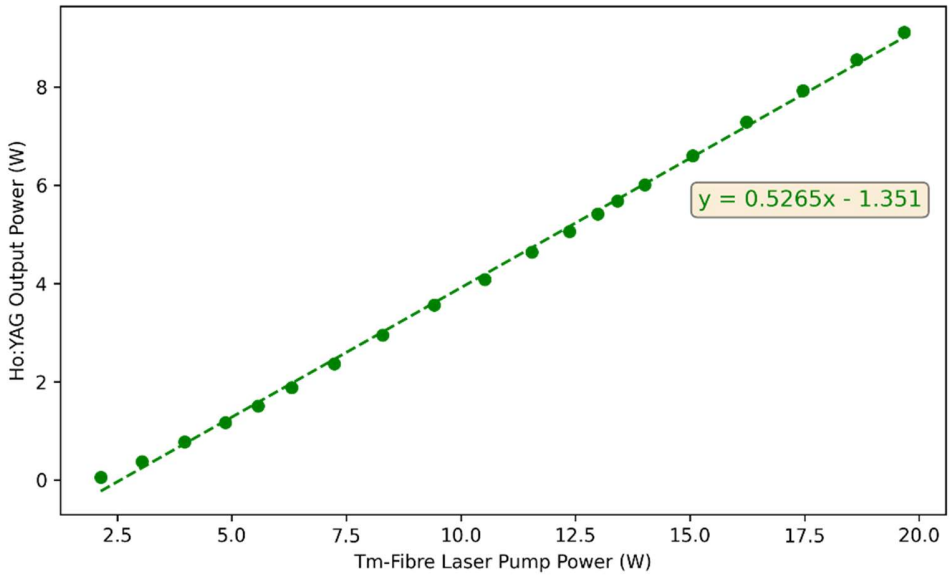


Figure 4.5: CW Ho:YAG output power as a function of pump power. The regression line indicates a slope efficiency of 52.65%.

On average, the standard deviation is only ~ 0.3% of the mean power for each unit of driving current, implying excellent power stability.

Figure 4.6 displays the optical spectrum of the Ho:YAG CW laser measured by the OSA. This reveals the presence of two emission lines at 2090.35 nm and 2096.55 nm with both peaks measuring a -3 dB signal corresponding to an averaged spectral bandwidth of ~ 0.10 nm . These peaks maintain consistency across all pump powers.

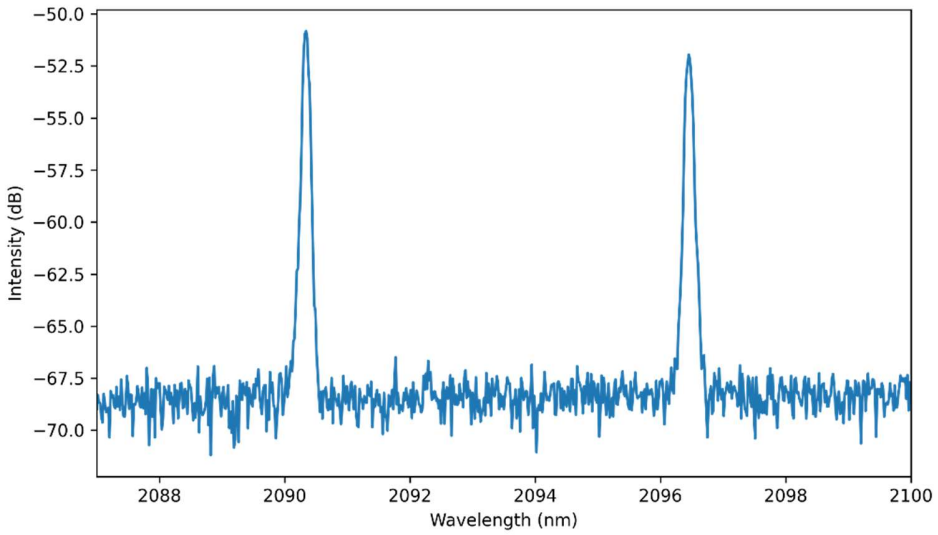


Figure 4.6: CW Ho:YAG optical spectrum featuring two peaks at 2090.35 nm and 2096.55 nm.

It is noted that prior to the characterisation process, preliminary tests were conducted to mitigate this dual emission. Although adjusting the resonator alignment could successfully increase the efficiency of one emission line over the other, the complete elimination of either emission line required the use of an etalon and hence, was not further explored [8].

The CW Ho:YAG laser operation produces a beam quality as shown in Figure 4.7. This assessment is undertaken using the built-in ISO 11146-compliant measurement option in the DataRay software, and the data fitted to the hyperbolic functions outlined in ISO 11146-1:2005. The data points are symmetrically sampled around the waist location, totaling 11 points which is in accordance with the minimum number of samples recommended by the standard. The resultant beam profile and beam quality values are obtained in the tangential axis (M_x^2) and in the sagittal axis (M_y^2).

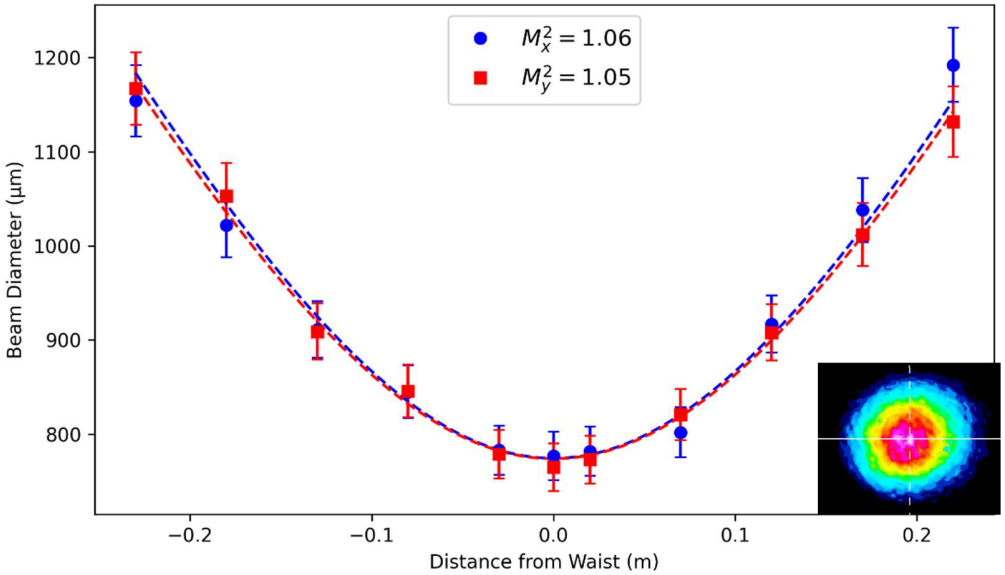


Figure 4.7: Beam profile of the CW Ho:YAG laser, corresponding to a beam quality of $M_x^2 = 1.06$ and $M_y^2 = 1.05$.

Thus, the CW lasing state operates with a slope efficiency of 52.65% at dual wavelengths centred at 2090.35 nm and 2096.55 nm with spectral bandwidths of ~ 0.10 nm. The beam quality is measured to be $M_x^2 = 1.06$ in the tangential axis and $M_y^2 = 1.05$ in the sagittal axis.

4.4 Passive SESAM Q-Switching Results

4.4.1 SESAM Specifications

As detailed in Chapter 2, a SESAM with a higher modulation depth warrants the need for a resonant SESAM achitecture, which is associated with a lower damage threshold than the anti-resonant equivalent. While this trade-off is relatively straight-forward, a complication arises when considering the energy extraction process. At higher modulation depths, the SESAM allows for a more effective blocking of lasing at lower intensities, allowing the gain to store more energy before releasing it as a pulse. This produces a higher energy pulse and hence, greater fluence on the SESAM. Thus, for a given resonator design, the overlap

between the pump powers required to achieve stable anti-resonant SESAM Q-switching (low modulation depth) yet stay below the damage threshold for resonant SESAM Q-switching (high modulation depth) may be limited if not nonexistent.

Designing a resonator capable of supporting and comparing both high and low modulation depth Q-switching therefore becomes nontrivial. As cavity length influences pulse duration as well as repetition rate, the cavity design selected ensures only minor modifications are required to meet adeque absorber saturation in each SESAM. This is done to isolate modulation depth as the primary independent variable changed across characterisations

The characteristic parameters of the SESAMs selected for this investigation are tabulated in Table 4.1. These are manufactured by BATOP GmbH and are soldered to 25.4 mm diameter cyclindrical copper heat sinks.

Table 4.1: Characteristic parameters of the three SESAMs under investigation.

Model	ΔR (%)	A_0 (%)	ΔA_{ns} (%)	F_{sat} (μJ/cm^2)	τ_s (ps)	Damage Threshold (mJ/cm^2)	Low Intensity Spectral Reflectance @ 2090 nm (%)	Low Intensity Spectral Reflectance @ 2097 nm (%)
SAM-2000-2-10ps-4	1.2	2	0.8	70	10	4	~ 98.5	~ 98.5
SAM-2000-20-10ps-4	12	20	8	65	10	2	~ 60	~ 40
SAM-2000-30-10ps-4	18	30	12	70	10	1	~ 67.5	~ 62.5

Recall that contrary to mode-locking, a Q-switched laser should be made to operate in as few longitudinal modes as possible. Since these modes are not phase-locked, the presence of more than one may lead to interference that results in an increased intensity noise throughout the pulse train. As governed by the FSR, this is achieved by choosing the laser resonator to be sufficiently short. The choice of a shorter cavity also ensures pulse durations are minimised.

4.4.2 SESAM Q-Switching with 1.2% Modulation Depth

The plano HR mirror is substituted with the ΔR = 1.2% SESAM model SAM-2000-2-10ps-4, with specifications listed in Table 4.1. The SESAM is held flat against a custom designed mount which is water-cooled at 20°C using a Thorlabs Thermoelectric Liquid Chiller (LK220).

The procedure for obtaining a time-averaged output power at each value of driving current is repeated from the CW characterisation, yielding a slope efficiency of 50.10%. This is then plotted alongside the CW efficiency for visual comparison, resulting in Figure 4.8.

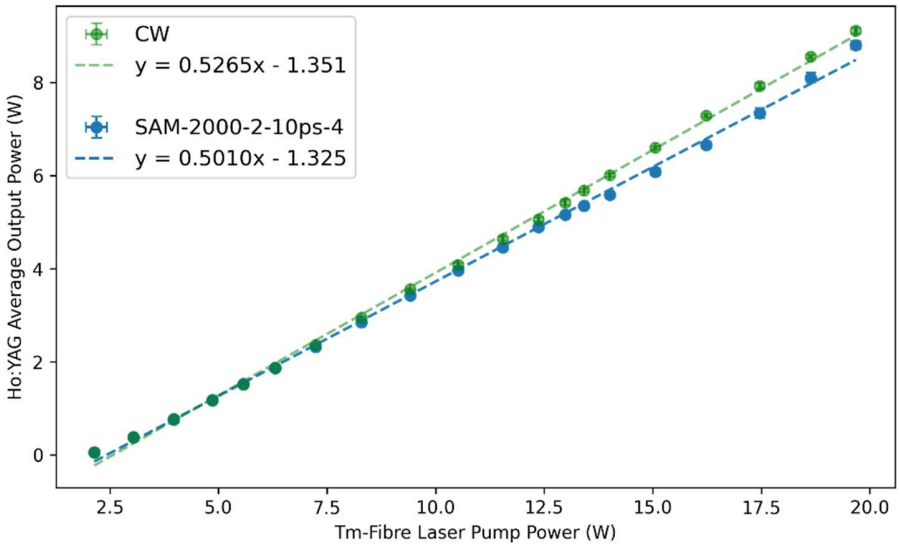


Figure 4.8: Ho:YAG average output power with the ΔR = 1.2% SESAM, plotted as a function of pump power alongside the equivalent CW output power. The regression line specifies a slope efficiency of 50.10%.

Figure 4.8 shows a decrease in efficiency of 2.55% from CW lasing to incorporating the ΔR = 1.2% SESAM. This reduction is attributed to the lower low-intensity spectral reflectance of the SESAM compared to the HR mirror, a result of the intrinsic non-saturable losses exhibited by the absorber.

Initial traces from the photodetector display pulse durations on the microsecond scale, with large beat notes dominating the overall pulse train in a chaotic and unstable manner. An oscilloscope trace of this behaviour is presented in Figure 4.9.

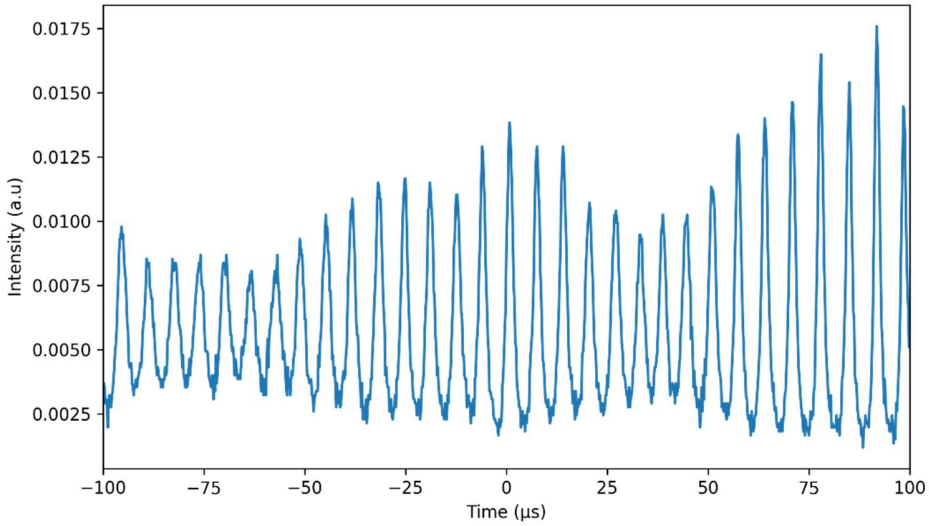


Figure 4.9: An example of the oscillatory intensity behaviour from the ΔR = 1.2% SESAM Q-switched Ho:YAG pulse train at a pump power of 13.5 W.

Towards higher pumping powers, there is a reduction in the magnitude of the large-scale oscillations. This may be indicative of multiple interfering modes pronounced by insufficient saturation of the SESAM. Despite these high intensity modulations however, preliminary assessments suggests that pulse durations and repetition rates have only minor fluctuations within each train, allowing for consistent and reproducible characterisation.

An assessment of pulse duration is hence conducted at the pump powers corresponding to each integer value of driving current. 10 pulse traces are gathered, normalised, and fitted to a Gaussian function, where the FWHM represents the pulse duration. Outliers among the 10 samples are eliminated using the interquartile range (IQR) method, and the remaining values are averaged to determine the mean pulse duration. The standard deviation then serves as the degree of error. An example of the pulse curve-fitting is shown in Figure 4.10, highlighting the asymmetric nature of Q-switched pulses with a fast leading-edge and a slower trailing-edge. This suggests that the response time of the absorber exceeds the recovery time.

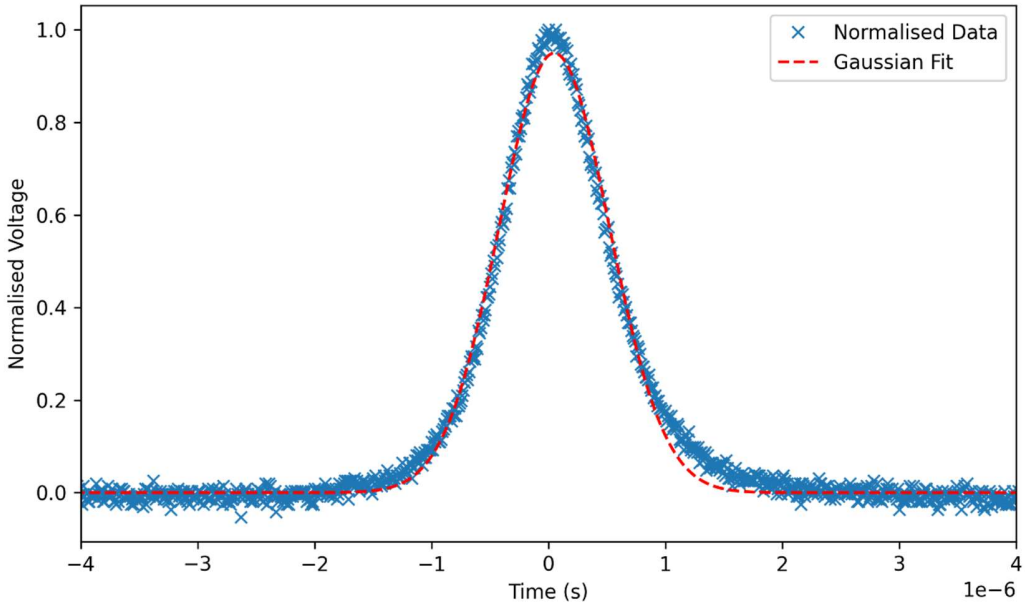


Figure 4.10: An example of Gaussian pulse curve-fitting with a ΔR = 1.2% SESAM Q-switched Ho:YAG pulse trace at a pump power of 18.5 W. The FWHM yields a pulse duration of 1.11 μs for this trace.

A similar approach is taken to determine the repetition rate. 10 traces of the pulse train are recorded, each containing no less than 25 pulses. The average distance between peaks is computed and averaged across the 10 traces, with outliers rejected via the IQR method. The standard deviation throughout the data is taken to be the degree of error, which in this case is also a visualisation of timing jitter. Pulse durations and repetition rates are then plotted as a function of pump power, as seen in Figure 4.11 (a). The corresponding pulse energies and pulse peak powers are computed using Equation (2.42) and Equation (2.43) and are presented in Figure 4.11 (b).

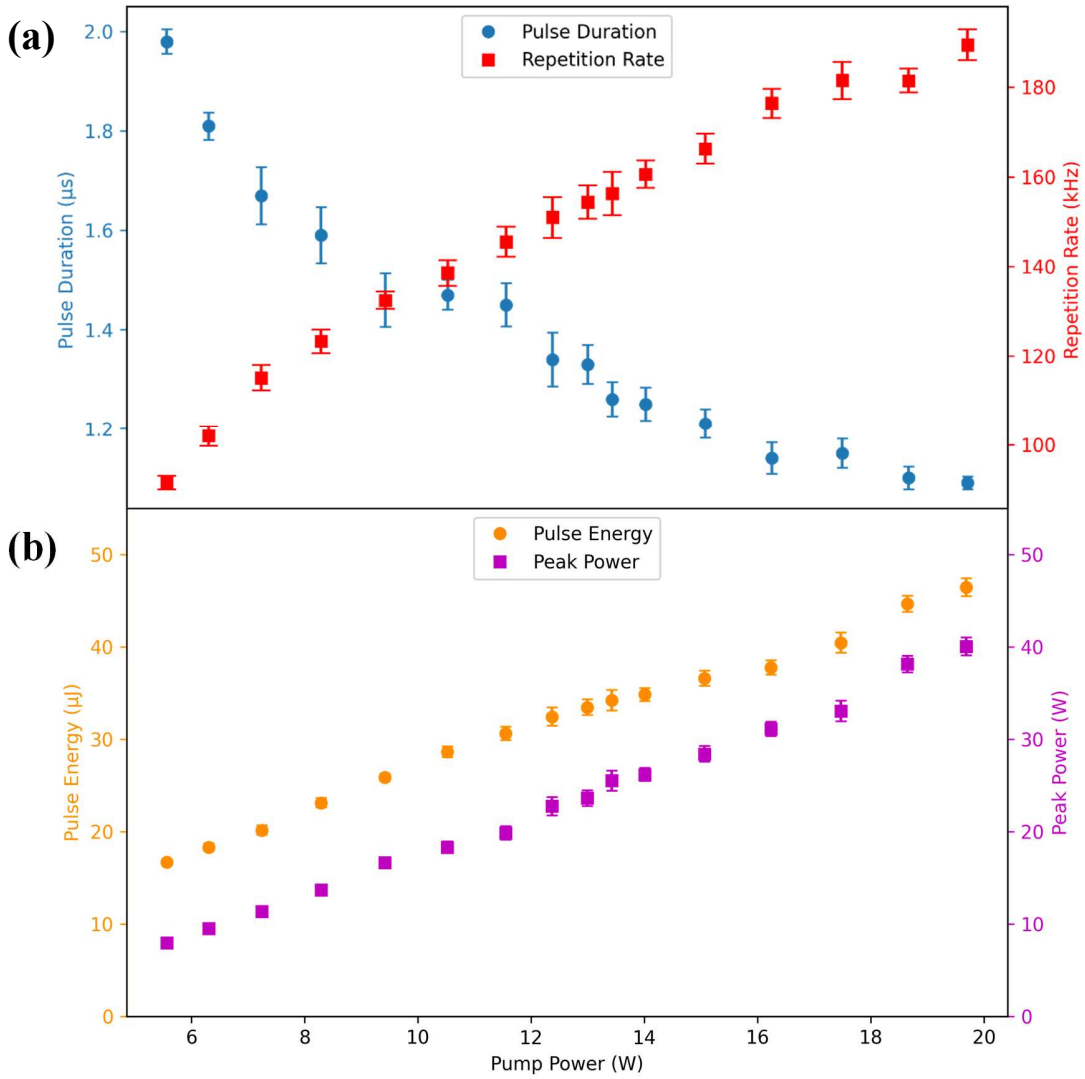


Figure 4.11: (a) Pulse durations and repetition rates and (b) pulse energies and peak powers of the ΔR = 1.2% SESAM Q-switched Ho:YAG plotted as a function of pump power.

Thus, pulse durations are shown to decrease with increasing pump power, while repetition rates increase. This trend corresponds to increasing values of both pulse energy and peak power with increasing pump power.

The optical spectrum of the output is measured by the OSA and presented in Figure 4.12. Dual emissions are observed at 2089.85 nm and 2096.95 nm, displaying only slight deviations from the wavelengths recorded at CW lasing. The spectral bandwidth is measured to be resolution limited with ~ 0.05 nm and ~ 0.10 nm respectively. No significant changes are observed in the spectrum throughout the full range of pump powers.

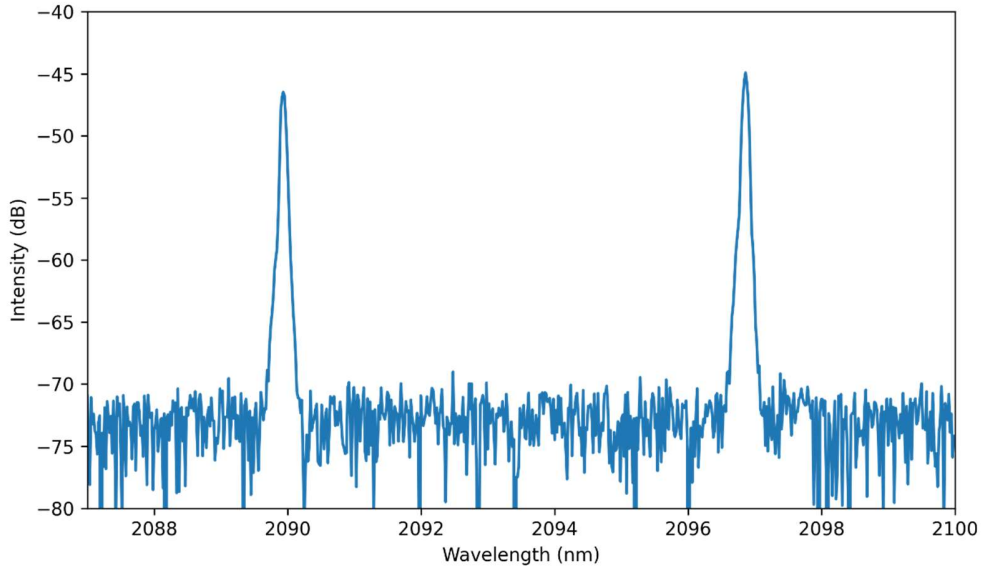


Figure 4.12: Optical spectrum of the ΔR = 1.2% SESAM Q-switched Ho:YAG laser. The spectrum displays dual emission at 2089.85 nm and 2096.95 nm.

The assessment of beam quality follows, utilising the same measurement locations as those used in the CW evaluation. The obtained beam quality values remain consistent at M_x^2 = 1.06 and M_y^2 = 1.05, indicating negligible deviation from the CW lasing state, with only slight variations in the measured beam radii. Figure 4.13 illustrates this beam profile.

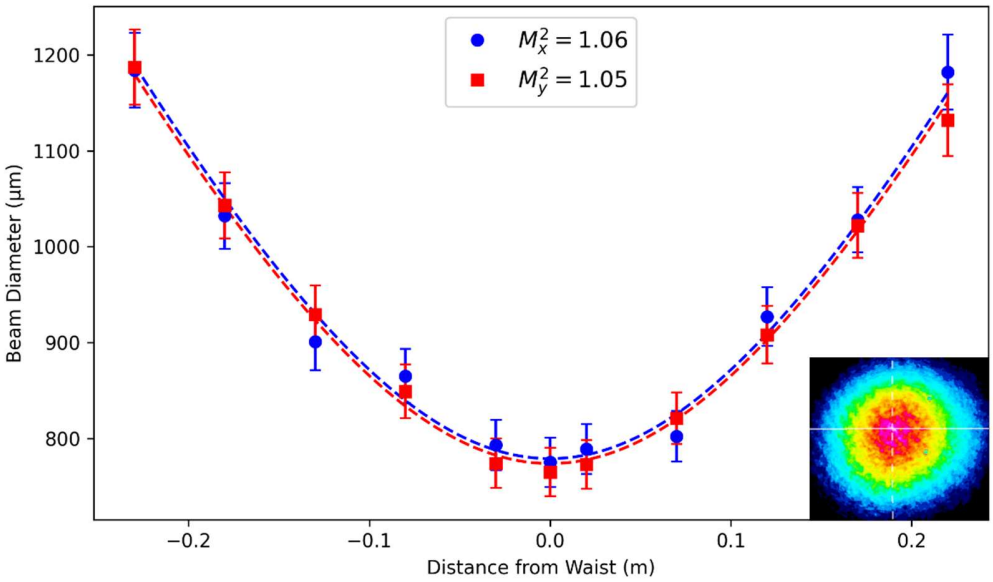


Figure 4.13: Beam profile of the ΔR = 1.2% SESAM Q-switched Ho:YAG laser. This corresponds to a beam quality of M_x^2 = 1.06 and M_y^2 = 1.05.

The resonator configuration illustrated in Figure 4.14 is trialled to evaluate the stability of the pulse train. This incorporates a shorter focal length lens for a more focused beam size on the SESAM. The beam radius throuhgout the cavity is described in Figure 4.15.

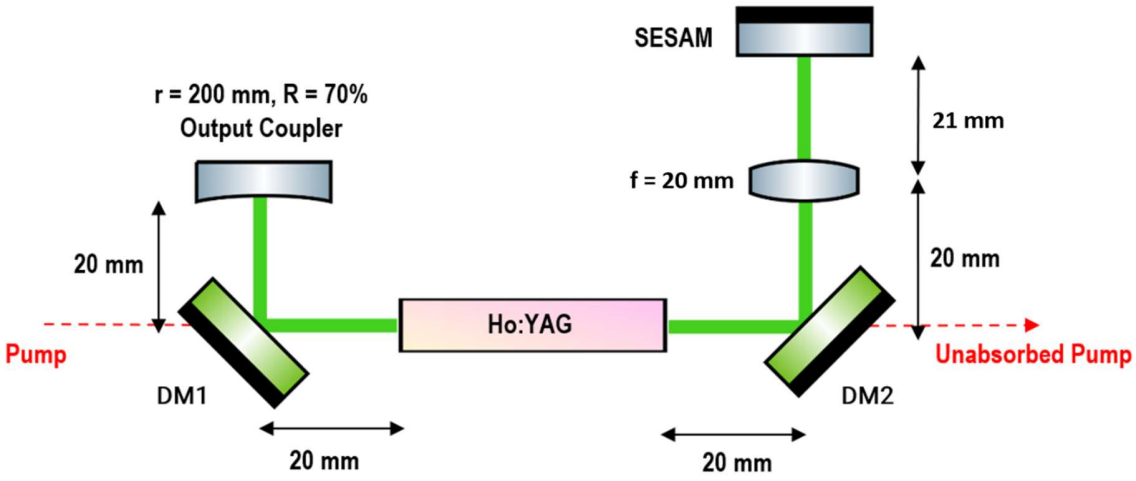


Figure 4.14: Schematic of the secondary resonator used for the SESAM Q-switching of the Ho:YAG laser under a tighter SESAM spot size. DM1 and DM2: Dichroic mirrors.

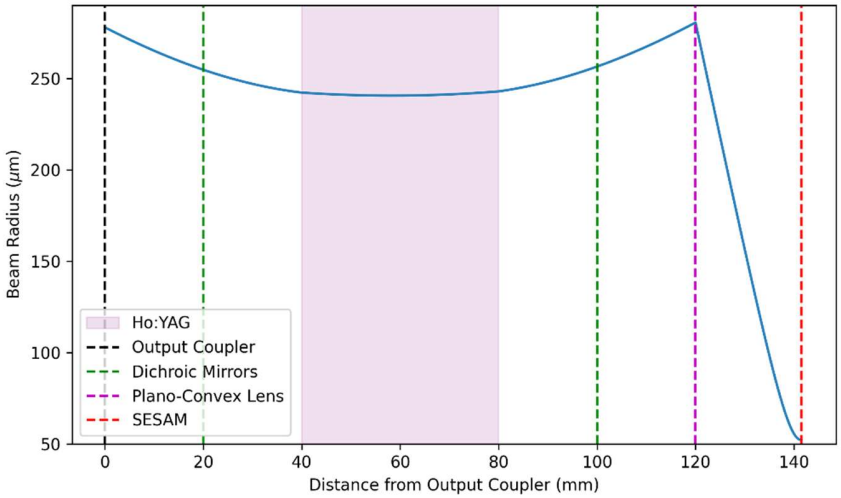


Figure 4.15: Beam radius within the secondary Q-switched resonator design as a function of distance across the cavity.

This design offers increased stability with $P_T = P_S = 0.185$, in addition to a smaller beam size of 100 μm focused onto the SESAM, which is facilitated by the higher damage threshold of the $\Delta R = 1.2\%$ SESAM relative to the other SESAMs. Despite a reduction in cavity length

by approximately 40 mm, the beam size within the Ho:YAG remains consistent with the previous configuration.

Although substantial intensity oscillations persist at lower driving currents, once pump powers surpass 15 W, a sudden transition to a more stable Q-switching regime occurs, with average powers, pulse durations and repetition rates largely consistent with those from the original cavity. The result is depicted in Figure 4.16.

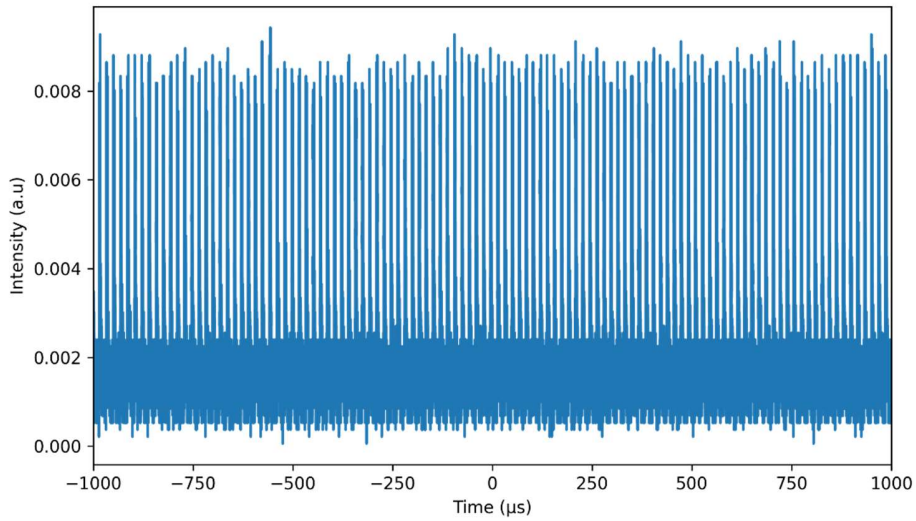


Figure 4.16: Example of a pulse train obtained from the ΔR = 1.2% SESAM Q-switched Ho:YAG laser.

Since a measured voltage peak is proportional to the pulse energy, which is also proportional to the peak power, Equation (2.41) may be used to estimate *RIN* from the mean peak intensity and standard deviation. This calculation is performed in Python for the dataset illustrated in Figure 4.16, yielding a *RIN* of 3.01%.

The ΔR = 1.2% SESAM demonstrates the ability to produce Q-switched pulses as short as 1.09 ± 0.01 µs at a repetition rate of 189 ± 3 kHz and average power of 8.80 ± 0.09 W. This corresponds to pulse energies of 46.5 ± 0.1 µJ and peak powers of 40.0 ± 0.1 W with a pulse train *RIN* of 3.01% provided adequate SESAM saturation. This configuration operates with a slope efficiency of 50.1% at a dual wavelength emission of 2089.85 nm and 2096.95 nm with a resolution limited spectral bandwidth of ~ 0.05 nm and ~ 0.10 nm respectively. The beam quality is measured to be M_x^2 = 1.06 and M_y^2 = 1.05.

4.4.3 SESAM Q-Switching with 12% Modulation Depth

The same characterisation process is undertaken for SESAM model SAM-2000-20-10ps-4, which has a modulation depth of 12%. Figure 4.17 presents the measured average output power efficiency.

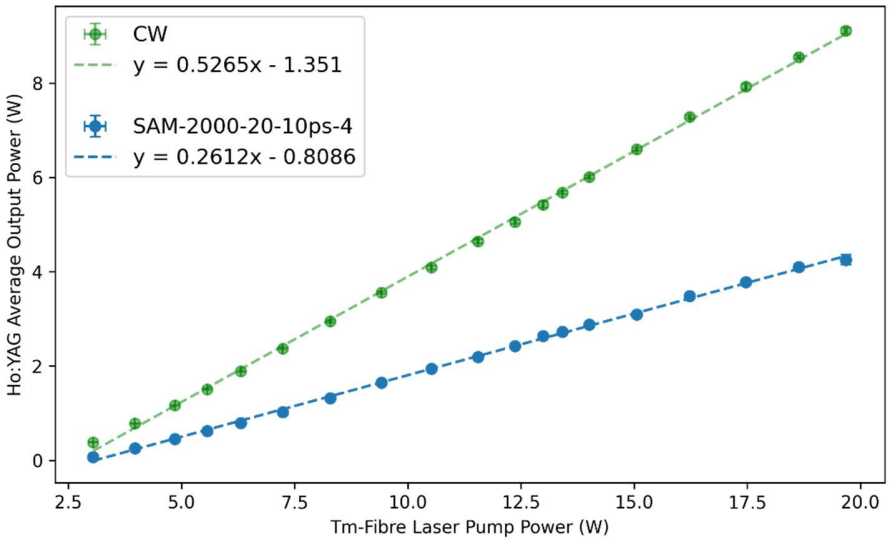


Figure 4.17: Ho:YAG average output power using the ΔR = 12% SESAM, plotted as a function of pump power alongside the equivalent CW output power. The regression line specifies a slope efficiency of 26.12%.

As indicated in Figure 4.17, the slope efficiency is computed to be 26.12%, which is notably lower than that of the previous SESAM. This is primarily due to the lower spectral reflectance at 2097 nm. An examination of Table 4.1 and the manufacturer-provided information reveals that ΔR = 12% and ΔR = 18% SESAMs are optimised for operation around 2050 nm, featuring a significantly reduced reflectance at 2097 nm. While this reduction affects efficiency, all other specifications are still applicable for 2097 nm. Hence, the capacity for pulse generation is presumed to be unaffected.

The pulse durations and repetition rates are then measured and plotted in Figure 4.18 (a), with the corresponding pulse energies and peak powers calculated and displayed in Figure 4.18 (b).

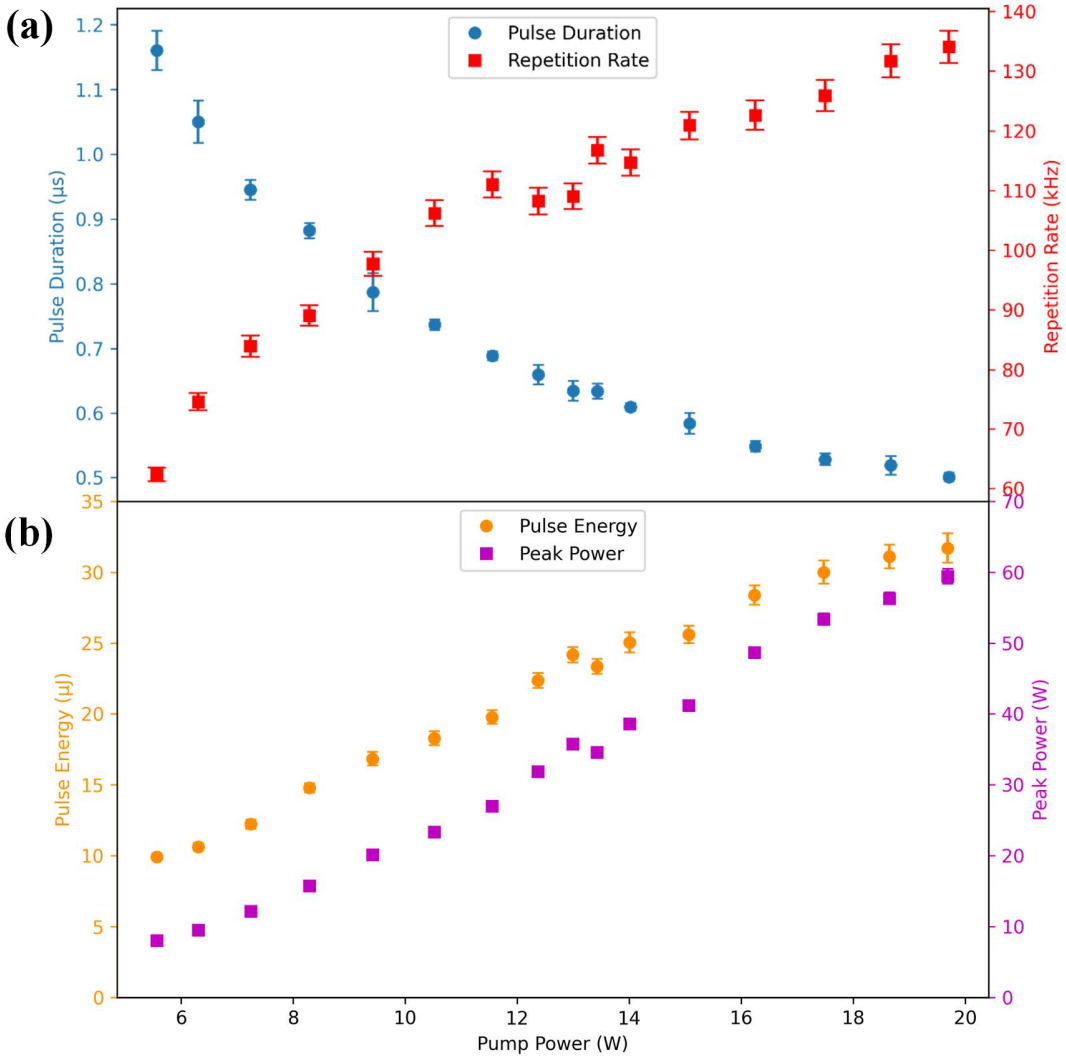


Figure 4.18: (a) Pulse durations and repetition rates and (b) pulse energies and peak powers of the ΔR = 12% SESAM Q-switched Ho:YAG, plotted as a function of pump power.

The optical spectrum of the output is measured by the OSA and presented in Figure 4.19. In a deviation from the CW lasing state and the previous SESAM, the ΔR = 12% SESAM does not readily support the lasing of dual emission lines but instead, operates at a single peak emission centred at 2090.15 nm with a -3 dB spectral bandwidth of ~ 0.10 nm.

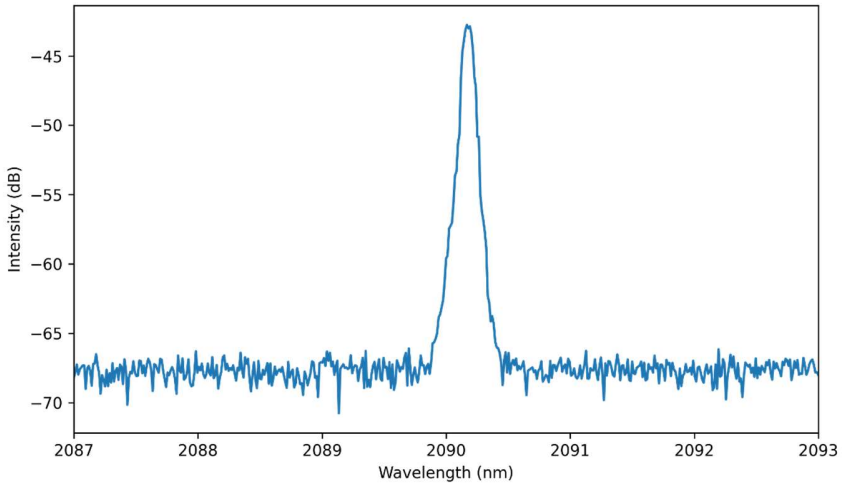


Figure 4.19: Optical spectrum of the ΔR = 12% SESAM Q-switched Ho:YAG laser. The spectrum features a single peak emission centred at 2090.15 nm.

The tendancy for only a single emission line is attributed to the ~ 20% decrease in low intensity SESAM reflectance for 2097 nm compared to 2090 nm as noted in Table 4.1. This shifts the resonator to favour the 2090 nm emission line rather than having competing peaks in the spectrum. No significant changes are observed in the spectrum throughout the full range of pump powers.

Beam radii measurements are conducted at the same locations along the optical path selected for the earlier characterisations. The curve-fit yields beam quality values of M_x^2 = 1.07 and M_y^2 = 1.08. This signifies only a marginal deviation from the previous SESAM and CW lasing. The measurements taken for the curve-fit are depicted in Figure 4.20.

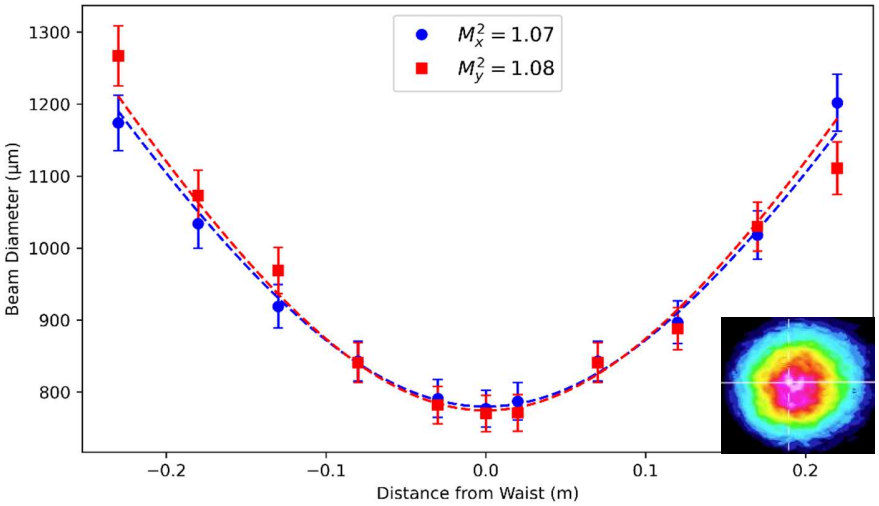


Figure 4.20: Beam profile of the ΔR = 12% SESAM Q-switched Ho:YAG laser. This illustrates a beam quality of M_x^2 = 1.07 and M_y^2 = 1.08.

To conclude the characterisation of the ΔR = 12% SESAM, an evaluation of pulse train stability is undertaken. Upon visual inspection of the pulse trains detected by the photodetector, it is evident that the same intensity fluctuations observed in the primary resonator design with the previous SESAM persist here. This is anticipated, as the pulse energies depicted in Figure 4.18 (b) suggest that the SESAM experiences a very similar level of saturation. Consequently, it is expected that modifying the beam radius on the SESAM to approximately 50 µm, as outlined in the setup in Figure 4.14, will result in a sudden increase in pulse train intensity stability, analogous to what was observed for the ΔR = 1.2% SESAM.

While large-scale intensity fluctuations are still present at lower pumping powers, towards higher powers the operation transitions to a more stable regime. This yields pulse durations, repetition rates and average powers consistent with the primary resonator design used to produce Figure 4.17 and Figure 4.18. The resultant pulse train is presented in Figure 4.21, with the associated *RIN* calculated to be 4.87%.

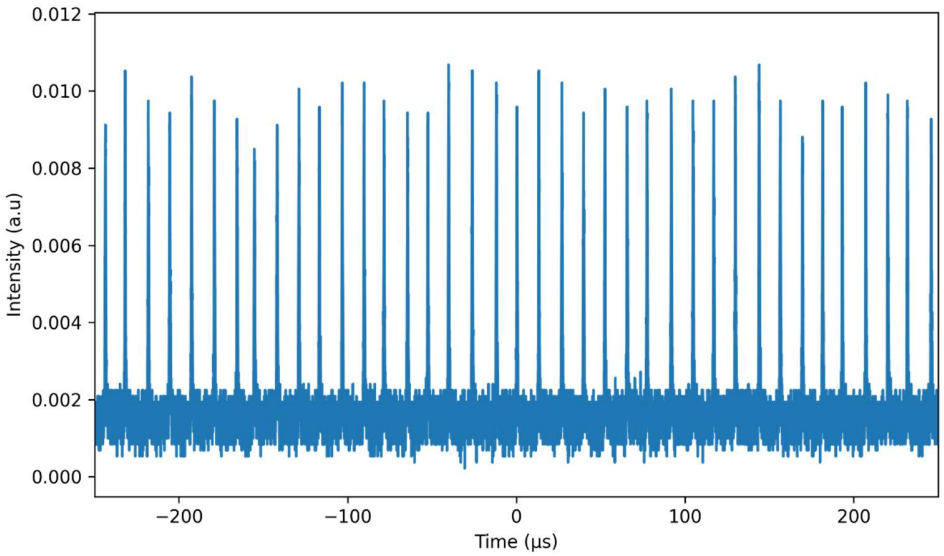


Figure 4.21: Example of a pulse train obtained from the ΔR = 12% SESAM Q-switched Ho:YAG laser.

Thus, the ΔR = 12% SESAM demonstrates the ability to produce Q-switched pulses down to 501 ± 7 ns at a repetition rate of 134 ± 3 kHz and average power of 4.25 ± 0.11 W. This corresponds to pulse energies of 31.7 ± 1.0 µJ and peak powers of 59.4 ± 1.0 W with pulse train *RIN* of 4.87% provided adequate SESAM saturation. This configuration achieves a

slope efficiency of 26.12% at 2090.15 nm with ~ 0.10 nm spectral FWHM and a beam quality of $M_x^2 = 1.07$ and $M_y^2 = 1.08$.

4.4.4 SESAM Q-Switching with 18% Modulation Depth

Finally, the same characterisation process is conducted using SESAM model SAM-2000-30-10ps-4, which has a modulation depth of 18%. The efficiency is assessed by plotting the average output power against pump power. However, similarly to the preceding SESAM, the $\Delta R = 18\%$ SESAM suffers from an unoptimised spectral reflectance at 2097 nm, thereby restricting its overall efficiency. The outcome of the measurements is presented in Figure 4.22, illustrating a slope efficiency of 22.80%.

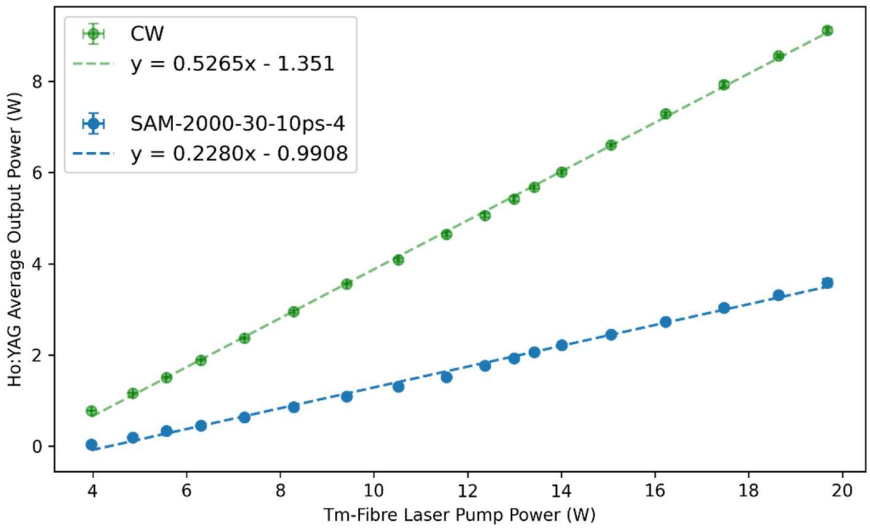


Figure 4.22: Ho:YAG average output power using the $\Delta R = 18\%$ SESAM, plotted as a function of pump power alongside the equivalent CW lasing output power. The regression line corresponds to a slope efficiency of 22.80%.

Upon initial inspection of the pulse train, a deviation from the behaviour observed in the previous Q-switching is evident. Notably, there are much shorter pulse durations at lower repetition rates. While substantial intensity fluctuations persist at lower pumping powers, the pulses exhibit a more chaotic nature, with dropouts frequent. Additionally, smaller sub-trains

of pulses with higher repetition rates occasionally manifest between the peaks of the main train.

However, as pump power increases, a rapid increase in stability is observed, characterised by fewer dropouts and more consistent peak-to-peak intensities. At the highest pump powers, a high level of stability is achieved without necessitating a tighter focus on the SESAM, unlike the other SESAMs. This can be attributed to the shorter pulse durations and lower repetition rates resulting in higher pulse energies which consequently deliver a greater fluence on the SESAM. Thus, achieving the required saturation for stable pulsing without needing such a tight focus on the SESAM.

The pulse durations and repetition rates are measured and plotted in Figure 4.23 (a), with the corresponding pulse energies and peak powers computed and displayed in Figure 4.23 (b).

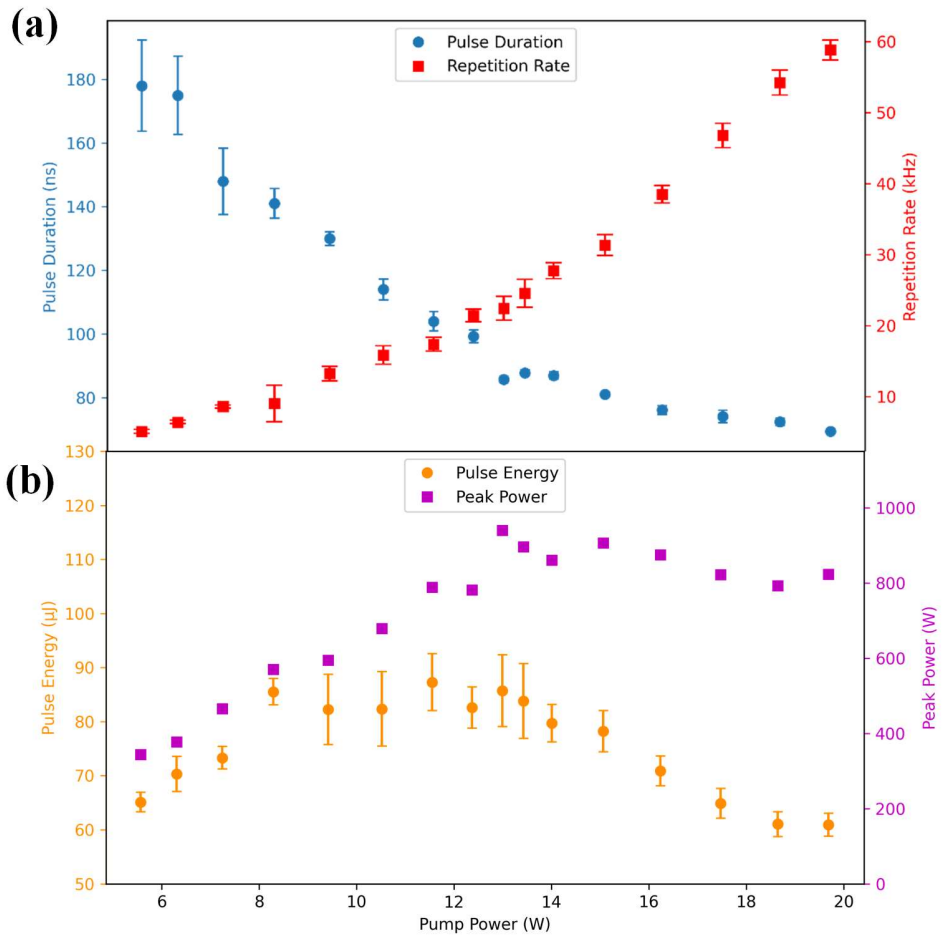


Figure 4.23: (a) Pulse durations and repetition rates and (b) pulse energies and peak powers of the ΔR = 18% SESAM Q-switched Ho:YAG laser, plotted as a function of pump power.

In contrast to the previous characterisations, once greater pulse train stability is achieved at a pump power of ~ 12 W, the repetition rate accelerates with respect to pump power, as seen in Figure 4.23 (a). The extent of this means that despite an increasing average output power, increasing the pump power generates so many extra pulses per unit of time that the average energy per individual pulse starts to decrease. This results in the 'turn-over' of pulse energies towards higher pump powers seen in Figure 4.23 (b).

While the same phenomenon might be expected for pulse peak powers, the pulse duration continues to decrease, which directly counteracts this effect. This leads to a considerably slower decline in peak power after reaching its maximum as evident in Figure 4.23 (b).

Since an alternative lens is not required to meet the saturation requirements of the ΔR = 18% SESAM, pulse train stability is also assessed here. Figure 4.24 displays the pulse train corresponding to 35 kHz, obtained at a pump power of 16 W. The computed *RIN* for this dataset is 2.76%.

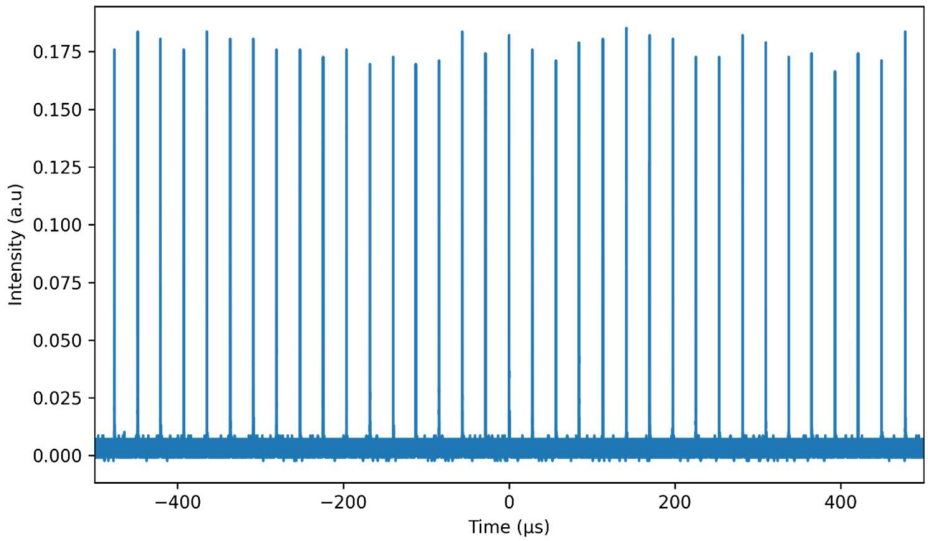


Figure 4.24: 35 kHz Q-switched Ho:YAG laser pulse train using the ΔR = 18% SESAM and corresponding to a RIN of 2.76%.

The optical spectrum is then measured. While all spectra obtained thus far have been static throughout the full range of pump powers, initial OSA traces suggest that some degree of spectral broadening is present when using the ΔR = 18% SESAM. This arises due to the nonlinear intensity-dependent interaction of the high pulse peak powers with the YAG within the gain medium. Figure 4.23 indicates peak powers up to 930 W. This corresponds to

approximately 3000 W of intracavity peak power passing through the gain. As noted in Table 2.1, YAG possesses a substantial nonlinear refractive index, making it particularly susceptible to such nonlinear effects.

Figure 4.25 showcases the degree of spectral broadening. The optical spectrum is assessed both at threshold (Figure 4.25 (b)) and under the highest pumping power of 19.7 W (Figure 4.25 (c)). For comparison, Figure 4.25 (a) illustrates the corresponding CW emission line.

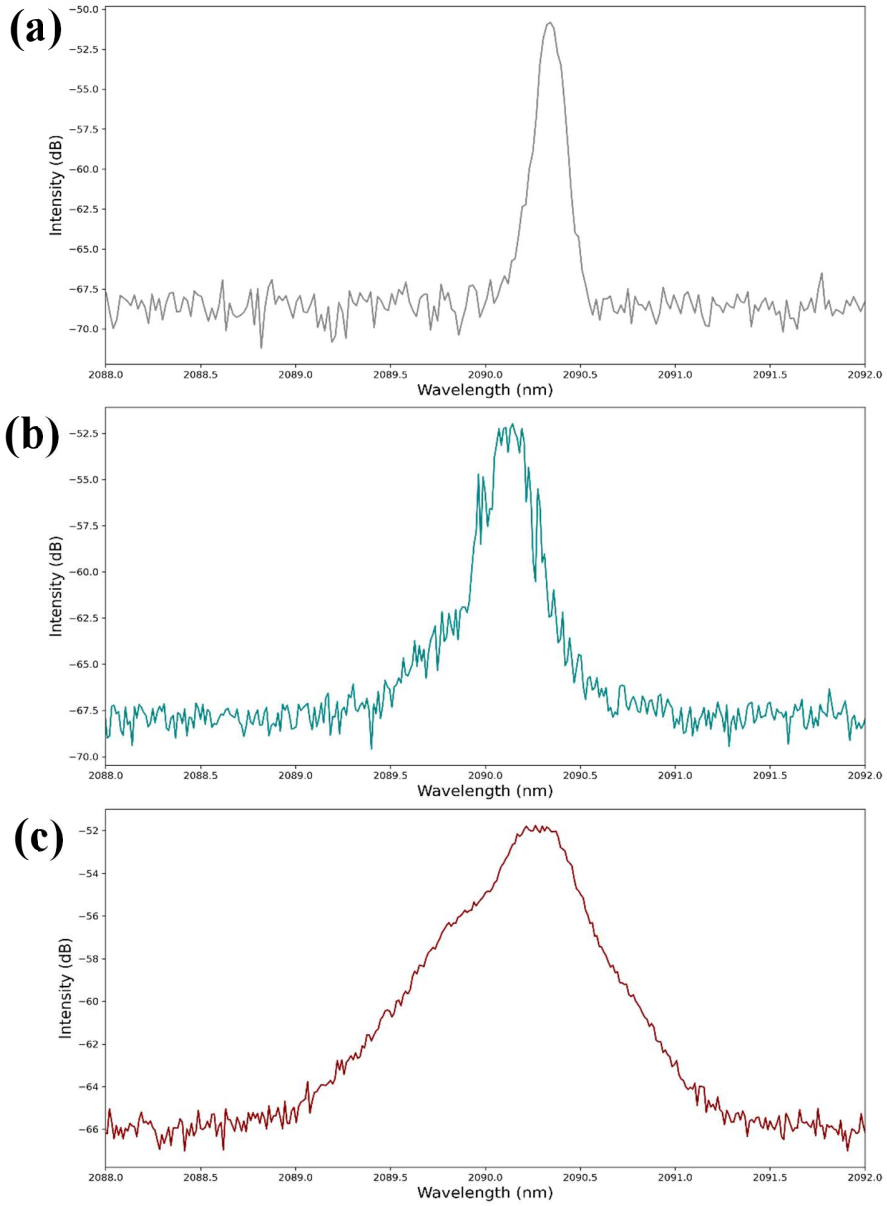


Figure 4.25: Optical spectrum of (a) CW lasing, and ΔR = 18% SESAM Q-switched Ho:YAG lasing at (b) threshold, and (c) a maximum pump power of 19.7 W.

The spectral bandwidth at threshold is calculated to be ~ 0.20 nm centred at 2090.15 nm, whereas the bandwidth at the maximum pump power is determined to be ~ 0.45 nm, centred at 2090.30 nm. This indicates a spectral broadening of 0.25 nm across the entire range of powers. Compared to the spectral bandwidth of CW lasing and the other SESAMs, this indicates a broadening of ~ 0.35 nm.

Finally, a beam quality assessment is undertaken which follows the same procedure used for the previous characterisations. This results in a beam quality of $M_x^2 = 1.06$ and $M_y^2 = 1.07$, as seen in Figure 4.26.

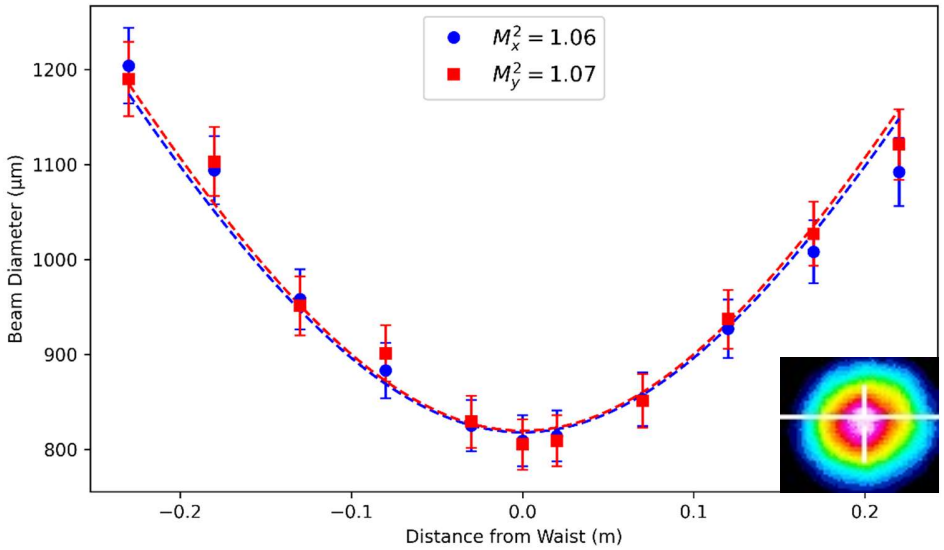


Figure 4.26: Beam profile of the ΔR = 18% SESAM Q-switched Ho:YAG laser. This illustrates a beam quality of $M_x^2 = 1.06$ and $M_y^2 = 1.07$.

Thus, the ΔR = 18% SESAM demonstrates the ability to produce Q-switched pulses down to 69.5 ± 0.7 ns at a repetition rate of 58.9 ± 1.4 kHz and an average power of 3.58 ± 0.09 W. These correspond to pulse energies of 60.9 ± 2.1 μJ and peak powers of 823 ± 2.1 W. However, the highest pulse energies and peak powers are found to be 87.3 ± 5.3 μJ and 939.7 ± 5.3 W respectively. These occur at pulse durations of 104 ± 3 ns, a repetition rate of 17.4 ± 1 kHz, and an average power of 1.09 ± 0.01 W. Additionally, a low *RIN* value of 2.76% is observed. The slope efficiency achieved is computed to be 22.8%, with a beam quality of $M_x^2 = 1.06$ and $M_y^2 = 1.07$. Spectral broadening is also present, extending the spectrum from a bandwidth of ~ 0.20 nm centred at 2090.15 nm, to ~ 0.45 nm, centred at 2090.30 nm.

4.5 Discussion and Comparison

Figure 4.27 presents a comparison of the slope efficiencies, pulse durations, repetition rates, pulse energies, and pulse peak powers for the three SESAMs assessed.

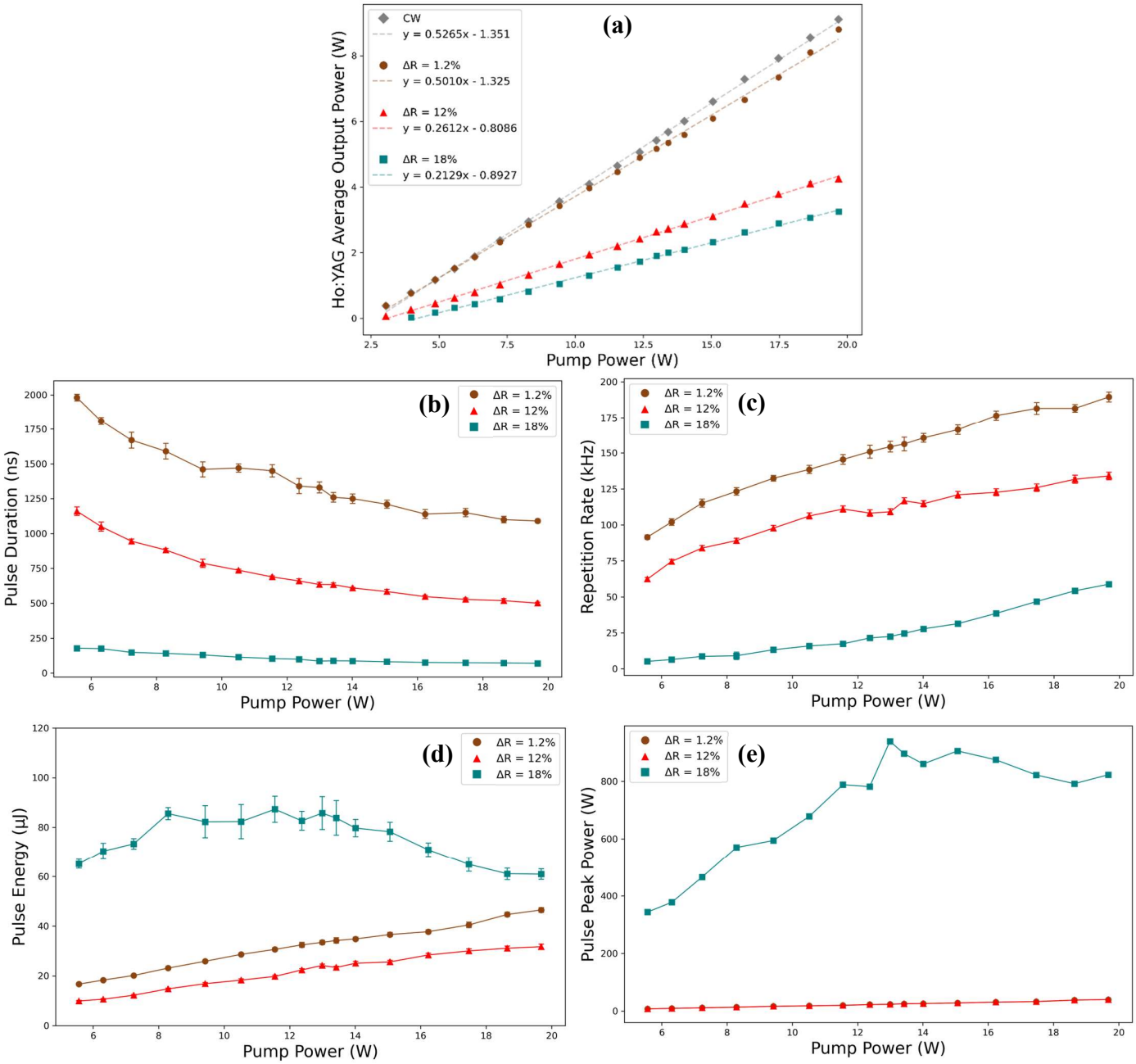


Figure 4.27: Comparative plots of (a) slope efficiency, (b) pulse durations, (c) pulse repetition rates, (d) pulse energies, and (e) pulse peak powers for the three characterised SESAMs.

To understand the influence of modulation depth on pulse dynamics, Figure 4.27 (a) highlights the slope efficiency for each SESAM characterised. This reveals an efficiency discrepancy, particularly with the ΔR = 1.2% SESAM, which significantly outperforms the other two. The ΔR = 1.2% SESAM achieves slightly lower average powers than CW lasing, while both the ΔR = 12% and ΔR = 18% models only approach approximately half of this. This is expected as a stronger absorber causes a stronger attenuation which results in lower output powers. Furthermore, as detailed in Table 4.1 and previously mentioned, the ΔR = 1.2% SESAM is the only one optimised for lasing at 2090 nm and 2097 nm, exhibiting higher low-intensity spectral reflectance in this range. In contrast, the other two SESAMs are optimised for lasing at 2000 - 2050 nm and have significantly lower low-intensity spectral reflectance at 2090 nm and 2097 nm. This lowers the average powers achieved by these SESAMs, resulting in a reduced slope efficiency. Additionally, single line emission at 2090 nm is favoured as opposed to dual emission at both 2090 nm and 2097 nm which is demonstrated by CW lasing and the ΔR = 1.2% SESAM. While this limitation doesn't impact functionality as a Q-switch, it is necessary to consider the constrained average power output when comparing other key pulse parameters relative to the ΔR = 1.2% SESAM.

Figure 4.27 (b) compares pulse durations. The plot indicates a clear trend: a higher modulation depth achieves shorter pulse durations which further decrease with increasing pump power. Notably, despite the modulation depth difference being nearly doubled between the ΔR = 1.2% and ΔR = 12% SESAMs compared to between the ΔR = 12% and ΔR = 18% models, the disparity is not mirrored in the data. This suggests a nonlinear relationship between modulation depth and the attainable pulse duration. To assess the relative change in pulse durations from threshold, Figure 4.28 is produced, which is plotted against both pump power (Figure 4.28 (a)) and output power (Figure 4.28 (b)).

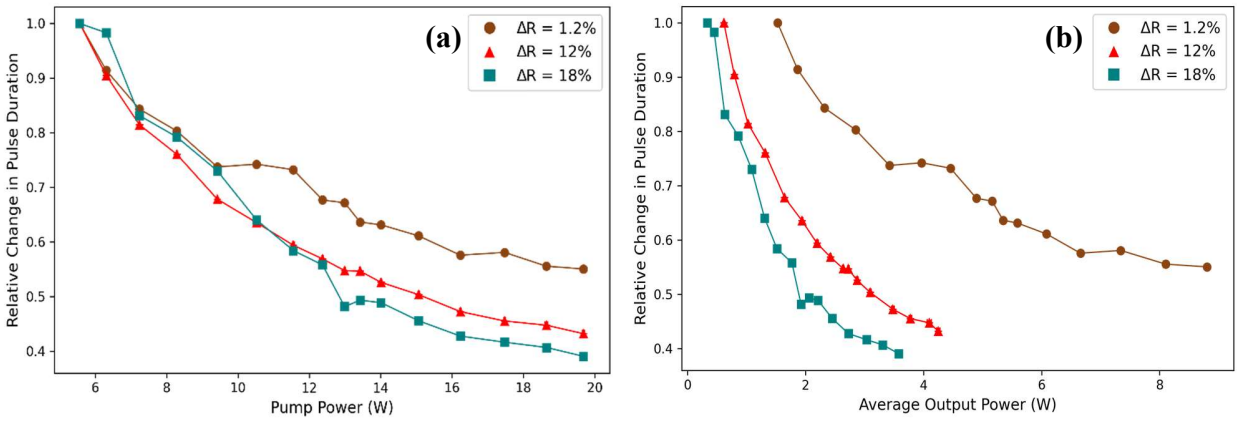


Figure 4.28: Relative change in pulse duration from threshold in the three SESAM models plotted against pump power (a) and average output power (b).

Both panels in Figure 4.28 indicate that not only does an increased modulation depth result in shorter pulse durations, but it also leads to the most significant relative change in pulse duration as both pump power and average power increase. Specifically, the $\Delta R = 18\%$ SESAM experiences a pulse duration reduction of 61% from threshold to maximum pump power, the $\Delta R = 12\%$ SESAM displays a reduction of 56%, and the $\Delta R = 1.2\%$ SESAM shows a reduction of only 45%.

Figure 4.27 (c) demonstrates that an increased modulation depth leads to a lower pulse repetition rate, which increases with pump power. Following a similar approach to Figure 4.28, Figure 4.29 is generated to emphasise the relative change in repetition rate.

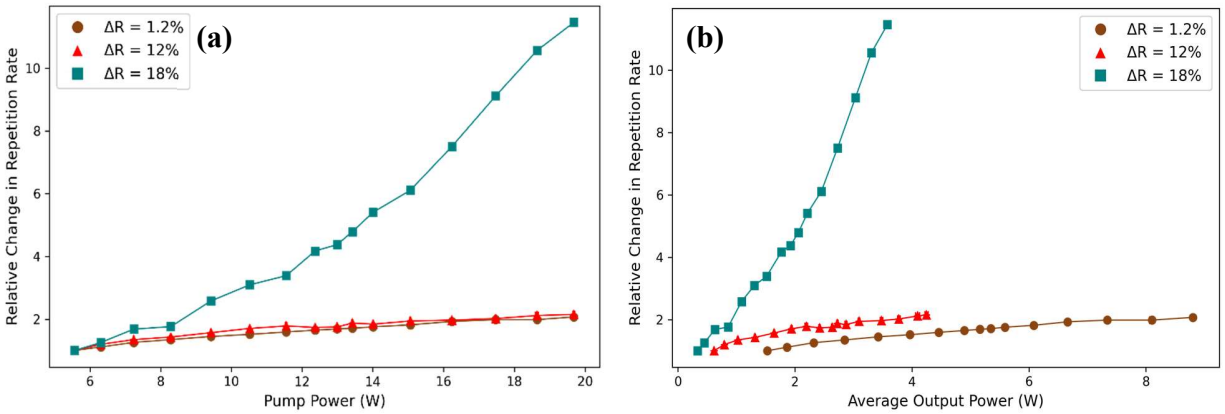


Figure 4.29: Relative change in pulse repetition rate from threshold in the three SESAM models plotted against pump power (a) and average output power (b).

Upon examining Figure 4.29 (a) and Figure 4.29 (b), it becomes evident that the SESAM with the highest modulation depth undergoes a significantly more pronounced relative change in repetition rate with increasing pump power and average output power. The gradient of the repetition rate is strong enough that, in Figure 4.27 (d), the average pulse energy starts to decrease for this SESAM, while the other SESAMs facilitate steady growth.

The trends observed in pulse durations and repetition rates suggest that a higher modulation depth corresponds to higher pulse energies and peak powers. However, this behavior is not corroborated by Figure 4.27 (d) and Figure 4.27 (e), where the ΔR = 1.2% SESAM exhibits pulse energies surpassing those of the ΔR = 12% SESAM, and pulse peak powers on par with the ΔR = 12% SESAM. This is attributed to the efficiency difference between these two SESAMs. Figure 4.30 is produced to emphasise this, illustrating the pulse energy per output power against pump power (a) and the pulse peak power per output power against pump power (b).

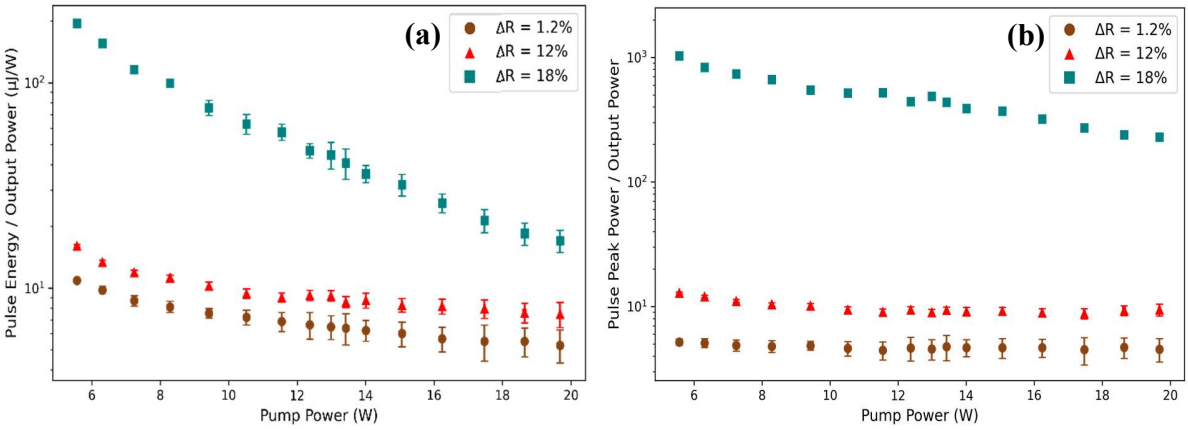


Figure 4.30: Pulse energy per output power (a) and pulse peak power per output power (b) as a function of pump power of each of the three characterised SESAM models.

Figure 4.30 (a) and Figure 4.30 (b) show that a higher modulation depth results in higher energy pulses with higher peak powers. In the case of the ΔR = 18% SESAM, the peak powers achieved are high enough that nonlinear spectral broadening starts to occur in the Ho:YAG. The spectral bandwidth increases by a factor of ~ 4.2 relative to the unbroadened bandwidth of the other two SESAMs. To mitigate this effect where it is undesirable, opting for a resonator design with a larger beam radius within the Ho:YAG will decrease the beam intensity, thus reducing the observed nonlinearity.

All three SESAMs are able to demonstrate a low *RIN* value, however in the case of the ΔR = 1.2% and ΔR = 12% SESAMs, an alternative lens is required to yield a higher SESAM fluence and achieve increased stability. Despite these adjustments, the new pulse durations and repetition rates remain consistent with the original cavity values, albeit with stabilised intensities. To further enhance the stability of the pulse trains, an etalon may be introduced for single-mode selection, effectively mitigating intensity fluctuations caused by the interference of out-of-phase modes.

No significant changes to the beam quality are observed through the four beam quality assessments.

4.6 Chapter Summary

This chapter presented the first demonstration of passive Q-switching in a Ho:YAG laser by SESAM. Three SESAMs with modulation depths of 1.2%, 12% and 18% were used and evaluated to determine the influence of modulation depth on Q-switched performance. As theorised, it was found that in general a higher modulation depth results in increased energy storage in the gain before the quality-factor switches, creating shorter pulse durations spaced at wider intervals. These shorter pulse durations and lower repetition rates produce higher energy pulses and peak powers.

Despite this however, it was found that the ΔR = 1.2% SESAM produced higher energy pulses and peak powers than the ΔR = 12% SESAM. This was attributed to the unoptimised ΔR = 12% SESAM for operation at 2090 nm. Furthermore, it was concluded that towards higher pump powers, the repetition rates using the ΔR = 18% SESAM increased faster than the average output power could support, resulting in a decrease in pulse energy.

Using the ΔR = 18% SESAM, stable Q-switched pulses with durations of 69.5 ± 0.7 ns at a repetition rate of 58.9 ± 1.4 kHz and an average power of 3.58 ± 0.09 W were observed. These values corresponded to pulse energies of 60.9 ± 2.1 μJ and peak powers of 823 ± 2.1 W. The highest pulse energies and peak powers were found to be 87.3 ± 5.3 μJ and

939.7 ± 5.3 W respectively. These occurred at pulse durations of 104 ± 3 ns, a repetition rate of 17.4 ± 1 kHz, and an average power of 1.09 ± 0.01 W. At these powers, spectral broadening was demonstrated in the gain medium, extending the spectrum from a bandwidth of ~ 0.20 nm centred at 2090.15 nm, to ~ 0.45 nm, centred at 2090.30 nm. The *RIN* was measured to be 2.76%, with a slope efficiency of 22.8%, and a beam quality of $M_x^2 = 1.06$ and $M_y^2 = 1.07$.

It is hypothesised that under careful saturation, a higher modulation depth SESAM optimised for 2.1 μm may support significantly higher pulse energies and pulse peak powers.

Chapter 5

Q-Switching and Continuous-Wave Mode-Locking of a Ho:YAG Laser

5.1 Introduction

This chapter presents the first reported mode-locking of a Ho:YAG slab laser using a SESAM. The approach reported here integrates the SESAM into a resonator designed to facilitate mode-locking and mitigate Q-switching instabilities. The onset of QML and CML is observed, with a discussion of QML state and a characterisation of the CML regime undertaken. This includes a direct follow-up and comparison with pulse characteristics identified in Chapter 4. While SESAM mode-locking in this gain media serves as the first of its kind, this work also showcases successful mode-locking at doping concentrations significantly lower than those typically employed in mode-locking experiments. This presents a promising pathway for power-scalable mode-locking where up-conversion and quenching results in undesirable thermal behaviour and limited efficiencies.

Chapter 4 covered the influence of modulation depth on Q-switched pulse dynamics. It was concluded that an increased modulation depth results in higher peak powers, offering favourable conditions for spectral broadening in nonlinear media — a desirable characteristic for mode-locking. However, recall that saturable absorbers used to initiate mode-locking are susceptible to the Hopf bifurcation outlined in Equation (2.40). This principle asserts that as

the modulation depth increases, so does the likelihood of Q-switching instabilities. Therefore, despite the promising peak powers and spectral qualities generated by the $\Delta R = 18\%$ SESAM, the $\Delta R = 1.2\%$ SESAM is chosen as the best candidate to achieve mode-locking while avoiding Q-switched behaviour.

The cavity design process is described in Section 5.2. While maintaining maximum spatial overlap between the pump and the laser, the resonator also requires a sufficient number of longitudinal modes in order to generate ultrashort pulses. To achieve optimal pulse shaping and prevent temporal stretching, the layout is structured to allow for the tuning of both dispersion and spectral broadening. As a preliminary step, CW lasing of the cavity is demonstrated and characterised using a HR mirror in place of the SESAM. This serves as a reference for the wavelengths and efficiencies attainable with the mode-locking cavity design.

QML and CML regimes are achieved through tuning the SESAM alignment, as outlined in Section 5.3. The laser dynamics are discussed and characterised.

The results and discussion are summarised in Section 5.4.

5.2 Resonator Configuration

5.2.1 Laser Cavity Design and Modelling

The gain medium used is the 2 x 3 x 40 mm Ho:YAG slab doped at 0.7 wt.%, which is mounted, and cooled in the same configuration described in Chapter 4. The Ho:YAG is then pumped by the thulium-fibre laser developed in Chapter 3. This operates at a centre wavelength of 1906.75 nm which closely overlaps with the peak absorption of the gain media at 1906.90 nm. The pump focussing optics are maintained from the previous chapters.

The cavity is designed using the ABCD ray matrix algorithm for simulating optical elements and is presented in Figure 5.1.

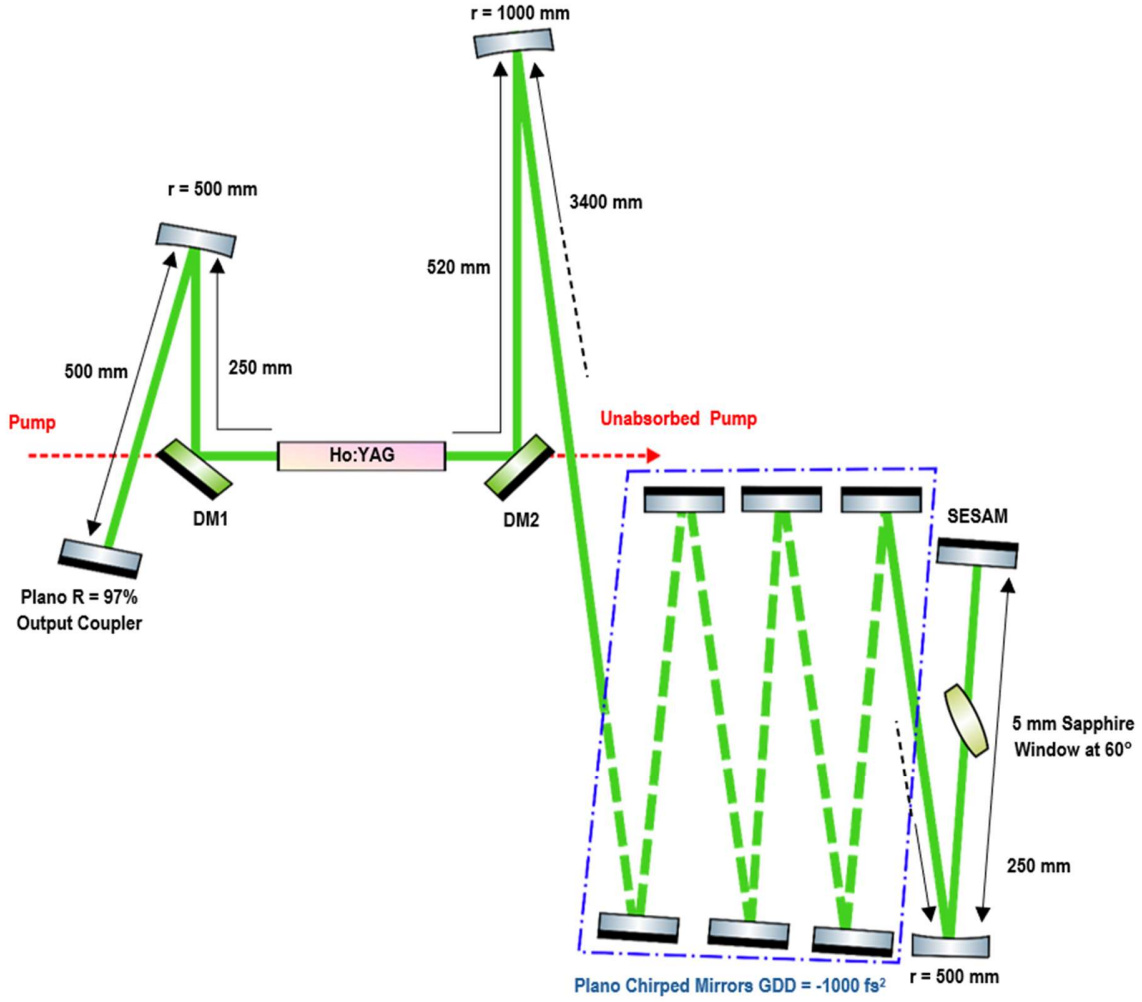


Figure 5.1: Resonator schematic for the SESAM mode-locking of the Ho:YAG laser. DM1 and DM2: Dichroic mirrors. The optional array of chirped mirrors for dispersion tuning is outlined in blue. A sapphire window is positioned between the r = 500 mm mirror and the SESAM.

The physical cavity length of this design is 4960 mm. Assuming the refractive index of YAG (n_1 = 1.799) closely approximates that of Ho:YAG, the optical path length is calculated using the length of the Ho:YAG slab (L_1), and the propagation distance through air (L_2) which has a refractive index of n_2 [2]. This value is used to determine the round-trip time. Taking the inverse of this time yields the round-trip frequency, which corresponds to the CML repetition rate. This calculation indicates a theoretical repetition rate of 30.03 MHz, as summarised in Equation (5.1).

$$\frac{c}{2\left(L_1(n_1)+L_2(n_2)\right)}=\frac{3.00\times10^8}{2((0.500+0.250+0.520+3.400+0.250)(1.0003)+0.04(1.7990))}=30.03\ MHz \quad (5.1)$$

The influence of the sapphire window on the theoretical repetition rate is considered to be negligible.

To minimise astigmatism, the angle of incidence for each mirror is kept below ~ 7°. Nonetheless, this practice introduces a disparity between the tangential and sagittal planes. The round-trip ABCD matrix for each is given by Equation (5.2) and Equation (5.3).

$$M_{\mathrm{T}}=\begin{bmatrix}-12.1 & -3.11\\ 49.5 & 12.7\end{bmatrix} \quad (5.2)$$

$$M_{\mathrm{S}}=\begin{bmatrix}-16.1 & -3.99\\ 63.6 & 15.7\end{bmatrix} \quad (5.3)$$

These yield the stability parameters presented in Equation (5.4) and Equation (5.5).

$$P_{\mathrm{T}}=\frac{A_{\mathrm{T}}+D_{\mathrm{T}}}{2}=0.313 \quad (5.4)$$

$$P_{\mathrm{S}}=\frac{A_{\mathrm{S}}+D_{\mathrm{S}}}{2}=-0.180 \quad (5.5)$$

Thus, the resonator design satisfies the stability criteria of $-1<P<1$ for both the tangential and sagittal planes.

The straight-through resonator cavity configuration allows for the pump entry and exit through two dichroic mirrors set at 45° to the optical path of the pump. At this angle, the pump light experiences a reflectivity of $R<1.0\%$ while 2097 nm light experiences a

reflectivity of $R > 99.9\%$. The placement of these dichroic mirrors creates two distinct cavity arms.

As shown in Figure 5.1, the cavity arm defined by DM1 ultilises a HR mirror with a radius of curvature $r = 500$ mm to ensure adequate mode-matching between the pump and resonator. The beam is then directed through a plano output coupler with a reflectivity of $R = 97\%$.

This output coupling fraction is frequently adopted in mode-locking attempts since it produces high enough intracavity powers to counter Q-switching instabilities and facilitate adequate SESAM fluence while maintaining significant average output powers. The high intracavity powers also enable the generation of additional spectral bandwidth and positive chirp through SPM, which is often advantageous when balanced with negative dispersion.

In the cavity arm defined by DM2, a HR mirror with a radius of curvature $r = 1000$ mm is positioned to direct the beam along an extended optical path towards another $r = 500$ mm HR mirror. This setup results in a focussed beam on the SESAM, which serves as the cavity end mirror. Between the $r = 1000$ mm and $r = 500$ mm mirrors, provisions are made for integrating up to 6 chirped mirrors, each with a *GDD* of -1000 fs² per pass, as shown in Figure 5.1. The inclusion of the chirped mirrors depends on the peak powers obtained, which directly influences the amount of spectral broadening generated in the YAG, necessitating the need for more or less dispersion to compensate. Regardless of how many chirped mirrors are in use, the optical path distance between the $r = 1000$ mm and $r = 500$ mm mirrors is adjusted to always ensure a total cavity length of 4960 mm.

An uncoated 5 mm sapphire window is placed on a translation stage along the beam path between the $r = 500$ mm mirror and the SESAM, oriented at Brewster's angle of approximately 60°. This window, which has a high nonlinear refractive index as noted in Table 2.1, serves the dual purpose of acting as a polariser as well as introducing a tunable degree of nonlinear response as it is scanned through the focal point of the beam. It is noted that while this SESAM is specified to be free of polarisation dependence, potential interference between different polarisations may contribute to unwanted mode-locked instabilities and noise.

Although the amount of dispersion required to achieve the shortest and most stable pulses can be theoretically calculated, an experimental approach is taken here by monitoring the pulse dynamics as the sapphire window is scanned through the beam focusing on the SESAM. The nonlinear phase shift can then be inferred through the peak powers obtained.

An estimation of the intracavity beam radius is extracted from reZonator and presented in Figure 5.2.

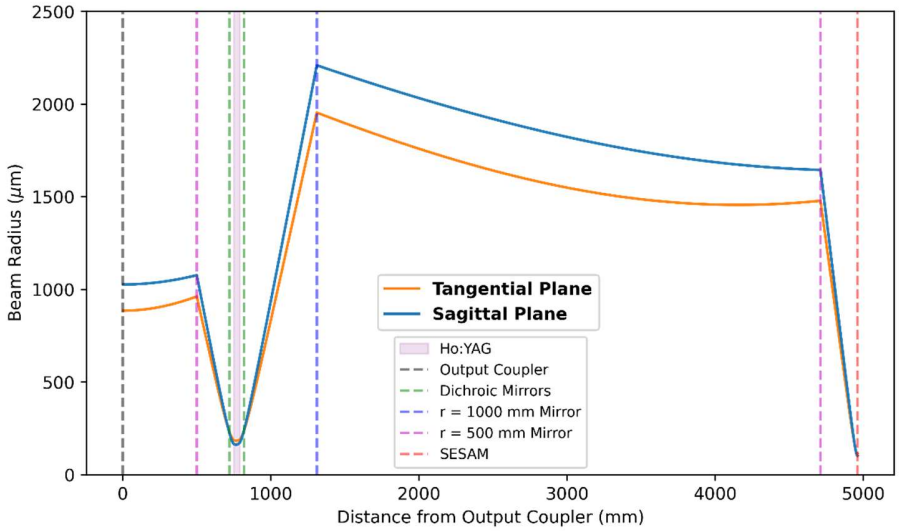


Figure 5.2: Tangential (orange) and sagittal (blue) beam radius within the mode-locked Ho:YAG resonator as a function of the distance across the cavity from the output coupler.

The beam radius at the centre of the crystal is estimated to be ~ 185 µm in the tangential plane, and ~ 160 µm in the sagittal plane, corresponding to a radius mismatch of only ~ 15 µm and ~ 40 µm between the pump and resonator modes, respectively. The focus at the SESAM is estimated to have a beam radius of ~ 110 µm in the tangential plane and ~ 100 µm in the sagittal plane. This chosen beam size on the SESAM is consistent with similar mode-locking designs [3, 4].

Although the stability is greatest with the element spacing specified in Figure 5.1 and Figure 5.2, the fluence on the SESAM is able to be adjusted by changing the distance between the r = 500 mm mirror and the SESAM from 239 mm to 263 mm without disrupting the overall stability of the cavity. This modifies the beam size on the SESAM and in the centre of the crystal according to Figure 5.3, which will later be a necessary consideration.

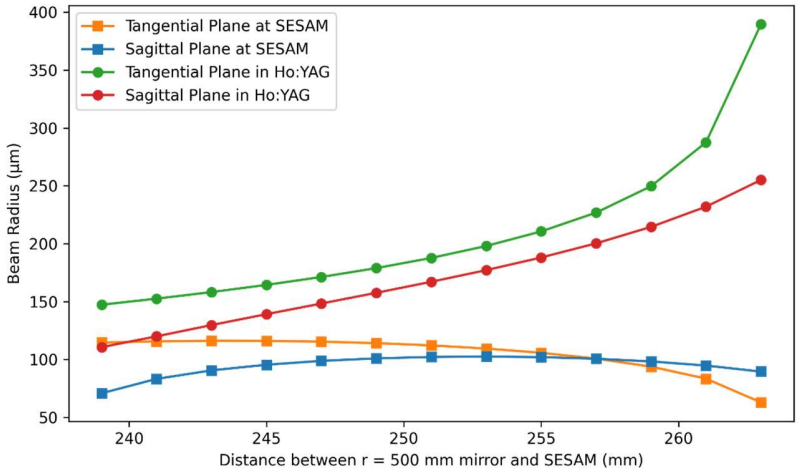


Figure 5.3: Tangential (orange) and sagittal (blue) beam radii at the SESAM and tangential (green) and sagittal (red) beam radii in the centre of the Ho:YAG slab as a function of distance between the r = 500 mm mirror and the SESAM.

5.2.2 Diagnostic Setup

The diagnostic setup presented in Figure 5.4 is used for the characterisation of the mode-locked dynamics.

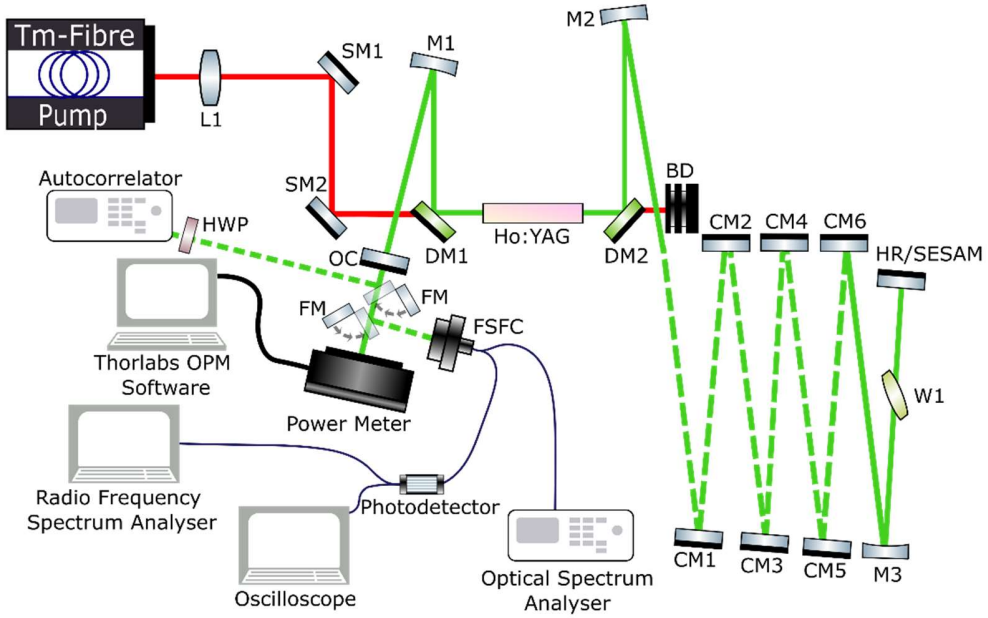


Figure 5.4: Laser resonator setup with the diagnostic arrangement used to characterise mode-locked Ho:YAG dynamics. L1: f = 25.5 mm aplanatic lens. SM1 and SM2: Steering mirror. DM1 and DM2: Dichroic mirror. OC: Output coupler. BD: Beam dump. FM: Flip mount installed with a CaF_2 wedge. M1 and M3: r = 500 mm mirror. M2: r = 1000 mm mirror. W1: 5 mm sapphire window at 60°. HWP: Half-wave plate. CM1-6: -1000 fs^2 chirped mirrors.

For the characterisations presented in this chapter, all optical power measurements are taken with a Thorlabs S425C-L Thermal Power Meter which is interfaced with the Thorlabs OPM software through a Thorlabs PM101 Thermal Power Sensor Interface. Power measurements are sampled at 180 Hz with a resolution of 100 μW, allowing for time-averaging of collected data through the OPM software.

An $R \sim 10\%$ CaF_2 wedge is mounted in a flip mount (FM). When flipped into the optical path, this redirects ~ 10% of the laser output into an $f = 11$ mm D-ZK3 glass aspheric lens which focuses the beam into a single mode fibre patch cable, forming a free-space to fibre coupler. The output of this cable can be switched between a photodetector and a YOKOGAWA AQ6375 OSA which operates at a resolution of 0.05 nm.

The photodetector used is a 6 GHz InGaAs/InP Discovery Semiconductors Photoreceiver which converts the optical signal to a voltage output. Subsequently, it is linked to either an InfiniiVision DSO6102A Digital Storage Oscilloscope which has a bandwidth of 1 GHz and a sampling rate of 4 GSa/s or a Rohde & Schwarz FSP-30 Radio Frequency Spectrum Analyser. This analyser has a resolution bandwidth of 3 kHz and a video bandwidth of 10 kHz, resulting in sweep times automatically set by the RFSA, on the order of minutes. This configuration provides ample resolution for measuring content between harmonics spaced in the MHz range.

A secondary FM installed with an $R \sim 10\%$ CaF_2 wedge is used to direct the beam through a half-wave plate polariser into a PulseCheck 150 MIR Autocorrelator. For a linearly polarised input, this operates with a resolution of 6 fs up to a maximum measurable pulse width of 35 ps.

5.2.3 Extended Cavity Continuous-Wave Lasing Characterisation

Prior to pulsed operation, a benchmark characterisation is conducted for the CW lasing state by using a plano HR mirror with a reflectivity of $R > 99.5\%$ at 2097 nm in place of the

SESAM. This is done to ensure the cavity design and alignment supports stable lasing and it is used to determine the maximum attainable efficiency as well as the favoured emission wavelengths.

At each increment of driving current, the laser is allowed a 5-minute period to reach equilibrium with the thermal load before any measurements are recorded. 21,600 samples of optical power are then taken over the course of 120 seconds before the driving current is increased and the process is repeated. The mean and standard deviation of each dataset is then extracted and plotted against the output power data for the thulium-fibre laser pump collected in Chapter 3. This yields a slope efficiency of 15.55%, with a lasing threshold of approximately 2.1 W, as shown in Figure 5.5. On average, the standard deviation is only ~ 0.9% of the mean power for each unit of driving current, which demonstrates excellent output power stability.

While the slope efficiency is significantly lower than the values obtained for CW lasing in the previous chapter, this is expected due to the much higher reflectivity output coupler.

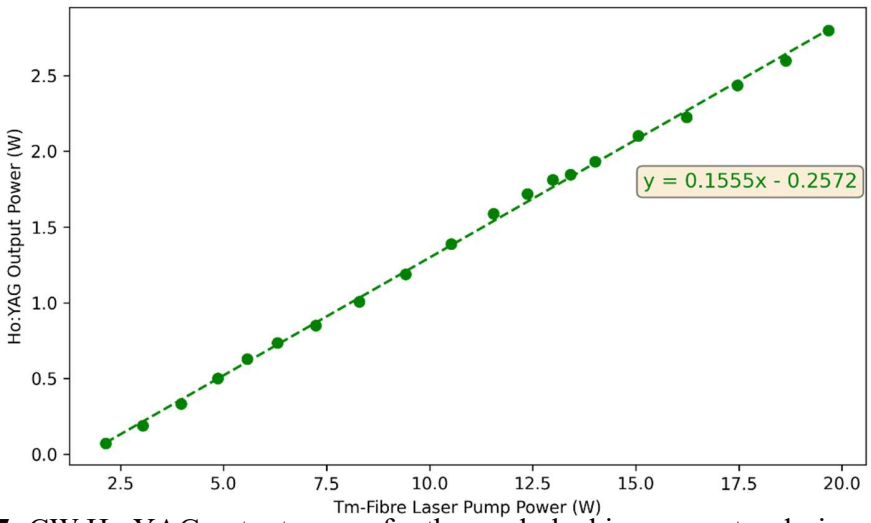


Figure 5.5: CW Ho:YAG output power for the mode-locking resonator design as a function of pump power, with a regression line indicating a slope efficiency of 15.55%.

Figure 5.6 displays the optical spectrum of the Ho:YAG CW laser measured by the OSA. This reveals the presence of two emission lines at 2090.30 nm and 2096.45 nm with both peaks measuring a -3 dB spectral FWHM of ~ 0.10 nm, demonstrating consistency with the

CW spectrum obtained in Chapter 4. The location of these peaks remains unchanged across all pump powers.

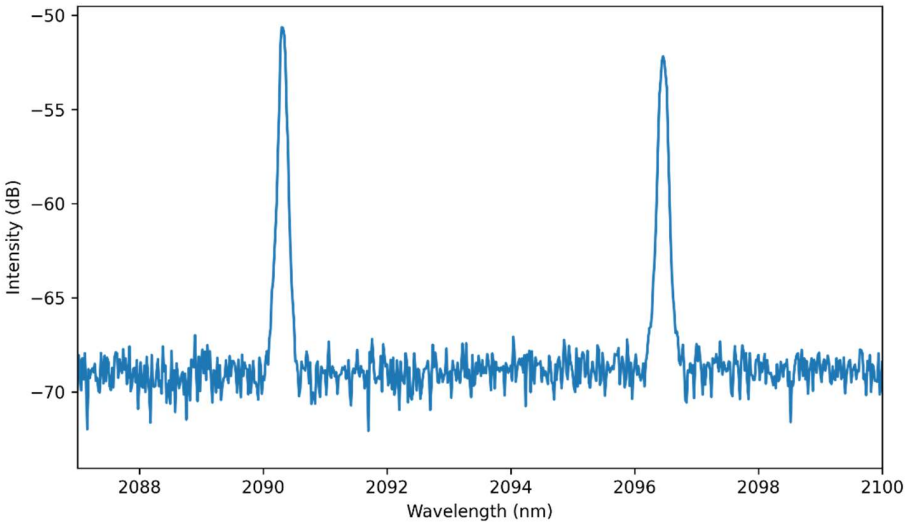


Figure 5.6: CW Ho:YAG optical spectrum for the mode-locking resonator design. Two emission lines are present, centred at 2090.30 nm and 2096.45 nm.

5.3 SESAM Mode-Locking Results and Discussion

5.3.1 Preamble

A challenge in obtaining stable, bandwidth-limited, mode-locked pulses in a bulk laser system is often found in balancing dispersion and nonlinearities such that pseudo-soliton pulse shaping can be established. Although it doesn't necessarily pose a constraint in achieving mode-locked pulses as shown by Wang *et al.*, precautions are taken such that additional SPM and negative *GDD* may be introduced to examine their impact on pulse duration [5].

Including a tunable source of dispersion or nonlinear phase shift is common in many mode-locking experiments. The work on Ho:YAG TDLs by Tomilov *et al.* demonstrates successful spectral broadening by scanning a sapphire plate through a cavity focus, an approach adopted

by this research [6, 7]. Tyazhev *et al.* proposes an alternative method, instead using a pair of prisms not only to offer tunable dispersion but also to be utilised as a source of nonlinearity [8].

While these approaches provide valid solutions when carefully integrated, the choice of a 40 mm long slab in this study creates added complexity. Where the dispersion and nonlinearities experienced through a thin disk or short gain media are often considered negligible, the 40 mm slab is a significant source of not only negative dispersion, but also nonlinearity [9, 10]. This effect is proven, as it was seen to manifest as spectral broadening in Chapter 4 under the high Q-switched pulse peak powers, broadening the optical spectrum from a FWHM of 0.10 nm to 0.45 nm.

While the dispersion can be easily calculated, the effect of nonlinearity is dependent on the pulse peak powers obtained, limiting the determination of a corresponding phase shift to be found experimentally. The *GDD* contributed by the Ho:YAG and the 5 mm sapphire window placed at 60° to the optical path is presented in Equation (5.6) and Equation (5.7). The values used for *GVD* are provided by Refractiveindex.info Database of Optical Constants, with the *GVD* for YAG assumed to closely approximate the 0.7% doped Ho:YAG [2].

$$GDD_{Ho:YAG} = (length)(GVD_{YAG}) = (40)(-77.79) = -3111.6\, fs^2 \qquad (5.6)$$

$$GDD_{Al_2O_3} = (length)\left(GVD_{Al_2O_3}\right) = (5.76)(-145.27) = -836.8\, fs^2 \qquad (5.7)$$

The *GDD* contributions from the mirrors and SESAM are considered negligible. Hence, the round-trip *GDD* of the resonator is calculated to be -7896.8 fs^2, tunable up to -19896 fs^2 in increments of -2000 fs^2 with the inclusion of all six chirped mirrors.

5.3.2 Q-Switched Mode-Locking

In the scope of the research, the primary regimes under examination are pure Q-switching, as seen in Chapter 4, and CML. Thus, while some points of interest of the QML regime are noted, a full characterisation of its performance is not conducted.

In the absence of the chirped mirrors and sapphire window, QML is achieved when the SESAM is moved through the region described by Figure 5.3. However, even minor adjustments to the SESAM placement result in significant variations to both the efficiency and pulse characteristics. Consequently, the optimisation of any specific pulse regime is largely constrained by the precision of the SESAM mount.

Under the maximum pump power of ~ 19.7 W, lasing up to 1.1 W is observed for two distinct QML regimes. These regimes are differentiated by the temporal duration of the Q-switched envelope, with one regime surpassing the other by an order of magnitude. Figure 5.7 illustrates the pulse envelope and pulse trains corresponding to each of these regimes.

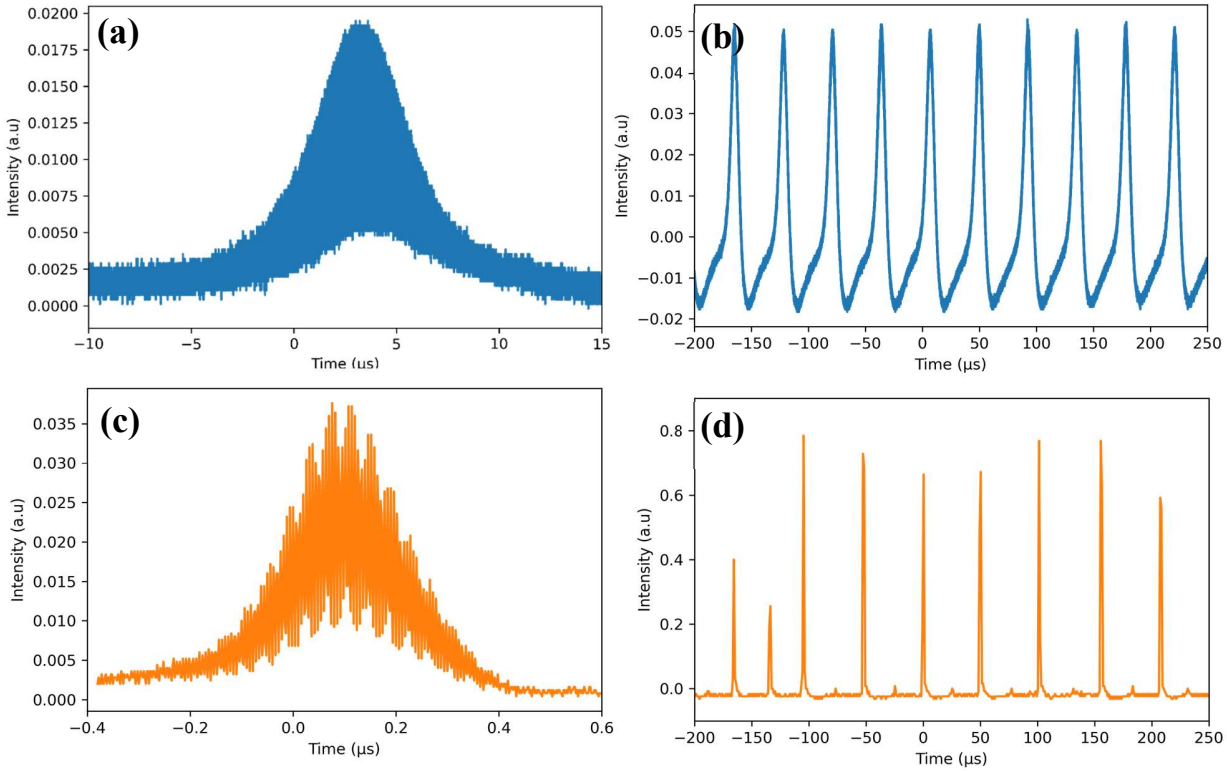


Figure 5.7: Q-switched envelope of the larger scale modulation QML regime (a) and the shorter scaler modulation QML regime (c), accompanied by their respective pulse trains illustrated in (b) and (d).

Utilising curve-fitting techniques, the modulation envelopes exhibit a close resemblance to Gaussian pulses, resulting in temporal FWHM values of 5.73 µs and 260 ns, respectively. The 5.73 µs QML regime aligns with the Q-switched pulse durations achieved in Chapter 4 using the same SESAM. On the other hand, the 260 ns QML regime resembles the pulse durations obtained by the ΔR = 18% SESAM, despite being produced by an absorber with 15 times less modulation depth. While a cavity length of only ~ 20 cm was used in Chapter 4, significantly shorter pulse envelopes are obtained using the same SESAM with a ~ 5 m cavity length here, albeit within a QML regime.

Figure 5.7 (b) presents the pulse train for the 5.73 µs QML regime, which has a mean repetition rate of 23.66 kHz. Concurrently, Figure 5.7 (d) presents the pulse train for the 260 ns QML regime, with a mean repetition rate of 24.04 kHz. From these plots, it is evident that the 5.73 µs QML regime exhibits a high level of stability with a *RIN* of 2.56%, unlike the 260 ns QML regime which has a *RIN* of 38.9%. This heightened *RIN* contributes to variability in pulse intensity, directly impacting the speed at which the quality factor is switched and consequently increasing the variability in repetition rate. This is seen in Figure 5.7 (d), with lower intensity pulses demonstrating higher repetition rates, while high-intensity pulses exhibit considerably lower repetition rates. It is noted that at the equivalent pumping power in Chapter 4, Q-switched pulses with a repetition rate of 189 kHz were obtained. Thus, in the case of the 260 ns QML regime, not only are shorter pulse durations produced, but also at much lower repetition rates. This yields potential for a QML envelope to demonstrate significantly higher pulse energies and peak powers than any Q-switched pulse generated by the same SESAM.

This prompts further investigation into the 260 ns QML regime. Using Equation (2.42) and Equation (2.43) from Chapter 2, the pulse energies and peak powers are calculated to be 45.8 µJ and 165 W, respectively. These values closely align with the pulse energies obtained with the same SESAM in Chapter 4 at 46.5 µJ but significantly exceeds the peak power of 40.0 W. Notably, a lower output coupling of 3% is utilised in this chapter, leading to intracavity peak powers of 5500 W. This surpasses the 3100 W intracavity peak powers obtained through Q-switched operation of the ΔR = 18% SESAM model which demonstrated significant spectral broadening.

The optical spectrum is measured and presented in Figure 5.8.

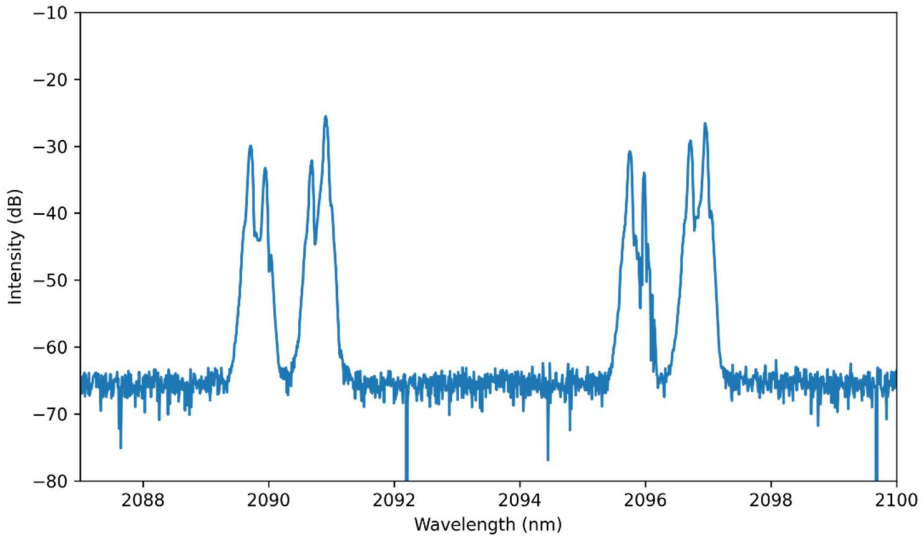


Figure 5.8: Ho:YAG optical spectrum in the QML regime, demonstrating spectral broadening in the form of split emission lines.

Figure 5.8 reveals a deviation in the optical spectrum from previous measurements. While additional spectrum has indeed been generated, the spectrum is instead spread out over 4 primary emission lines, arranged in pairs either side of the CW lasing emission line locations at 2090.30 nm and 2096.45 nm. Moderate variations in the optical spectrum are also seen between successive OSA traces taken. While the peak-to-peak intensity variations observed in the pulse train will have some influence on this, the nature of this spectrum is primarily attributed to the excitation of higher-order transverse and polarisation modes as well as etalon effects in the cavity.

In the confines of the stability condition, the placement of the SESAM significantly influences the mismatch between the pump and resonator modes, as illustrated in Figure 5.3. When this mismatch is large, the probability of lasing across additional transverse modes rises. As shown in a practical demonstration by Ezekiel *et al.*, the introduction of higher-order transverse modes causes a "splitting" of the single-mode emission lines, which may also result in temporal oscillations in spectral intensity [11]. The effect described and demonstrated by Ezekiel *et al.* closely resembles what is observed in the OSA traces from the QML regime. Optimising single transverse mode operation as well as conducting a full characterisation of the QML regime is left as future work.

In addition to QML, hybrid asymmetric pulse regimes are also observed depending on the cavity alignment and configuration, often consisting of a combination of QML and Q-switched envelopes simultaneously. While reaching considerable intensities on the photodetector, these regimes are highly irregular and undesirable. An example of such is presented in Figure 5.9.

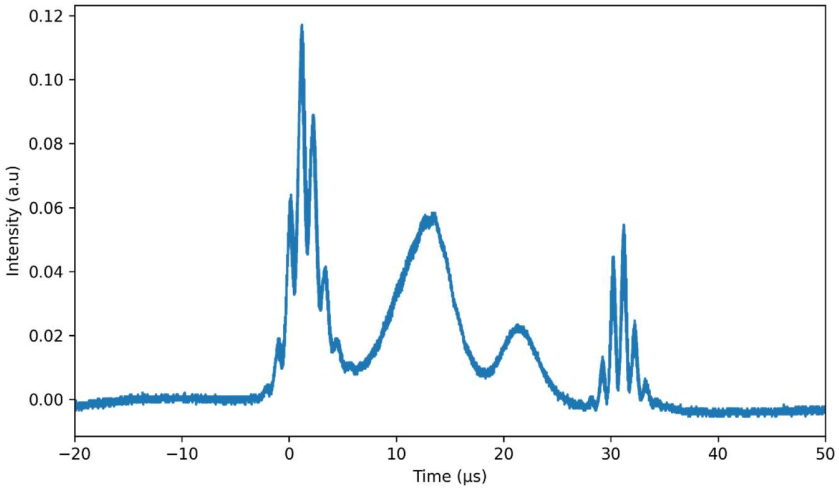


Figure 5.9: An example of the oscilloscope trace obtained for a highly irregular and asymmetric hybrid pulse regime in the Ho:YAG resonator.

5.3.3 Continuous-Wave Mode-Locking

Initially without the sapphire window and chirped mirrors in place, when the SESAM is positioned at the focal point of the r = 500 mm mirror, the lasing regime is observed to transition from CW to QML and eventually to CML with increasing pumping powers. As previously noted, the extensive cavity length makes optimisation for any one of these regimes difficult without further precision controls in place.

Following the procedure for time-averaged optical power measurements previously used, the average output power is recorded and plotted in Figure 5.10. A regression line is fitted, resulting in a slope efficiency of 6.71%, and the averaged pump powers corresponding to the transitions between pulse regimes are depicted on the plot.

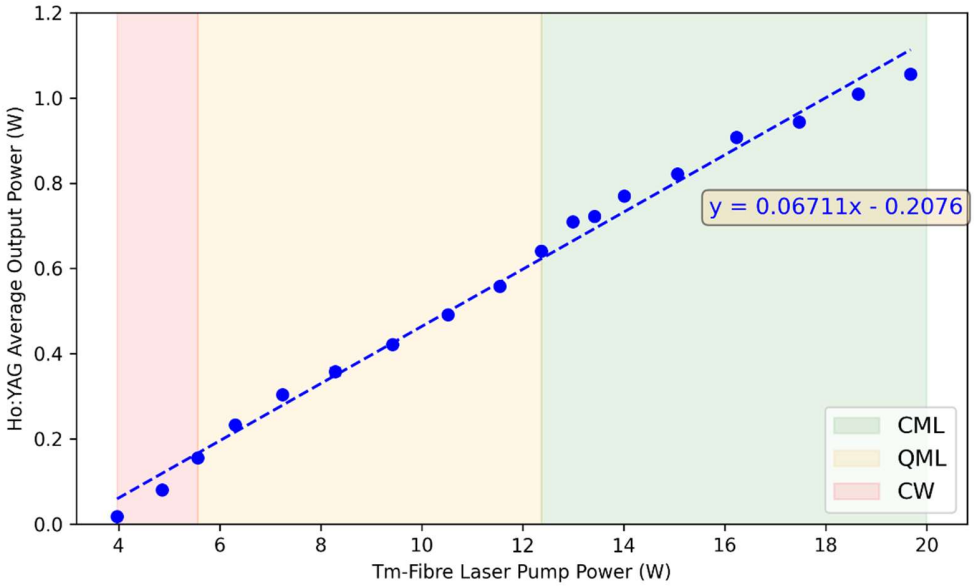


Figure 5.10: Ho:YAG average output power for CW (red), QML (yellow), and CML (green) regimes as a function of pump power. The regression line indicates a slope efficiency of 6.71%.

This plot is consistent with the progression of pulse regimes demonstrated across similar mode-locking experiments [12, 13]. Furthermore, it reinforces Equation (2.40) from Chapter 2 which suggests that an increase in intracavity pulse energy may overcome Q-switching instabilities.

A typical oscilloscope trace of the pulse train at the maximum average output power of 1.05 W is recorded, along with an enlarged pulse train featuring 5 pulses, as displayed in Figure 5.11 (a) and Figure 5.11 (b), respectively. These traces highlight the continuous nature of the pulse regime, showcasing the lack of large-scale modulations that dominated the QML regime.

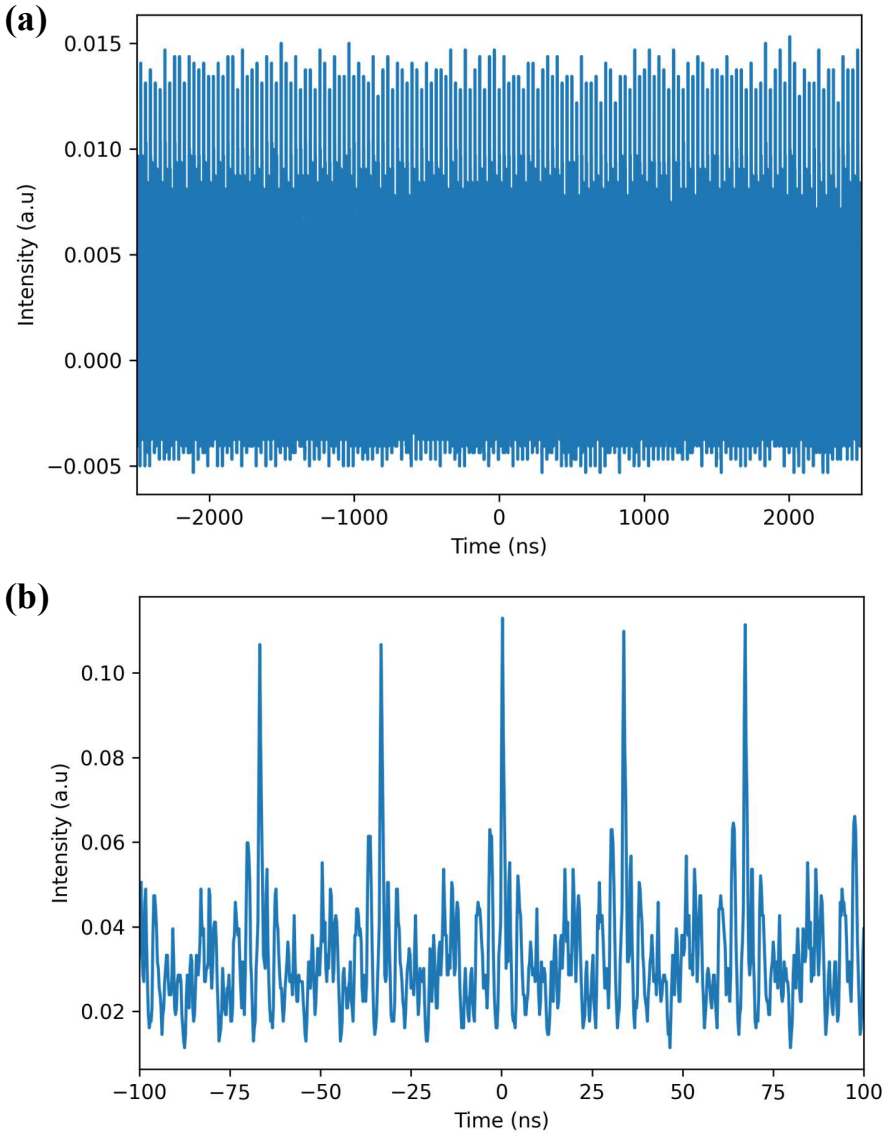


Figure 5.11: A typical oscilloscope trace of (a) the Ho:YAG CML train pulse, and (b) an enlarged pulse train featuring 5 pulses.

Although distinct mode-locked pulses are evident, there are significant periodic features and power fluctuations between pulses. While this is undesirable, other CML results in literature report similar levels of inter-pulse power fluctuations [14-16]. With higher precision control, adjustments to the cavity alignment and the SESAM positioning could drastically reduce these fluctuations. Additionally, the water cooling used in the SESAM mount introduces micro-vibrations into the system. These vibrations primarily manifest as timing jitter as the cavity length, and therefore the FSR fluctuates. However, the fluctuating alignment, FSR and SESAM saturation due to these vibrations also introduces amplitude noise. Thus, employing

thermoelectric-based cooling instead of water cooling may aid in reducing inter-pulse power. Nevertheless, even under ideal mode-locking conditions, the simulation used to produce Figure 2.7 in Chapter 2 illustrates that inter-pulse powers are inversely proportional to the number of longitudinal modes. Additionally, similar periodic features are reported from dual-wavelength mode-locked lasers. Hence, the inter-pulse features are attributed to an unoptimised alignment, a low number of longitudinal modes, and potential dual-wavelength operation. This is to be further explored upon characterisation of the optical spectrum.

Figure 5.10 (a) displays a mean repetition rate of 29.92 MHz across 149 pulses, with a standard deviation of 0.11 MHz, and a peak-to-peak *RIN* of 4.92%. This closely aligns with the theoretical repetition rate of 30.03 MHz calculated previously in Equation (5.1). Although the standard deviation of the repetition rate suggests minimal timing jitter, and the *RIN* indicates only minor peak intensity fluctuations, these measurements are limited by the sampling rate of the oscilloscope and the rise time of the photodetector. Therefore, a more comprehensive assessment of stability is warranted using the radio frequency spectrum analyser.

The RF spectrum is measured using a resolution bandwidth (RBW) of 100 kHz and presented in Figure 5.12.

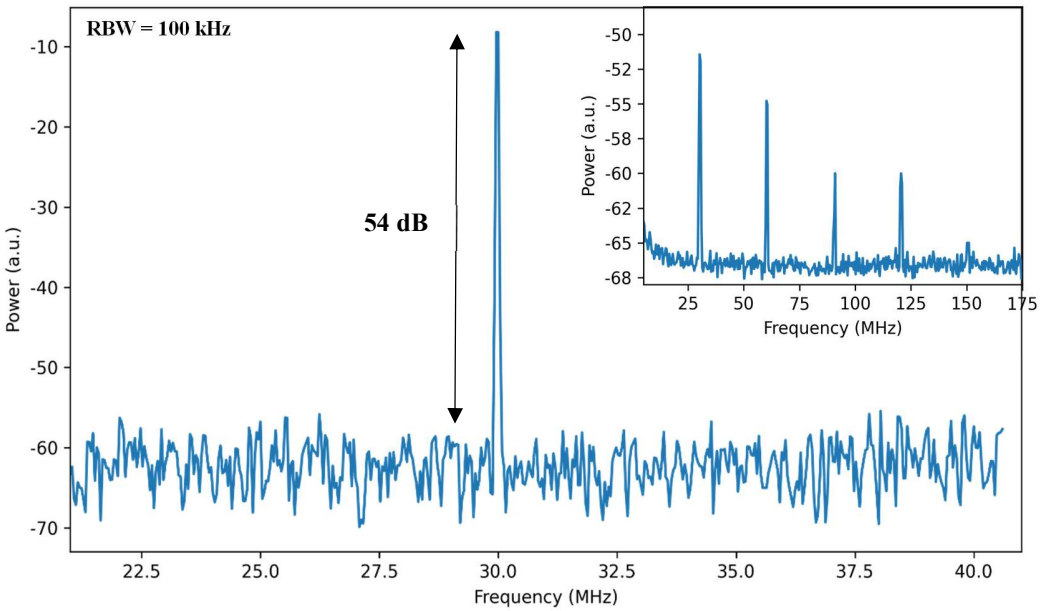


Figure 5.12: RF spectrum of the mode-locked Ho:YAG laser, covering a range of 20 MHz centered around the fundamental frequency of 29.96 MHz. The spectrum was measured using a RBW of 100 kHz. The inset shows a spectrum spanning 180 MHz, encompassing the generated harmonics of the fundamental frequency.

The fundamental frequency is observed at 29.96 MHz, closely matching the repetition rate computed from the oscilloscope trace and the round-trip frequency calculated in Equation (5.1). The SNR is shown to be ~ 54 dB, which is considered indicative of a stable mode-locked signal [17]. However, the inset in Figure 5.12 reveals a strong amplitude modulation across the harmonics, leading to the complete extinction of harmonic signals after only a limited number. This largely stems from amplitude noise, which is expected due to the amplitude fluctuations present in the oscilloscope trace in Figure 5.11, resulting in a fast dB roll-off across the harmonics [18].

An autocorrelation trace of the pulse profile is then attempted, but ultimately unsuccessful. The beam path in the second cavity arm is redirected to pass through 1 to 6 of the chirped mirrors before reaching the SESAM. The sapphire window is also placed in front of the SESAM at a Brewster's angle and scanned across the focus of the beam for each configuration. Despite being able to achieve a similar CML regime, no autocorrelation trace is attainable. Thus, it is concluded that the pulse durations exceed 35 ps, which corresponds to the maximum measurable pulse durations of the autocorrelator.

Although the pulse duration is unable to be directly measured, in the case of ideal mode-locking, an estimate may be obtained for the bandwidth-limited pulse duration by assessing the spectral content. The OSA is used to measure the optical spectrum of the output, which is shown in Figure 5.13.

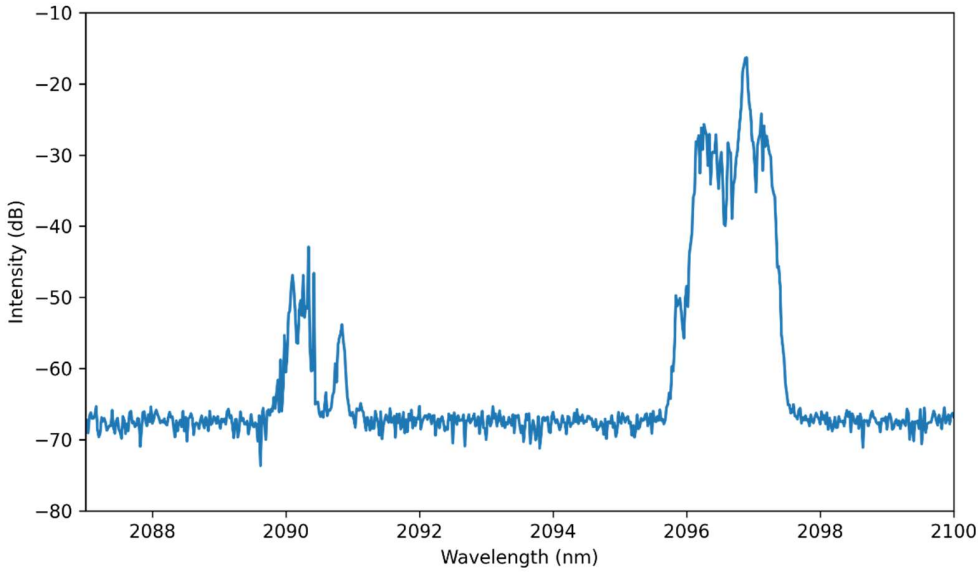


Figure 5.13: Ho:YAG optical spectrum in the CML regime, demonstrating dual wavelength mode-locking as well as spectral broadening.

This plot reveals significant spectral broadening in the lower intensity regions of the optical spectrum across the emission lines centred at 2090.35 nm and 2096.20 nm. While this still indicates significant intracavity peak powers, much of the spectral intensity is concentrated within the narrow linewidth defined by the peak at 2096.90 nm. The FWHM of this peak is computed to be ~ 0.10 nm, which does not exceed the spectral bandwidth of the CW lasing state. It is also noted that the addition of the sapphire window does not contribute to any significant spectral broadening. This is attributed to the lower nonlinear refractive index of sapphire relative to YAG as indicated in Table 2.1. This prompts the need for higher peak powers or a tighter beam focus within the sapphire to generate additional spectra.

Moreover, the presence of two emission lines combined with the oscilloscope trace and RF spectrum suggests synchronously propagating mode-locked pulses. Although two mode-locked pulses at different wavelengths are present, the repetition rate is measured to be the inverse cavity length period, thus confirming that the two mode-locked pulses at different wavelengths are synchronised and temporally overlapped to a certain extent. This behaviour is due to the saturable absorber. While the two wavelengths are expected to walk-off under the influence of dispersion, the loss generated by the saturable absorber continuously removes the part of the pulse that has walked off and hence effectively binds the wavelengths together [19].

Consequently, as reported by other synchronised dual-wavelength mode-locking experiments, a frequency beating phenomenon emerges between the two wavelengths [20-22]. This results in a 0.40 THz (2.5 ps) amplitude modulation across the pulse profile which corresponds to the frequency variance between the two centre wavelengths. The intensity of this modulation is highly dependent on the spectral intensity ratio as well as the pulse duration and frequency difference [20]. While not typically associated with mode-locked sources, dual wavelength operation offers various potential applications including frequency difference generation, pump-probe measurements, remote sensing, single cycle optical wave synthesis, THz sources, and dual-comb spectroscopy [23, 24].

With the spectral FWHM, Equation (2.32) is used to calculate the resonator free-spectral-range to be 443 fm, which indicates the support of ~ 248 longitudinal modes within the cavity. Using Equation (2.6) and assuming a Gaussian pulse shape, the estimated bandwidth-

limited pulse duration is computed to be 58.8 ps provided all modes are in phase, far exceeding the capability of detection with the model of autocorrelator. Furthermore, the dependency on initial pulse duration expressed by Equation (2.16) indicates that at 58.8 ps, a *GDD* of -10000000 fs^2 would be required to change the pulse duration by even 1 ps. Hence, although the tunability range of -7896.8 fs^2 to -19896 fs^2 exceeds that of most bulk mode-locking systems, it has a negligible effect on pulse durations of this length.

Using the measured average power, repetition rate and the estimated pulse durations, Equation (2.42) and Equation (2.43) indicate pulse energies of 35 nJ and pulse peak powers of 559.2 W. While this implies intracavity peak powers of ~ 18 kW, Figure 5.11 shows that much of the optical power is distributed as amplitude fluctuations rather than concentrated purely in the pulses. Thus, the true values of pulse energy and pulse peak powers are likely to be significantly lower, making the corresponding nonlinear phase shift unable to be calculated accurately.

5.4 Chapter Summary

This chapter successfully demonstrated the first reported SESAM mode-locking of crystalline Ho:YAG in both the QML and CML regimes. Synchronous dual-wavelength 30 MHz mode-locked pulses were produced at 2090.35 nm and 2096.20 nm with estimated pulse durations of 58.8 ps at an average power of 1.05 W, an SNR of 54 dB, and a slope efficiency of 6.71%. Significant low spectral-intensity spectral broadening was observed but did not effectively increase the spectral FWHM.

Although the cavity was configured to offer dispersion tuning through the integration of chirped mirrors, the pulse durations achieved were unable to be altered without impractical amounts of dispersion. Additionally, a sapphire window was moved throughout a cavity focus to spectrally broaden the pulses but was unsuccessful due to insufficient peak powers.

The results highlight the limitations imposed from a low doping concentration in the gain media. The narrow emission spectra resulting from this doping concentration led to long

pulse durations with insufficient peak powers to effectively generate additional spectra, thus limiting further reduction in pulse durations and increase in peak powers. Despite a 5 m cavity length, only 248 longitudinal modes were supported by the spectral FWHM. This, coupled with a need for further alignment precision control, made achieving the CML regime challenging. Additionally, oscilloscope traces and the RF spectrum indicated significant amplitude noise, stemming from the low number of longitudinal modes and an unoptimised alignment.

However, with the introduction of motorised kinematic mounts as well as an alternative means to generate spectrum broadening through SPM, this system shows strong potential to deliver high average power, mode-locked pulses at 2.1 μm with minimised thermomechanical stresses and upper-state lifetime quenching compared to a higher doped gain medium counterpart.

In addition to achieving the CML regime, two QML regimes were also successfully obtained. Although a comprehensive investigation of these states was not conducted, initial findings indicated Gaussian pulse envelopes as short as 260 ns at a repetition rate of 23 kHz. These results yield notably higher pulse energies and peak powers compared to any purely Q-switched pulse produced by the same SESAM. Hence, the QML regime presents a promising alternative to Q-switching for high pulse energies and peak powers, encouraging further exploration in future research.

Chapter 6

Conclusion

6.1 Introduction

This thesis presented the development of a low-doped Ho:YAG slab laser to explore the effectiveness of different resonator designs and SESAM modulation depths for Q-switched and mode-locked operation.

The key objectives addressed in this thesis included:

- The design, development, characterisation, and thermally induced wavelength tuning of a CW thulium-fibre source to align with the peak absorption wavelength of Ho:YAG.

- The design, development, and characterisation of various CW Ho:YAG laser cavities operating at 2.1 μm.

- The first demonstration and characterisation of Q-switching in a Ho:YAG laser using a SESAM.
- Exploration on the influence of modulation depth on Q-switched pulse dynamics in a Ho:YAG laser using a variety of SESAMs.

- The first demonstration of QML in a Ho:YAG slab laser using a SESAM.

- The first demonstration and characterisation of CML in a Ho:YAG slab laser using a SESAM.

To the best of our knowledge, the combined research objectives form the first investigation into the use of a SESAM to achieve short and ultrashort pulse generation in a Ho:YAG laser at 2.1 μm outside of TDLs and ceramics.

Chapter 1 provided an overview of short and ultrashort pulsed lasers operating in the 2.1 μm wavelength region. In addition to introducing the relevant nomenclature to the topic of research, applications for this technology in various fields were discussed, highlighting the motivation for this study. A literature review was presented which described similar experimental work and the proposed contribution to literature. Finally, the research objectives and outline for the thesis were detailed.

Chapter 2 presented the theoretical background underpinning the physics relevant to the experimental aims of the project. The primary focus was placed on the mechanisms responsible for driving passive pulse operation in bulk laser resonators, as well as how pulse characterisation assessments are conducted for various pulse regimes.

Chapter 3 reported the development of a thulium-fibre laser for use as a pump source for the Ho:YAG resonators described in the subsequent chapters. This involved the development and characterisation of the system, including measurements for optical power, optical spectrum, and beam quality. Furthermore, absorption spectroscopy was conducted on the Ho:YAG crystal to closely align the emission wavelength of the thulium-fibre laser with the peak absorption through thermal tuning of the FBGs.

Chapter 4 explored the development and characterisation of a CW Ho:YAG resonator, followed by the passive Q-switching by integration of a SESAM. Three SESAMs with different modulation depths were trialed. Through characterisation of pulse durations, repetition rates, pulse energies, pulse peak powers, and pulse train stabilities, a

comparison on the performance of each SESAM was reported and discussed. A relationship between different modulation depth and the pulse dynamics was established, indicating that higher modulation depths favour higher pulse energies and peak powers. Additionally, spectral broadening was observed and assessed under high pulse peak powers.

Chapter 5 investigated the capability for mode-locking using the Ho:YAG slab. Following the design and construction of a suitable resonator cavity, QML and CML were successfully demonstrated. Although a full characterisation of the QML lasing state was not undertaken, several pulse characteristics were compared with the findings of Chapter 4. These indicated that the QML state may offer a notable improvement in achieving higher peak powers and pulse energies compared to pure Q-switching. Finally, a characterisation and discussion were conducted for the CML lasing state. The results obtained indicated a significant limitation in attainable pulse durations due to the spectral constraints intrinsic to the low doping concentration in the Ho:YAG. Despite this, the successful demonstration of CML lasing in a low doped Ho:YAG slab showcased potential for a stable, high-average power, dispersion compensated system under a higher degree of SPM.

Chapter 6 provides a conclusion to the thesis, beginning with a summary of results presented in Section 6.2, followed by an outline of proposed future work in Section 6.3, and concluding with final remarks presented in Section 6.4.

6.2 Summary of Results

6.2.1 Continuous-Wave Laser Resonator Results

Throughout Chapters 3-5, numerous CW laser resonators were designed, assembled, and characterised. Initially, the thulium-fibre laser was developed which served as the basis for the Ho:YAG system. Two CW Ho:YAG resonators were assessed to serve as benchmarks

for evaluating the Q-switching cavity design and the mode-locking cavity design. Table 6.1 summarises the performance of each resonator.

Table 6.1: Continuous-wave laser resonator performance summary.

Gain Medium	Pump Source	Target Pulse Regime	Slope Efficiency (%)	Central Wavelength (nm)	Spectral FWHM (nm)	Beam Quality	Output Coupling Reflectivity (%)	Cavity Length (mm)	Maximum Optical Power (W)
Thulium-Fibre	793 nm Diode Laser	N/A	44	1906.9	0.05	1.07 (T)	7.4	2000	19.68
Ho:YAG	Thulium-Fibre Laser	Q-switching	53	2090.3 2096.6	0.10 0.10	1.06 (T) 1.05 (S)	70	180	9.12
Ho:YAG	Thulium-Fibre Laser	Mode-locking	16	2090.3 2096.5	0.10 0.10	N/A	97	4960	2.93

6.2.2 Q-Switched Results

Chapter 4 showcased three Q-switched Ho:YAG laser resonators, all employing a similar cavity design but featuring different SESAMs. Minor adjustments to the cavity were made to ensure sufficient SESAM saturation for assessing *RIN*. Table 6.2 presents the performance summary for each of these Q-switched resonators. While the ΔR = 1.2% and ΔR = 12% SESAMs exhibited the highest pulse energies and peak powers at their maximum average output powers, the ΔR = 18% SESAM did not. Therefore, two performance summaries are provided for the ΔR = 18% SESAM: one corresponding to the highest average output power and another corresponding to the highest pulse energies and peak powers.

While evaluating the spectral reflectance of each SESAM alongside the measured data, a distinct trend emerged: a higher modulation depth results in shorter pulses at lower repetition rates, consequently yielding higher pulse energies and peak powers. This result aligns well with the expected outcome based on the theory discussed in Chapter 2.

Table 6.2: Q-switched Ho:YAG laser resonator performance summary.

SESAM Modulation Depth (%)	Slope Efficiency (%)	Central Wavelength (nm)	Spectral FWHM (nm)	Beam Quality	Mean Pulse Duration (µs)	Mean Repetition Rate (kHz)	Mean Pulse Energy (µJ)	Mean Peak Power (W)	*RIN* (%)	Average Output Power (W)
1.2	50.1	2089.9 2096.9	0.07 0.09	1.06 (T) 1.05 (S)	1.09	189	46.5	40.0	3.01	8.80
12	26.12	2090.2	0.11	1.07 (T) 1.08 (S)	0.501	134	31.7	59.4	4.87	4.25
18	22.80	2090.1	0.46	1.06 (T) 1.07 (S)	0.0695 0.104	58.9 17.4	60.9 87.3	823 940	2.76	3.58 1.09

6.2.3 Mode-Locked Results

In Chapter 5, mode-locking was demonstrated across two QML regimes and one CML regime using the ΔR = 1.2% SESAM. The ΔR = 12% and ΔR = 18% SESAMs were not trialed as the Q-switch instability at these modulation depths makes mode-locking unfeasible. While certain key QML characteristics were measured, a comprehensive characterisation was beyond the scope of the research; however, characterisation was conducted for CML state. Table 6.3 provides the performance summary for each of these regimes. It is worth noting that although pulse energies and peak powers were computed for the CML lasing state, significant power manifested as amplitude noise between pulses. Therefore, the values listed are for equivalent ideal pulse stability with no power between pulses. Performing a separate measurement to obtain the pulse energy and peak power of an isolated pulse is left as future work.

Based on the measured pulse dynamics, it was concluded that the ML pulse durations, and consequently the peak powers, were restricted by the spectral FWHM, an inherent characteristic of the low doping concentration in the Ho:YAG.

Table 6.3: Mode-locked Ho:YAG laser resonator performance summary.

Pulse Regime	Slope Efficiency (%)	Central Wavelength (nm)	Spectral FWHM (nm)	Mean Pulse Duration	Mean Repetition Rate	Mean Pulse Energy (nJ)	Mean Peak Power (W)	SNR (dB)	Average Output Power (W)
QML	N/A	N/A	N/A	5.73 µs	23.66 kHz	46490 (envelope)	7.62 (envelope)	N/A	~ 1.10
		N/A	N/A	260 ns	24.04 kHz	45800 (envelope)	165 (envelope)		
CML	6.71	2090.3 and 2096.2	0.10	58.8 ps	29.96 MHz	35	559	54	1.05

6.3 Future Work

The research outcomes summarised in Sections 6.1 and 6.2 demonstrated successful completion of the thesis objectives outlined in Section 1.6. Additionally, numerous limitations which adversely affected the performance of each system were identified, as well as various avenues that merit further investigation.

Future efforts towards improving the work of this thesis are outlined in this section.

6.3.1 Improvements to the Pump Source

Chapter 3 detailed the development of a thulium-fibre laser to act as a pump source for the Ho:YAG resonators constructed in the following chapters. While the system developed served adequately, there are several modifications to be made which would improve the efficiency and longevity of the laser.

Absorption spectroscopy was conducted on the Ho:YAG crystal to thermally tune the wavelength of the thulium-fibre laser for optimal pump absorption. A similar approach could be employed for the diode laser. By utilising an objective lens, light from a supercontinuum source could be coupled into the thulium active fibre and measured to reveal the absorption characteristics of the optical fibre. Subsequently, the wavelength of the diode laser could be

measured as a function of chiller temperature, thereby identifying the optimal temperature to align with the peak absorption. This has the potential to enhance the overall efficiency considerably.

Furthermore, the FBGs utilised in this configuration were manufactured for a centre wavelength of 1906.43 nm, which happened to coincide with atmospheric absorption. To address this issue, the two FBGs were affixed to a Peltier module and heated to high temperatures, causing the grating spacing to shift and support wavelengths beyond this narrow spectral region. However, an optimal solution would be to use FBGs manufactured to operate closer to 1907 nm, not only to circumvent atmospheric absorption but also to better match the peak absorption of the Ho:YAG without requiring additional tuning. Alternatively, exploring individual and separate heating of the FBGs could manipulate the output wavelength. It is conceivable that the target wavelength could be attained without both FBGs needing excessive heating, thus aiding in prolonging the lifespan of the system.

Finally, incorporating a higher-power diode would be advantageous, along with the production of a fibre end cap. Fibre end caps facilitate even expansion of incoming light within the homogeneous material [1]. Upon being spliced onto a fibre, the end cap reduces the intensity at the air-to-glass interface of the fibre face, thereby averting potential damage from high-power sources and enhancing the output power stability [1].

6.3.2 Q-Switched Pulse Train Stability and Power Scaling

The most significant results garnered from the Q-switched resonators were obtained using the ΔR = 18% SESAM model, yielding high pulse energies and peak powers. While the pulse train exhibited impressive stability at high average powers, lower powers led to frequent pulse dropouts and significant intensity fluctuations due to insufficient SESAM saturation. By carefully designing the resonator and considering SESAM saturation modeling, placing a lens on a motorised translation stage could provide tunable fluence on the SESAM, given adequate mode-matching and resonator stability is upheld. This setup would not only ensure

stability at lower powers but also mitigate the risk of exceeding the damage threshold at higher powers by automatically adjusting the lens position to reduce SESAM fluence.

6.3.3 SESAM Optimisation for Q-Switching

Chapter 4 examined Q-switching capabilities using three SESAMs, of which only one was optimised for 2097 nm, while the remaining two were optimised for 2050 nm. Despite drawing satisfactory conclusions regarding the modulation depth and pulse dynamics relationship, the lower spectral reflectance at these wavelengths resulted in significantly lower efficiencies compared to the SESAM model optimised for 2097 nm. For future research, collaborative efforts could be initiated to produce custom-made SESAMs with parameters better aligned with project objectives.

6.3.4 Q-Switching Capabilities Across Output Couplers

As detailed in Chapter 1, Evans *et al.* demonstrated the variability of Q-switched pulse dynamics across a range of output couplers [2]. Building upon the research in Chapter 4, exploring pulse dynamics as a function of output coupling fraction could be a valuable extension. This endeavor has the potential to alter the fluence on the SESAM significantly without necessitating a change in focus, thereby facilitating the development of a more optimised resonator design.

6.3.5 Additional Spectrum Generation for Mode-Locking

A limitation in achieving ultrashort and stable mode-locked pulses was identified to stem from the low doping concentration within the Ho:YAG, restricting the total number of longitudinal modes supported by the cavity. This resulted in prolonged pulses with

inadequate peak powers to induce significant spectral broadening, alongside considerable amplitude fluctuations between pulses. While extending the cavity could increase the number of longitudinal modes, additional spectrum could also be generated through alternative methods. One option is to enhance the resonator beam focus within the Ho:YAG. While this would amplify the spectral broadening occurring in this material, a tighter focus raises the risk of optical damage and undesired thermal effects such as thermal lensing. Another option is to establish a separate focus within the cavity specifically for the sapphire window. Although the sapphire window did not contribute to any spectral broadening in this research, a tighter focus might be sufficient to initiate this effect. Alternatively, undoped YAG, with a nonlinear refractive index double that of sapphire, could be utilised.

6.3.6 Pulse Energy and Peak Power Measurements

The presence of amplitude noise in the mode-locked train made it impossible to accurately determine the pulse energy and peak power from the repetition rate, pulse duration, and average power. However, several techniques can be employed to address this issue.

One common option is to utilise a pulse picker, which is essentially an electrically controlled optical switch [3]. Typically, a pulse picker consists of either an electro-optic modulator or an acousto-optic modulator, combined with a suitable electronic driver [4]. In the case of an electro-optic device, a pulse picker comprises of a Pockels cell and polarising optics. The Pockels cell manipulates the polarisation state, while the polariser transmits or blocks the pulse based on its polarisation [4]. This setup enables the deflection of the desired pulse into a slightly modified direction, allowing it to pass through an aperture while blocking other pulses and noise.

An alternative approach would involve indirect measurement through nonlinear effects. As outlined in Chapter 2, the strength of a Kerr lens depends on the peak power of an optical pulse [5]. Therefore, by utilising a material with a well-known nonlinear refractive index, the measurement of the Kerr lens established could be employed to infer the peak powers exhibited by the pulse.

6.3.7 Dispersion Management

If additional spectrum can yield sufficiently short pulses, the chirped mirrors trailed in this research could potentially be employed to generate pulses detectable by the autocorrelator. However, it remains uncertain whether the level of nonlinearity needed to sustain such short pulses would necessitate impractical amounts of dispersion for compensation. Therefore, various modelling techniques to determine the feasibility of this would be explored.

6.3.8 Alignment Precision Controls and SESAM Cooling

During the alignment of the long cavities detailed in Chapter 5, a constraint was identified concerning the level of precision control. To achieve optimal overlap of laser modes, minimise losses, maximise power extraction, and fine-tune the fluence on the SESAM, additional precision controls are necessary to ensure stable and efficient laser operation. These precision controls may include motorised translation stages and motorised kinematic mounts. Furthermore, as discussed in Chapter 5, the use of water cooling to cool the SESAM mount introduces micro vibrations into the system, leading to timing jitter and amplitude noise. To mitigate this effect, Peltier modules should be utilised instead, provided they can maintain a robust and consistent temperature across various SESAM fluence levels.

6.4 Final Remarks

This chapter provided an overview of the future directions and improvements for the project. All initial objectives outlined in Chapter 1 have been successfully addressed.

The successful demonstration of SESAM Q-switching in a Ho:YAG slab marks a significant milestone as the first of its kind. The trends obtained across various modulation depths were consistent with theoretical predictions. It was observed that at sufficiently high modulation

depths, pulse durations and average powers could generate peak powers significant enough to initiate substantial nonlinear processes. Consequently, the developed resonator holds promise for various applications, including the pumping of frequency mixing processes such as optical parametric oscillators for the generation of MIR wavelengths [6, 7]. Moreover, the successful implementation of this method presents an economical, simplistic, and compact alternative to traditional active Q-switching methods [8].

Additionally, the work conducted on the mode-locking regime demonstrated the first SESAM mode-locked Ho:YAG laser outside of TDLs and ceramics. With further optimisation strategies, the slab geometry exhibits strong potential for high-power scalability without necessitating the complex and expensive pumping configuration typical of TDLs [9, 10]. The inherent dispersion contribution from the slab also reduces the reliance on additional dispersion compensation elements like chirped mirrors, which reduces the cost, losses, and simplifies the overall configuration of the resonator. Furthermore, the comparatively lower doping concentration employed in this experiment holds promise for power scaling, circumventing limitations associated with thermal effects and quenching of the upper-state lifetime observed in higher-doped counterparts [11-13].

Appendix A

Two-Photon Absorption

Two-photon absorption (TPA) refers to the simultaneous absorption of two photons to excite a molecule from one state (typically the ground state) to a higher energy state. When this process occurs for two photons of different frequency, it is known as non-degenerate TPA [1]. Given that TPA is dependent on the simultaneous absorption of two photons, the likelihood of TPA is directly proportional to the square of the light intensity, making it a nonlinear optical process [1]. The energy difference between the lower and upper states involved in the molecule is equal to or smaller than the sum of the photon energies of the two absorbed photons. TPA is classified as a third-order process, exhibiting an absorption cross-section typically several orders of magnitude smaller than that of one-photon absorption [1].

In dielectric materials or semiconductors, TPA generally occurs only if the photon energy is at least half the band gap energy. Consequently, ultrashort pulses at a wavelength of 800 nm propagating in a silica fibre experience no losses via TPA [2]. However, semiconductors such as GaAs, with a significantly smaller band gap, can exhibit TPA at the same wavelength [2].

As a result, TPA has the capacity to significantly alter the saturation characteristics of saturable absorbers such as SESAMs, leading to a roll-over of the saturation curve. This modification can be beneficial in suppressing Q-switching instabilities, among other applications [2]. However, this may also be detrimental if strong pulse shaping is required.

References

[1] "Appendix C - Two photon absorption" in *Optical Spectroscopy*, N. V. Tkachenko Ed. Amsterdam: Elsevier Science, 2006, pp. 293-294.

[2] R. Paschotta. "Two-photon Absorption." RP Photonics Encyclopedia. https://www.rp-photonics.com/two_photon_absorption.html#:~:text=Two%2Dphoton%20absorption%20(TPA),sum%20of%20the%20photon%20energies. (accessed 12/11/23)

Appendix B

Frequency-Resolved Optical Gating

Frequency-resolved optical gating (FROG) is a general method to effectively measure the full time-dependent electric field and hence spectral phase of an optical pulse [1]. While there are many variants, second-harmonic FROG (SHG FROG) is typically considered the most quintessential approach across literature [1]. This shares the same fundamental concept of intensity autocorrelation. It involves combining a pulse with itself in a nonlinear medium. As a nonlinear medium generates the desired signal only when both pulses coincide (i.e., "optical gating"), adjusting the delay between the identical pulses and measuring the signal at each delay provides an estimate of the pulse length. However, while intensity autocorrelation measures the intensity of the SHG field strength, FROG instead measures the spectrum of the signal at each delay (hence “frequency-resolved”), using a spectrometer in place of the photodetector [1].

The FROG trace produced by this technique is a kind of spectrogram and displays intensity as a function of time delay and optical frequency through a colour scale [1]. The expression for the trace in terms of the pulse field is given by Equation (B.1) [2].

$$I_{SHG\ FROG}(\omega,\tau) = \left|\int_{-\infty}^{\infty} E(t)E(t-\tau)e^{i\omega t}dt\right|^2 \qquad \text{(B.1)}$$

Based on this trace, a sophisticated iterative phase retrieval algorithm can be applied to reconstruct the pulse shape and the underlying electric field [2]. Thus, FROG serves as one

of the most “complete” single characterisation techniques for the assessment of ultrashort optical pulses.

References

[1] R. Paschotta. "Frequency-resolved Optical Gating." RP Photonics Encyclopedia. https://www.rp-photonics.com/frequency_resolved_optical_gating.html (accessed 12/11/23).

[2] U. Keller, *Ultrafast Lasers*. Zürich, Switzerland: Springer, 2021, p. 810.

Appendix C

Ho:YAG Energy Scheme

The energy scheme for Ho:YAG is presented in Figure C.1 with the relevant transitions for 2.1 µm laser operation [1].

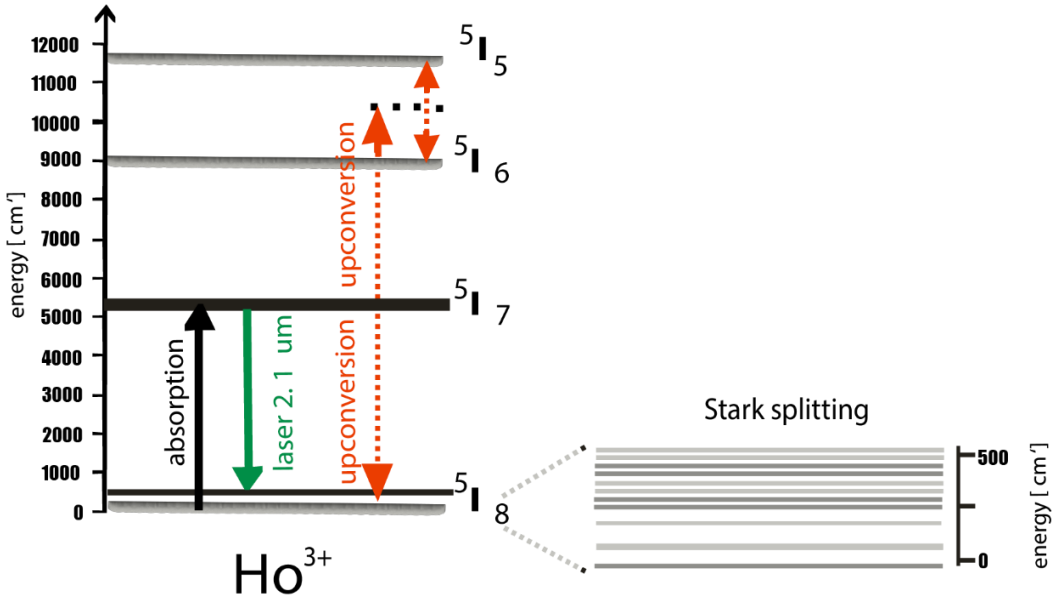


Figure C.1: Energy scheme for Ho:YAG, including the relevant transitions for pumping and the Stark splitting distribution [1]. Stark splitting is shown only for $^5I_8$ for simplicity.

The emission at 2.1 µm originates from a transition that begins in the upper laser level $^5I_7$ and concludes in the thermally populated sublevels of the $^5I_8$ ground state manifold. Both energy levels involved exhibit significant Stark splitting with the higher level comprising 14

sublevels ranging from 5228 cm^{-1} to 5455 cm^{-1}, and the ground state splitting into 11 sublevels from 0 cm^{-1} to 535 cm^{-1} [2].

At room temperature in YAG, only 10% of the Ho^{3+} ions, excited to the $^5I_7$ manifold, occupy the Stark level, which serves as the upper laser level [1]. In contrast, for Tm^{3+} ions, this percentage is approximately 46%. Consequently, the temperature dependence of Ho-lasers is greater [1]. The upconversion process, wherein a Ho^{3+} ion is excited into the $^5I_5$ or $^5I_6$ manifold, is a non-resonant, phonon-assisted process. This process requires two closely spaced holmium ions that are excited into the $^5I_7$ manifold, making it significant when the population density of the $^5I_7$ energy level is high [1]. As a result, the upconversion process becomes most crucial during Q-switched operation when there is substantial energy storage in the upper laser level.

References

[1] S. Karsten, L. Samir, K. Philipp, and F. Peter, "2 µm Laser Sources and Their Possible Applications" in *Frontiers in Guided Wave Optics and Optoelectronics*, P. Bishnu Ed. Rijeka: IntechOpen, 2010, p. Ch. 21.

[2] A. Kaminskii, *Crystalline Lasers Physical Processes and Operating Schemes*. 1996, p. 592.

Appendix D

Introduction to Optical Fibres

An optical fibre is a flexible glass or plastic medium capable of transmitting light from one end to the other. It comprises a cylindrical structure that includes a core, cladding, and coating [1]. The refractive index difference between the core and cladding is determined by the dopants. In step-index fibers, light traverses the central core with a refractive index of n_1, surrounded by a cladding layer with a lower refractive index of n_2. The light is confined to the fibre core through total internal reflection (TIR) due to the refractive index of the core, n_1, surpassing that of the cladding, n_2. This confinement is referred to as a waveguide [2]. Consequently, light launched at an angle exceeding the critical angle at the core-cladding interface undergoes complete reflection. This is as illustrated in Figure D.1.

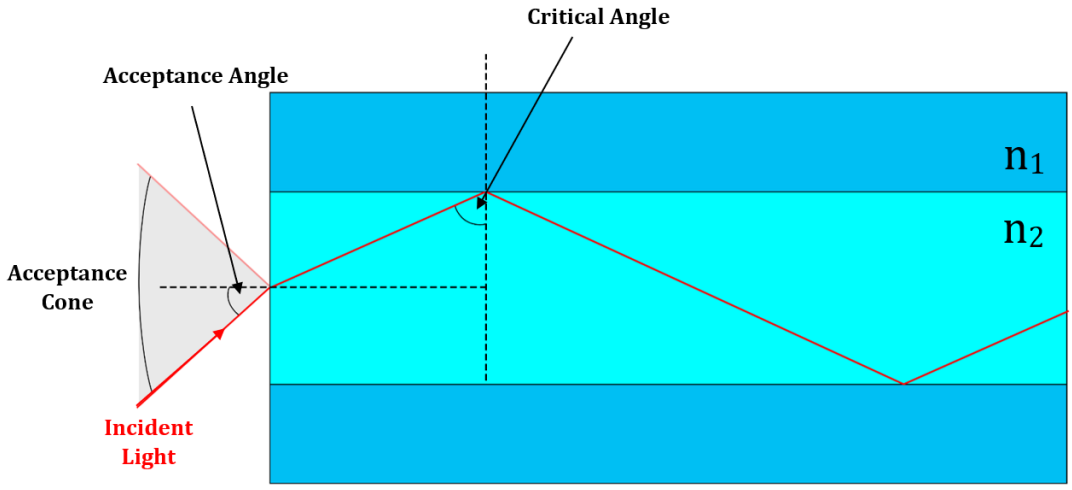


Figure D.1: Typical geometry of a step-index, singly clad optical fibre with a core refractive index of n_1 and a cladding refractive index of n_2.

The normalised frequency, denoted by V and defined by Eq. (D.1), determines the quantity of modes capable of propagating in a fibre [1].

$$V = 2\pi r\left(\frac{NA}{\lambda_0}\right) \tag{D.1}$$

where λ_0 is the vacuum wavelength of the propagating radiation, r is the fibre core radius and NA is the numerical aperture, which represents how easily light is coupled into the core and is given by Eq. (D.2).

$$NA = \sqrt{n_1^2 - n_2^2} \tag{D.2}$$

References

[1] R. Vallée, "The Optical Fibre" in *Fibre Optic Communication Devices*: Springer, 2001, pp. 21-70.

[2] K. Rajagopal, *Textbook Of Engineering Physics (Part I)*. PHI Learning Pvt. Ltd., 2008.

Appendix E

Beam Quality Assessment

Knife-Edge Method

The technique selected for obtaining a measure of beam quality is based on the knife-edge method. This involves moving a sharp blade or edge through the cross-section of the beam path and measuring the transmitted light's power. By curve-fitting the power reduction as the blade traverses the beam, valuable information about the laser's spatial profile can be extracted. Gathering measurements at multiple locations along the beam path after some converging optic provides additional information such as Rayleigh range and, in particular interest of this characterisation, a measure of beam quality.

The power $P(x)$ and knife-edge displacement $(x - x_0)$ are related to the beam width w_x through Equation (E.1) using statistical curve-fitting techniques [1].

$$P_N(x) = \frac{1}{1+\exp\left(-(a_0+a_1 t+a_2 t^2+a_3 t^3)\right)} \tag{E.1}$$

$$a_0 = -6.71387 \times 10^{-3}, a_1 = -1.55115,\ a_2 = -5.13306 \times 10^{-2}, a_3 = -5.49164 \times 10^{-2}$$

$$t = \left(\frac{2}{w_x}\right)(x - x_0) \text{ and } P_N(x) = \frac{P(x)}{P_{Total}} \text{ is the normalised power.}$$

This equation is derived through the differentiation of a Gaussian-shaped beam intensity profile with respect to position [1, 2]. However, due to the non-analytic nature of the resulting

expression, calculating exact analytical solutions becomes impractical [2]. As a result, various approximations are often employed, leading to numerous alternative formulations of Equation (E.1), each tailored to specific constraints and assumptions [2, 3].

The selection of Equation (E.1) as an appropriate curve-fitting function is based on a linear least-squares approximation, as presented by Khosrofian *et al*. [1]. This approach is frequently favoured due to its computational efficiency and its capability to achieve an estimated accuracy of 0.05% under ideal data acquisition conditions [1-3].

Once the beam radii have been determined at several locations along the beam path using the knife-edge method, a procedure for relating this to beam quality is outlined in ISO 11164-1, an internationally recognised standard for acquiring and characterising laser beam parameters [4]. In accordance with this standard, the beam width data obtained over a propagation distance z is fitted to Equation (E.2) using statistical curve-fitting in Python [4].

$$d(z) = \sqrt{a + bz + cz^2} \tag{E.2}$$

The beam quality M^2 and Rayleigh range Z_R are subsequently determined using Equation (E.3) and Equation (E.4), respectively [4].

$$M^2 = \left(\frac{\pi}{8\lambda}\right)\sqrt{4ac - b^2} \tag{E.3}$$

$$Z_R = \left(\frac{1}{2c}\right)\sqrt{4ac - b^2} \tag{E.4}$$

Although the Rayleigh range does not contribute to characterising the thulium-fibre laser, a calculation of its value will be required for designing the Ho:YAG laser in the following chapter.

Although the objective of this approach is to obtain a measurement of beam quality in accordance with the international standard, the assessment of beam quality remains a contentious issue across literature. Various metrics exist, but their interpretations often hinge on how one defines beam width [5]. Moreover, the standard upon which this research is built has only recently become accessible, with the latest edition locked behind a paywall. Consequently, there is no single, universally applicable, and universally meaningful definition of laser beam quality that can be encapsulated in a singular number or a concise set of parameters. Another contributing factor is that the quality of a given beam profile is contingent upon the intended application, leading to variations in value depending on the chosen metric [5].

Beam Profiler Automation

While the measurements for beam width may be obtained manually, an initiative is taken to automate the process for future use. This involves the development of an automated beam profiler, which utilises a NEMA17 Stepper Motor and an Arduino Uno R3 to create a programmable optical breadboard "trolley." This trolley can move with millimetre precision to designated positions on an optical table via rack and pinion. By mounting a motorised translation stage and knife-edge on this breadboard and interfacing it with Python, a hands-free method is established for acquiring knife-edge measurements at various points along the beam propagation path, providing a means to assess beam quality without tedium. A Thorlabs K-Cube Brushed DC Servo Motor Controller (KDC101) is integrated into the system for control over any compatible Thorlabs motorised stage.

The Arduino Uno R3 onboard the trolley is programmed to execute the following sequence:

1. A scan of the knife-edge blade across the beam is initiated, recording both the knife's displacement and power measurements as it traverses the cross-section of the optical path until the beam is entirely obstructed by the knife.

2. The acquired data is subjected to a curve-fitting process based on Equation (E.1), resulting in a plotted graph of optical power against displacement, and an estimation of the beam radius at that location.
3. The trolley then moves the knife-edge setup along the length of the beam path to the next data acquisition point and repeats steps 1 and 2.
4. Steps 1-3 are reiterated until the specified number of beam radii is obtained. At this juncture, the profiler employs curve fitting based on Equation (E.2) and produces a plot. The values for beam quality and Rayleigh range are subsequently calculated from the curve-fit using Equation (E.3) and Equation (E.4).
5. All produced plots and calculated parameters are then output to a specified folder.

All designs for the optical breadboard trolley are produced in Autodesk Inventor Professional 2023 and components 3D printed using a PRUSA MK3S+. Figure E.1 presents the CAD designs for the trolley alongside the final product.

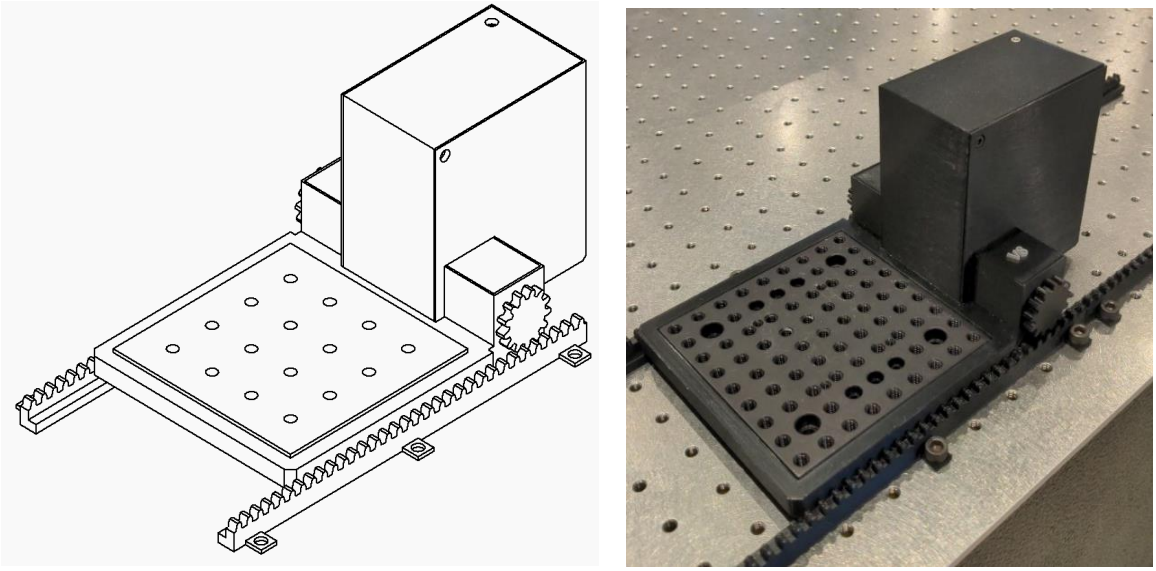


Figure E.1: Programmable optical breadboard trolley CAD design (LEFT) alongside final product (RIGHT).

Furthermore, a simple graphical user interface (GUI) is developed using Python to simplify user interaction with the automation script. A screenshot of the program is presented in Figure .

The GUI includes the ability to:

- Set the movement bounds, scan velocity and scan frequency for the knife-edge measurements.
- Set the direction, distance, and speed that the trolley moves between knife-edge measurements.
- Set the total number of measurements to be collected before program termination.
- Input the initial starting location, lens distance, and data iteration number. These values are exported with the program output files for future reference.

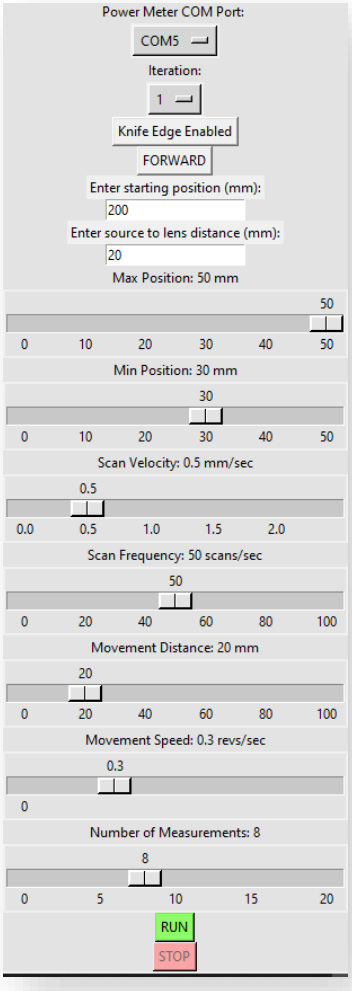


Figure E.2: Screenshot of the Python GUI used for the beam profiler automation.

Data Acquisition and Results

The motorised stage selected is a Thorlabs 50 mm Linear Motorised Translation Stage (MT S50-Z8). Using the automated beam profiler GUI, the knife scanning speed is set to 0.1 mm/sec. By aligning the sampling rate with the thermal power meter's sampling time, this configuration theoretically provides a scanning resolution of 0.6 μm for the beam radius.

To expedite the computational process for large beam radii, the acquired knife-edge data is truncated to only include every 20th data point. This significantly enhances computational efficiency while preserving the essential characteristics of the beam profile.

An example of a knife-edge plot produced by the beam profiler is presented in Figure E.3.

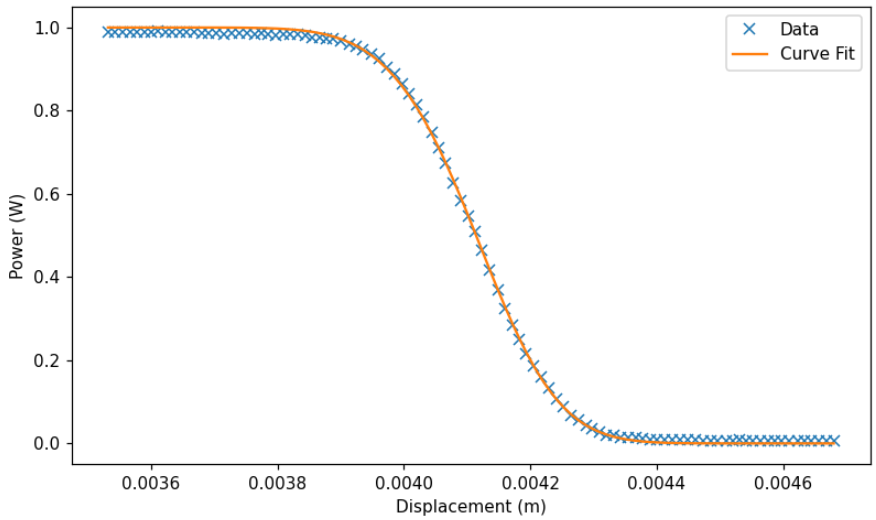


Figure E.3: Plot of the knife-edge power displacement data for a thulium-fibre laser beam diameter of 405.61 μm.

For the output plot of the beam profile and beam quality, refer back to Chapter 3.

References:

[1] J. M. Khosrofian and B. A. Garetz, "Measurement of a Gaussian laser beam diameter through the direct inversion of knife-edge data" *Appl. Opt.*, vol. 22, no. 21, pp. 3406-3410, 1983/11/01 1983, doi: 10.1364/AO.22.003406.

[2] M. A. de Araújo, R. Silva, E. de Lima, D. P. Pereira, and P. C. de Oliveira, "Measurement of Gaussian laser beam radius using the knife-edge technique: improvement on data analysis" *Appl. Opt.*, vol. 48, no. 2, pp. 393-396, 2009/01/10 2009, doi: 10.1364/AO.48.000393.

[3] L. Bachmann, D. Zezell, and E. Puig Maldonado, "Determination of Beam Width and Quality for Pulsed Lasers Using the Knife-Edge Method" *Instrumentation Science & Technology*, vol. 31, pp. 47-52, 01/03 2003, doi: 10.1081/CI-120018406.

[4] *ISO 11146-1:2021(en) Lasers and laser-related equipment — Test methods for laser beam widths, divergence angles and beam propagation ratios*, I. O. f. Standardization, 2021. [Online]. Available: https://www.iso.org/obp/ui/en/#iso:std:iso:11146:-1:ed-2:v1:en

[5] A. E. Siegman, "How to (Maybe) Measure Laser Beam Quality" in *DPSS (Diode Pumped Solid State) Lasers: Applications and Issues*, Washington, D.C., M. Dowley, Ed., 1998/01/01 1998, vol. 17: Optica Publishing Group, in OSA Trends in Optics and Photonics, p. MQ1, doi: 10.1364/DLAI.1998.MQ1. [Online]. Available: https://opg.optica.org/abstract.cfm?URI=DLAI-1998-MQ1

Appendix F

Beam Profiling Camera Error Assessment

The fluctuations in the measurements obtained by the DataRay WinCamD-IR-BB 2-16 μm Beam Profiler are measured using the diagnostic setup described in Chapter 4. At 7 locations along the optical path, 30 measurements of beam diameter are recorded and Tabulated in Table F.1.

Table F.1: Beam diameter at 7 locations using the beam profiler.

Location 1 Beam Diameter (µm)	Location 2 Beam Diameter (µm)	Location 3 Beam Diameter (µm)	Location 4 Beam Diameter (µm)	Location 5 Beam Diameter (µm)	Location 6 Beam Diameter (µm)	Location 7 Beam Diameter (µm)
600.6	511.8	867.9	1228	1639	2335	4066
595.5	510.2	896.4	1203	1637	2397	4063
594.1	508.7	902.5	1194	1640	2399	4114
597.8	512.3	871.5	1207	1681	2392	4074.3
594.3	505.9	898.7	1204	1651	2399	3979
593.3	506.2	877	1195	1653	2374	4007
609.3	507.4	902.7	1197	1655	2344	3939
597.4	509.5	888.6	1200	1692	2361	3941
600.6	512.1	882.6	1205	1682	2344	3977
598.8	504.6	868.8	1235	1661	2352	3996
604.6	509.7	875.1	1199	1685	2295	4009
598.4	510.5	916.4	1190	1680	2315	4008
594.3	506.8	871	1206	1658	2310	3999
599	503.6	902.5	1194	1647	2332	3972
603	505.4	896.4	1187	1654	2287	3985
595.5	503.7	893.5	1228	1642	2298	3988
592.8	504.9	868.8	1226	1648	2358	4017
594.3	508.4	882.6	1189	1642	2387	4031
600.4	507.2	902.7	1199	1646	2295	3961
599.3	511.3	867.9	1191	1653	2278	4037
600.7	503.9	898.7	1231	1656	2287	3992
603	508.6	877	1233	1639	2352	4102
597.4	511.7	873	1242	1690	2465	3990
600.4	511.4	946.8	1216	1690	2335	4173
609.3	505.2	917.6	1189	1657	2354	3982
592.8	512.6	895	1203	1651	2344	3997
610.4	509.4	925.2	1191	1640	2317	4091
595.5	508.2	902.5	1187	1654	2382	4127
604.8	506.6	873	1223	1627	2345	4109
598.4	512.4	902.7	1203	1642	2378	4082

The mean values, standard deviations and coefficient of variations are listed. in Table F.2.

Table F.2: Statistics on the beam diameters at 7 locations using the beam profiler.

	Location 1	Location 2	Location 3	Location 4	Location 5	Location 6	Location 7
Mean Beam Diameter (µm)	599.2	508.3	899.5	1206	1656	2347	4026
Standard Deviation (µm)	4.891	2.905	29.44	16.51	18.15	42.51	59.48
Coefficient of Variation	0.008162	0.005714	0.03273	0.01368	0.01096	0.01811	0.01477

References

Chapter 1

[1] J. Achenbach. "Three scientists win Nobel Prize in physics for probing electrons." The Washington Post. https://www.washingtonpost.com/science/2023/10/03/nobel-prize-physics-winners-electrons/ (accessed 26/02/24).

[2] U. Keller, *2.1 Ultrafast solid-state lasers*.

[3] R. Paschotta, "Active Mode Locking" in *RP Photonics Encyclopedia*, ed.

[4] U. Keller, *Ultrafast Lasers*. Zürich, Switzerland: Springer, 2021, p. 810.

[5] C. Lasers, B. Astronomy, and D. Sciences, *Opportunities in Intense Ultrafast Lasers: Reaching for the Brightest Light*. 2018, pp. 1-327.

[6] A. Donodin *et al.*, *Femtosecond thulium-doped fiber-ring laser for mid-IR spectroscopic breath analysis*. 2019, p. 8.

[7] L. Orazi, L. Romoli, M. Schmidt, and L. Li, "Ultrafast laser manufacturing: from physics to industrial applications" *CIRP Annals*, vol. 70, no. 2, pp. 543-566, 2021/01/01/ 2021, doi: https://doi.org/10.1016/j.cirp.2021.05.007.

[8] S. J. Mihailov *et al.*, "Ultrafast Laser Processing of Optical Fibers for Sensing Applications" *Sensors*, vol. 21, no. 4, doi: 10.3390/s21041447.

[9] P. W. Smith, "Mode-locking of lasers" *Proceedings of the IEEE*, vol. 58, no. 9, pp. 1342-1357, 1970, doi: 10.1109/PROC.1970.7926.

[10] V. P. Gupta, "Chapter 1 - Introduction and overview" in *Molecular and Laser Spectroscopy*, V. P. Gupta Ed.: Elsevier, 2022, pp. 3-24.

[11] R. Berera, R. van Grondelle, and J. T. Kennis, "Ultrafast transient absorption spectroscopy: principles and application to photosynthetic systems" (in eng), *Photosynth Res*, vol. 101, no. 2-3, pp. 105-18, Aug-Sep 2009, doi: 10.1007/s11120-009-9454-y.

[12] R. D. Pensack, K. M. Banyas, L. W. Barbour, M. Hegadorn, and J. B. Asbury, "Ultrafast vibrational spectroscopy of charge-carrier dynamics in organic photovoltaic materials" *Physical Chemistry Chemical Physics*, 10.1039/B817113K vol. 11, no. 15, pp. 2575-2591, 2009, doi: 10.1039/B817113K.

[13] F. A. Hegmann, O. Ostroverkhova, and D. G. Cooke, "Probing Organic Semiconductors with Terahertz Pulses" 2006.

[14] E. Hendry, J. M. Schins, L. P. Candeias, L. D. A. Siebbeles, and M. Bonn, "Efficiency of Exciton and Charge Carrier Photogeneration in a Semiconducting Polymer" *Physical Review Letters*, vol. 92, no. 19, p. 196601, 05/13/ 2004, doi: 10.1103/PhysRevLett.92.196601.

[15] J. Shah, "Ultrafast Studies of Semiconductors" in *Encyclopedia of Modern Optics (Second Edition)*, B. D. Guenther and D. G. Steel Eds. Oxford: Elsevier, 2005, pp. 82-86.

[16] C. Reiss, "Ultrashort Laser Pulses in Biomedical Research" in *Laser Applications in Medicine and Biology: Volume 4*, M. L. Wolbarsht Ed. Boston, MA: Springer US, 1989, pp. 133-166.

[17] S. Svanberg, "Some Medical and Biological Applications of Ultrafast Lasers" in *Ultrafast Optics IV: Selected Contributions to the 4th International Conference on Ultrafast Optics, Vienna, Austria*, F. Krausz, G. Korn, P. Corkum, and I. A. Walmsley Eds. New York, NY: Springer New York, 2004, pp. 437-448.

[18] J. Bell. "Femtosecond lasers: How the medical industry is benefitting from ultrafast optical technology." NS Medical Devices. https://www.nsmedicaldevices.com/analysis/femtosecond-lasers-medical-industry/ (accessed 03/11/23).

[19] S. Prakash and S. Kumar, "6 - Microchannel fabrication via direct laser writing" in *Microfabrication and Precision Engineering*, J. P. Davim Ed.: Woodhead Publishing, 2017, pp. 163-187.

[20] C. Latz, T. Asshauer, C. Rathjen, and A. Mirshahi, "Femtosecond-Laser Assisted Surgery of the Eye: Overview and Impact of the Low-Energy Concept" (in eng), *Micromachines (Basel)*, vol. 12, no. 2, Jan 24 2021, doi: 10.3390/mi12020122.

[21] H. Lubatschowski *et al.*, "Medical applications for ultrafast laser pulses" *RIKEN Review,* vol. 50, 02/21 2003, doi: 10.1117/12.486505.

[22] E. Optics, "2μm MEDICAL LASER APPLICATIONS" 2018.

[23] S. Karsten, L. Samir, K. Philipp, and F. Peter, "2 μm Laser Sources and Their Possible Applications" in *Frontiers in Guided Wave Optics and Optoelectronics*, P. Bishnu Ed. Rijeka: intechopen, 2010, p. Ch. 21.

[24] S. Lei *et al.*, "Ultrafast Laser Applications in Manufacturing Processes: A State of the Art Review" *Journal of Manufacturing Science and Engineering,* vol. 142, pp. 1-43, 01/14 2020, doi: 10.1115/1.4045969.

[25] J. Saunders, M. Elbestawi, and Q. Fang, "Ultrafast Laser Additive Manufacturing: A Review" *Journal of Manufacturing and Materials Processing*, vol. 7, no. 3, doi: 10.3390/jmmp7030089.

[26] V. Bogdan *et al.*, "Material processing with ultra-short pulse lasers working in 2μm wavelength range" in *Proc.SPIE*, 2015, vol. 9350, p. 935014, doi: 10.1117/12.2078651. [Online]. Available: https://doi.org/10.1117/12.2078651

[27] B. Voisiat *et al.*, "Material processing with ultra-short pulse lasers working in 2μm wavelength range" *Proceedings of SPIE - The International Society for Optical Engineering,* vol. 9350, 03/04 2015, doi: 10.1117/12.2078651.

[28] J. Shepard. "Rapid Pulse Laser Weapons Could Be The Pentagon's Future Edge." Breaking Defence. https://breakingdefense.com/2021/10/rapid-pulse-laser-weapons-could-be-the-pentagons-future-edge/ (accessed 04/11/23.

[29] H. L. Xu and S. L. Chin, "Femtosecond Laser Filamentation for Atmospheric Sensing" *Sensors*, vol. 11, no. 1, pp. 32-53doi: 10.3390/s110100032.

[30] J. Kasparian and J.-P. Wolf, "Physics and applications of atmospheric nonlinear optics and filamentation" *Opt. Express,* vol. 16, no. 1, pp. 466-493, 2008/01/07 2008, doi: 10.1364/OE.16.000466.

[31] S. L. Chin, *Femtosecond laser filamentation*. Springer, 2010.

[32] E. M. Epperlein, "Kinetic theory of laser filamentation in plasmas" *Physical Review Letters,* vol. 65, no. 17, pp. 2145-2148, 10/22/ 1990, doi: 10.1103/PhysRevLett.65.2145.

[33] P. Qi *et al.*, "Sensing with Femtosecond Laser Filamentation" *Sensors*, vol. 22, no. 18, doi: 10.3390/s22187076.

[34] S. L. Chin *et al.*, "Advances in intense femtosecond laser filamentation in air" *Laser Physics*, vol. 22, no. 1, pp. 1-53, 2012/01/01 2012, doi: 10.1134/S1054660X11190054.

[35] Q. Luo, W. Liu, and S. L. Chin, "Lasing action in air induced by ultra-fast laser filamentation" *Applied Physics B*, vol. 76, no. 3, pp. 337-340, 2003/03/01 2003, doi: 10.1007/s00340-003-1115-9.

[36] T. Elder and J. Strong, "The infrared transmission of atmospheric windows" *Journal of the Franklin Institute*, vol. 255, no. 3, pp. 189-208, 1953/03/01/ 1953, doi: https://doi.org/10.1016/0016-0032(53)90002-7.

[37] J. W. Salisbury and D. M. D'Aria, "Emissivity of terrestrial materials in the 8–14 μm atmospheric window" *Remote Sensing of Environment*, vol. 42, no. 2, pp. 83-106, 1992/11/01/ 1992, doi: https://doi.org/10.1016/0034-4257(92)90092-X.

[38] K. Woohong *et al.*, "Holmium-doped laser materials for eye-safe solid state laser application" in *Proc.SPIE*, 2014, vol. 9081, p. 908105, doi: 10.1117/12.2050922. [Online]. Available: https://doi.org/10.1117/12.2050922

[39] J. A. Curcio and C. C. Petty, "The Near Infrared Absorption Spectrum of Liquid Water" *J. Opt. Soc. Am.*, vol. 41, no. 5, pp. 302-304, 1951/05/01 1951, doi: 10.1364/JOSA.41.000302.

[40] K. Hassan. "Lidar vs. Radar: Comprehensive Comparison and Analysis." Wevolver. https://www.wevolver.com/article/lidar-vs-radar-detection-tracking-and-imaging (accessed 04/11/23).

[41] P. Rairoux *et al.*, "Remote sensing of the atmosphere using ultrashort laser pulses" *Applied Physics B*, vol. 71, no. 4, pp. 573-580, 2000/10/01 2000, doi: 10.1007/s003400000375.

[42] K. Jerome *et al.*, "Ultrashort laser applications in lidar and atmospheric sciences" in *Proc.SPIE*, 2003, vol. 5226, pp. 238-248, doi: 10.1117/12.519494. [Online]. Available: https://doi.org/10.1117/12.519494

[43] E. Margalith. "The OPO goes from concept to commercial tool." Laser Focus World. https://www.laserfocusworld.com/test-measurement/research/article/16555475/the-opo-goes-from-concept-to-commercial-tool (accessed 04/11/23).

[44] P. Budni, L. Pomeranz, M. Lemons, P. Schunemann, T. Pollak, and E. P. Chicklis, "10W mid-IR holmium pumped ZnGeP2 OPO" in *Advanced Solid State Lasers*, 1998: Optica Publishing Group, p. FC1.

[45] A. Hildenbrand *et al.*, "Compact efficient mid-infrared laser source: OP-GaAs OPO pumped by $Ho3^{+}$:YAG laser" in *Proc.SPIE*, 2011, vol. 8187, p. 81870H, doi: 10.1117/12.898118. [Online]. Available: https://doi.org/10.1117/12.898118

[46] B. Cole *et al.*, "Compact and efficient mid-IR OPO source pumped by a passively Q-switched Tm:YAP laser" *Optics Letters*, vol. 43, no. 5, pp. 1099-1102, 2018/03/01 2018, doi: 10.1364/OL.43.001099.

[47] A. Hemming *et al.*, "A high power mid-IR ZGP ring OPO" in *CLEO: 2013*, 9-14 June 2013 2013, pp. 1-2, doi: 10.1364/CLEO_SI.2013.CW1B.7.

[48] M. Pötzlberger, "High-power femtosecond laser sources for mid-infrared generation" Ludwig Maximilians Universität München, 2021.

[49] K. J. Yang *et al.*, "Mode-locked Tm,Ho:YAP laser around 2.1 μm" *Opt. Express*, vol. 21, no. 2, pp. 1574-1580, 2013/01/28 2013, doi: 10.1364/OE.21.001574.

[50] R. Paschotta, "Optical Parametric Oscillators" in *RP Photonics Encyclopedia*, ed.

[51] A. S. Johnson *et al.*, "High-flux soft x-ray harmonic generation from ionization-shaped few-cycle laser pulses" (in eng), *Sci Adv*, vol. 4, no. 5, p. eaar3761, May 2018, doi: 10.1126/sciadv.aar3761.

[52] J. Marangos, "High-harmonic generation: Solid progress" *Nature Physics*, vol. 7, pp. 97-98, 02/01 2011, doi: 10.1038/nphys1913.

[53] P. B. Corkum, "Plasma perspective on strong field multiphoton ionization" *Physical Review Letters*, vol. 71, no. 13, pp. 1994-1997, 09/27/ 1993, doi: 10.1103/PhysRevLett.71.1994.

[54] A. S. Johnson *et al.*, "High-flux soft x-ray harmonic generation from ionization-shaped few-cycle laser pulses" *Science Advances*, vol. 4, no. 5, p. eaar3761, 2018, doi: doi:10.1126/sciadv.aar3761.

[55] D. Seligson, L. Pan, P. King, and P. Pianetta, "Soft X-ray dosimetry and its application on the lithography beamline at SSRL" *Nuclear Instruments and Methods in Physics Research Section A: Accelerators, Spectrometers, Detectors and Associated Equipment*, vol. 266, no. 1, pp. 612-618, 1988/04/01/ 1988, doi: https://doi.org/10.1016/0168-9002(88)90454-8.

[56] X. Liu, W. Yang, and Z. Liu, "Recent Progress on Synchrotron-Based In-Situ Soft X-ray Spectroscopy for Energy Materials" *Advanced Materials*, https://doi.org/10.1002/adma.201304676 vol. 26, no. 46, pp. 7710-7729, 2014/12/01 2014, doi: https://doi.org/10.1002/adma.201304676.

[57] W. Chao, P. Fischer, T. Tyliszczak, S. Rekawa, E. Anderson, and P. Naulleau, "Real space soft x-ray imaging at 10 nm spatial resolution" *Opt. Express*, vol. 20, no. 9, pp. 9777-9783, 2012/04/23 2012, doi: 10.1364/OE.20.009777.

[58] M. Hentschel *et al.*, "Attosecond metrology" *Nature*, vol. 414, no. 6863, pp. 509-513, 2001/11/01 2001, doi: 10.1038/35107000.

[59] L. Monroy, C. Quevedo-Galán, A. Serrano, J. Tijero, and I. Esquivias, "Low-cost dual-comb spectrometer for CO2 monitoring based on gain-switched semiconductor lasers" *Results in Physics*, vol. 58, p. 107516, 02/01 2024, doi: 10.1016/j.rinp.2024.107516.

[60] T. Fortier and E. Baumann, "20 years of developments in optical frequency comb technology and applications" *Communications Physics*, vol. 2, no. 1, p. 153, 2019/12/06 2019, doi: 10.1038/s42005-019-0249-y.

[61] R. Paschotta, "Frequency Combs" in *RP Photonics Encyclopedia*, ed.

[62] J. A. Whitaker-Lockwood, S. K. Scholten, F. Karim, A. N. Luiten, and C. Perrella, "Comb spectroscopy of CO2 produced from microbial metabolism" *Biomed. Opt. Express*, vol. 15, no. 3, pp. 1553-1570, 2024/03/01 2024, doi: 10.1364/BOE.515988.

[63] N. Bourbeau Hébert, S. K. Scholten, A. P. Hilton, R. F. Offer, C. Perrella, and A. N. Luiten, "Orthogonalizing the control of frequency combs for optical clockworks" *Optics Letters*, vol. 46, no. 19, pp. 4972-4975, 2021/10/01 2021, doi: 10.1364/OL.435219.

[64] E. A. Anashkina *et al.*, "Optical frequency combs generated in silica microspheres in the telecommunication C-, U-, and E-bands" in *Photonics*, 2021, vol. 8, no. 9: MDPI, p. 345.

[65] A. Schliesser, N. Picqué, and T. W. Hänsch, "Mid-infrared frequency combs" *Nature Photonics*, vol. 6, no. 7, pp. 440-449, 2012/07/01 2012, doi: 10.1038/nphoton.2012.142.

[66] S. Duval, M. Bernier, V. Fortin, J. Genest, M. Piché, and R. Vallée, "Femtosecond fiber lasers reach the mid-infrared" *Optica*, vol. 2, no. 7, pp. 623-626, 2015/07/20 2015, doi: 10.1364/OPTICA.2.000623.

[67] A. Kolovinos, "Experimental and Numerical Optimisation of a SESAM Mode-locked Holmium Fibre Laser" University of Adelaide, 2022.

[68] K. R. Michael, "Ultrafast laser IR countermeasures" in *Proc.SPIE*, 2009, vol. 7325, p. 73250W, doi: 10.1117/12.816557. [Online]. Available: https://doi.org/10.1117/12.816557

[69] A. Hemming *et al.*, "A high power hybrid mid-IR laser source" *Optics Communications*, vol. 283, no. 20, pp. 4041-4045, 2010/10/15/ 2010, doi: https://doi.org/10.1016/j.optcom.2010.05.078.

[70] T. Day, D. Arnone, S. Crivello, and M. Weida, *Miniaturized external cavity quantum cascade lasers for broad tunability in the mid-infrared*. 2006, pp. 1-2.

[71] R. Paschotta, "Passive Mode Locking" in *RP Photonics Encyclopedia*, ed.

[72] S. Tomilov *et al.*, "50-W average power Ho:YAG SESAM-modelocked thin-disk oscillator at 2.1μm" *Opt. Express*, vol. 30, no. 15, pp. 27662-27673, 2022/07/18 2022, doi: 10.1364/OE.460298.

[73] T. Brabec, C. Spielmann, P. Curley, and F. Krausz, "Kerr lens mode locking" *Optics letters*, vol. 17, no. 18, pp. 1292-1294, 1992.

[74] R. Paschotta, "Kerr Lens Mode Locking" in *RP Photonics Encyclopedia*, ed.

[75] G. Cerullo, S. De Silvestri, and V. Magni, "Self-starting Kerr-lens mode locking of a Ti: sapphire laser" *Optics letters*, vol. 19, no. 14, pp. 1040-1042, 1994.

[76] S. Tomilov *et al.*, "40 W SESAM-modelocked Ho:YAG thin-disk laser at 2090 nm" in *2021 Conference on Lasers and Electro-Optics Europe & European Quantum Electronics Conference (CLEO/Europe-EQEC)*, 21-25 June 2021 2021, pp. 1-1, doi: 10.1109/CLEO/Europe-EQEC52157.2021.9542367.

[77] Y. Wang *et al.*, *73-fs SESAM mode-locked Tm,Ho:CNGG laser at 2061 nm*. 2020, p. 80.

[78] W. Yicheng *et al.*, "73-fs SESAM mode-locked Tm,Ho:CNGG laser at 2061 nm" in *Proc.SPIE*, 2020, vol. 11259, p. 1125929, doi: 10.1117/12.2548180. [Online]. Available: https://doi.org/10.1117/12.2548180

[79] Y. Wang *et al.*, "Broadly tunable mode-locked Ho:YAG ceramic laser around 2.1μm" *Opt. Express*, vol. 24, no. 16, pp. 18003-18012, 2016/08/08 2016, doi: 10.1364/OE.24.018003.

[80] K. Yang *et al.*, "Mode-locking of 2 μm Tm,Ho:YAG laser with GaInAs and GaSb-based SESAMs" *Opt. Express*, vol. 21, no. 4, pp. 4311-4318, 2013/02/25 2013, doi: 10.1364/OE.21.004311.

[81] R. Paschotta. "Thin-disk Lasers." RP Photonics Encyclopedia. https://www.rp-photonics.com/thin_disk_lasers.html (accessed 07/11/23).

[82] Y. Zhao *et al.*, "SESAM mode-locked Tm:LuYO(3) ceramic laser generating 54-fs pulses at 2048 nm" (in eng), *Appl Opt*, vol. 59, no. 33, pp. 10493-10497, Nov 20 2020, doi: 10.1364/ao.408650.

[83] P. Valentin *et al.*, "Sub-100-fs bulk solid-state lasers near 2-micron," in *Proc.SPIE*, 2019, vol. 11209, p. 112094G, doi: 10.1117/12.2549618. [Online]. Available: https://doi.org/10.1117/12.2549618

[84] X. Mateos *et al.*, "Ho:$KY(WO_4)_2$ thin-disk laser passively Q-switched by a GaSb-based SESAM" *Opt. Express*, vol. 26, no. 7, pp. 9011-9016, 2018/04/02 2018, doi: 10.1364/OE.26.009011.

[85] U. Parali *et al.*, "Diode-pumped Alexandrite laser with passive SESAM Q-switching and wavelength tunability" *Optics Communications*, vol. 410, pp. 970-976, 2018/03/01/ 2018, doi: https://doi.org/10.1016/j.optcom.2017.09.047.

[86] C. R. Pollock *et al.*, "Mode locked and Q-switched Cr:ZnSe laser using a Semiconductor Saturable Absorbing Mirror (SESAM)" in *Advanced Solid-State Photonics (TOPS)*, Vienna, C. Denman and I. Sorokina, Eds., 2005/02/06 2005, vol. 98: Optica Publishing Group, in OSA Trends in Optics and Photonics, p. 252, doi: 10.1364/ASSP.2005.252. [Online]. Available: https://opg.optica.org/abstract.cfm?URI=ASSP-2005-252

[87] J. W. Evans, P. A. Berry, and K. L. Schepler, "A Passively Q-Switched, CW-Pumped Fe:ZnSe Laser" *IEEE Journal of Quantum Electronics*, vol. 50, no. 3, pp. 204-209, 2014, doi: 10.1109/JQE.2014.2302233.

[88] Y. Wang *et al.*, "Broadly tunable mode-locked Ho:YAG ceramic laser around 2.1 μm" (in eng), *Opt Express*, vol. 24, no. 16, pp. 18003-12, Aug 8 2016, doi: 10.1364/oe.24.018003.

[89] M. Ganija, A. Hemming, K. Boyd, A. Gambell, and N. Simakov, "Progress Towards High Power Scaling of Ho: YAG Lasers" in *2020 Conference on Lasers and Electro-Optics Pacific Rim (CLEO-PR)*, 2-6 Aug. 2020 2020, pp. 1-2, doi: 10.1364/CLEOPR.2020.C9A_2.

Chapter 2

[1] R. Paschotta. "Carrier–envelope Offset." RP Photonics. https://www.rp-photonics.com/carrier_envelope_offset.html (accessed 24-07-2023, 2023).

[2] "Group Velocity and Phase Velocity." https://phas.ubc.ca/~mav/p200/groupandphase.pdf

[3] "Phase and Group Velocity." George Mason University Department of Physics & Astronomy. https://science.gmu.edu/academics/departments-units/physics-and-astronomy-department

[4] FiberCore. "Group Index and Velocity." FiberCore. https://fibercore.humaneticsgroup.com/services-support/fiberpaedia/g/group-index-and-velocity

[5] J.-C. Diels and L. Arissian, "Carrier to Envelope Offset and Carrier to Envelope Phase How Their Control Impacts Femtosecond and Attosecond Phenomena" in *Frontiers in Optics 2010/Laser Science XXVI*, Rochester, New York, 2010/10/24 2010: Optica Publishing Group, in OSA Technical Digest (CD), p. FTuX1, doi: 10.1364/FIO.2010.FTuX1. [Online]. Available: https://opg.optica.org/abstract.cfm?URI=FiO-2010-FTuX1

[6] D. Giannotti, E. Suerra, F. Canella, S. Cialdi, P. Laporta, and G. Galzerano, "Carrier-envelope offset frequency measurement by means of an external optical resonator" (in English), *Frontiers in Physics*, Original Research vol. 11, 2023-May-24 2023, doi: 10.3389/fphy.2023.1197654.

[7] N. Jornod *et al.*, "Carrier-envelope offset frequency stabilization of a gigahertz semiconductor disk laser" *Optica*, vol. 4, no. 12, pp. 1482-1487, 2017/12/20 2017, doi: 10.1364/OPTICA.4.001482.

[8] H. R. Telle, G. Steinmeyer, A. E. Dunlop, J. Stenger, D. H. Sutter, and U. Keller, "Carrier-envelope offset phase control: A novel concept for absolute optical frequency measurement and ultrashort pulse generation" *Applied Physics B*, vol. 69, no. 4, pp. 327-332, 1999/10/01 1999, doi: 10.1007/s003400050813.

[9] D. G. M. John G. Proakis, *Digital Signal Processing*, Third ed. Prentice-Hall International, 1996.

[10] A. M. Weiner, *Ultrafast Optics*. Wiley, 2009, p. 595.

[11] V. Kumar. "Chapter 3: The Uncertainty Principle & Time-Bandwidth Product." Indian Institute of Technology. https://www.ee.iitb.ac.in/course/~pawar/Wavelet%20Applications/Chapters_review/ch03_Gr3_Gr2.pdf (accessed 2023).

[12] R. Paschotta. "Bandwidth-limited Pulses." RP Photonics Encyclopedia. https://www.rp-photonics.com/bandwidth_limited_pulses.html (accessed 01-08-23).

[13] R. Paschotta. "Pulse Compression." RP Photonics Encyclopedia. https://www.rp-photonics.com/pulse_compression.html (accessed 01-08-23).

[14] A. M. Weiner, *Ultrafast Optics* (no. 595). Wiley, 2009, pp. 414-416.

[15] R. Paschotta. "Doping Concentration." RP Photonics Encyclopedia. https://www.rp-photonics.com/doping_concentration.html (accessed 30/10/23).

[16] Z. Chang, *Fundamentals of Attosecond Optics*. Taylor and Francis Group, 2011.

[17] D. F. Hotz, "Gain Narrowing in a Laser Amplifier" *Appl. Opt.*, vol. 4, no. 5, pp. 527-530, 1965/05/01 1965, doi: 10.1364/AO.4.000527.

[18] J. Seres *et al.*, "Sub-10-fs, terawatt-scale Ti:sapphire laser system" *Optics Letters*, vol. 28, no. 19, pp. 1832-1834, 2003/10/01 2003, doi: 10.1364/OL.28.001832.

[19] R. Ell *et al.*, "Generation of 5-fs pulses and octave-spanning spectra directly from a Ti:sapphire laser" *Optics Letters*, vol. 26, no. 6, pp. 373-375, 2001/03/15 2001, doi: 10.1364/OL.26.000373.

[20] R. Paschotta. "Dispersion." RP Photonics Encyclopedia. https://www.rp-photonics.com/dispersion.html (accessed 05-08-23).

[21] J. A. Harrington, *Infrared Fibers and Their Applications*. SPIE Press, 2004.

[22] "What is Chromatic Dispersion? (Material Dispersion and Waveguide Dispersion)" FOSCO. https://www.fiberoptics4sale.com/blogs/archive-posts/95044870-what-is-chromatic-dispersion-material-dispersion-and-waveguide-dispersion

[23] M. H. Weik, "waveguide dispersion," in *Computer Science and Communications Dictionary*, M. H. Weik Ed. Boston, MA: Springer US, 2001, pp. 1912-1912.

[24] M. C. T. Bahaa E. A. Saleh, *FUNDAMENTALS OF PHOTONICS*. Wiley, 2019, p. 2751.

[25] "Dispersion (optics)." ScientificLib. https://www.scientificlib.com/en/Physics/Optics/DispersionOptics.html (accessed 07-08-23).

[26] R. Paschotta. "Chromatic Dispersion." RP Photonics Encyclopedia. https://www.rp-photonics.com/chromatic_dispersion.html (accessed 07-08-23).

[27] D. Popmintchev, S. Wang, X. Zhang, and T. Popmintchev, *Theory of the Chromatic Dispersion, Revisited*. 2020.

[28] A. S. Goodspeed, "Measuring the dispersion of laser cavity mirrors using white-light interferometry" Degree of Master of Science, Air Force Institute of Technology, Department of the Air Force Air University, Wright-Patterson Air Force Base, Ohio, 2008. [Online]. Available: https://apps.dtic.mil/sti/tr/pdf/ADA483325.pdf

[29] J. W. Gooch, "Sellmeier Equation" in *Encyclopedic Dictionary of Polymers*, J. W. Gooch Ed. New York, NY: Springer New York, 2011, pp. 653-654.

[30] G. P. Agrawal, *Nonlinear Fiber Optics*, Third ed. Optics and Photonics, 2001, p. 481.

[31] W. Lin, "PHYSICALLY AWARE AGILE OPTICAL NETWORKS" Doctor of Philosophy in Engineering, MONTANA STATE UNIVERSITY, Bozeman, Montana, 2008.

[32] P. Dombi, V. S. Yakovlev, K. O'Keeffe, T. Fuji, M. Lezius, and G. Tempea, "Pulse compression with time-domain optimized chirped mirrors" *Opt. Express*, vol. 13, no. 26, pp. 10888-10894, 2005/12/26 2005, doi: 10.1364/OPEX.13.010888.

[33] Y. Shaked, S. Yefet, and A. Pe'er, "The Prism-Pair: Simple Dispersion Compensation and Spectral Shaping of Ultrashort Pulses" *International Journal of Experimental Spectroscopic Techniques*, vol. 1, pp. 1-4, 04/07 2016, doi: 10.35840/2631-505X/8507.

[34] C. H. Jérémie LÉONARD, *Ultrafast Laser Technologies and Applications*. France: The authors, 2022, p. 272.

[35] R. F. Matthew Sands, Robert B. Leighton, *The Feynman Lectures on Physics*. 1963.

[36] U. Keller, *Ultrafast Lasers*. Zürich, Switzerland: Springer, 2021, p. 810.

[37] M. P. H. Mansoor Sheik-Bahae, *OSA Handbook of Optics*. 2000.

[38] R. Paschotta. "Kerr Lens." RP Photonics Encyclopedia. https://www.rp-photonics.com/kerr_lens.html (accessed 16-08-23).

[39] R. Paschotta. "Self-focusing." RP Photonics Encyclopedia. https://www.rp-photonics.com/self_focusing.html (accessed 16-08-23).

[40] P. T. Lab. "Self-Phase Modulation." Photolab. https://photolab4640.ntut.edu.tw/var/file/10/1010/img/2926/weak10self-phasemodulation.pdf

[41] R. Paschotta. "Self-phase Modulation." RP Encyclopedia. https://www.rp-photonics.com/self_phase_modulation.html (accessed 20-08-23).

[42] R. Paschotta, "Effect of Self-phase Modulation on the Pulse Bandwidth" 2015.

[43] C. Finot, F. Chaussard, and S. Boscolo, "Simple guidelines to predict self-phase modulation patterns," *J. Opt. Soc. Am. B*, vol. 35, no. 12, pp. 3143-3152, 2018/12/01 2018, doi: 10.1364/JOSAB.35.003143.

[44] E. R. Andresen, J. M. Dudley, D. Oron, C. Finot, and H. Rigneault, "Transform-limited spectral compression by self-phase modulation of amplitude-shaped pulses with negative chirp" *Optics Letters*, vol. 36, no. 5, pp. 707-709, 2011/03/01 2011, doi: 10.1364/OL.36.000707.

[45] S. A. Planas, N. L. Mansur, C. H. Cruz, and H. L. Fragnito, "Spectral narrowing in the propagation of chirped pulses in single-mode fibers" (in eng), *Opt Lett*, vol. 18, no. 9, pp. 699-701, May 1 1993, doi: 10.1364/ol.18.000699.

[46] W. J. Tomlinson, R. H. Stolen, and C. V. Shank, "Compression of optical pulses chirped by self-phase modulation in fibers" *J. Opt. Soc. Am. B*, vol. 1, no. 2, pp. 139-149, 1984/04/01 1984, doi: 10.1364/JOSAB.1.000139.

[47] F. X. Kaertner, *Ultrafast Optics*. 2005, p. 394.

[48] R. Paschotta. "Solitons." RP Photonics Encyclopedia. https://www.rp-photonics.com/solitons.html (accessed 23-08-23).

[49] R. Alfano, *The Supercontinuum Laser Source*. New York, NY 10031, USA: Springer, 1989, p. 469.

[50] "Encyclopedia of Physical Science and Technology" vol. Third, R. A. Meyers, Ed., ed: Elsevier Science Ltd., 2001.

[51] C. Rullière, *Femtosecond Laser Pulses Principles and Experiments*, Second ed. Springer, 2005, p. 438.

[52] U. Keller, "Recent developments in compact ultrafast lasers" *Nature*, vol. 424, no. 6950, pp. 831-838, 2003/08/01 2003, doi: 10.1038/nature01938.

[53] R. Paschotta, *Field Guide to Laser Pulse Generation*. Bellingham, Washington USA: SPIE Press, 2008, p. 133.

[54] R. a. A. M. Yusoff, A. A. A. Jafry, N. Kasim, N. F. Zulkipli, M. Yasin, and S. W. Harun, "Generation of Q-switched and mode-locked pulses using neodymium oxide as saturable absorber" *Results in Optics*, vol. 1, p. 100032, 2020/11/01/ 2020, doi: https://doi.org/10.1016/j.rio.2020.100032.

[55] J. J. Zayhowski, "Microchip Lasers" in *Encyclopedia of Modern Optics (Second Edition)*, B. D. Guenther and D. G. Steel Eds. Oxford: Elsevier, 2018, pp. 415-423.

[56] A. Butler, D. Spence, and D. Coutts, "Scaling Q-switched microchip lasers for shortest pulses," *Applied Physics B*, vol. 109, 10/01 2012, doi: 10.1007/s00340-012-5223-2.

[57] A. Penttinen, A. Härkönen, and M. Guina, "SESAM Q-switched 1534 nm microchip lasers: pulse duration, repetition rate, and peak-power optimization for LIDAR application" in *2019 Conference on Lasers and Electro-Optics Europe and European Quantum Electronics Conference*, Munich, 2019/06/23 2019: Optica Publishing Group, in OSA Technical Digest, p. ca_p_12, doi: 10.1364/CLEO_EUROPE.2019.ca_p_12. [Online]. Available: https://opg.optica.org/abstract.cfm?URI=CLEO_Europe-2019-ca_p_12

[58] G. J. Spühler *et al.*, "Passively Q-switched Yb:YAG microchip laser using a semiconductor saturable absorber mirror" in *Advanced Solid State Lasers*, Boston, Massachusetts, M. I. H. Fejer and U. Keller, Eds., 1999/01/31 1999, vol. 26: Optica Publishing Group, in OSA Trends in Optics and Photonics, p. TuC2, doi: 10.1364/ASSL.1999.TuC2. [Online]. Available: https://opg.optica.org/abstract.cfm?URI=ASSL-1999-TuC2

[59] R. Haring, R. Paschotta, R. Fluck, E. Gini, H. Melchior, and U. Keller, "Passively Q-switched microchip laser at 1.5 μm" *Journal of The Optical Society of America B-optical Physics - J OPT SOC AM B-OPT PHYSICS*, vol. 18, 12/01 2001, doi: 10.1364/JOSAB.18.001805.

[60] A. C. Buter, D. J. Spence, and D. W. Coutts, "Generating picosecond pulses from Q-switched microchip lasers" in *2011 International Quantum Electronics Conference (IQEC) and Conference on Lasers and Electro-Optics (CLEO) Pacific Rim incorporating the Australasian Conference on Optics, Lasers and Spectroscopy and the Australian Conference on Optical Fibre Technology*, 28 Aug.-1 Sept. 2011 2011, pp. 632-634, doi: 10.1109/IQEC-CLEO.2011.6193702.

[61] G. J. Spühler *et al.*, "Experimentally confirmed design guidelines for passively Q-switched microchip lasers using semiconductor saturable absorbers" *J. Opt. Soc. Am. B*, vol. 16, no. 3, pp. 376-388, 1999/03/01 1999, doi: 10.1364/JOSAB.16.000376.

[62] R. Fluck, R. Häring, R. Paschotta, E. Gini, H. Melchior, and U. Keller, "Eyesafe pulsed microchip laser using semiconductor saturable absorber mirrors" *Applied Physics Letters*, vol. 72, no. 25, pp. 3273-3275, 1998, doi: 10.1063/1.121621.

[63] U. Keller *et al.*, "Semiconductor saturable absorber mirrors (SESAM's) for femtosecond to nanosecond pulse generation in solid-state lasers," *IEEE Journal of Selected Topics in Quantum Electronics*, vol. 2, no. 3, pp. 435-453, 1996, doi: 10.1109/2944.571743.

[64] R. Paschotta. "Saturable Absorbers." RP Photonics Encyclopedia. https://www.rp-photonics.com/saturable_absorbers.html (accessed 15-09-23).

[65] S. Tomilov *et al.*, "50-W, >2-μJ SESAM-modelocked Ho:YAG thin-disk oscillator at 2.1 μm" *EPJ Web of Conferences*, vol. 267, 10/18 2022, doi: 10.1051/epjconf/202226701042.

[66] A. Abouelez, E. Eldiwany, M. El_Mashade, and H. Konber, "Modelling and simulation of p-i-n quantum dot semiconductor saturable absorber mirrors" *Progress In Electromagnetics Research C*, vol. 82, pp. 39-53, 01/01 2018, doi: 10.2528/PIERC17112804.

[67] R. Paschotta. "Kerr Lens Mode Locking." RP Photonics Encyclopedia. https://www.rp-photonics.com/kerr_lens_mode_locking.html (accessed 15-09-23.

[68] R. Paschotta. "Semiconductor Saturable Absorber Mirrors." RP Photonics Encyclopedia. https://www.rp-photonics.com/semiconductor_saturable_absorber_mirrors.html (accessed 20/09/23).

[69] "Bragg mirror." BATOP Optoelectronics. https://www.batop.de/information/r_Bragg.html (accessed 13/10/23).

[70] A. Diebold *et al.*, "Optimized SESAMs for kilowatt-level ultrafast lasers" *Opt. Express,* vol. 24, no. 10, pp. 10512-10526, 2016/05/16 2016, doi: 10.1364/OE.24.010512.

[71] A. Khadour, S. Bouchoule, G. Aubin, J.-C. Harmand, J. Decobert, and J.-L. Oudar, "Ultrashort pulse generation from 156 μm mode-locked VECSEL at room temperature" *Opt. Express,* vol. 18, pp. 19902-13, 09/01 2010, doi: 10.1364/OE.18.019902.

[72] "SAM - Saturable Absorber Mirror." BATOP Optoelectronics. https://www.batop.de/information/SAM_infos.html (accessed 20/09/23).

[73] G. J. Spühler *et al.*, "Semiconductor saturable absorber mirror structures with low saturation fluence" *Applied Physics B,* vol. 81, no. 1, pp. 27-32, 2005/07/01 2005, doi: 10.1007/s00340-005-1879-1.

[74] G. Spuehler, S. Reffert, M. Haiml, M. Moser, and U. Keller, "Output-coupling semiconductor saturable absorber mirror" *Applied Physics Letters,* vol. 78, pp. 2733-2735, 04/30 2001, doi: 10.1063/1.1370122.

[75] H. JANG, "SESAM Design and Characterization" Master of Science Thesis, Department of Applied Physics, KTH, Stockholm, Sweden 2010, 2005. [Online]. Available: https://www.kth.se/polopoly_fs/1.422570.1600688567!/Menu/general/column-content/attachment/Jang_msc_thesis.pdf

[76] M. Haiml, R. Grange, and U. Keller, "Optical characterization of semiconductor saturable absorbers" *Applied Physics B,* vol. 79, no. 3, pp. 331-339, 2004/08/01 2004, doi: 10.1007/s00340-004-1535-1.

[77] J. Jeon, J. Lee, and J. H. Lee, "Numerical study on the minimum modulation depth of a saturable absorber for stable fiber laser mode locking" *J. Opt. Soc. Am. B,* vol. 32, no. 1, pp. 31-37, 2015/01/01 2015, doi: 10.1364/JOSAB.32.000031.

[78] F. X. Kurtner, J. A. d. Au, and U. Keller, "Mode-locking with slow and fast saturable absorbers-what's the difference? " *IEEE Journal of Selected Topics in Quantum Electronics,* vol. 4, no. 2, pp. 159-168, 1998, doi: 10.1109/2944.686719.

[79] I. D. Jung, F. X. Kärtner, L. R. Brovelli, M. Kamp, and U. Keller, "Experimental verification of soliton mode locking using only a slow saturable absorber" *Optics Letters,* vol. 20, no. 18, pp. 1892-1894, 1995/09/15 1995, doi: 10.1364/OL.20.001892.

[80] U. Keller, *2.1 Ultrafast solid-state lasers*.

[81] H. A. Haus, "Theory of mode locking with a fast saturable absorber" *Journal of Applied Physics,* vol. 46, no. 7, pp. 3049-3058, 2008, doi: 10.1063/1.321997.

[82] S. Wang, B. S. Marks, and C. R. Menyuk, "Comparison of models of fast saturable absorption in passively modelocked lasers" *Opt. Express,* vol. 24, no. 18, pp. 20228-20244, 2016/09/05 2016, doi: 10.1364/OE.24.020228.

[83] J. Hausen, K. Lüdge, S. V. Gurevich, and J. Javaloyes, "How carrier memory enters the Haus master equation of mode-locking" *Optics Letters,* vol. 45, no. 22, pp. 6210-6213, 2020/11/15 2020, doi: 10.1364/OL.406136.

[84] M. Nizette and A. G. Vladimirov, "Generalized Haus master equation model for mode-locked class-B lasers" *Physical Review E,* vol. 104, no. 1, p. 014215, 07/26/ 2021, doi: 10.1103/PhysRevE.104.014215.

[85] A. M. Perego, B. Garbin, F. Gustave, S. Barland, F. Prati, and G. J. de Valcárcel, "Coherent master equation for laser modelocking" *Nature Communications,* vol. 11, no. 1, p. 311, 2020/01/16 2020, doi: 10.1038/s41467-019-14013-4.

[86] H. A. Haus, "The master equations of mode-locking" in *Technical Digest. Summaries of papers presented at the Conference on Lasers and Electro-Optics. Postconference Edition. CLEO '99. Conference on Lasers and Electro-Optics (IEEE Cat. No.99CH37013)*, 28-28 May 1999 1999, p. 57, doi: 10.1109/CLEO.1999.833873.

[87] A. Perego, B. Garbin, F. Gustave, S. Barland, F. Prati, and G. de Valcarcel, "Coherent master equation for laser modelocking" *Nature Communications,* vol. 11, p. 311, 01/16 2020, doi: 10.1038/s41467-019-14013-4.

[88] B. H. Kolner, "Noise and Stability in Modelocked Soliton Lasers" in *Encyclopedia of Complexity and Systems Science*, R. A. Meyers Ed. New York, NY: Springer New York, 2009, pp. 6116-6175.

[89] F. Sanchez, A. Komarov, and G. Semaan, "Dissipative soliton resonance in fiber lasers" *Optics Communications,* vol. 541, p. 129543, 2023/08/15/ 2023, doi: https://doi.org/10.1016/j.optcom.2023.129543.

[90] R. Paschotta. "Passive Mode Locking With Slow Saturable Absorbers: Surprisingly Stable!" RP Photonics Encyclopedia. https://www.rp-photonics.com/spotlight_2017_08_31.html (accessed 19/10/23).

[91] R. Paschotta. "Haus Master Equation." RP Photonics Encyclopedia. https://www.rp-photonics.com/haus_master_equation.html (accessed 19/10/23).

[92] H. Haus, "Theory of mode locking with a slow saturable absorber" *IEEE Journal of Quantum Electronics,* vol. 11, no. 9, pp. 736-746, 1975, doi: 10.1109/JQE.1975.1068922.

[93] E. A. Stappaerts and W. H. Long, Jr., "Mode locking with a slow saturable absorber in a transverse resonator" (in eng), *Opt Lett,* vol. 3, no. 6, pp. 226-8, Dec 1 1978, doi: 10.1364/ol.3.000226.

[94] F. X. Kartner, I. D. Jung, and U. Keller, "Soliton mode-locking with saturable absorbers" *IEEE Journal of Selected Topics in Quantum Electronics,* vol. 2, no. 3, pp. 540-556, 1996, doi: 10.1109/2944.571754.

[95] R. Paschotta. "Soliton Mode Locking." https://www.rp-photonics.com/soliton_mode_locking.html (accessed 21/10/23).

[96] F. X. Kärtner and U. Keller, "Stabilization of solitonlike pulses with a slow saturable absorber" *Optics Letters,* vol. 20, no. 1, pp. 16-18, 1995/01/01 1995, doi: 10.1364/OL.20.000016.

[97] C. Hönninger, R. Paschotta, F. Morier-Genoud, M. Moser, and U. Keller, "Q-switching stability limits of continuous-wave passive mode locking" *J. Opt. Soc. Am. B,* vol. 16, no. 1, pp. 46-56, 1999/01/01 1999, doi: 10.1364/JOSAB.16.000046.

[98] N. H. Rizvi, P. M. W. French, and J. R. Taylor, "Continuously self-mode-locked Ti:sapphire laser that produces sub-50-fs pulses" *Optics Letters,* vol. 17, no. 4, pp. 279-281, 1992/02/15 1992, doi: 10.1364/OL.17.000279.

[99] P. Tchofo Dinda, A. Malfondet, P. Grelu, G. Millot, and A. Kamagate, "Strategies for accessing the multipulse regime of mode-locked fiber lasers" *Physical Review A,* vol. 107, no. 3, p. 033513, 03/21/ 2023, doi: 10.1103/PhysRevA.107.033513.

[100] T. Kolokolnikov, T. Erneux, N. Joly, and S. Bielawski, "The Q-switching instability in passively mode-locked lasers" in *EQEC '05. European Quantum Electronics Conference, 2005.,* 12-17 June 2005 2005, p. 122, doi: 10.1109/EQEC.2005.1567293.

[101] J. Aus-der-Au, D. Kopf, F. Morier-Genoud, M. Moser, and U. Keller, "60-fs pulses from a diode-pumped Nd:glass laser" *Optics letters,* vol. 22, pp. 307-9, 04/01 1997, doi: 10.1364/OL.22.000307.

[102] J. Lee, J. Koo, Y. M. Chang, P. Debnath, Y.-W. Song, and J. H. Lee, "Experimental investigation on a Q-switched, mode-locked fiber laser based on the combination of active mode locking and passive Q switching" *J. Opt. Soc. Am. B,* vol. 29, no. 6, pp. 1479-1485, 2012/06/01 2012, doi: 10.1364/JOSAB.29.001479.

[103] L. Dahlström, "Passive mode-locking and Q-switching of high power lasers by means of the optical Kerr effect" *Optics Communications,* vol. 5, no. 3, pp. 157-162, 1972/06/01/ 1972, doi: https://doi.org/10.1016/0030-4018(72)90055-7.

[104] T. Kolokolnikov, M. Nizette, T. Erneux, N. Joly, and S. Bielawski, "The Q-switching instability in passively mode-locked lasers" *Physica D: Nonlinear Phenomena,* vol. 219, no. 1, pp. 13-21, 2006/07/01/ 2006, doi: https://doi.org/10.1016/j.physd.2006.05.006.

[105] C. Frerichs and U. B. Unrau, "Passive Q-Switching and Mode-Locking of Erbium-Doped Fluoride Fiber Lasers at 2.7 μm" *Optical Fiber Technology,* vol. 2, no. 4, pp. 358-366, 1996/10/01/ 1996, doi: https://doi.org/10.1006/ofte.1996.0041.

[106] C. Yung-Fu and S. W. Tsai, "Simultaneous Q-switching and mode-locking in a diode-pumped Nd:YVO_4-Cr^{4+}:YAG laser," *IEEE Journal of Quantum Electronics,* vol. 37, no. 4, pp. 580-586, 2001, doi: 10.1109/3.914408.

[107] J. Hou, J.-L. Xu, Y. Yang, J.-L. He, B.-T. Zhang, and K.-J. Yang, "High-stability passively mode-locked laser based on dual SESAM" *Applied Physics B,* vol. 116, no. 2, pp. 347-351, 2014/08/01 2014, doi: 10.1007/s00340-013-5698-5.

[108] A. Haboucha, A. Komarov, H. Leblond, F. Sanchez, and G. Martel, "Mechanism of multiple pulse formation in the normal dispersion regime of passively mode-locked fiber ring lasers" *Optical Fiber Technology,* vol. 14, no. 4, pp. 262-267, 2008/10/01/ 2008, doi: https://doi.org/10.1016/j.yofte.2008.01.001.

[109] B. G. Bale, K. Kieu, J. N. Kutz, and F. Wise, "Transition dynamics for multi-pulsing in mode-locked lasers" *Opt. Express,* vol. 17, no. 25, pp. 23137-23146, 2009/12/07 2009, doi: 10.1364/OE.17.023137.

[110] D. Waldburger *et al.*, "Multipulse instabilities of a femtosecond SESAM-modelocked VECSEL" *Opt. Express,* vol. 26, no. 17, pp. 21872-21886, 2018/08/20 2018, doi: 10.1364/OE.26.021872.

[111] R. Paschotta. "Nonlinear Pulse Distortion." RP Photonics Encyclopedia. https://www.rp-photonics.com/nonlinear_pulse_distortion.html (accessed 26/10/23).

[112] E. Shlizerman, E. Ding, M. Williams, and J. Kutz, "Characterizing and suppressing multi-pulsing instabilities in mode-locked lasers" *Proc SPIE*, vol. 7933, 02/01 2011, doi: 10.1117/12.873970.

[113] C. R. Smith, R. D. Engelsholm, and O. Bang, "Pulse-to-pulse relative intensity noise measurements for ultrafast lasers" *Opt. Express*, vol. 30, no. 5, pp. 8136-8150, 2022/02/28 2022, doi: 10.1364/OE.450819.

[114] D. Eliyahu, R. A. Salvatore, and A. Yariv, "Noise characterization of a pulse train generated by actively mode-locked lasers" *J. Opt. Soc. Am. B*, vol. 13, no. 7, pp. 1619-1626, 1996/07/01 1996, doi: 10.1364/JOSAB.13.001619.

[115] M. A. Hafez, G. Afifi, A. Y. Madkhli, and S. Abdulrhmann, "Investigation of pulse-to-pulse timing jitter in an ultrafast Cr:LiSAF laser for synchronization of radiation pulses" *Optik*, vol. 274, p. 170504, 2023/03/01/ 2023, doi: https://doi.org/10.1016/j.ijleo.2022.170504.

[116] R. S. Hegde and S. Khatua, "Chapter 9 - Hot Carrier Generation in Plasmonic Nanostructures: Physics and Device Applications" in *Nanoelectronics*, B. K. Kaushik Ed.: Elsevier, 2019, pp. 289-315.

[117] R. Paschotta, "Pulse Energy" in *RP Photonics Encyclopedia*, ed.

[118] R. Paschotta, "Peak Power" in *RP Photonics Encyclopedia*, ed.

[119] "A Primer on Pulsed Measurements." Microwaves&RF. https://www.mwrf.com/technologies/test-measurement/article/21849224/a-primer-on-pulsed-measurements (accessed 28/10/23).

[120] X. Wang *et al.*, "Nanocomposites with gold nanorod/silica core-shell structure as saturable absorber for femtosecond pulse generation in a fiber laser" *Opt. Express*, vol. 23, pp. 22602-22610, 09/14 2015, doi: 10.1364/OE.23.022602.

[121] D. McAfee, "Operating Regimes and Automated Control of Holmium and Thulium Non-linear Polarisation Rotation Mode-locked Fibre Optic Lasers" M.Phil, School of Physical Sciences, University of Adelaide, 2020.

[122] P. Cheng, Y. Du, M. Han, and X. Shu, "Mode-locked and Q-switched mode-locked fiber laser based on a ferroferric-oxide nanoparticles saturable absorber" *Opt. Express*, vol. 28, no. 9, pp. 13177-13186, 2020/04/27 2020, doi: 10.1364/OE.391006.

[123] H. Ahmad, N. H. Mansor, S. A. Reduan, and R. Ramli, "Generation of mode-locked pulses based on D-shaped fiber with CdTe as a saturable absorber in the C-band region" *RSC Advances,* 10.1039/D1RA09069K vol. 12, no. 14, pp. 8637-8646, 2022, doi: 10.1039/D1RA09069K.

[124] M. Nadipally, "Chapter 2 - Optimization of Methods for Image-Texture Segmentation Using Ant Colony Optimization" in *Intelligent Data Analysis for Biomedical Applications*, D. J. Hemanth, D. Gupta, and V. Emilia Balas Eds.: Academic Press, 2019, pp. 21-47.

[125] J. Zhang, D. Wu, R. Zhao, R. Wang, and S. Dai, "Generation of 100 nJ pulse, 1 W average power at 2μm from an intermode beating mode-locked all-fiber laser," *High Power Laser Science and Engineering,* vol. 7, p. e65, 2019, Art no. e65, doi: 10.1017/hpl.2019.50.

[126] D. von der Linde, "Characterization of the noise in continuously operating mode-locked lasers" *Applied Physics B,* vol. 39, no. 4, pp. 201-217, 1986/04/01 1986, doi: 10.1007/BF00697487.

[127] YOKOGAWA. "AQ6375B Long Wavelength Optical Spectrum Analyzer 1200 - 2400 nm." https://tmi.yokogawa.com/au/solutions/discontinued/aq6375b-optical-spectrum-analyzer/#Details_Features (accessed 20/06/2023.

[128] R. Paschotta. "Optical Spectrum Analyzers." RP Photonics Encyclopedia. https://www.rp-photonics.com/optical_spectrum_analyzers.html (accessed 20/06/23).

[129] J. Li *et al.*, "Kelly sideband suppression and wavelength tuning of a conventional soliton in a Tm-doped hybrid mode-locked fiber laser with an all-fiber Lyot filter" *Photon. Res.,* vol. 7, no. 2, pp. 103-109, 2019/02/01 2019, doi: 10.1364/PRJ.7.000103.

[130] R. Paschotta. "Kelly Sidebands." RP Photonics Encyclopedia. https://www.rp-photonics.com/kelly_sidebands.html (accessed 28/10/23).

[131] N. J. Smith, K. J. Blow, and I. Andonovic, "Sideband generation through perturbations to the average soliton model" *Journal of Lightwave Technology,* vol. 10, no. 10, pp. 1329-1333, 1992, doi: 10.1109/50.166771.

[132] W. Zhao, C. Yang, and M. Shen, "Enhanced Kelly sidebands of mode-locking fiber lasers for efficient terahertz signal generation" *Optics & Laser Technology,* vol. 137, p. 106802, 2021/05/01/ 2021, doi: https://doi.org/10.1016/j.optlastec.2020.106802.

[133] Thorlabs. "Rise Time, Frequency Response, and 3 dB Bandwidth." Thorlabs. https://www.thorlabs.com/images/TabImages/Rise_Time_3dB_Bandwidth_Relationship_Lab_Fact.pdf (accessed 08/01/24, 2023).

[134] R. L. Fork and F. A. Beisser, "Real-time intensity autocorrelation interferometer" *Appl. Opt.*, vol. 17, no. 22, pp. 3534-3535, 1978/11/15 1978, doi: 10.1364/AO.17.003534.

[135] R. Trebino, *Frequency-Resolved Optical Gating: The Measurement of Ultrashort Laser Pulses*. Kluwer Academic Publishers, 2000, p. 428.

Chapter 3

[1] S. Karsten, L. Samir, K. Philipp, and F. Peter, "2 μm Laser Sources and Their Possible Applications" in *Frontiers in Guided Wave Optics and Optoelectronics*, P. Bishnu Ed. Rijeka: IntechOpen, 2010, p. Ch. 21.

[2] D. Cao *et al.*, "A 200 W diode-side-pumped CW 2 μm Tm:YAG laser with water cooling at 8°C" *Applied Physics B*, vol. 103, no. 1, pp. 83-88, 2011/04/01 2011, doi: 10.1007/s00340-010-4303-4.

[3] P. Valentin *et al.*, "Sub-100-fs bulk solid-state lasers near 2-micron" in *Proc.SPIE*, 2019, vol. 11209, p. 112094G, doi: 10.1117/12.2549618. [Online]. Available: https://doi.org/10.1117/12.2549618

[4] R. Paschotta. "YAG Lasers." RP Photonics Encyclopedia. https://www.rp-photonics.com/yag_lasers.html (accessed 04/11/23).

[5] "Laser rods - Holmium doped." Crytur. https://www.crytur.com/products/laser-rods-holmium-doped/ (accessed 04/11/23).

[6] P. Liu, L. Jin, X. Liu, H. Huang, and D. Shen, "High efficiency Tm:YAG slab laser with hundred-watts-level output power" *Applied Optics*, vol. 55, no. 10, pp. 2498-2502, 2016/04/01 2016, doi: 10.1364/AO.55.002498.

[7] R. C. Stoneman and L. Esterowitz, "Efficient, broadly tunable, laser-pumped Tm:YAG and Tm:YSGG cw lasers" *Optics Letters*, vol. 15, no. 9, pp. 486-488, 1990/05/01 1990, doi: 10.1364/OL.15.000486.

[8] E. C. Honea *et al.*, "115-W Tm:YAG diode-pumped solid-state laser" *IEEE Journal of Quantum Electronics,* vol. 33, no. 9, pp. 1592-1600, 1997, doi: 10.1109/3.622641.

[9] S. Lamrini, P. Koopmann, M. Schäfer, K. Scholle, and P. Fuhrberg, "Efficient high-power Ho:YAG laser directly in-band pumped by a GaSb-based laser diode stack at 1.9 μm" *Applied Physics B,* vol. 106, no. 2, pp. 315-319, 2012/02/01 2012, doi: 10.1007/s00340-011-4670-5.

[10] L. F. Johnson, "Optical Maser Characteristics of Rare-Earth Ions in Crystals" *Journal of Applied Physics,* vol. 34, no. 4, pp. 897-909, 2004, doi: 10.1063/1.1729557.

[11] Y. Wang *et al.*, "Broadly tunable mode-locked Ho:YAG ceramic laser around 2.1μm" *Opt. Express,* vol. 24, no. 16, pp. 18003-18012, 2016/08/08 2016, doi: 10.1364/OE.24.018003.

[12] W. Koechner, *Solid state laser engineering / Walter Koechner* (Springer series in optical sciences ; v. 1., no. Accessed from https://nla.gov.au/nla.cat-vn2145134). New York: Springer-Verlag, 1976.

[13] NKTPhotonics, "SUPERK COMPACT Product Guide" 08-2022 2022.

[14] J. Šulc, M. Němec, D. Vyhlídal, H. Jelínková, K. Nejezchleb, and J. Polák, *Holmium doping concentration influence on Ho:YAG crystal spectroscopic properties* (SPIE LASE). SPIE, 2021.

[15] M. Ganija, N. Simakov, A. Hemming, J. Haub, P. Veitch, and J. Munch, "Efficient, low threshold, cryogenic Ho:YAG laser" *Opt. Express,* vol. 24, no. 11, pp. 11569-11577, 2016/05/30 2016, doi: 10.1364/OE.24.011569.

[16] "227-W output all-fiberized Tm-doped fiber laser at 1908 nm" *Chinese Physics B,* vol. 23, no. 10, p. 104206, 2014/08/10 2014, doi: 10.1088/1674-1056/23/10/104206.

[17] W. Wang, J. Leng, J. Cao, S. Guo, X. Xu, and Z. Jiang, "Method for stripping cladding light in the High power fiber laser" *Optics Communications,* vol. 287, pp. 187-191, 2013/01/15/ 2013, doi: https://doi.org/10.1016/j.optcom.2012.09.028.

[18] K. Boyd *et al.*, "CO2 laser-fabricated cladding light strippers for high-power fiber lasers and amplifiers" *Appl. Opt.,* vol. 55, no. 11, pp. 2915-2920, 2016/04/10 2016, doi: 10.1364/AO.55.002915.

[19] A. Wetter, M. Faucher, and B. Sévigny, "High power cladding light strippers" *Proceedings of SPIE - The International Society for Optical Engineering*, vol. 6873, 03/01 2008, doi: 10.1117/12.763003.

[20] H. Y. Liu, G.-D. Peng, and P. L. Chu, "Thermal tuning of polymer optical fiber Bragg gratings" *Photonics Technology Letters, IEEE*, vol. 13, pp. 824-826, 09/01 2001, doi: 10.1109/68.935816.

[21] P. Schubel, R. Umer, and E. K. G. Boateng, "Modelling heat transfer through an FBG optical fibre" *Composites Part A: Applied Science and Manufacturing*, vol. 109, pp. 184-196, 2018/06/01/ 2018, doi: https://doi.org/10.1016/j.compositesa.2018.02.031.

[22] S. L. Buchwalter. "Glass Transition Temperature." https://www.sciencedirect.com/topics/materials-science/glass-transition-temperature#:~:text=3.1.&text=The%20glass%2Dtransition%20temperature%20(T,chemical%20structure%20of%20the%20elastomer. (accessed 20/06/23.

Chapter 4

[1] "reZonator Software" ed.

[2] J. W. Evans, P. A. Berry, and K. L. Schepler, "A Passively Q-Switched, CW-Pumped Fe:ZnSe Laser" *IEEE Journal of Quantum Electronics*, vol. 50, no. 3, pp. 204-209, 2014, doi: 10.1109/JQE.2014.2302233.

[3] S. Tomilov *et al.*, "50-W average power Ho:YAG SESAM-modelocked thin-disk oscillator at 2.1μm" *Opt. Express*, vol. 30, no. 15, pp. 27662-27673, 2022/07/18 2022, doi: 10.1364/OE.460298.

[4] S. Tomilov *et al.*, "40 W SESAM-modelocked Ho:YAG thin-disk laser at 2090 nm" in *2021 Conference on Lasers and Electro-Optics Europe & European Quantum Electronics Conference (CLEO/Europe-EQEC)*, 21-25 June 2021 2021, pp. 1-1, doi: 10.1109/CLEO/Europe-EQEC52157.2021.9542367.

[5] Y. Zhao *et al.*, "SESAM mode-locked Tm:LuYO(3) ceramic laser generating 54-fs pulses at 2048 nm" (in eng), *Appl Opt*, vol. 59, no. 33, pp. 10493-10497, Nov 20 2020, doi: 10.1364/ao.408650.

[6] Y. Wang *et al.*, "Broadly tunable mode-locked Ho:YAG ceramic laser around 2.1 μm" (in eng), *Opt Express*, vol. 24, no. 16, pp. 18003-12, Aug 8 2016, doi: 10.1364/oe.24.018003.

[7] K. Yang *et al.*, "Mode-locking of 2 μm Tm,Ho:YAG laser with GaInAs and GaSb-based SESAMs" (in eng), *Opt Express*, vol. 21, no. 4, pp. 4311-8, Feb 25 2013, doi: 10.1364/oe.21.004311.

[8] R. Paschotta, "Etalons" in *RP Photonics Encyclopedia*, ed.

Chapter 5

[1] "reZonator Software" ed.

[2] M. N. Polyanskiy, "Refractiveindex.info database of optical constants" *Scientific Data*, vol. 11, no. 1, p. 94, 2024/01/18 2024, doi: 10.1038/s41597-023-02898-2.

[3] Y. Wang *et al.*, "Broadly tunable mode-locked Ho:YAG ceramic laser around 2.1μm" *Opt. Express*, vol. 24, no. 16, pp. 18003-18012, 2016/08/08 2016, doi: 10.1364/OE.24.018003.

[4] K. Yang *et al.*, "Mode-locking of 2 μm Tm,Ho:YAG laser with GaInAs and GaSb-based SESAMs" (in eng), *Opt Express*, vol. 21, no. 4, pp. 4311-8, Feb 25 2013, doi: 10.1364/oe.21.004311.

[5] Y. Wang *et al.*, "Broadly tunable mode-locked Ho:YAG ceramic laser around 2.1 μm" (in eng), *Opt Express*, vol. 24, no. 16, pp. 18003-12, Aug 8 2016, doi: 10.1364/oe.24.018003.

[6] S. Tomilov *et al.*, "50-W average power Ho:YAG SESAM-modelocked thin-disk oscillator at 2.1μm" *Opt. Express*, vol. 30, no. 15, pp. 27662-27673, 2022/07/18 2022, doi: 10.1364/OE.460298.

[7] S. Tomilov *et al.*, "40 W SESAM-modelocked Ho:YAG thin-disk laser at 2090 nm" in *2021 Conference on Lasers and Electro-Optics Europe & European Quantum Electronics Conference (CLEO/Europe-EQEC)*, 21-25 June 2021 2021, pp. 1-1, doi: 10.1109/CLEO/Europe-EQEC52157.2021.9542367.

[8] A. Tyazhev *et al.*, "Passively Mode-locked (Tm,Ho):YLF Laser" in *Laser Congress 2018 (ASSL)*, Boston, Massachusetts, 2018/11/04 2018: Optica Publishing Group, in OSA Technical Digest, p. ATu2A.31, doi: 10.1364/ASSL.2018.ATu2A.31. [Online]. Available: https://opg.optica.org/abstract.cfm?URI=ASSL-2018-ATu2A.31

[9] C. J. Saraceno *et al.*, "Sub-100 femtosecond pulses from a SESAM modelocked thin disk laser" *Applied Physics B,* vol. 106, no. 3, pp. 559-562, 2012/03/01 2012, doi: 10.1007/s00340-012-4900-5.

[10] S. Tomilov *et al.*, "50-W, >2-μJ SESAM-modelocked Ho:YAG thin-disk oscillator at 2.1 μm" *EPJ Web of Conferences,* vol. 267, 10/18 2022, doi: 10.1051/epjconf/202226701042.

[11] S. Ezekiel, "Demonstrations in laser fundamentals Laser Transverse Modes" ed: Massachusetts Institute of Technology, 2008.

[12] Z. Tian *et al.*, "Mode-locked thulium fiber laser with MoS 2" *Laser Physics Letters,* vol. 12, p. 065104, 06/01 2015, doi: 10.1088/1612-2011/12/6/065104.

[13] Y. Zhou *et al.*, "Recent progress in passively mode-locked fiber lasers based on low dimensional nanomaterials" *Results in Optics,* vol. 9, p. 100302, 2022/12/01/ 2022, doi: https://doi.org/10.1016/j.rio.2022.100302.

[14] Y. Wang, L.-Q. Zhang, Z. Zhuo, S. Guo, D. Wei, and G. Tian, "All-normal dispersion fiber lasers with magneto-optical polarization controllers" *Appl. Opt.,* vol. 56, p. 404, 01/20 2017, doi: 10.1364/AO.56.000404.

[15] N. Davoudzadeh, G. Ducourthial, and B. Spring, "Custom fabrication and mode-locked operation of a femtosecond fiber laser for multiphoton microscopy" *Scientific Reports,* vol. 9, p. 4233, 03/12 2019, doi: 10.1038/s41598-019-40871-5.

[16] Y. Ling *et al.*, "L -Band GHz Femtosecond Passively Harmonic Mode-Locked Er-Doped Fiber Laser Based on Nonlinear Polarization Rotation" *IEEE Photonics Journal,* vol. PP, pp. 1-1, 07/10 2019, doi: 10.1109/JPHOT.2019.2927771.

[17] H. Ahmad, M. F. M. Azri, R. Ramli, M. Z. Samion, N. Yusoff, and K. S. Lim, "2 μm passively mode-locked thulium-doped fiber lasers with Ta2AlC-deposited tapered and side-polished fibers" *Scientific Reports,* vol. 11, no. 1, p. 21278, 2021/10/28 2021, doi: 10.1038/s41598-021-99928-z.

[18] D. McAfee, "Operating Regimes and Automated Control of Holmium and Thulium Non-linear Polarisation Rotation Mode-locked Fibre Optic Lasers" M.Phil, School of Physical Sciences, University of Adelaide, 2020.

[19] W. Q. Zhang, D. G. Lancaster, T. M. Monro, and S. A. Vahid, "Synchronised dual-wavelength mode-locking in waveguide lasers" *Scientific Reports,* vol. 8, no. 1, p. 7821, 2018/05/18 2018, doi: 10.1038/s41598-018-26152-7.

[20] X. Sun *et al.*, "Dual-wavelength synchronously mode-locked Nd:LaGGG laser operating at 1.3 μm with a SESAM" *RSC Advances*, 10.1039/C7RA04768A vol. 7, no. 51, pp. 32044-32048, 2017, doi: 10.1039/C7RA04768A.

[21] J. Ma, Z. Qin, G. Xie, L. Qian, and D. Tang, "Review of mid-infrared mode-locked laser sources in the 2.0 μ m–3.5 μ m spectral region" *Applied Physics Reviews,* vol. 6, p. 021317, 06/01 2019, doi: 10.1063/1.5037274.

[22] Z. Qin *et al.*, "Open Access Femtosecond and Dual-Wavelength Picosecond Operations of Nd,La:SrF 2 Disordered Crystal Laser Femtosecond and Dual-Wavelength Picosecond Operations of Nd,La:SrF 2 Disordered Crystal Laser" *IEEE Photonics Journal,* vol. 9, p. 1502007, 04/07 2017, doi: 10.1109/JPHOT.2017.2688418.

[23] T. Liu, M. Yan, Z. Guo, and H. Zeng, "Mechanisms of dual-wavelength dissipative soliton mode-locking in net-normal dispersion fiber lasers" *Results in Physics,* vol. 36, p. 105464, 2022/05/01/ 2022, doi: https://doi.org/10.1016/j.rinp.2022.105464.

[24] P. Rigaud *et al.*, "Dual-wavelength synchronous ultrashort pulses from a mode-locked Yb-doped multicore fiber laser with spatially dispersed gain" *Optics Express,* vol. 23, p. 25308, 09/21 2015, doi: 10.1364/OE.23.025308.

Chapter 6

[1] THORLABS. "Fiber End Caps." THORLABS. https://www.thorlabs.com/newgrouppage9.cfm?objectgroup_id=13120 (accessed 31/01/24).

[2] J. W. Evans, P. A. Berry, and K. L. Schepler, "A Passively Q-Switched, CW-Pumped Fe:ZnSe Laser," *IEEE Journal of Quantum Electronics,* vol. 50, no. 3, pp. 204-209, 2014, doi: 10.1109/JQE.2014.2302233.

[3] A. Kolovinos, "Experimental and Numerical Optimisation of a SESAM Mode-locked Holmium Fibre Laser" MPhil, School of Physics, Chemistry and Earth Sciences, University of Adelaide, 2022.

[4] R. Paschotta, "Pulse Pickers," in *RP Photonics Encyclopedia*, ed.

[5] M. C. T. Bahaa E. A. Saleh, *FUNDAMENTALS OF PHOTONICS*. Wiley, 2019, p. 2751.

[6] P. A. Budni, L. A. Pomeranz, M. L. Lemons, C. A. Miller, J. R. Mosto, and E. P. Chicklis, "Efficient mid-infrared laser using 1.9-µm-pumped Ho:YAG and ZnGeP2 optical parametric oscillators," *J. Opt. Soc. Am. B,* vol. 17, no. 5, pp. 723-728, 2000/05/01 2000, doi: 10.1364/JOSAB.17.000723.

[7] M. Griesbeck *et al.*, "Mid-infrared optical parametric oscillator pumped by a high-pulse-energy, Q-switched Ho^{3+}:YAG laser" *Appl. Opt.,* vol. 60, no. 22, pp. F21-F26, 2021/08/01 2021, doi: 10.1364/AO.424039.

[8] A. Penttinen, "SESAM based Q-Switched Microchip Lasers" 2020.

[9] R. Paschotta, "Rod Lasers" in *RP Photonics Encyclopedia*, ed.

[10] R. Paschotta, "Thin-disk Lasers" in *RP Photonics Encyclopedia*, ed.

[11] R. Paschotta, "Quenching" in *RP Photonics Encyclopedia*, ed.

[12] S. M. Mian, S. B. McGee, and N. Melikechi, "Experimental and theoretical investigation of thermal lensing effects in mode-locked femtosecond Z-scan experiments" *Optics Communications,* vol. 207, no. 1, pp. 339-345, 2002/06/15/ 2002, doi: https://doi.org/10.1016/S0030-4018(02)01395-0.

[13] R. Paschotta *et al.*, "Diode-pumped passively mode-locked lasers with high average power" *Applied Physics B,* vol. 70, no. 1, pp. S25-S31, 2000/06/01 2000, doi: 10.1007/s003400000269.